Investigating the Mechanism of Transgranular Stress Corrosion Cracking in Near-Neutral pH Environments on Buried Fuel Transmission Pipelines

A Dissertation
Presented to
The Academic Faculty

by

Stefanie Lynn Asher

In Partial Fulfillment
of the Requirements for the Degree
Doctor of Philosophy in the
School of Materials Science and Engineering

Georgia Institute of Technology
December 2007

Investigating the Mechanism of Transgranular Stress Corrosion Cracking in Near-Neutral pH Environments on Buried Fuel Transmission Pipelines

Approved by:

Dr. Preet M. Singh, Advisor
School of Materials Science and Engineering
Georgia Institute of Technology

Dr. Arun M. Gokhale
School of Materials Science and Engineering
Georgia Institute of Technology

Dr. Thomas H. Sanders, Jr.
School of Materials Science and Engineering
Georgia Institute of Technology

Dr. Miroslav Marek
Materials Science and Engineering
Georgia Institute of Technology

Dr. Naresh N. Thadhani
School of Materials Science and Engineering
Georgia Institute of Technology

Dr. Richard Neu
School of Mechanical Engineering *U.S.*
Georgia Institute of Technology

Date Approved: November 9, 2007

ACKNOWLEDGEMENTS

This work could not have been accomplished without the help and support of many individuals. I would like to first thank Dr. Preet Singh for his guidance, assistance, and patience in advising me in this project. I would also like to thank Battelle for providing financial support and materials for this research. I would like to recognize Jamshad Mahmood for all his assistance with research equipment and guidance. I would also like to express my appreciation to Stephen Asher, Andrew Weeks, Vikas Behrani, Melanie Kirkham, Todd Walters, Georgetta Maghiari, Tosin Ige, David Pena, Charles Andry, Charles Brookshire and Tim Banks for their help in this project.

On a personal note, I would like to thank my parents, Jan and Rusty Belcher, for the continued support and faith in me. Finally, I would like to thank my wonderful husband, Bill Asher, for his support during my graduate studies.

TABLE OF CONTENTS

LIST OF TABLES

Page

LIST OF FIGURES

Page

LIST OF SYMBOLS AND ABBREVIATIONS

EAC	Environmentally Assisted Cracking
HIC	Hydrogen Induced Cracking
SCC	Stress Corrosion Cracking
HELP	Hydrogen Enhanced Localized Plasticity
TGSCC	Transgranular Stress Corrosion Cracking
BCC	Body Center Cubic
BCT	Body Center Tetragonal
FCC	Face Center Cubic
HCP	Hexagonal Close Packed
IGSCC	Intergranular Stress Corrosion Cracking
CPR	Crack Propagation Rate
OCP	Open Circuit Potential
SMYS	Specified Minimum Yield Strength
CTOD	Crack Tip Opening Displacement
CT	Compact Tensile
SCE	Saturated Calomel Electrode
SSRT	Slow Strain Rate Test
NNPHG	Near-Neutral pH Hydrogen Generation
SEM	Scanning Electron Microscope
ICP	Inductively Coupled Plasma Spectroscopy
XRD	X-ray Diffraction
EDS	Electron Dispersive Spectroscopy

AWQ	Annealed Water Quenched
z	valences of solvated species
F	Faraday's constant
M	Molar
N	Normal
E_{corr}	Open Circuit Potential
ΔK	Stress Intensity Factor
ΔK_{th}	Threshold Stress Intensity Factor

SUMMARY

This research investigates the mechanism of transgranular stress corrosion cracking on fuel transmission pipelines. This research proposes that in near-neutral pH environments, hydrogen can be generated by the dissociation of carbonic acid and the reaction of metal ions with bicarbonate solutions, significantly increasing the available hydrogen for diffusion into the pipeline steel. This research has shown that TGSCC of pipeline steels is possible in simple groundwater solutions containing bicarbonate ions and carbon dioxide. Microstructural characterization coupled with hydrogen permeation indicates that the level of strain in the microstructure has the most influence on hydrogen diffusivity. Hydrogen accumulation occurs preferentially in at high energy discontinuous interfaces such as inclusion interfaces. It was determined that a stress concentration is required to facilitate sufficient hydrogen accumulation in the pipeline steel in order to initiate TGSCC. It was discovered that these stress concentrations develop from inclusions falling out of the pipeline surface. Slow strain rate tests found that TGSCC occurred in a wide range of compositions and temperatures as long as near-neutral conditions were maintained. Microcracks ahead of the crack tip provide evidence of hydrogen in these cracking processes. Morphology of these microcracks indicates that cracks propagate by the coalescence of microcracks with the main crack tip. Further research findings, scientific impact, and potential future work are also discussed.

CHAPTER 1

INTRODUCTION

1.1 Stress Corrosion Cracking

Environmentally-assisted cracking (EAC) is a general term given to failures that occur due to a combination of environmental exposure and tensile stress. EAC is divided into several subcategories that include corrosion fatigue, stress corrosion cracking (SCC), and hydrogen induced cracking (HIC) [1]. SCC is a brittle fracture of materials that occurs under tensile stresses that are considered to be relatively low and sometimes below yield stress. In order for this cracking type to occur, three conditions must be present simultaneously: a corrosive environment, a susceptible material, and a component of tensile stress. This is shown schematically in Figure 1. The elimination of any one of the variables will eradicate the prospective for stress corrosion cracking [1].

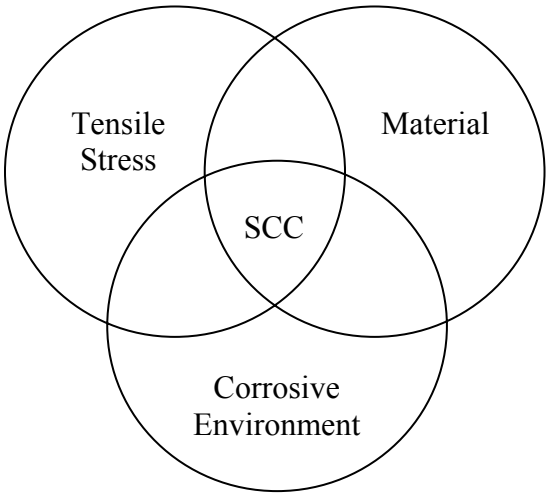

Figure 1 - Requirements to produce SCC

Research on SCC has shown that there are four broad mechanisms: anodic dissolution, film induced cleavage, atomic surface mobility and adsorption induced embrittlement. Anodic dissolution proceeds by the preferential dissolution of pre-existing active paths such as grain boundaries or solute free zones adjacent to precipitates. In this mechanism, the crack walls and tip are covered by a passive film. This passive film is ruptured by plastic strain, and active corrosion then occurs at the crack tip along the active path. The passive film then reforms on the crack tip and the process repeats producing dominantly intergranular cracking [2-4]. Environments that produce SCC are often specific to particular alloy systems and are typically found in narrow potential ranges where the passive film is unstable [1].

Film-induced cleavage is a similar mechanism but varies in that a brittle film is formed on the sample and there are no preferential dissolution paths. Plastic strain will rupture the brittle film, propagating the brittle crack some distance into the metal. The brittle crack is blunted by the plastic strain. This process repeats with the formation of further brittle film [3, 4].

Atomic surface mobility is applicable when materials exposed to environments at temperatures less than half their melting temperature. This mechanism, proposed by Galvele, suggests that environmentally assisted cracks propagate by the capture of vacancies at the crack tip. The vacancy's movement to the crack tip is countered by diffusion of atoms away from the crack tip, generally toward the crack walls and material surface. The mechanism is viable in the presence of low melting point compounds as surface mobility is maximized. However, no direct evidence of this mechanism has been obtained [5, 6].

The mechanism of absorption induced embrittlement occurs by the decrease in mechanical integrity at the crack tip due to the adsorption of selective corrosive species from the environment. This occurs most commonly with the absorption of hydrogen. Essentially, the absorbed species produced by the environment diffuses to the areas of high tensile stress ahead of the crack tip. Brittle fracture of the affected area causes the crack to advance. The crack is blunted by the plastic deformation as the crack grows past the region of embrittlement. There are several different theories on the method of mechanical degradation that depends on the loading conditions and the type of adsorbed species [1].

In the case of hydrogen embrittlement, there are several different theories on the mechanism of damage. There is no singular mechanism that can account for all cases of hydrogen induced failures, nor can all observations be accounted for by a single mechanism. The type of material, environment, and stress condition dictate the hydrogen damage mechanism. However, there are three mechanisms that are viable at room temperature: stress induced hydride formation and cleavage, hydrogen enhanced localized plasticity (HELP), and hydrogen induced decohesion [7].

Stress induced hydride formation occurs in materials that thermodynamically favor the formation of hydrides, such as titanium, tantalum, zirconium, uranium, and niobium. These hydrides are brittle, increasing the tensile strength of the material while decreasing the ductility. However, at tensile stresses, the hydride will fracture. The crack will propagate through the hydride and cease when it reaches the matrix metal. New hydrides will form either autocatalytically due to the consequence of hydride

volume dilation, or due to stresses from external loading. This process repeats until global material failure [8].

The mechanisms of HELP have been developed based on experimental observations and theoretical calculation [7]. It is based on the theory, first proposed by Beachem [9] and supported by Birnbaum [10], that the presence of hydrogen in a lattice will decrease the barrier to dislocation mobility and increase the amount of deformation that occurs in the localized region ahead of the crack tip. The area surrounding the crack tip tends to have the highest concentration of hydrogen due to the facilitated slip process or effect of stress on the chemical potential of the hydrogen [11]. This mechanism has been observed in a variety of materials with BCC, FCC, and HCP lattice structures. The underlying principle to the HELP mechanism is hydrogen shielding the dislocation elastic interactions from obstacles [12]. The fracture process consists of highly localized plastic failure rather than embrittlement [11].

The third room temperature mechanism of hydrogen embrittlement is hydrogen induced decohesion. This is the earliest proposed mechanism and is often the most cited one. This mechanism proposes that the hydrogen decreases the force required to separate the matrix along the crystallographic plane, grain boundary, or interfaces. This mechanism is supported by evidence of ab-initio calculations, theoretical calculations, thermodynamic arguments, and the fact that hydrogen embrittlement occurs in non-hydride materials without the presence of significant local deformation. However, direct evidence of hydrogen induced decohesion has still has not been obtained [7, 13].

1.2 Historical Perspective of SCC on Pipelines

Natural gas and other forms of petroleum products are transported throughout the world primarily via means of pipelines. These pipelines are often buried underground and are subjected to hoop stresses due to internal pressure along with stresses from ground shifting and other external environmental pressures [14]. To protect the pipelines from corrosion, they are typically covered with an external protective coating. Cathodic potentials between -0.85 and -1.25 V_{SCE} are also applied to protect the pipelines from corrosion. With time, however, the external protective coating often de-bonds to allow a corrosive environment to be introduced next to the pipe surface. This environment often leads to the development of SCC on the external surface of the pipeline. The danger in these external SCC incidents is that these cracks fail as ruptures rather than leaks. This causes catastrophic failures that endanger the public and can destroy large quantities of natural resources [15].

The first documented case of SCC pipeline failure was in Natchioches, Louisiana, in the mid 1960s. This was a natural gas pipeline and the failure resulted in gas release, explosion, and fire with several fatalities. It was determined that the cracking was intergranular and was caused by a high pH, concentrated bicarbonate environment. SCC leading to reportable incidents has occurred mainly on gas pipelines, but SCC has also caused incidents on a few liquid transmission pipelines [15]. Since this initial failure, pipeline companies have recorded type and cause of failures. In 2006, the Office of Pipeline Safety, within the U.S. Department of Transportation Pipeline and Hazardous Materials Safety Administration, reported that external corrosion accounted for 22 incidents with more than 4.5 million dollars worth of property damage and caused 3

injuries with 1 fatality. In 2005, the 25 incidents of external corrosion came to over 101 million dollars in damage [16].

Intergranular Stress Corrosion Cracking (IGSCC) was the prodominent form of cracking until three in-service failures occurred between 1985 and 1986 on the Trans-Canadian natural gas pipeline in Northern Ontario. These failures revealed a new type of transgranular stress corrosion cracking (TGSCC). Subsequent re-evaluation of previous pipeline failures has traced this form of cracking back to the late 1970's [17]. This type of cracking was thought to be associated with cold temperatures, but a number of failures have shown that TGSS problem is not unique to Canada, with incidences occurring on pipelines in Australia, Iran, Iraq, Italy, Pakistan, Saudi Arabia, Russia, and the United States [14].

1.3 Intergranular Stress Corrosion Cracking on Pipelines

Intergranular stress corrosion cracking of pipelines is associated with conditions where the protective coating covering the pipe fails, allowing the pipe to be exposed to a corrosive media. However, the cathodic current still reaches the pipe surface. This results in a concentrated environment of bicarbonate, carbonate solution with pH of greater than 9.3 [18]. In this high pH environment, the pipeline forms a magnetite film with incorporation of small quantities of iron carbonate [19]. Researchers have determined that the mechanism of IGSCC is anodic dissolution at the crack tip. At the crack tip, periodic stress cycling causes a cyclic process of passive film formation, rupture and subsequent dissolution. These films are adherent to the crack sides, preventing lateral dissolution of the crack walls and producing a sharp, narrow crack. This is beneficial for crack modeling as the crack morphology is retained over the whole

crack propagation process [19, 20]. This has allowed research to determine that the kinetics of the initiation and growth are similar for IGSCC of pipeline steel [4].

Researchers have been able to calculate the crack propagation rate based on the dissolution current densities measured on the bulk metal [21]. The propagation rate is based on Farday's law and is given by:

$$CPR = \frac{i_a \cdot M}{z \cdot F \cdot d} \quad \textbf{(1)}$$

where CPR is the crack propagation rate, i_a is the anodic current density, M is the atomic weight, z is the valences of solvated species, F is Faraday's constant, and d is the density of the metal [22].

Because IGSCC mechanism is based on the dissolution process, controlling parameters of IGSCC are "reasonably well understood" [23]. Therefore the rate limiting factors would be the same factors that control corrosion [15]. It has been determined that the rate limiting step is the formation of passivating Fe_3O_4 film that ruptures to expose bare pipeline material. The rate of film formation is controlled by three environmental factors: potential, temperature, and solution composition. The formation of Fe_3O_4 film is possible in a narrow potential rate [15]. Laboratory simulation of IGSCC exposes samples at -650 mV_{SCE}. Further, there is a strong correlation between IGSCC and temperature with over 90 percent of IGSCC failures occur within 16 km downstream of a compressor station where the temperature can be 75^{o}C or higher [24]. Laboratory work has shown that the IGSCC propagation rate increases according to an Arrhenius relationship with temperature [22]. Temperature also increases the stability of the potential within the critical range, increasing the range of strain rates at which the cracking will occur [25]. Subsequently laboratory tests to produce IGSCC are performed

at 70°C. Finally, crack velocities increase with solution concentration. Subsequently, laboratory simulated IGSCC are produced in 1 N Na_2CO_3 and 1 N $NaHCO_3$ solutions [23].

Cracks form in colonies usually located on the bottom surface of the pipeline in the longitudinal orientation along the pipe [22]. There have been a few cases of transverse cracking, but these cases involve a secondary stress such as a dent or bending due to ground movement. IGSCC has been associated with hoop stress levels around 60% yield stress. In cases were SCC of low stress pipelines was reported, there has always been secondary loading or a stress concentration [15]. These cracks coalesce to form long, shallow flaws that ultimately lead to rupture [26]. Based on field failures, it has been determined that the average age of the pipeline at the time of failure from IGSCC is 22.9 years [15]. IGSCC has been associated with pipelines coated with coal tar, asphalt and tap coatings that allow for cathodic protection to reach the pipe [22]. Most reported cases are on tar coated pipelines; however, this may be circumstantial as tar coatings are found on older pipelines that simply may have had more opportunity to crack. It has been determined that SCC on pipelines tends to occur in soils that are alternately wet and dry. SCC occurs frequently in clay soils that have moisture draining across or along the pipeline. SCC also tends to form at the bottom of hills where ground water my easily accumulate. However, areas that are continuously wet, such in rivers or lakes, have little tendency to form SCC [15].

1.4 Transgranular Stress Corrosion Cracking on Pipelines

For TGSCC, field data and fractography of failed pipeline sections have provided the most concrete information [27]. TGSCC is characterized by a quasicleavage fracture

surface which is mixture of smooth brittle features and ductile dimpling. Fracture surfaces often have secondary, internal cracks not connected to the outside surface. Field observation relates the formation of significant amounts of white powder, identified as iron (II) carbonate and corrosion products, surrounding the crack walls [28]. TGSCC occurs in patches along the pipe surface and has been found on pipes that also have IGSCC. In these areas of high density, cracks can interact and coalesce with each other to make bigger cracks that can grow faster and add to the severity on high pressure gas pipelines [22]. Two thirds of TGSCC incidents are axial cracking. The larger frequency of transverse cracking is attributed to the difference in the pipeline profiles that suffer SCC [15].

The TGSCC crack morphology is distinct from IGSCC in that TGSCC cracks experience significant lateral dissolution and produce moderately adherent corrosion products in the crack features. The dissolution of the crack walls destroys the crack path, so the transgranular nature can only be established near the crack tip where there has been little opportunity for dissolution [19].

CHAPTER 2

PRIOR RESEARCH ON TRANSGRANULAR STRESS CORROSION CRACKING ON PIPELINE STEEL

Dolgov et al. performed an in-tube inspection of two gas pipelines of a single 110 km section of a multi-line pipeline in Russia. Inspection reported the number of flaws and stress corrosion cracks detected and depth range of these features. It was determined that most flaws had a depth of 33% of wall thickness, regardless of location on the pipe and distance from compressor station, which is the location of highest stress and temperature. Maximum flaw density was 25-30 km from the compressor station and had the largest flaws at 44% and 55% of wall thickness. The inspection also determined that there were twice as many SCC than general corrosion flaws. It was determined that there was no connection between weld seams or edge pipe zones in the development of SCC. However, SCC had a tendency to form near the compressor station, although cracks were detected along the entire length of the inspected pipeline. This is attributed to the higher pressure and stress at these locations. Further, it was discovered that SCC flaws had no correlation to depth and width. Longer cracks were neither the deeper nor wider cracks, indicating the method of crack growth was the coalescence of smaller cracks [29].

Chen et al. characterized the appearance and distribution of two near-neutral crack patches from an X-65 pipeline that ruptured after 19 years of service. They determined that in one patch the interspacing of cracks was greater than 20% of the wall thickness and defined as sparse crack patch. The second patch had an interspacing of parallel

cracks was less than 20% of wall thickness and was defined as a dense crack patch. In the dense patch, cracks were blunt, wide, and filled with corrosion products. The dissolution of the crack was not limited to the crack tip but occurred along the whole crack surface. There were several observed cases of crack-like defects at the bottom of pits. Developed crack crevices at the crack mouth were very wide, indicating that cracks initiated at round spots at the pipe surface. Also, the direction of small cracks was along the orientation of hoop stress direction. Crack depth and length distributions were not significantly different between the two observed patches of cracks. Further, there was a direct relationship between the crack width and the crack depth. When observing the relationship between crack depth and crack length it was determined that there were two classes of cracks. The first class was linked cracks that developed due to the coalescence of smaller cracks. These features had at least two depth maxima along the length of the crack. The second type of crack was independent cracks that had a single depth peak. It was determined that the linked cracks were considerably longer than the independent cracks. The linked cracks were generally shallower than independent cracks and appeared to grow in the length and width direction rather than in depth. This led Chen et al. to define these cracks as dormant. The dormancy of these features was attributed to the crack coalescence accompanied by active corrosion in the width direction [30].

2.1 Material

Carbon steel that is used in the oil and gas industry, specifically in the United States, is manufactured following guidelines issued by the American Petroleum Institute (API) specification 5L [31, 32]. These pipelines vary in diameter from 114 to 1067 mm and vary in wall thickness from 3.2 to 9.4 mm. Pipeline steels are made of carbon steels

which comes in a range of compositions, shown in Table 1, with carbon content ranging from 0.18-0.30 weight percent [33]. The API 5L specifications regulates the manufacturing by mechanical requirements, such as yield strength, tensile strength, and fracture toughness, rather than with elemental composition or microstructure requirements. There are a few limitation of elements such as carbon, manganese, sulfur or phosphorous to ensure weldability, formability or corrosion resistance. However, the limit of these monitored elements differs between seamless, welded, and cold work pipes. This leads to a significant variation in compositional and microstructural properties between pipes of the same grade [31].

Table 1 - Chemical composition and material properties of selected pipeline steels. Chemical compositions given in weight % and signify the maximum amount allowed by API specifications [32]

Steel	C	Mn	P	S	Minimum Yield Stress		Minimum UTS	
					psi	MPa	psi	MPa
X-52	0.30	1.35	0.3	0.3	52000	358	66000	455
X-65	0.26	1.40	0.03	0.03	65000	448	77000	530
X-70	0.23	1.60	0.03	0.03	70000	482	82000	565
X-80	0.18	1.80	0.03	0.018	80000	551	90000	620

Over the past 40 years, the demands on pipeline operation have evolved pipeline processing and material composition. Initial pipeline steel manufactured in the 1950s and 1960s were hot rolled and normalized with higher carbon content. In the 1970s, processing changed to thermomechanical rolling, creating pipelines steel grades to X-70. These steels were microalloyed with niobium and vanadium to reduce the carbon content and increase strength. In the 1980s, accelerated cooling was added to the thermomechanical rolling process to further reduce the carbon content and enhance field

weldabilty. These processing charges are used to produce the X-80 grade pipeline. Recently, additions of molybdenum, copper, and nickel have been added to produce the X-100 grade pipeline [34].

As the pipeline steel manufacturing method developed, so did the microstructural features such as grain size, dislocation density, grain boundaries, and precipitates. The difference in the combination of these features attributes to an increase in the strength and toughness of carbon steels. For X-60 pipeline steels, thermomechanical processing results in ferrite grain size reduction of the ferrite grains, improving both strength and toughness. The decrease in pearlite content is compensated by precipitation and dislocation hardening. X-80 pipeline steel microstructure is unique in that the rapid cooling process produces a ferrite-bainite microstructure as compared to the standard ferrite-pearlite microstructure of lower API grades. The lower carbon content also results in further reducing the grain size and increasing dislocation density [34].

Since pipelines can vary in elemental composition, Grabke and Riecke performed a series of exposure tests in hydrogen environments of either water purged with hydrogen gas or electrolytic charging in 1 M H_2SO_4 to determine the effect of alloying elements on corrosion and hydrogen adsorption. It was determined that copper, chromium, and silicon decrease the corrosion rate and hydrogen absorption. This is due to silicon decreases hydrogen solubility. It was determined that chromium acts as hydrogen traps, which is a microstructural feature that binds to hydrogen prohibiting its diffusion through the metal. Phosphorous was found to increase the corrosion rate. Hydrogen absorption is increased by the presence of sulfur, selenium, arsenic, antimony, and tin. In exposure tests it was determined that during the corrosion process sulfur and carbon becomes

enriched at the surface. In contrast, silicon and chromium are preferentially dissolved and are depleted at the surface. Nickel has no significant effect. Tin and copper experience minor dissolution, becoming slightly enriched at the surface and ultimately decreasing the corrosion rate [35].

To form the banitic steel, pipelines are alloyed with molybdenum, vanadium, niobium, titanium, and zirconium to form fine carbides and nitrides that pin grain boundaries and dislocations. These precipitates also act as hydrogen traps, making the pipeline more susceptible to hydrogen embrittlement. In studying the effect of elemental additions, it was determined that alloyed pipeline steel has less permeation as compared to pure iron. This is attributed to the precipitates reducing the cross sectional area free for diffusion and forming regions of compressive stress. Non-steady state measurement of effective diffusion demonstrated the effect of alloying elements and precipitates. It was found that hydrogen diffusivity is inversely proportional to the atomic size of the alloying element. The carbide and nitride precipitates decreased the diffusivity by one order of magnitude. This is attributed to the high energy of flat and deep traps. Whereas, hydrogen solubility was proportional to the atomic size with hydrogen traps and extended interstitial sites being created near the alloying substitutional atoms. Further, vanadium and zirconium are potential hydride forming elements [35].

Pipelines have been manufactured in varied ways [36]. The vast majority of large diameter pipelines are produced by one of the seam-welded processes, while smaller-diameter pipeline are typically constructed from either seamless or electrical resistance welded line pipe. Seamless pipeline is hot formed into cylinder shape from solid bars of steel. Seam welded plates are formed by pressurized high temperature lap welds of

overlapped edges of steel plate or by ambient temperature welds from flat rolled plates or coil strips [36].

The evolution of manufacturing practices means that the microstructure of existing pipeline can be varied with differing amounts of ferrite, pearlite, and bainite. Further there can be significant variations in the grain size due to varied controlled rolling procedures in the manufacturing process. In spite of both significant and subtle differences in the chemical composition and microstructure of existing line pipe, there is no strong evidence that any of the differences either promote or inhibit TGSCC [36]. TGSCC appears to have no correlation to manufacturing method or manufacture, with one exception being the electric-resistance weld longitudinal seam pipe manufactured in the 1950's by Youngstown Sheet and Tube. The weld seam in this pipe had lower resistance than the base metal due to lower facture toughness. Pits and arc burns were reported to lead to higher than normal residual stresses [14].

Asahi et al. assert the uniformity in the microstructure of pipeline steel as the key factor in its susceptibility to TGSCC [33]. This was also asserted by Kushida et al. in their study of different variations of X-65 pipeline. They found that the effect of microstructure on TGSCC was predominating when comparing steels of the same level of strength. Steels with inhomogeneous microstructures, such as ferrite-pearlite, had the highest susceptibility. Uniform banitic structures were least susceptible. They also asserted that if the microstructure is homogenous, the susceptibility will be dependent on the strength with lower strength steels being more resistant to TGSCC [37].

It has been well asserted that the pipelines with banitic structures are superior to that of standard pearlite/ferrite microstructure. To explore this effect on TGSCC, Kimura

et al. performed pre-notched flat tensile SSR tests with ferrite/pearlite steel and banitic steel formed by quench and tempering. They found that no SCC occurred on banitic steel that was stressed up to the yield strength. However, SCC was found in the ferrite steel. They found that in the banitic steel, the material had a uniform structure with very little area of plastic deformation at the notch tip. In contrast, the ferritic steel had large plastic deformation at the notch tip and lower microhardness [38].

Chu et al. furthered this research by demonstrating a strong correlation between metallurgical discontinuities such as pearlite colonies, grain boundaries, and inclusion to crack initiation in X-65. These sites experienced localized corrosion and microcrack initiation [39, 40]. This was confirmed by Wang et al. who found that crack initiation in simulated groundwater solutions is dependent on the inhomogeneties at the surface. They found that crack initiation sites are related to stress raisers, which encompass inclusions, microstructural defects, or surface irregularities. Most laboratory samples are polished to a smooth finish, but the surfaces of field pipelines are rough and discontinuous. Most of the inhomogeneties were nonmetallic inclusions that form pits at the early stages of exposure to a corrosive environment that further develop into crack with continued exposure. Crack initiation can also be influenced by other pre-existing cracks or defects, leading to crack coalescence [41].

2.2 Environment

These pipelines are often buried underground, and are typically covered with an external protective coating to protect the pipelines from corrosion. TGSCC occurs in wide range of geographic locations with soil types ranging from the sandy and fine to clay and rock type [30]. From a study performed by TransCanandian Pipeline (TCPL) on

excavated pipelines, it was determined that clays and silts are 7.5 times more prevalent to develop TGSCC as compared to sands and gravels. This is because the clay drains poorly and results in the retention of the ground water and cracking environment [19]. Poorly drained soils provide a source of water; however, areas that have constant high moisture have a lower probability of producing TGSCC than the areas where the moisture levels fluctuate [14]. Organic and mineral composition of the soil varies from one location to another. Jack et al. examined the solutions found under disbanded polyethylene tape coating at a site in Alberta, Canada. They determined that differences between groundwater and trapped electrolyte at the pipeline surface were relatively small. Major ions present in extracted pipeline solutions were determined to be bicarbonate, sulfate, chloride, calcium, magnesium, and sodium [28].

Chen et al. sought to determine if certain soils have more propensity of SCC by examining the soil samples collected from locations of TGSCC on TCPL. Their work established that the soil varied from highly organic to inorganic and varied in mineral content as shown in Table 2. Since there were only four soil extracts in their study, they were unable to quantitatively determine the effect of soil chemistry. However they qualitatively determined that the presence of CO_2 is more critical than the soil chemistry. The major chemical components effecting SCC were calcium and bicarbonate with chlorides having a minor effect. The final pH and open circuit potential was a function of HCO_3^- ions [42].

Table 2 - Analysis of Soil Extracts[42]

Element (mg/L)	**Soil 1** Sandy till	**Soil 2** Organic+Clay	**Soil 3** Organic	**Soil 4** Organic
Calcium	59.0	66.6	9.2	21.0
Magnesium	12.5	14.7	2.7	4.0
Potassium	1.94	3.02	1.82	<1.0
Sodium	4.8	12.3	8.0	17.3
Iron	0.22	0.45	0.44	0.55
Manganese	0.672	0.082	0.038	0.051
Bicarbonate	249	283	29.9	58.0
Chloride	2.6	16.1	18.8	3.9
Sulfate	4.7	3.7	3.1	51.4

Probably the most extensive study on the reaction of pipeline steel with carbonate-bicarbonate environments found to cause pipeline SCC was performed by Parkins and Zhou. Using slow strain rate samples, they subjected pipeline steel to dilute and concentrated bicarbonate solutions with varying levels of carbon dioxide. They found that the type of cracking was bounded by concentration of the solution and subsequently the pH and potential. Transgranular cracking was found to occur at lower potentials below the active-passive range of film formation and above the potentials where hydrogen discharge is possible for the pH values of the solutions tested. Further, they observed a transition from intergranular to transgranular as the concentration of bicarbonate increased and as the potential was increased. This indicates that the potentials of the cracking domain are related to the concentration of carbonates and bicarbonates and subsequently the pH of the solution. They found that the bounds of each type of SCC are related to a particular pH and concluded that these regimes were related to relative ratios of carbonate and bicarbonate ions in solution that controlled the overall mode and mechanism of cracking [43, 44].

To simulate the environment that initiates TGSCC, several synthetic solutions have been created. Based on the analysis of solutions from the initial failures, solutions termed NS1, NS2, NS3, and NS4 were developed to simulate TGSCC environments in the laboratory. The range of compositions for these solutions is sodium bicarbonate (480 – 1000 mg/L), potassium chloride (40 - 150 mg/L), calcium chloride (10 – 180 mg/L), and magnesium sulfate (90 – 250 mg/L). NS1 was developed to simulate environment from a specific region of pipeline with severe cracking. NS2 simulates major cracking regions where the concentration of bicarbonate ions is greater than 10 mmol/L. NS3 was developed to simulate the mean value of combined major and minor cracking regions [45]. Whereas, NS4 solution seems to have become the standard for crack propagation experiments in most laboratories. Testing in each synthetic environment showed no difference in crack susceptibility [19]. However, the specific role of the ions in TGSCC mechanism is yet to be discovered. So far it has been very difficult to reproduce cracks in the laboratory with characteristics similar to the ones found on pipelines [6, 46, 47].

It was originally thought that anaerobic environments were required in order to obtain a near-neutral pH environment [14]. Johnson et al. demonstrated that oxygen decreases the rate of hydrogen permeation and increases the corrosion potential by reducing the reduction reactions that generate hydrogen. Oxygen can block hydrogen entry by adsorbing atomic hydrogen or facilitating the formation of corrosion products on the metal surface. However, their work also indicated that providing 10% oxygen purging in the test environments increased the crack growth rates. Their results also indicated that the effects of oxygen were small in comparison to the effect of carbon dioxide [48]. The effect of oxygen was further studied by Gu et al. who showed that

there was a decrease in reduction of area for samples exposed to air rather that that purged with inert gas [49]. Further, testing of precracked samples in aerobic and anaerobic environments by Ahmed et al. showed that precracks exposed to aerobic environment results in extensive secondary corrosion, producing wide precracks. However, in anaerobic environments, the precracks remained narrow with a small crack tip radius. This indicates that the presence of oxygen may facilitates the anodic dissolution that has been observed on crack sides of field failures [50].

Analysis of samples of liquid collected from under the coatings revealed the pH to be approximately 6.5. However, the pH of the solution could be slightly lower as the liquid was effervescent when removed with a hypodermic syringe. This suggests the presence of an evolving gas, most likely CO_2 [19]. Soil analysis near TCPL reported by Delanty and O'Beirne established that the CO_2 concentrations vary between 23% and 4% depending on the season with the lower range occurring in the winter and higher values in spring. The ground water chemistry also fluctuates seasonally, becoming more acidic and concentrated during the winter months [17].

To study the magnitude of seasonal changes in pipeline environment conditions and cathodic protection, King et al. performed an extensive 2-year study of twelve in-service pipelines in a wide range of geographic locations in Canada and U.S. During this study, field measurements of soil resistitivity, redox potential, corrosion rate, soil pH, temperature, and precipitation were made on unbonded coupons installed next to the pipeline and coupons attached to the pipeline. It was found that significant variations in cathodic protection and environmental conditions occurred due to seasonal shifts. Soil resistitivity varied considerably during the year with a minimum occurring in the summer

and spring and a maximum occurring in the winter. The decrease in resistitivity in the spring and summer months is attributed to the increase in rainfall that occurred at the measurement sites. Seasonal fluctuations were also observed in measurement of the redox potential, which is a measure of the relative amount of oxidant, or dissolved oxygen. It was determined that the wetter, lower resistive soils tended to be anaerobic. These fluctuations resulted in the pipelines being marginally cathodically protected in the early winter months, when precipitation is at a minimum. However, measurements made on New Mexico, U.S. sites show that episodic rainfall events do not have a large impact on polarization levels. Rather, long term seasonal trends are more important to the pipeline environment [51].

Since the environment of TGSCC is at near-neutral pH, it was initially thought that the corrosion was due to microbial bacteria. These bacteria reduce sulfate to sulfide and can degrade the coating adhesive. Microbial metabolism is also associated with production of carbon dioxide, so the presence of the bacteria could contribute to the presence of bicarbonate. However, no microbial bacteria have been found at the Canadian sites of TGSCC. Further, cultures of soil samples taken from in-service failures have not produced any sulfide reducing bacteria [28].

Pipelines experience a range of temperatures depending on weather conditions as well as distance from a compressor station. Highest temperatures occur at the compressor station and decay with distance. There is a higher tendency for TGSCC to take place at locations of lower temperatures whereas IGSCC cracks are more abundant at higher temperatures. According to Delanty and O'Beirne, 50 percent of TGSCC failures occurred within 16 km downstream of a compressor, and more than 20 percent

have been more than 30 km down stream of a compressor station. They attribute this trend to the higher solubility of CO_2 in water at lower temperatures [17]. Parkins et al. performed slow strain rate tests at a range of temperatures from 5°C to 45°C on an X-65 steel. Their findings show that cracking is unrelated to temperature and, subsequently, distance away from a compressor [19]. However, there was significant scatter in their data that could mask any apparent trend. Further work by Parkins et al. found that transgranular cracking was only observed at ambient temperatures in a study where samples were tested from 23°C to 80°C [44].

Cathodic protection is applied to pipelines to protect against corrosion by forcing the potential of the steel to a range outside of active dissolution. If any cathodic current reaches the pipeline, hydroxyl ions will be generated and the pH will increase favoring formation of HCO_3^- ions and potentially creating the environment of IGSCC [18]. TGSCC is associated with carbon steel of pipelines where the cathodic protection has failed or was working inadequately. It has been established that the pH values depend on the partial pressure of CO_2 and the potential of the steel. In the absence of cathodic protection, the pH of the trapped solution depends upon the equilibrium between dissolved CO_2 and the bicarbonate ions present. The environment at the pipe surface is dynamic with seasonal influences and changing water levels. It is possible that the pipe can experience conditions where they receive intermittent cathodic current or no current.

Rebak et al. found X52 line pipe steel in 0.1 N and 0.01 N HCO_3^- at 50°C actively dissolved above E_{corr} and showed passive behavior. However, passivity does not occur in the presence of sulfate or chlorite ions [52, 53]. As the concentration of bicarbonate ion decreased the passive region increased. Tests with applied cathodic potentials showed

TGSCC occurrence increases as the potential decreased whereas the tests at anodic potentials showed lower susceptibility with increasing potentials. Similar results were found by Gu et al. [49]. They asserted this trend as evidence that TGSCC mechanism is that of hydrogen embrittlement [52]. The presence of passive behavior, however, has not been agreed upon. Further, the passive behavior observed by Rebak was at temperatures beyond TGSCC incident. Anodic curves in groundwater solutions produced by Johnson et al. showed evidence of either pseudo-passiviation behavior or ohmic potential drop. Cathodic polarization tests have not typically been performed, but cathodic kinetics exhibit linear behavior, indicating that anodic kinetics may be pseudo-passivation. This means that any films formed decelerate anodic kinetics but are not protective [48].

2.3 Stress

Pipelines experience stresses due to internal pressure along with stresses from ground shifting and other external pressures. Fuel transmission pipelines are designated by their specified minimum yield strength (SMYS) in ksi which vary from 35 (241 MPa) to 70 (483 MPa) [14]. Natural gas is compressed to pressures as high as 8,700 kPa (1260 psi) in transmission pipes [14]. Pipelines are regulated to limit maximum operating stress up to 85% of the specified minimum yield strength (SMYS), yet most operate to only 75 % SMYS [14]. Although pipelines are designed as statically loaded structures, they operate with fluctuating pressure and stress [18]. Gas transmission pipelines tend to have small amplitude cycling along with a high mean pressure due to the variations in supply and demand [54]. Further, it has been shown that pipelines have unevenly distributed residual stress, and SCC tends to initiate in areas of high residual stress [39].

Most studies performed on TGSCC in terms of stress have been performed using slow strain rate testing. This testing technique rapidly strains the sample in the proposed environment. The constant elongation forces the specimen to deform at a give rate, overriding the creep and strain hardening properties of the material. This allows for electrochemical effects such as dissolution and passivation kinetics to be emphasized [55]. A consequence of this technique is that crack growth can be sensitive to the strain rate. Typical elongation rates used for SCC testing of carbon steels are in the vicinity of 10^{-6} inch/sec. Even at such slow strain rates, crack growth rates are still very low. Subsequently, most researchers also report reduction of area data to demonstrate the change in ductility [56].

2.3.1 Initiation

For TGSCC, researchers have suggested five factors that influence crack initiation: inclusions, aligned surface defects, persistent slip bands, preexisting defects, and coating disbondment. In field construction of pipeline steels, the pipe surface is grit blasted before applying the protective coating. This is to ensure better bonding and even application of cathodic protection. Grit blasting will also induce compressive stresses at the pipe surface.

However, most pipelines develop a millscale on the surface, and it has been determined that the millscale enhances susceptibility to SCC. The millscale consists of a mixture of magnetite (Fe_3O_4) and maghemite (γ-Fe_2O_3) along with trace levels of iron carbonate. The structure of millscale is porous and cracked, allowing for easy transport of environment through the structure [57]. The coexistence of different iron oxidation states allows the millscale to be electrochemically active and catalytic towards the

cathodic reduction of water and oxygen. This cathode reaction accelerates the anodic dissolution at the bottom of the millscale [58]. This contributes to the development of pits in the scale that can hold the potential within the critical pitting potential range. These pits also act as areas of stress concentration allowing the SCC to initiate at lower stresses than for a polished sample [22]. Millscale tends to develop perpendicular to the maximum hoop stress along the longitudinal direction of the pipeline. This produces elongated pits that can initiate aligned longitudinal cracks [58]. Parkins et al. performed SSRT with flat tensile samples with one polished side and one side with mill coating. It was found that no cracks formed on the polished surface where the mill scale surface was highly susceptible to SCC [19].

Kimura et al. assert that TGSCC initiates at the bottom of pits. As a result, they assume that the initiation and early stages of crack growth account for approximately 90% of failure time [38]. The average age of pipelines that have TGSCC incidence is 21.3 years [15]. To produce TGSCC failures in a laboratory environment, they pre-pitted flat tensile samples with either Vickers hardness indentations or Charpy test V notches. They found that crack initiation depended on the degree of plastic deformation. Subsequently, no TGSCC cracks were produced on Vickers indented samples. This was attributed to Vickers indentation producing local work hardening that prohibited plastic deformation by tensile stress. Charpy V notches, however, produced little work hardening at the notch tip, allowing plastic deformation to occur during tensile testing. Charpy V notches also produced an area of stress concentration that is larger than Vickers indentation [38].

Yunovich et al. further examined the effect of work hardening by creating tensile samples with different degrees of cold deformation by crimping the sample with bending dies. Samples subjected to greater than 20% cold work strain behaved similar to samples pulled in air. This suggests that mechanical factors are more prevalent above 20% strain and that more heavily cold worked samples fail mechanically before any corrosion can occur. However, samples subjected up to 20% cold work strain exhibited an increase in susceptibility [59].

Work performed by Parkins and Beavers indicated that TGSCC cracks were associated with pits that had formed at inclusions exposed to the surface. Initial slow strain rate tests performed by Parkins et al. were executed using samples cut from the pipe in the longitudinal and transverse directions. It was determined that there was no dramatic change in stress corrosion susceptibility or reduction of area with orientation [19]. However, there were some differences in the tendency for cracks to develop. Longitudinal samples cracked mainly in the necking region, even when there was substantial reduction in ductility. The transverse samples cracked over the whole gauge length [19]. This is attributed to X-65 pipeline steel samples that are cute transversely to the rolling direction have a relatively large number of inclusions exposed to the surface [56].

Slow strain rate tests were performed by Parkins and Beavers to examine crack initiation and crack growth rates. SEM of the samples that were removed from straining prior to necking indicated that cracks were associated with pits. They also observed that secondary cracks tended to form at 45^{o} from stress direction. This cracking at 45^{o} is indicative of hydrogen influence with shear localization. It is interesting to note that in

this study, early cracking appeared to follow an intergranular path rather than the transgranular path that occurs in deep, long term cracking. Samples that were strained until failure showed that the deepest cracks occurred in the necked region of the fractured specimen. This is due the continuous deformation and increased rate of deformation in the necking region. Metallography of the failed samples also showed that cracks were associated with pits although not all pits formed cracks. Pits often initiated at nonmetallic inclusions that were exposed at the surface. It was also determined that some pits grew from arrested cracks with pit depth being two or three times their width [56].

2.3.2 Propagation

Once the protective coating has been breached and a corrosive environment accumulates next to the pipeline surface, a colony of small shallow cracks form on the pipe surface. Most of these cracks are innocuous and have been shown to be dormant. However, some of them propagate to become significant cracks to compromise the integrity of the pipeline. To fully understand the mechanism of TGSCC, the factors that cause crack growth from a small crack to a propagating crack must be understood. For pipeline situations the process is very complex, accounting for changing environment and varying stresses.

Fessler and Krist reviewed the observed TGSCC crack growth rates on pipelines. They reported that the crack growth rate can decrease by several orders of magnitude and has even been observed to stop at early stages of growth. This crack dormancy would account for the fewer failures that occur in service compared with the number of cracks discovered during inspection. Only 1 percent of the 1900 SCC colonies excavated on TCPL pipelines after 15 years of service had cracks over 10 percent of the wall thickness.

Only 4 percent of the colonies had cracks deeper than 5 percent of the wall thickness [55]. To examine this phenomenon they subjected precracked specimens of X-60 pipe steel in near-neutral pH environments to static and cyclic loads at varying frequencies. Measuring crack depth, they found that there was no obvious trend for greater depths at longer times. Many of the samples stopped growing within the first few weeks. The cracks that continued to grow were subjected to higher stresses and larger stress fluctuations than what would be experienced in service. They proposed several reasons for crack deceleration in a constant environment and stress conditions: creep exhaustion, chemical species depletion, resistant microstructural features, and depletion of residual tensile stress [55].

Parkins et al. performed cyclic tests in NS4 solution at OCP using flat tensile samples that still had millscale. They observed no correlation between crack numbers and time or between crack density and time. However, crack velocity did increase with crack density. This is attributed to the enhanced probability of crack coalescence. Cracks did appear to form in bands indicating the site for crack nucleation was dependent or related to the location of existing cracks. It was also determined that initial growth of cracks was due to coalescence, but the later growth was dominated by growth of an individual cracks [19].

The combination of stress and operating temperature allows for static creep to occur. This creep is limited by the work hardening that results in an increase in internal stress. This internal stress can reduce the net force on mobile dislocations and reduce the rate of plastic strain. This reduction of plastic strain will stop the cracking process unless the decrease in strain rate is countered by crack extension or inelastic straining. It is

unlikely that inelastic straining will be able to support the cracking process as inelastic straining is usually depleted in the early lifetime of the pipeline. Therefore it is also unlikely that static creep is the cause of stress corrosion cracking [54].

Parkins and Evans studied the effect of cyclic loading on creep in C-Mn steel. They found that creep is sensitive to small reductions in stress. This creep sensitivity translates to low stresses acting on mobile dislocation. When the applied stress is removed, recovery occurs due to dislocations moving back to their original positions. This movement and alteration of the microstructure significantly affects crack growth [60]. Parkins et al. found that cyclic loading enhances the microplastic deformation and facilitates cracking in near-neutral environments. If a pre-cracked specimen is allowed to creep while being exposed in solution at a non-cracking potential, the crack does not grow further when potential is brought to cracking range even if the stress intensity factor is above K_{Iscc} [18].

A fracture mechanics approach was adopted by some researchers to study the growth of a single TGSCC crack with precracked compact tensile (CT) samples. Hagiwara et al. considered the linear-elastic behavior not applicable to pipeline conditions since they assumed that cracking does not occur in the elastic range [61]. Instead they used crack tip opening displacement (CTOD) testing on X-65 pipeline steel subjected to cathodic protection. Cathodic over-potential, however, had no effect on δ_c at larger testing rates, so to evaluate the effect of the cathodic current, loading rate had to be lowered to less than 0.01 mm/min. As the current density on the sample decreased, the δ_c increased. With the results of the CTOD testing, they calculated the maximum tolerable defect size to be about 11 mm but determined that since δ_c depends on cathodic

protection conditions so does the maximum defect size [61]. Although this research provides correlation of the defect size and crack tip opening displacement, the assumption that cracking does not occur in the elastic range is not valid for stress corrosion cracks. Also, TGSCC occurs in high density patches of cracks. These small cracks interact with each other to either suppress crack growth or accelerate crack growth by coalescing [26]. Studying a single crack is not indicative of the actual environment, crack initiation and growth, and stress dynamics that are experienced by field pipes.

Fracture mechanics has also revealed the changes in crack tip morphology during propagation. Guo et al. found that the morphology changed with changes in stress intensity factor and the environment. Initially, when the cracks were small and had low stress intensity factor amplitude (ΔK), and the environment determined crack behavior. As ΔK increased, growth rate increased and cracks grew in length but remained tight with no evidence of surface plastic deformation. When ΔK reached 24.8 $MPa \cdot m^{0.5}$, the crack opening widened and plastic slip occurred. During this stage, cracks appeared transgranular with sharp crack tips. As ΔK increased further, crack tip widened. Once the crack had reached K_{max}, the crack propagation exhibited unstable growth and the crack tip split. These changes indicate the role of environment was dominate until the beginning of propagation, and propagation was dominated by mechanical influences [62]. While this information is suitable for liquid pipelines that have high cycle rates, it is less important for gas pipelines that have very few cycles of sufficient ΔK to explain observed cracking [58].

Work on crack propagation by Parkins and Beavers indicated that crack velocity decreases with increasing time. However, the slope of the line relating crack velocity

with time increases with increasing pH, indicating that the cracking process is related to hydrogen ingress. Further, the slope of this line is less than negative one. This indicates that the deepest crack formed early in the test but had stopped propagating before failure occurred. The arrest of crack growth is incompatible with stress-based arguments as the stress intensity factor will increase with increasing crack depth and load. Crack velocities will decrease with time if there is work hardening in the crack tip region or localized changes in the environment. A decrease in crack velocity could also be due to the increase of crack number with time, resulting in changes in the crack tip strain rate [56].

Gabetta et al. sought to further explore the relationship between crack velocity and loading conditions. Slow strain rate testing has a competitive relationship between loading due to the loading frame and unloading due to crack growth. Subsequently, tests were performed with rising loading conditions under load control. This was accomplished by using notched CT specimens. Results indicate a decrease in plasticity due to environmental effects. However, the load corresponding to onset of crack growth for SCC was comparable to pure mechanical damage, indicating that the SCC process is more time dependent than stress dependent [6].

Harle and Beavers performed work to identify crack driving force parameters and to evaluate the effect of environment and mechanical parameters on crack propagation. They used J-integral and CT tests with electric potential drop to measure crack growth. They found that crack propagation occurred with significant plastic deformation. Plots of J-integral versus crack velocity showed a monotonic relationship, suggesting that J-integral was an adequate parameter for crack propagation [46].

2.4 Evidence of Hydrogen on TGSCC

Quasicleavage fracture surface and secondary, internal cracks on failed line pipes indicate that the hydrogen is involved in the mechanism of TGSCC on pipeline steels. Further, potentiodynamic polarization measurements made in near-neutral environments on pipeline steel do not demonstrate significant anodic current density to account for the crack growth rates experienced by TGSCC [56]. Subsequently, research has been focused on understanding how hydrogen interacts with pipeline steel. Research has been performed in both TGSCC groundwater environments and standard hydrogen producing environments in order to characterize hydrogen interaction in terms of environment, microstructure and stress.

2.4.1 Hydrogen Generation in Carbon Dioxide Enviroment

It has been established that the environment of TGSCC is based on the ion species of carbonate that form through the dissociation of carbon dioxide into the groundwater that accumulate next to the pipeline surface. Carbon dioxide corrosion is not a new phenomenon on pipelines and often occurs on the inside of the pipelines when contamination is introduced into the pipeline. Carbon dioxide corrosion or "sweet corrosion" has been reported to cause 25% of safety incidents, 2.2% of tangible asset and 5% lost/deferred production. Corrosion of carbon steel in carbon dioxide environment is a complex phenomenon that still requires further examination [63].

The corrosion process starts by gaseous carbon dioxide dissolving in water to form the carbonic acid, a weak acid, in the following reaction:

$$CO_2 + H_2O \Leftrightarrow CO_2 - H_2O \cong H_2CO_3 \Leftrightarrow H^+ + HCO_3^- \quad \textbf{(2)}$$

The debate in literature is the rate determine step in the proceeding reaction of the acid's reaction with steel. Schwenk proposed that carbonic acid provides a source of hydrogen

ions by cathodic hydrogen evolution [64]. This method of hydrogen generation asserts that there a direct production of hydrogen by the dissociation of carbonic acid in the presence of free electrons. These reactions assume an oxygen free environment and are as follows:

$$(HCO_3^-)H^+ + e^- \Rightarrow H \quad \textbf{(3)}$$

Whereas, de Waard and Milliams propose that carbonic acid is directly reduced at the steel surface producing reactions [65]. These reactions are as follows:

$$H_2CO_3 + e^- \Rightarrow H + HCO_3^- \quad \textbf{(4)}$$

$$HCO_3^- + H^+ \Leftrightarrow H_2CO_3 \quad \textbf{(5)}$$

Finally, Ogundele and White proposed that bicarbonate ions are reduced directly as follows [66]:

$$HCO_3^- + e^- \Rightarrow H + CO_3^{-2} \quad \textbf{(6)}$$

$$HCO_3^- + H + e^- \Rightarrow H_2 + CO_3^{-2} \quad \textbf{(7)}$$

However, the Ogundele reactions are only viable during alkaline pH conditions. Further, the Schwenk and deWaard reactions have yet to be proven. Crolet et al. have proposed a mechanism of anodic dissolution with iron at different pH conditions in high pressure environments [67].

Further, the concentration of dissolved carbon dioxide and the mass transport of to the steel surface are critical to the reaction rate. Every species present in the environment can contribute the cathodic reactions. Subsequently, the solution chemistry in contact with the pipeline is critical to the acidification and buffering capacity of the environment [63].

Parameters that influence carbon dioxide corrosion are environmental, physical and metallurgical. Corrosion scale plays an important role in the mechanism as well as the kinetics of CO_2 corrosion on pipeline steels. When a protective scale is present, the rate controlling factor becomes the mass transfer to and from the metal surface rather than the cathodic hydrogen evolution rate. This invalidates the de Waard-Milliams mechanistic theory as corrosion becomes nonuniform and localized. A protective scale has been shown to reduce the rate of general corrosion by 3 orders of magnitude, effectively reducing the corrosion rate to zero [68]. Subsequently, the importance of a protective film in CO_2 corrosion is well recognized and studied. However, there are still several issues that have yet to be resolved. These issues include quantifying scale protection, understanding the kinetics of the corrosion process in the presence of scale, and understanding how environmental variables affect the proactive nature of the scale [68].

2.4.2 Hydrogen Embrittlement of Carbon Steel

A very important component to hydrogen embrittlement is the initial transport stage. Hydrogen atoms must be adsorbed and absorbed into the material. Then hydrogen must diffuse either by lattice diffusion or dislocation transport to internal microstructural defects, heterogeneities, traps or lattice site [69]. The rate of hydrogen entry can be defined by the hydrogen concentration just below the surface as this concentration will be in constant contact with the source of hydrogen. However, this concentration cannot be directly measured and must be determined by indirect measurements of either the hydrogen absorbed by the sample, the mechanical properties that are affected, or the permeation rate through a membrane. Measurement of absorbed hydrogen depends on

the rate of entry, shape of specimen, and the time of hydrogen charging. Time is a key variable as it must be sufficient enough to attain steady state and hydrogen saturation. The other issues with hydrogen absorption measurements are that hydrogen can absorb in the interstitial solid solution, structure defects such as dislocations, and as molecular hydrogen in blisters/interfaces. Measurement of hydrogen effect by measuring mechanical properties depends primarily on the character and extent of irreversible changes. Therefore, these measurements may fail to correlate the rate of hydrogen entry.

The most common method of hydrogen study is permeation, which measures the extent of hydrogen flux through a membrane/sample. This process depends exclusively on the hydrogen entry process. Hydrogen permeation can be divided into three stages, each characterized by their respective resistance. The permeation rate is therefore inversely proportional to the sum of the three resistances. The first stage is hydrogen entry. The membrane must be sufficiently thick in order to minimize the resistance of this first stage and model diffusion of hydrogen into the bulk material. The second stage is diffusion of hydrogen in the membrane. It is desirable to make this stage the largest resistance in order for permeation to measure directly diffusion. The final stage is the exit of hydrogen from the membrane. If a suitable anodic potential is maintained, all of exiting hydrogen ionizes. This means that the concentration of hydrogen is effectively zero and the resistance of this stage can be ignored [70].

Several researchers have performed hydrogen permeation tests to observe the direct evidence of hydrogen ingress into pipeline steels under near-neutral pH conditions. Work done by Parkins and Beavers was performed at range of pHs in NS4 solutions at various potentials. They found that at pH values of 6.3 and 5.1 hydrogen permeation was

limited by the formation of carbonate films on the charging side of the cell. This also occurred at potentials lower than $-1V_{SCE}$. It was also determined that hydrogen permeation was dependent on the concentration of CO_2 in the system. The absorption of CO_2 in the test solutions to obtain a pH of around 6.3 resulted in a half-an-order of magnitude increase in the hydrogen ingress as compared to solutions without CO_2 with a pH of 8.3. In studying the trapping effect of hydrogen, it was determined that X52 pipeline had the highest amount of traps whereas X-60 has the lowest density. This correlates to the quantity of pearlite in their structure and associated carbon content [56].

Scoppio et al. performed a series of electrochemical permeation tests on X-65 pipeline steel and pure iron to determine the relevant contributions to diffusion and diffusion rates. Using 2.5 mm thick samples and standard solution of 0.1 N NaOH, they found that for the X-65 steel the maximum anodic current density was $7.2x10^{-3}$ A/m^2 and the diffusion coefficient was approximately 4 to 5 $x10^{-10}$ m^2s^{-1}. This is contrasted with a diffusion coefficient in pure iron of 1 to 2 $x10^{-9}$ m^2s^{-1}. These values are slightly less than what is reported elsewhere in the literature. They attributed this to unsteady electrochemical reactions occurring at defect sites that produced non-steady state diffusion. This was due to oxide layer growth on the input surface of the metal, where hydrogen enters the metal, and the passive layer growth on the anodic side of the sample. Therefore, passive layer controlled the hydrogen diffusion rate [71].

To determine the effect of environmental parameters, hydrogen permeation has also been performed using groundwater solutions instead of standard NaOH solutions. Johnson et al. performed permeation to determine the effect of CO_2 and O_2 concentration on hydrogen permeation. They found that increasing CO_2 concentration resulted in an

increase in hydrogen permeation and a decrease in breakthrough time. In contrast, permeation decreases with increasing oxygen concentration. This is attributed to the addition of another reduction reaction that minimizes the generation of hydrogen [48]. Beavers et al. performed permeation tests to determine soil environments that produced maximum hydrogen flux. They discovered no apparent trend in breakthrough time or permeation rate for the different environments [72].

In studying the effect of cathodic charging, Hardie et al. found that cathodic charging of X-60, X-80 and X100 steel tensile samples in 0.5 M sulfuric acid and straining in air caused reduced ductility regardless of steel strength level. In all cases of charging, microcracks were observed parallel to the major rolling direction of the steel and along the banded microstructure. Several of these microcracks were intergranular but final fracture was consistently transgranular. However, if the sample was allowed to sit in air for 7 days, all ductility was recoverable even though microcracks were still present. This was attributed to desorption of hydrogen and indicates that the primary cause of hydrogen embrittlement is due to hydrogen in solution rather than microcrack formation due to charging [73].

Hydrogen ingress has also been studied in terms of cathodic reactions produced by cathodic potentials. He et al. generated hydrogen by cathodic potentials ranging from OCP to -1.5 V_{SCE} in NS4 solutions. Hydrogen ingress was characterized by LECO RH-402 hydrogen determinator and hydrogen permeation testing. They discovered that trapped hydrogen accounted for only 20% of hydrogen that diffused into the steel. They also determined that hydrogen ingress was strongly influenced by formation of carbonate

films and that dependence of flux on cathodic potential is greater for samples with carbonate film [74].

Yan and Weng also examined the amount of hydrogen that enters the steel in comparison to the hydrogen that recombines to form molecular hydrogen. Using monocell hydrogen permeation method, they found that the hydrogen retention was 0.01 to 0.1 percent using the equation:

$$R = \frac{Q}{i_c t} \quad \textbf{(8)}$$

where R is the retention ratio, i_c is the current in the charging process, and t is the charging time. They attribute this low retention ratio to surface saturation. Once the surface is saturated with hydrogen, hydrogen will no longer diffuse easily into the steel and would preferentially form molecular hydrogen [75].

In examining the hydrogen mobility and distribution, Luppo et al. performed hydrogen microprinting to examine the effect of microstructure on hydrogen diffusion. They used a ferritic carbon-manganese steel with low sulfur content heat treated to develop different microstructures. They found that hydrogen preferentially accumulated at cementite, ferrite-cementite interface and inclusion-matrix interfaces. More hydrogen was detected in pearlite than ferrite, and they attributed this to the larger hydrogen specific saturation at Fe_3C interfaces. Microstructure consisting of lamellae pearlite had low quantity of desorbed hydrogen, high steady state flux, and low hydrogen embrittlement susceptibility [76].

The effect of alloying on hydrogen diffusion was further studied by Albert et al. who focused their studies on the influence of alloying elements chromium and molybdenum in carbon steel [77]. Their results indicate that increasing alloy content

resulted in a decrease in diffusion of hydrogen and an increase in solubility. They attributed this behavior to an increase in trapping sites created by additional binding energy of solute atoms and dislocations. They also observed the increase in carbon equivalent, which is another representation of hardness and weldability, resulted in a decrease in hydrogen diffusivity. They also reiterate that hydrogen has a higher diffusivity in fully ferritic microstructure than in martensitic [77].

Microprinting was also used to study the effect of stress and strain induced defects using three point bending samples. Studies by Ohmisawa indicate that straining substantially increased the hydrogen adsorption of low carbon steel under charging conditions. Microprinting showed hydrogen accumulation along ferrite boundaries and in pearlite grains in non-deformed specimens. In strained samples, slip bands were the preferred site of hydrogen accumulation. When strain samples were annealed, no silver particles were detected. This indicates that the defects that previously acted as hydrogen traps were annealed out of the sample [78].

2.4.3 Role of Stress on Hydrogen Ingress

The effect of stress on hydrogen ingress and distribution was also studied by Qiao et al. using compact tensile samples of X-80 and X52. Theses samples were loaded with a wedge in NS4 solution. Hydrogen distribution was determined by secondary-ion mass spectroscopy (SIMS) with a spot diameter of 50 micron and sequential measurements were taken along the notch direction. The intensity of hydrogen measured was converted to absolute concentration of hydrogen by molten method gas chromatography. Results indicate that hydrogen accumulates at two locations ahead of the crack tip. The first location of accumulation is directly in front of the crack tip and the second is about 1 mm

from the crack tip. In solutions acidified to pH of 3, hydrogen concentration was measured to be more than 7 ppm in front of the crack tip and around 6 ppm at 1 mm from the crack. Samples subjected to cathodic potential showed the same distribution of hydrogen as samples at OCP [79]. To determine the effect of K_I on hydrogen distribution, loading was changed by using wedges of different thickness. It was determined that the concentration of hydrogen increased with increase in K_I. Distance between hydrogen concentrations also increased with increasing K_I [80]. This accumulation of hydrogen at the crack tip is accounted for by the plastic zone in front of the crack tip and the concentration of dislocations. Stressed specimens develop an elastic stress field with a singularity. The singular stress is relaxed due to plastic deformation at the crack tip and the formation of dislocation sources. The interaction energy of hydrogen and a dislocation is approximately 20 kJ/mol and even greater for hydrogen and dislocation core. Subsequently, dislocations act as strong traps for hydrogen, leading to a high localized hydrogen concentration in areas of high dislocation density. This makes the hydrogen concentration proportional the plastic strain. The second location of hydrogen accumulation can be accounted for by hydrostatic stress area ahead of crack tip that occurs in the presence of a local tensile stress gradient [79, 80].

Nagu et al. examined the effect of heat treatment on hydrogen ingress of X-65 pipeline steel using delayed failure with notched tensile samples. They tested as received controlled-rolled samples and normalized microstructures. They determined that an incubation time was required to accumulate hydrogen to a critical concentration at the region of stress concentration where the crack nucleates. The crack will propagate when the hydrogen reaches the critical concentration to reduce the cohesive strength and grow

until the crack reaches beyond the hydrogen saturated region. In the as-received sample, it was determined that grain boundaries and dislocations at the ferrite-carbide interface acted as hydrogen traps and delayed the transportation of hydrogen through the sample. This resulted in a long incubation period. The normalized sample had a course grain structure and low dislocation density, resulting in rapid diffusion and short incubation period [81].

Parkins and Beavers examined the role of hydrogen by pre-exposing samples to TGSCC solution and then straining the sample in the TGSCC environment. Samples pre-exposed to TGSCC solution and then strained in environment showed reduced ductility. Samples pre-exposed in solution but strained in air had similar reduction in area values with samples simply strained in air. Gu et al. also found similar results [49]. The restoration of ductility when samples were removed from solution and strained in air, even at high strain rates to minimize loss of hydrogen to atmosphere, was constant for all steels and environments tested. This was attributed to hydrogen adsorption being enhanced by deformation. This means that TGSCC requires the presence of hydrogen generating solution and stress simultaneously [56].

These results were similar to those found by Fang et al. who pre-charged samples with high pressure hydrogen gas conditions prior to testing [82]. Samples that were precharged with hydrogen and strained in TGSCC environment were subjected to hydrogen content measurements post failure. It was determined that these samples had approximately 29 ppm hydrogen whereas samples that were strained in environment without precharging had only 1.5 ppm hydrogen. This discrepancy of hydrogen intake was attributed to the weak intake of hydrogen at OCP. In cases of SCC on pipelines, it is

asserted that hydrogen entry to the pipeline is induced by the presence of strain. The strain can be divided into elastic and plastic strain. To independently examine each type of strain, cyclic tests were performed in TGSCC environment at stress considered to induce elastic strain. Samples did not fail after 143.9 hours (10 cycles) so they were broken by continuous straining. The fracture surface was slightly quasi-cleavage. However, when samples were cycled under plastic straining conditions it took very few (60) cycles to fail and much higher hydrogen content was measured. Therefore, it was asserted that plastic deformation was necessary in order to observe significant hydrogen effects [82].

There is some difficulty in using slow strain rate testing to observe the effect of hydrogen on tested materials. Since SSRT exposes the sample to large amounts of plastic deformation, the amount of damage that hydrogen causes would not be realistic to the general surface of pipelines that are not loaded to yield strength. Hydrogen can reduce the ductility of the sample strained to failure without producing multiple cracks. However, the same amount of hydrogen in steel at stresses below yield stress may not have any detrimental effect. To simply account for reduction of area data is dangerous when considering operating pipelines [55]. Subsequently, specimens must be metallographically examined to further detect evidence of embrittlement and indications of the cracking process.

2.5 Previous Theories on the Mechanism of TGSCC of Pipeline Steel

Transgranular stress corrosion cracks on pipeline steel have shown preferential attack of ferrite grains exposed to the TGSCC environment at OCP. Subsequently, it can be assumed that dissolution does occur in the region of crack tip. This is consistent with

the evidence of dissolution of crack walls on failed field pipelines. However, even the highest current density measured on pipelines can not account for the observed crack growth rates at relevant strain rates in terms of simple anodic dissolution model of TGSCC.

There is also evidence of hydrogen with the presence of secondary internal cracks and quasicleavage fracture surface. Hydrogen involvement in the mechanism of TGSCC could simply be to promote dissolution at OCP. However, the involvement of hydrogen is yet to be understood [56]. Further, any mechanism that accounts for TGSCC must also explain the generation of hydrogen in a near-neutral environments and the presence of large amounts of $FeCO_3$ associated with such cracks in the field.

2.5.1 Anodic Dissolution

One characteristic of near-neutral pH stress corrosion cracking on pipelines is that the crack walls are significantly dissolved. This feature has led researchers to propose two potential mechanisms. The first is that TGSCC occurs in an active potential region above potentials that create cathodically charged hydrogen. The second is that cathodic protection leads to hydrogen induced cracking with periods of anodic dissolution when cathodic protection is not available to pipeline surface.

Puiggali et al. examined the behavior of pipeline steel surface under a range of cathodic currents to identify the optimum conditions to initiate cracking. The pipe surfaces are assumed to be void of cathodic current because of the coating failure. Further, local electrochemical potential measurements of buried pipelines have indicated that both anodic and cathodic potentials are experienced by the same pipeline. The polarization curve showed no active-passive behavior of pipeline steel in simulated

groundwater. They found that low cathodic polarization (up to -1.15 V_{SCE}) suppressed dissolution but did not produce sufficient hydrogen to embrittle the steel. At high cathodic polarization, or overprotection, large amounts of hydrogen were produced, facilitating hydrogen induced cracking. The most crack initiation occurred with alternating polarization that caused ingress of hydrogen [83]. However, their experimentation did not form $FeCO_3$. Instead a protective layer of $CaCO_3$ was deposited at cathodic potentials.

Vasil'ev et al. explored the theory that internal or residual stresses can activate and localize the anodic dissolution process, termed activated anodic dissolution. Potentiodynamic polarization of pipe steel in fresh soil taken near a removed service pipe showed no passivity. Activated anodic dissolution requires a range of passivity and a passive-active transition because it involves the rupture of passive film. The lack of any passive region indicates that TGSCC can not be caused by activated anodic dissolution of cracks; rather anodic dissolution would result in the general uniform corrosion of the surface [84].

Gu et al. proposed that the mechanism of TGSCC is anodic dissolution leading to pitting. This theory postulates that as the anodic potential nears OCP, local dissolution occurs to create pitting on the surface of the material. Within these pits, acidification occurs to create a hydrogen environment to simulate crack initiation and growth. However, this theory is countered by the evidence that addition of chlorides, which increase the pitting probability, did not affect the susceptibility of the steel in the near-neutral environment [49].

Further concern regarding the theory of anodic dissolution is the discrepancies of crack velocities. Faraday's Law predicts a crack velocity of 10^{-8} mm/sec according to the anodic current density of 10 microamps/cm^2 measured near open circuit potential in cracking environments [85]. However, field and laboratory cracks have a velocity of typically 10^{-6} mm/sec. This discrepancy of two orders of magnitude from Faraday's Law casts further doubt as to the credibility that the TGSCC mechanism for pipeline steel is purely due to anodic dissolution [36].

2.5.2 Corrosion Fatigue

Since pipelines experience variable stress, some researchers assert that the mechanism of TGSCC is simply corrosion fatigue. Pipelines experience random stress patterns depending on the demand and the type of transported fuel [54]. Further, cycles in pipelines consist of periods of activity and periods with no stress [86]. Level of cycling also depends on the type of fuel transported. Gas lines tend to have an average of 10 cycles a year. Liquid lines have an average of over 2500 cycles yearly with an R ratio of less than 0.5. This is due to the compressible nature of the fuel type. As the gas is highly pressurized, a significant amount of gas must be removed from the pipe to experience a load drop. However, liquid fuel is virtually incompressible and the pressure can change with flow rate and other variables that do not entail the removal of fuel from the line. Subsequently, fatigue work is more appropriate for liquid transmission pipelines [58]. Further, the rate of change in pressure as well as the R ratio depends on the nature of the fuel. Liquid pipelines can experience rapid changes from minimum to maximum stress because of the incompressible nature of liquid. It has been recorded that this extreme loading can take as little as 15 minutes. Gas transmission pipelines do not

experience such drastic changes. It requires more than 24 hours to experience the same change in stress [58].

Based on the cycling history of the pipelines, cyclic tests have been performed to determine the relationship between cycling and stress corrosion cracking. Most work has been performed in IGSCC environments, but the stressing behavior can be related to TGSCC as well [26]. Cyclic testing in pipeline environment show that pipeline steel exhibit a cycle dependent creep that follows a power law relationship, dependent on cycles, for approximately the first 500 cycles. This is equivalent to approximately 1.5 years. As cycling continues, the work hardening causes the creep rate to decrease. However, with further application of cycles, the creep process is reactivated. This reactivation is cyclic softening and can be numerically predicted using constitutive equations. It is believed that the long term SCC process on pipeline is due to cyclic-softening [54].

Eadie et al. performed cyclic fatigue testing on pipeline steel in dilute near-neutral environments exposed to 10% CO_2 and determined that there is a strong effect of frequency on the cracking process. Decreasing the frequency by a factor of ten resulted in $10^{0.5}$ increase in the cracking rate. The fatigue curves produced when cycling at an R ratio between 0.65 and 0.85 showed a threshold stress intensity factor (ΔK_{th}) that is followed by a horizontal plateau until the ΔK reaches the fatigue for the material in air or the onset of plastic instability. The plateau value was dependent on the frequency with higher values occurring at lower frequencies. The ΔK_{th} could not be determined but their results suggested it was below 10.7 MPa $m^{0.5}$ [86]. This is a lower value than what had been determined by Beavers and Jaske who had determined that the ΔK_{th} was between 13

and 21 $MPam^{0.5}$ for the X-70 pipeline steel in NS4 solutions exposed to 5% CO_2. This discrepancy of ΔK_{th} suggests that the threshold is not only frequency dependent but is also solution dependent. This counters the perception that TGSCC is solely a corrosion fatigue phenomenon. Cracks growing from initiation to depths where the ΔK is above ΔK_{th} for crack propagation is not accounted for with corrosion fatigue. Pipelines experience significant cycling around an R ratio of 0.65 [86].

The ΔK_{th} of 10 $MPam^{0.5}$ determined by Eadie et al. results would be achieved with a stress of 75% yield stress and a crack depth of 2 mm. The required crack depth would increase with stress and it is conceivable that stress enhancement could occur by stress raisers like pits, scratches, or residual stress. However, even with stress enhancement, it is unlikely that corrosion fatigue is the dominate mechanism of TGSCC as there must be some explanation of how cracks grow to the critical crack depth in order for corrosion fatigue to be effective crack growth mechanism to produce TGSCC [86].

Work on precracked X-70 pipeline samples with cyclic loading in NS4 solution by Ahmed et al. showed that low frequency and high R ratio induced microvoid coalescence mixed with flat transgranular fracture to produce quasi-cleavage fracture surfaces. Further, SEM observations of the fracture surface did not have the frequency dependent striations typically detected in fatigue failures. They also determined that preconditioning the sample in the environment under static load resulted in the highest crack growth rate. They attribute this to the time-dependent accumulation of hydrogen at the plastic zone ahead of the crack tip at the beginning of each test [50].

Zhang et al. used fatigue testing to try to establish a crack growth model for TGSCC cracks [87]. They determined that under cyclic loading conditions crack growth

rates were highest at low frequencies due to the extended time for environmental crack growth to occur. They also observed that the crack growth occurred during static loading. Subsequently, they applied a superposition model, adding the growth rates of static EAC and fatigue in air, to express the total environmental crack growth rate, as follows:

$$\left.\frac{da}{dN}\right|_T = \left.\frac{da}{dN}\right|_f + \left.\frac{da}{dN}\right|_{EAC} \quad \textbf{(9)}$$

where $\left.\frac{da}{dN}\right|_T$ is the total cyclic crack growth rate, $\left.\frac{da}{dN}\right|_f$ is the cyclic crack growth rate in air and $\left.\frac{da}{dN}\right|_{EAC}$ is the cyclic EAC crack growth rate. The cyclic EAC crack growth rate can be given by:

$$\left.\frac{da}{dN}\right|_{EAC} = \frac{da}{dt} \times \frac{dt}{dN} = \left.\frac{da}{dt}\right|_{EAC} \times \frac{1}{f} \quad \textbf{(10)}$$

where $\left.\frac{da}{dt}\right|_{EAC}$ is the static environmentally assisted crack growth rate and f is the cyclic frequency. Although this superposition model fit some data, it assumes a constant static growth rate. The work presented had significant variation in static crack growth, so the crack growth may not be continuous. Further work would be required in order to validate this model of crack growth.

Further discrepancies in the perception of TGSCC as a corrosion fatigue phenomenon are that stress cycles are not regular and are stochastic in nature. There is an often large delay between cycles that can lead to crack tip blunting and reduced stress at the crack tip [58].

2.5.3 Hydrogen Embrittlement

Some researchers assert that TGSCC is simply Hydrogen Induced Cracking (HIC). HIC is a brittle fracture caused by permeation of atomic hydrogen into the lattice structure of an alloy. The mechanism of HIC is still not fully agreed upon, but there are several proposed theories of which the prominent ones are outlined in Section 3.1. However, not all characteristics of HIC are applicable to TGSCC. For example, TGSCC is thought to occur without the presence of cathodic protection, whereas in HIC removal of cathodic protection reduces and stops cracking. Further, Parkins and Zhou found that TGSCC was associated with potentials in the active range above the potentials where hydrogen discharge is possible. They concluded that TGSCC occurred at potentials and higher pH than that required for HIC in the same solution [43].

2.5.4 Hydrogen Facilitated Anodic Dissolution

Mao, Luo et al. developed a theory of hydrogen-facilitated dissolution. This approach considers the synergistic effect of stress and the presence of hydrogen. When hydrogen is generated, it will move to the highly stressed zone. This accumulation of hydrogen changes the internal energy and entropy of the material, which may increase the anodic dissolution rate [88]. Hydrogen that is trapped within the steel causes lattice dilatation and decreases the interactive atomic cohesion. They also assert that hydrogen will decrease the stability of any passive film. To support their theory, they exposed CT tests to NS4 solution with 5% CO_2 for 72 hours. The CT specimens were pre-fatigued and loaded with a wedge to different factors of stress intensity. After the 72 hours they used secondary-ion mass spectroscopy (SIMS) to determine hydrogen distribution along the notch direction. They found that hydrogen accumulated at the crack tip and hydrogen

concentration deceased sharply with distance away from crack tip. Hydrogen concentration at the crack tip increased when the pH of the solution decreased, when cathodic potential was applied, or when stress intensity factor increased. They associated stress intensity to induce plastic strain [88]. They also performed potentiodynamic polarization tests with and without pre-charging with hydrogen to observe the effect of hydrogen on anodic dissolution. Results from these tests indicate that pre-charging pipeline steel could deteriorate the passivation behavior in high concentration bicarbonate environments. Further, pre-charging increased the anodic current in NS4 solutions as well as concentrated and dilute bicarbonate environments [89]. However, slow strain rate tests showed that pre-charging did not play a role in SCC. At high anodic potentials, general dissolution occurred; whereas at cathodic potentials, hydrogen constantly entered the steel and the hydrogen concentration exceeds the value obtained by pre-charging [89].

With these results, they performed a thermodynamic analysis on the interaction between stress and hydrogen to outline the change in free energy during the corrosion process. The simplistic reaction that occurs during the corrosion of a metal in aqueous solution is:

$$M + 2H^{+} \Leftrightarrow M^{+2} + H_2 \qquad \textbf{(11)}$$

It is asserted that this reaction is the same reaction that occurs in the high stressed regions at the crack tip. However, the electrochemical potential and the reaction rate between the corrosion reaction occurring at the crack tip and in the bulk are different. This change in potential attributed solely to the change in free energy, $\Delta G_M(\sigma, H)$. Consider the free energy of bulk corrosion reaction to be ΔG_1, and the free energy of the corrosion reaction

at the crack tip to be ΔG_2. Subsequently, the electrochemical potential, E, of the corrosion reaction at equilibrium can be presented as:

$$\Delta G_1 = G_{M^{+2}} + G_{H_2} - G_M - 2G_{H^+} = -nFE_1 \quad \textbf{(12)}$$

$$\Delta G_2 = G_{M^{+2}} + G_{H_2} - G_M(\sigma, H) - 2G_{H^+} = \Delta G_1 - \Delta G_M(\sigma, H) = -nFE_2 \quad \textbf{(13)}$$

where n is the number of electrons exchanged in the reaction and F is the Faraday's constant. The $\Delta G_M(\sigma, H)$ term is caused by the presence of stress and hydrogen in the metal.

The anodic dissolution current in the bulk corrosion reaction, without the presence of stress and hydrogen, is given as:

$$i_A = i_o \exp\left(\frac{-\Delta G_1}{RT}\beta\right) = i_o \exp\left(\frac{nFE_1}{RT}\beta\right) \quad \textbf{(14)}$$

where β is the charge-transfer coefficient and i_o is the exchange current density. Further, the dissolution current at the stress crack tip can be given as:

$$i(\sigma, H) = i_o(\sigma, H)\exp\left(\frac{-\Delta G_2}{RT}\beta\right) = i_o(\sigma, H)\exp\left(\frac{-\Delta G_1 - \Delta G_M(\sigma, H)}{RT}\beta\right) \quad \textbf{(15)}$$

Since hydrogen and stress does not change $i_{o,}$, then equation (5) can be represented as:

$$i(\sigma, H) = i_A \exp\left(\frac{\Delta G_M(\sigma, H)}{RT}\beta\right) \quad \textbf{(16)}$$

At constant pressure, i.e. stress and constant temperature, $\Delta G_M(\sigma, H)$ can be equated as:

$$\Delta G_M(\sigma, H) = \Delta U - T\Delta S + P\Delta V \quad \textbf{(17)}$$

where ΔU is the internal energy, ΔS is the change in entropy, P is the pressure, and ΔV is the volume change. In terms of this system, pressure can be equated to the negative of

the stress at the crack tip. The internal energy and entropy are functions of the chemical composition and temperature but not the applied stress.

When there is no stress, P is zero and:

$$\Delta G_M(\sigma = 0, H) = \Delta U - T\Delta S \quad \textbf{(18)}$$

$$i(\sigma = 0, H) = i_A \exp\left(\frac{\Delta U - T\Delta S}{RT}\beta\right) = k_H i_A \quad \textbf{(19)}$$

where k_H is a hydrogen factor. When stress is applied, work is done on the metal. This work can be represented as two terms. The first term, W_1, is the strain energy density. The second term, W_2, is the interaction energy between the strain field of hydrogen atoms and the stress field. When stress is applied without the presence of hydrogen then ΔU, ΔS, and W_2 are zero. This means that W_1 can be given as:

$$W_1 = \frac{M\left(\sigma_1^{\,2} + \sigma_2^{\,2} + \sigma_3^{\,2}\right)}{2E\rho} \quad \textbf{(20)}$$

where M is the molar weight, σ_i (i=1,2,3) are the principle stresses, E is the Young's modulus, and ρ is the density. Substituting equation 10 and its constraints into equation 6 and 7 yields the effect of stress on anodic dissolution rate:

$$i(\sigma, H = 0) = i_A \exp\left(\frac{W_1}{RT}\beta\right) = i_A \exp\left[\frac{M(\sigma_1^{\,2} + \sigma_2^{\,2} + \sigma_3^{\,2})}{2E\rho RT}\beta\right] = k_{\sigma_1} \times k_{\sigma_2} \times k_{\sigma_3} i_A \quad \textbf{(21)}$$

where $k_{\sigma i}$ (i=1,2,3) is a stress factor.

The presence of hydrogen, the interaction energy between the strain field of hydrogen atoms and external stress field is given by:

$$W_2 = \sigma_h V_H \quad \textbf{(22)}$$

where σ_h is the volume stress and V_H is the partial molar volume of hydrogen in the metal.

When both hydrogen and stress are present, there is a synergistic effect on the anodic dissolution rate that can be modeled as:

$$i(\sigma,H) = i_A \exp\left(\frac{\Delta H - T\Delta S}{RT}\beta\right) \times \exp\left(\frac{M\left(\sigma_1^{\,2} + \sigma_2^{\,2} + \sigma_3^{\,2}\right)}{2E\rho RT}\beta\right) \times \exp\left(\frac{\sigma_h V_H}{RT}\beta\right) \qquad \textbf{(23)}$$

This can be simplified as:

$$i(\sigma,H) = k_H k_\sigma k_{H\sigma} i_A \qquad \textbf{(24)}$$

where:

$$\begin{aligned} k_H &= \exp\left(\frac{\Delta U - T\Delta S}{RT}\beta\right) \\ k_{\sigma i} &= \exp(\tilde{\sigma}_i^{\,2} \times \lambda b) \\ k_\sigma &= k_{\sigma_1} \times k_{\sigma_2} \times k_{\sigma_3} \\ k_{H\sigma} &= \exp\left(\tilde{\sigma}_h \times \lambda_H \times \beta\right) \end{aligned} \qquad \textbf{(25)}$$

where $\tilde{\sigma} = \sigma_i / \sigma_o$ is the principal stress normalized by yield stress and $\tilde{\sigma}_h = \sigma_h / \sigma_o$ is the volume stress normalized by yield stress. It is these three variables that encompass the synergistic action of stress and hydrogen. The term λ is defined by:

$$\lambda = \frac{W}{2E\rho RT}\sigma_o^{\,2} \qquad \textbf{(26)}$$

and is approximately 2.5×10^{-3} for X-80 pipeline steel.

At a stress corrosion crack tip, the local stresses can increase five to six times the yield stress. The synergistic effect of stress and hydrogen on anodic dissolution is much more significant than the effect of stress alone. It has been calculated that with 1% hydrogen concentration the atomic bonding energy is reduced by 5% for pipeline steels [90].

In this mechanism, the hydrogen is assumed to come from ions reduced from the solution from cathodic potential. So, lower pH values and cathodic potentials were found

to cause higher hydrogen concentrations [89]. This model uses environments that are beyond pipeline conditions that experience TGSCC. Further, these explanations fail to recognize the fact that application of cathodic protection will increase the pH due to the formation of OH^- ions in aqueous solutions. This will eventually favor the environment typically associated with IGSCC [83]. Further, passive behavior is only seen in high pH environments and not near-neutral environments so the assertion that hydrogen reduces the stability of passive film may be irrelevant.

CHAPTER 3

PROPOSED MECHANISM FOR TGSCC OF PIPELINE STEEL IN NEAR-NEUTRAL pH GROUND WATER SOLUTIONS

Any mechanism to explain TGSCC initiation and growth of cracks on pipelines should be able to explain the production of hydrogen, the dissolution of crack walls, and the formation of copious amounts of iron carbonate found near such failures in the field. Although the involvement of hydrogen in TGSCC is generally accepted, the mechanisms of hydrogen production in bicarbonate containing solutions are not well understood. Previous theories of the TGSCC mechanism have generally assumed the production of hydrogen either to be due to the cathodic reaction associated with the anodic dissolution of carbon steel or as the result of the applied cathodic current for pipeline protection. In either case, the pH of the solution, especially at the surface of pipeline, will increase due to associated hydrogen discharge reactions. It has already been established that cathodic protection will lead to the formation of carbonate/bicarbonate solutions with high pH, promoting IGSCC on pipeline steels [23].

This research proposes a mechanism for near-neutral pH stress corrosion cracking of carbon steel pipelines in which the underlying drivers for TGSCC are based on the CO_2-H_2O system. Depending on the pH of the solution, there are three equilibrium species that can exist when carbon dioxide dissolves in water, as given in reactions (27) and (28) [91].

$$H_2CO_3 = HCO_3^- + H^+ \quad \textbf{(27)}$$

$$HCO_3^- = CO_3^{-2} + H^+ \quad \textbf{(28)}$$

The equilibrium of these species is determined from the equilibrium constants given respectively for the each reaction in Equations (29) and (30). Subsequently, the nature of the species is a function of the pH of the solution.

$$\log\left(\frac{HCO_3^-}{H_2CO_3}\right) = -6.37 + pH \quad \textbf{(29)}$$

$$\log\left(\frac{CO_3^{-2}}{HCO_3^-}\right) = -10.33 + pH \quad \textbf{(30)}$$

Lines in Figure 1 exhibit the regions of predominance for different species, based on the equilibrium constants for the reactions (27) and (28). Equimolar amount of bicarbonate ions and carbonic acid are at equilibrium at pH of 6.37, whereas equimolar amount of carbonate and bicarbonate ions are at equilibrium at pH of 10.33. Low pH favors carbonic acid, whereas high pH favors carbonate ions. At the intermediate pH ranges, bicarbonate ions are at equilibrium with these two species. The minimum in Figure 2, at a pH value of 8.4, represents the point of concentrated bicarbonate. At intermediate pH values between 6.4 and 10.3, the bicarbonate ions predominate. Field testing has indicated that the pH of the solutions found near TGSCC failure of pipelines was approximately 6.4, where the roughly equimolar ratio of carbonic acid and bicarbonate ions exist. The pH will remain at 6.4 as long as the species for the reactions are available in the solution. Intergranular stress corrosion cracking of pipeline steel is associated with high pH (~10.5) carbonate/bicarbonate solutions at the pipeline surface.

As shown in the Figure 2, the changing environments can account for both intergranular and transgranular SCC of pipeline steel. This is notable as both types of cracking have been reported to occur on the same section of pipelines [19].

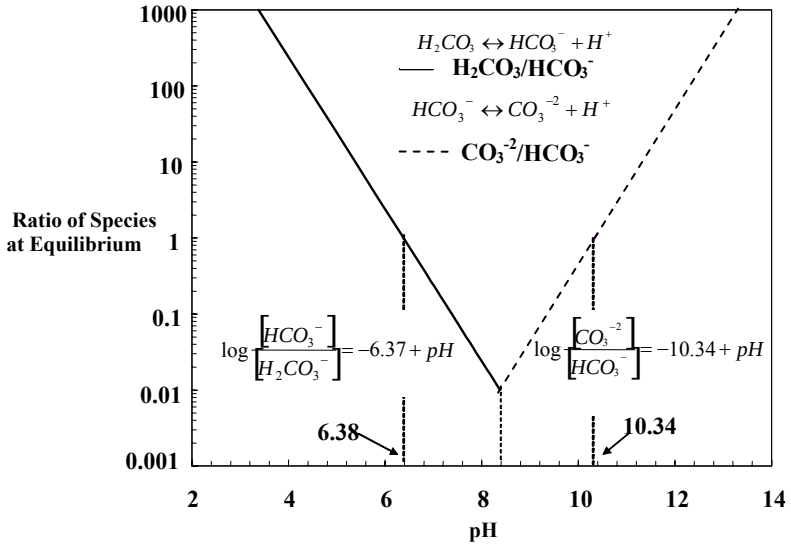

Figure 2 - Calculated equilibrium constant values as a function of ratio of species at equilibrium and pH

The proposed mechanism for the hydrogen generation at the pipeline surface is based simply on the availability of CO_2 and H_2O at the pipeline surface, as described by the following reaction steps:

$$H_2CO_3 \leftrightarrow HCO_3^- + \mathbf{H^+} \quad \textbf{(31)}$$

$$Fe \leftrightarrow Fe^{+2} + 2e^- \quad \textbf{(32)}$$

$$HCO_3^- + Fe^{+2} \rightarrow \mathbf{FeCO_3} + \mathbf{H^+} \quad \textbf{(33)}$$

$$H^+ + 2e^- + H^+ \rightarrow \mathbf{2H}\ (\text{ads}) \quad \textbf{(34)}$$

Carbonic acid, formed by the carbon dioxide dissolved in water, dissociates to form bicarbonate ions. The hydrogen released from the reaction of bicarbonate ions with metal ion and the hydrogen formed from the dissociation of carbonic acid are available to ingress into the surface of the steel. The production of $FeCO_3$ accounts for the iron carbonate found at the site of TGSCC [92-94]. This mechanism of hydrogen generation in carbon dioxide environments will be termed as the Near-Neutral pH Hydrogen Generation (NNPHG) mechanism.

Although not required, the presence of other ions in the solutions may affect the overall NNPHG mechanism. Specifically, this mechanism can account for the increase in crack growth rate when the environment is exposed to oxygen. Other studies have shown that the presence of oxygen increases TGSCC susceptibility [48-50, 58]. It is proposed that the presence of oxygen can accelerate the corrosion process by contributing to an additional cathodic reduction reaction to form hydroxide. This will not alter the pH as hydroxide can react with free CO_2 to produce bicarbonate as follows:

$$2CO_2 + 2OH^- \leftrightarrow 2HCO_3^- \quad \textbf{(35)}$$

$$Fe \leftrightarrow Fe^{+2} + 2e^- \quad \textbf{(36)}$$

$$2HCO_3^- + Fe^{+2} \rightarrow \mathbf{FeCO_3} + 2H^- \quad \textbf{(37)}$$

$$2e^- + 2H^+ \rightarrow \mathbf{2H}\ (\text{ads}) \quad \textbf{(38)}$$

This leads to further production of iron carbonate and hydrogen, facilitating the embrittlement process. This reaction would also be activated if the pipeline is exposed to low levels of cathodic protection in seasons of high groundwater levels. Further, iron carbonate is the more thermodynamically stable phase, so any production of iron hydroxide would most likely convert to iron carbonate at equilibrium. However,

application of high levels of cathodic protection would generate hydrogen cathodically, increasing the solution pH and changing the equilibrium composition of solution to one that favors IGSCC rather than TGSCC on pipeline steels.

Once the hydrogen has been generated in the near-neutral pH environment, it is proposed that hydrogen diffuses into the pipeline steel to accumulate at regions of high stress and high trap energy. Results from this study have shown that on pipeline steel, cracks initiate from surface pits that are formed from dissolved inclusions. Hydrogen will accumulate at areas of high dislocation densities in front of the initial short crack tip to form microcracks ahead of the crack tip. Crack propagation will occur by coalescence of the main crack with the microcracks ahead of the crack-tip. This will lead to a quasicleavage fracture surface where the microcracks ahead of the crack tip account for the brittle areas on the fracture surface while the coalescence of cracks may account for the ductile part of fracture surface in this system.

CHAPTER 4

EXPERIMENTAL PROCEDURES

Samples used in this study were machined out of a section of X-65 pipeline. The nominal chemical composition of X-65 steel is given in Table 1 in Chapter 2. Confirmation of the steel composition was performed by combustion and optical emission techniques, and results are given in Table 3.

Table 3 - Measured Composition of X-65 Pipeline Steel

Element	C	Mn	Si	S	P	Fe
wt %	0.25	1.1	<0.03	0.019	0.011	Bal.

A section of the pipeline was polished to 0.05 micron finish and etched with 2% Nital to reveal microstructure. Figure 3 shows a typical API X-65 pipeline pearlite/ferrite microstructure with banding in the rolling direction.

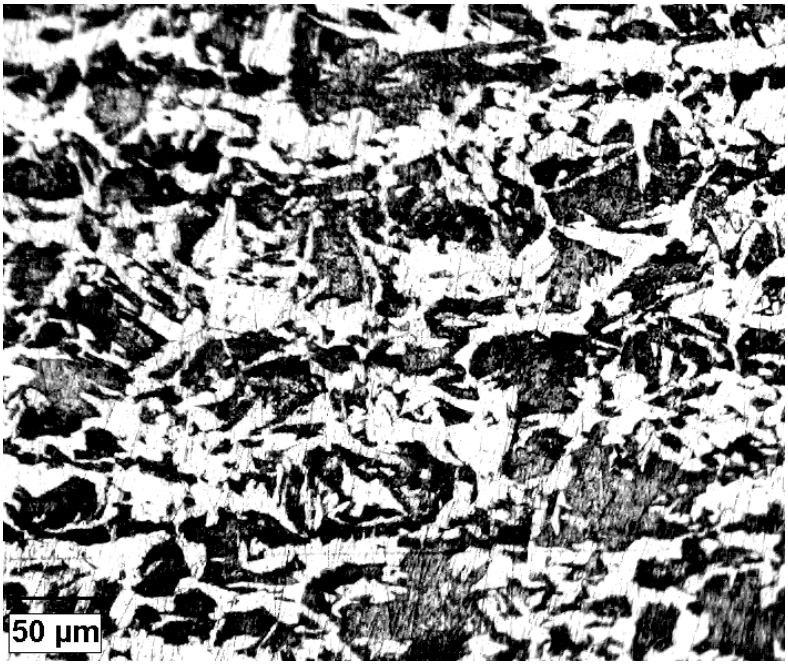

Figure 3 - Microstructure of X-65 pipeline with banding of ferrite and pearlite

4.1 Stress Corrosion Cracking Tests

Stress corrosion susceptibility of pipeline steel in different test solutions was determined using constant extension rate tests (CERT) or slow strain rate tests (SSRT) as outlined by ASTM G129-00. These tests were conducted using round tensile specimens, machined out of X-65 pipeline. Design and dimension of test samples are shown in Figure 4. Specimens were machined so that the length of the tensile specimens was in the longitudinal direction of pipe. Tensile samples were prepared by polishing up to 2000 grit axially and finished with 2000 grit longitudinal strokes. This would ensure that cracks did not originate at residual scratch marks in the radial direction. Samples were rinsed and wiped with acetone prior to testing to remove oil and contaminants from the surface of the sample.

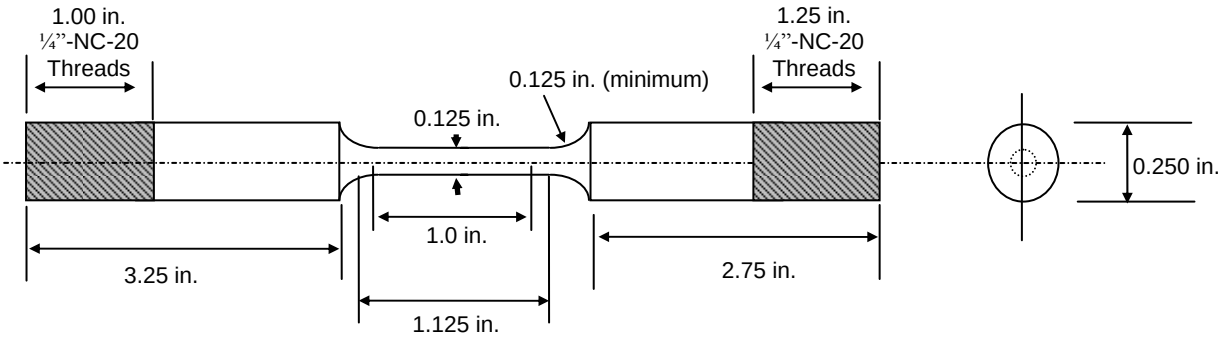

Figure 4 - Slow strain rate sample design and dimensions

A glass cell with rubber sides was used to expose the gage length of the specimen to the test environment. Schematic of the test apparatus is shown in Figure 5. The cell design allowed gas to be bubbled into the test solution and pH to be continuously monitored. If potential was measured or applied to the sample, a salt bridge was used to connect the test environment to an external saturated calomel electrode (SCE). Potential was applied with a Wenking^{TM} Potentiostat. Initial strain rates were controlled for each test depending on the desired exposure time for that sample, but the range of extension rate used was $1.0e^{-7}$ to $2.5e^{-6}$ inch/sec. Displacement reading and RPM measurements of control gear was used to calibrate the motor speed to achieve a given extension rate. Test temperature was controlled within $\pm 1^{o}C$ of the test temperature. Multiple samples were tested in some conditions to check the reproducibility of SCC results. The matrix of all smooth slow strain rate samples is given in Table 4.

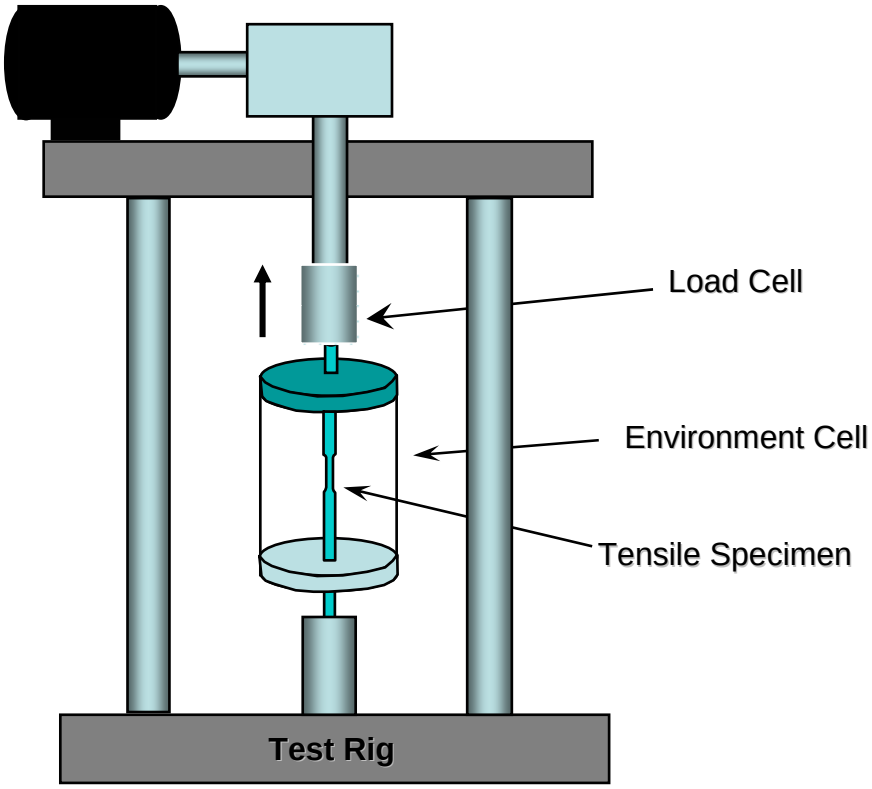

Figure 5 - Slow strain rate testing apparatus

Table 4 - Smooth Sample Slow Strain Rate Test Matrix

Environment	% CO_2 Exposure	Strain Rate (inch/sec)	Temp. (^oC)	Potential (V_{SCE})
DI water	5	2 e^{-6}	RT	OCP
DI water	0	2 e^{-6}	RT	OCP
Air	0	2 e^{-6}	RT	OCP
0.5 g/L $NaHCO_3$	5	2 e^{-6}	RT	OCP
0.1 g/L $NaHCO_3$	5	2 e^{-6}	RT	OCP
1 g/L $NaHCO_3$	5	2 e^{-6}	RT	OCP
1 N $NaHCO_3$, 1 N Na_2CO_3	0	1 e^{-6}	70	-0.650
Effect of Temperature and CO_2				
0.1 g/L $NaHCO_3$	5	2 e^{-6}	15	OCP
0.5 g/L $NaHCO_3$	5	2 e^{-6}	15	OCP
1 g/L $NaHCO_3$	5	2 e^{-6}	15	OCP
5 g/L $NaHCO_3$	5	2 e^{-6}	15	OCP
10 g/L $NaHCO_3$	5	2 e^{-6}	15	OCP
5 g/L $NaHCO_3$	100	2 e^{-6}	15	OCP
10 g/L $NaHCO_3$	100	2 e^{-6}	15	OCP
0.1 g/L $NaHCO_3$	5	2 e^{-6}	35	OCP
0.5 g/L $NaHCO_3$	5	2 e^{-6}	35	OCP
1 g/L $NaHCO_3$	5	2 e^{-6}	35	OCP
0.5 g/L $NaHCO_3$	5	2 e^{-6}	45	OCP
Effect of Applied Potential				
0.5 g/L $NaHCO_3$	5	2 e^{-6}	RT	-0.650
0.5 g/L $NaHCO_3$	5	2 e^{-6}	RT	-0.700
0.5 g/L $NaHCO_3$	5	2 e^{-6}	RT	-0.693
0.5 g/L $NaHCO_3$	5	2 e^{-6}	RT	-0.751
0.5 g/L $NaHCO_3$	5	2 e^{-6}	RT	-0.709
0.5 g/L $NaHCO_3$	5	2 e^{-6}	RT	-0.850
0.5 g/L $NaHCO_3$	5	2 e^{-6}	RT	-1.05
0.5 g/L $NaHCO_3$	5	2 e^{-6}	RT	-1.25
0.5 g/L $NaHCO_3$	5	2 e^{-6}	RT	-1.75
0.5 g/L $NaHCO_3$	5	2 e^{-6}	RT	-1
Effect of Solution Components				
0.5 g/L $NaHCO_3$+0.122 g/L KCl	5	2 e^{-6}	RT	OCP
0.5 g/L $NaHCO_3$+0.131 g/L $MgSO_4$	5	2 e^{-6}	RT	OCP
0.5 g/L $NaHCO_3$+0.137 g/L $CaCl_2$	5	2 e^{-6}	RT	OCP
0.5 g/L $NaHCO_3$+0.122 g/L KCl	5	2 e^{-6}	15	OCP
0.5 g/L $NaHCO_3$+0.131 g/L $MgSO_4$	5	2 e^{-6}	15	OCP
0.5 g/L $NaHCO_3$+0.137 g/L $CaCl_2$	5	2 e^{-6}	15	OCP
NS4	5	2 e^{-6}	15	OCP
NS4	5	2 e^{-6}	RT	OCP
NS4	5	2 e^{-6}	35	OCP

Upon failure, samples were rinsed with acetone and dried with hot air to ensure that the fracture surface does not corrode further during sample storage and characterization. Final gauge length and diameter were determined to calculate the reduction of area and the percent elongation for each test. One half of the failed sample was sectioned, mounted and polished to characterize crack depth, density, and morphology. Longest crack depth in each sample was used to calculate the crack velocity for that test. Crack length was measured both by the linear depth of crack into the sample and length of actual crack path, termed as crack profile length in this thesis. Crack density was determined by counting the number of cracks on both sides of sectioned sample up to 1cm away from the fracture surface. Samples were further examined by SEM to observe any small scale features that may contribute to the cracking process such as microcracks ahead of the crack tip or secondary cracks at the fracture surface. Since the samples were imbedded in bakelite, charging was an issue. Samples were imaged by covering the area near the sample with carbon tape and ensuring that carbon tape was continued down to the sample holder. To reduce charging conditions, imaging was accomplished using 3kV.

In some tests the samples were subjected to environmental shifts to simulate the changing environments experienced by pipelines. The samples were initially exposed to 1N $NaHCO_3$ and 1N Na_2CO_3 at 70^{o}C and -650 mV_{SCE} loaded to 85% yield strength. Samples were allowed to soak in this environment and load for 5 days. The environment was then removed and the sample was rinsed with DI water to remove any excess chemicals. Samples were then exposed to 0.5g/L $NaHCO_3$ with 5%CO_2 at room temperature and loaded continuously until failure.

A finite number of tensile samples were notched in order to observe the effect of stress concentration on hydrogen ingress and TGSCC using modified ASTM E602-03 procedure. Design of such samples is given in Figure 6. Sample notches were imaged by optical microscopy and the notch root radius for each sample was measured. Samples were polished up to 2000 grit and sonicated in acetone to remove debris from notch. Confirmation of clean notch was determined by optical microscopy before each test. Notched slow strain rate sample matrix is given in Table 5. Extension rate used to test notched samples was $2e^{-7}$ inch/sec to ensure that environmental interaction occurred before ductile failure. A series of tests were performed where the samples were held at a constant load corresponding to approximately 85% yield strength for a specific amount of time. Upon failure, fracture surfaces were examined using SEM to determine fracture morphology.

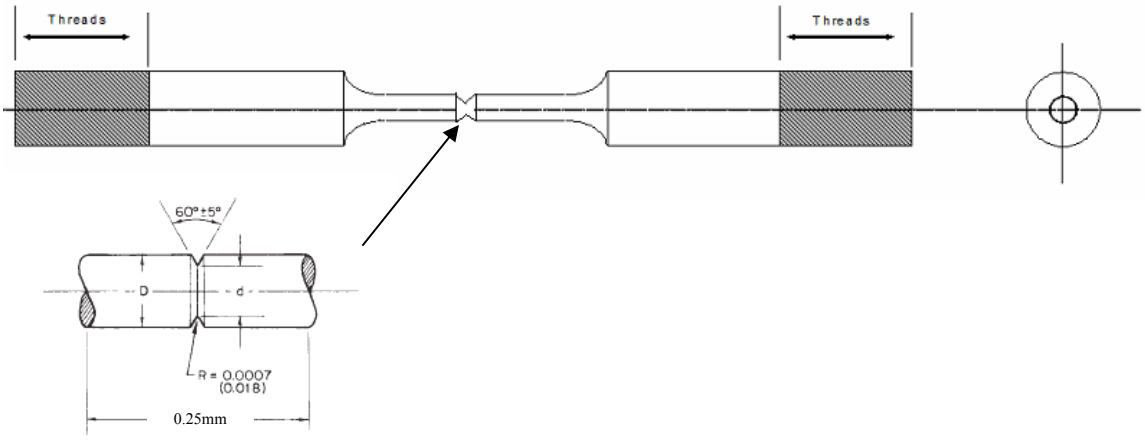

Figure 6 - Schematic of Notched Slow Strain Rate Sample

Table 5 - Notched Slow Strain Rate Sample Test Matrix

Environment	Temp. (^oC)	Potential (V_{SCE})
Air	RT	OCP
0.5 g/L $NaHCO_3$ with 5% CO_2	RT	OCP
0.5 g/L $NaHCO_3$ with 5% CO_2 with load hold for 7 days	RT	OCP
0.5 g/L $NaHCO_3$ with 5% CO_2 with load hold for 15 days	RT	OCP
0.5 g/L $NaHCO_3$ with 5% CO_2 with load hold for 30 days	RT	OCP
0.5 g/L $NaHCO_3$ with 5% CO_2	RT	-1
0.5 g/L $NaHCO_3$ with 5% CO_2	RT	-1 (24 hours prior to testing)

4.2 General Corrosion Tests

Coupon exposure corrosion tests were performed on flat samples prepared from X-65 pipeline steel. Tests were carried out in glass vessels containing approximately 720mL of test solution. Samples were spot welded to a stainless steel wire. Weld and wire were coated with Corona X Dope™ Insulating Varnish to prevent galvanic corrosion and corrosion of suspension wire. The suspension wires provided electrical connection to measure and apply potential to the steel sample. Exposure tests were performed in two series.

The first series of coupon exposure tests were carried out to determine environmental conditions under which iron carbonate could form in simple bicarbonate solutions with carbon dioxide bubbling through the solution. The test matrix for these experiments included bicarbonate solutions with concentrations ranging from 0.1 g/L to 10 g/L and temperatures ranging from 15 to 45^{o}C in controlled temperature water baths. Additional chemicals typically found in ground water were also added, either individually or in combination, to simple bicarbonate solutions in the quantities similar in the NS4

solutions (i.e. 0.122 g/L KCl, 0.137g/L $CaCl_2$, and 0.131g/L $MgSO_4$). Coupon exposure tests were performed either without any CO_2 gas or by bubbling 5% CO_2/N_2 or 100% CO_2 gas through the solution. The samples were exposed for 72 hours with continuous monitoring of pH. At the end of each test, the test solution was analyzed for chemical composition by titration. Any precipitates formed in the solutions were filtered and analyzed for their chemical composition. Cations present were analyzed by Inductively Coupled Plasma Spectroscopy (ICP) whereas anions were either analyzed by titration method or by electrophorasis technique. Surface film formed on the pipeline steel was characterized by x-ray diffraction (XRD) to determine the reaction products at the surface.

The second series of coupon exposure tests were performed to determine the effect of applied potential on TGSCC environment. pH of the solution was continuously monitored through the use of Nico2000 8 Channel Ion/pH Analyzer data acquisition system. Potentials tested were -800 mV_{SCE}, -850 mV_{SCE}, -900 mV_{SCE}, and -1 V_{SCE}. Some tests were performed at -1.25 V_{SCE} to determine the effect of extreme cathodic potentials experience by pipeline due to defective equipment. Carbon dioxide gas was initially bubbled through the solution prior to sample emersion in order to achieve equilibrium. Steel samples were then introduced to the test solution and the gas bubbling was continued for 24 hours prior to application of potential. Gas bubbling was stopped when potential was applied to the test sample. Solution remained stagnate until the solution pH reached some equilibrium value. At equilibrium, carbon dioxide was reintroduced to observe the effect on pH. Corrosion rate in all coupon exposure tests was determined by measuring the initial and final weight.

4.3 Surface pH Measurements

Surface pH of the exposed steel samples was measured to understand the environment at the surface of the sample and diffusion effect of the bulk solutions. Diffusion or mixing characteristics of the solution was monitored to further understand the local environment of TGSCC at the steel surface. Test configuration is shown schematically in Figure 7. Samples were electrically connected and suspended in the test solution in the same manner as General Corrosion Tests as described in Section 4.2. Stainless steel wire was spot welded on the test sample the wire was coated with insulating varnish. pH probes were place 4 cm apart and was continuously monitored for 72 hours. pH data was recorded for each probe using a Nico2000 8 Channel Ion/pH Analyzer.

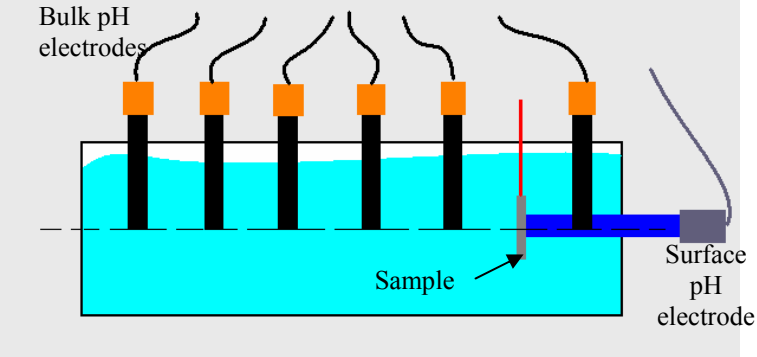

Figure 7 - Schematic of surface pH experimental set-up

Bubbling of CO_2 resulted in solution agitation. In order to observe changes in the solution due to diffusion of chemical species, any mode of agitation was minimized from the system. Experiments were performed by saturating the solution for three hours with

5% CO_2. CO_2 bubbling was then stopped and the pipeline steel sample was placed in the cell.

Environments studied are given in Table 6. Potentials were applied potential using a Wenking potentiostat and potential were measured using a SCE reference electrode. As there was difficulty altering the temperature with this experimental apparatus, all tests were performed at room temperature.

Table 6 - Surface pH Test Matrix

$NaHCO_3$ Concentration	Addition Chemical Concentration	Applied Potential (SCE)
0.5 g/L	-	OCP
0.5 g/L	-	-750 mV
0.5 g/L	-	-800 mV
0.5 g/L	-	-850 mV
0.5 g/L	-	-900 mV
0.5 g/L	-	-1.25 V
0.1 g/L	-	OCP
1 g/L	-	OCP
0.5 g/L	0.122 g/L KCl	OCP
0.5 g/L	0.137 g/L $CaCl_2$	OCP
0.5 g/L	0.131 g/L $MgSO_4$	OCP
0.5 g/L	0.122 g/L KCl + 0.137 g/L $CaCl_2$ + 0.131 g/L $MgSO_4$	OCP

4.4 Potentiodynamic Polarization Tests

To determine the effect of environmental parameters on electrochemical behavior of the pipeline steel, potentiodynamic tests were performed using Gamry CMS100 Electrochemical Measurement System. Tests were performed following general guidelines of ASTM G5-94 and G3-89. Cylindrical samples, machined out of X-65 pipeline steel used in this study, had a surface area of 5.76 cm^2. Samples were prepared by polishing at 320, 600, and 1000 grit. Samples and sample holder were rinsed and

wiped with acetone prior to testing to remove any oil or contaminants. Volume of the test solutions for each test was 1 liter. Potential sweeps were performed at a scan rate of 5 mV/s starting at -0.5 V_{SCE} below OCP and sweeping to 1 V_{SCE} above OCP. Samples were immersed in the test solution for one hour prior to testing in order to allow OCP to stabilize. Test pH and condition of sample was recorded at the completion of the test. A matrix of environments studied is given in Table 7. Multiple tests were performed in each environment in order to ensure the reproducibility of these tests.

Table 7 - Matrix for Potentiodynamic Polarization Tests

Chemical Concentrations	Temperature (^oC)	% CO^2 exposure	Scan Rate (mV/sec)
0.5 g/L $NaHCO_3$	15	5	5
0.5 g/L $NaHCO_3$	25	5	5
0.5 g/L $NaHCO_3$	35	5	5
0.1 g/L $NaHCO_3$	25	5	5
1 g/L $NaHCO_3$	25	5	5
5 g/L $NaHCO_3$	25	5	5
0.5 g/L $NaHCO_3$, 0.122 g/L KCl	25	5	5
0.5 g/L $NaHCO_3$, 0.131 g/L $MgSO_4$	25	5	5
0.5 g/L $NaHCO_3$, 0.137 g/L $CaCl_2$	25	5	5
NS4	15	5	5
NS4	25	5	5
NS4	35	5	5

4.5 Effect of Thermo-Mechanical Treatments on Steel Microstructure

Heat treatments were performed on X-65 pipeline steel in order to alter the microstructure and observe the effect of resulting microstructure on hydrogen permeation and diffusion. Heat treatments were selected based on the time-temperature-transformation curve for equivalent pipeline steel 1527 [95] shown in Figure 8 and based

on previous microstructural studies performed on X-65 pipeline [38, 81, 96-98]. Heat treatments used in this study are outlined in Table 8 along with determined microstructures. All heat treatments were performed after purging the furnace for 1 hour with argon. Argon was continued throughout the heat treatment to minimize oxide film formation. Temperature of the furnace was controlled within +/- 10 degrees of target temperature. Water quenching was performed in static water at room temperature.

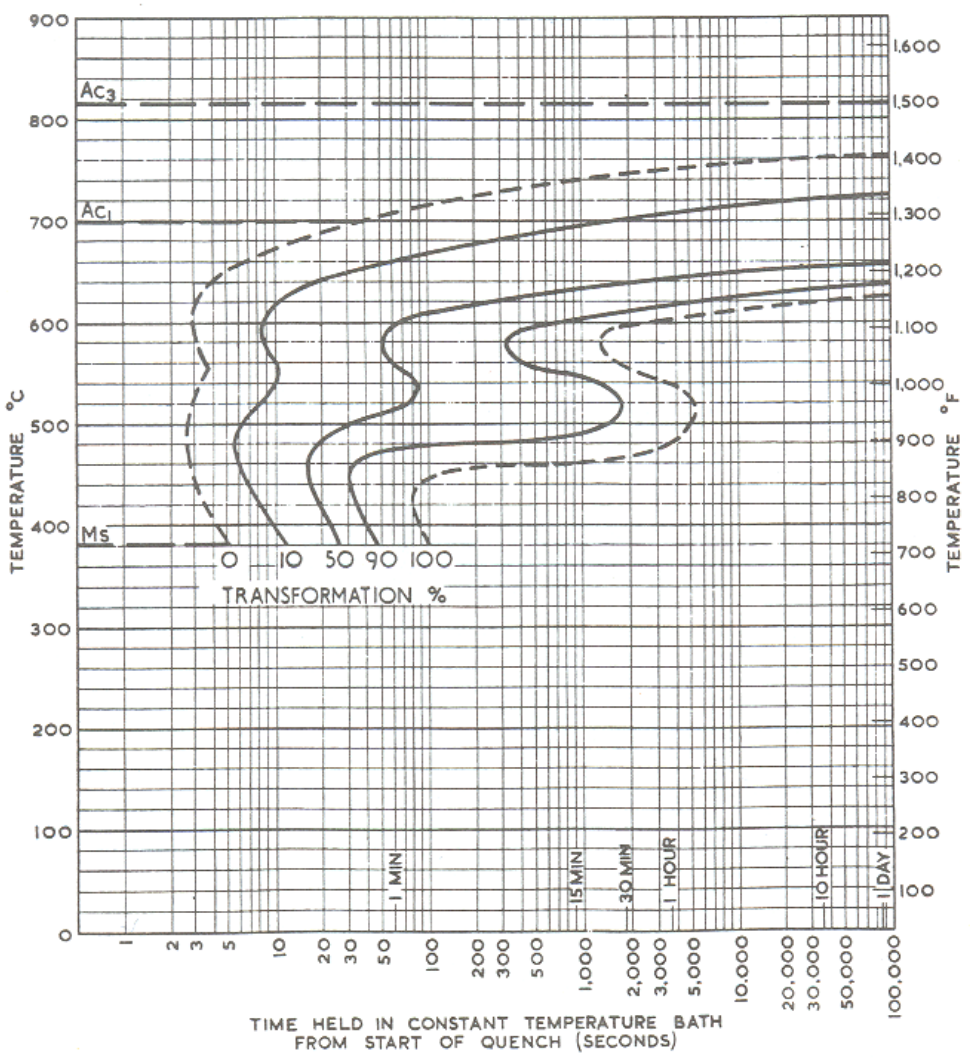

Figure 8 - Time-Temperature-Transformation diagram for 1527 steel which is the British equivalent to X-65 pipeline steel. Data provided by The Iron and Steel Institute [95]

Table 8 - Heat Treatment and Resulting Microstructures for X-65 Pipeline

Heat Treatment	Microstructure
950°C 1 hours, air cooled	Ferrite/pearlite microstructure
950°C 1 hour, water quenched	Martensite
950°C 1 hour, water quenched 350°C temper 1 hour, air cooled	Tempered Martensite
950°C 1 hour, water quenched 400°C temper 1 hour, air cooled	Tempered Martensite
950°C 1 hour, water quenched 475°C temper 1 hour, air cooled	Tempered Martensite
950°C 1 hour, water quenched 650°C temper 1 hour, air cooled	Tempered Martensite with fine carbides
950°C 1 hour, water quenched 650°C temper 1 day, air cooled	Tempered Martensite with carbides
950°C 1 hour, water quenched 650°C temper 1 week, air cooled	Tempered Martensite with coarse carbides

Microstructure of heat treated pipeline steel samples was characterized by polishing samples to 0.05 micron alumina polishing and etching the samples with 2% Nital solution. Quantification of microstructure was performed by determining the volume fraction of the different phases, *Vv*, by point counting. Surface area of the examined features, S_v, was determined by line intersection method. Mean intercept grain size (*l)* was determined by using the equation $l = S_v / 2$. Whereas, mean chord length (λ) was determined by $\lambda = 4V_v / S_V$. Only the side of the sample that is exposed to the test solution for hydrogen absorption was characterized.

It was determined that optical characterization was insufficient for the martensitic and tempered martensitic steels. Subsequently, microstructure of water quenched steels was imaged by LEO 1550 SEM in order to characterize carbide size. Martensitic structure was also characterized by quantifying the percent martensite.

Water quenched samples were further characterized by XRD method using a PANalytical X'Pert Pro^{TM} equipment with a copper source. Diffusion spectra were obtained with a diffracted beam monochrometer to remove iron florescence and parallel beam optics generated by a Göbel mirror. Full spectrums were taken between 40 and 130 degrees 2θ and closer inspection was performed on the 64 and 98 2θ peaks. For each peak, data on the 2θ, d spacing, peak intensity, full-width-half-max, and area were quantified using Jade 7 program to characterize lattice relaxation during heat treatment. Error in 2θ was less than ±0.003 and error for the d spacing was ±0.0001. The error in FWHM measurement was limited to ±0.010.

4.6 Hydrogen Permeation Tests

To evaluate the effect of microstructure on diffusion and trapping characteristics of the pipeline steel, hydrogen permeation tests were achieved using a modified procedure from ASTM G148-97. A standard Devanathan cell, shown schematically in Figure 9, was designed and constructed such that the area of test sample exposed to the solution was 1.767 cm^2. Typical sample thickness used in these tests was approximately 3 mm to measure hydrogen diffusion through the bulk of the steel. Individual sample thickness was recorded for each test to ensure proper calculation of diffusion parameters.

Permeation tests were performed by first exposing the steel sample to the anodic environment, 0.1 N NaOH, for a period of one hour to allow the environment to reach stable open circuit conditions. After this initial equilibrium time, the anodic chamber was polarized to 250 mV_{SCE} in order to create a stable anodic film on the sample surface to reduce errors in current density measurement. Potential was maintained at 250 mV_{SCE} +/- 2 mV by use of Gamry Potentiostat. After one hour of polarization, 0.5 g/L $NaHCO_3$

solution and 5% CO_2 bubbling was introduced to the cathodic cell. The cathodic chamber was kept under open circuit conditions to simulate realistic pipeline conditions that are associated with TGSCC. The test cell was placed in a Farday's cage to avoid any electromagnetic interference. All permeation tests were performed at room temperature. Hydrogen permeation through the steel was detected by an increase in the current density on the anodic side of the Devanathan cell. Current and potential data was collected throughout the test by a Gamry CMS100 Electrochemical Measurement System. A sample period of 60 seconds was used to maximize data collection. Tests were allowed to run for 16 hours to ensure hydrogen permeation occurred during the testing time. Hydrogen generation under open circuit conditions can be highly variable, so at least three samples were tested for each condition. Reported results are the average of successful test data. Steel samples were also exposed to deionized distilled water as a baseline to compare hydrogen production in this environment.

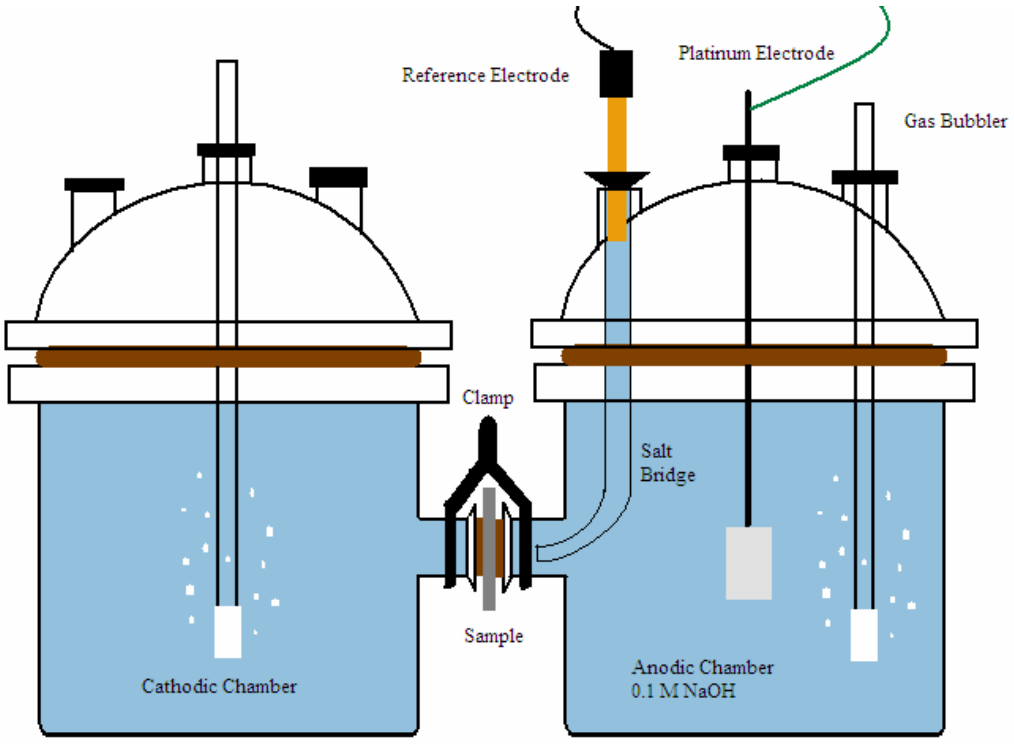

Figure 9 - Schematic of Devanathan Hydrogen Permeation Setup

Hydrogen permeation was detected by an increase in the cell current on the anodic side of the cell, as shown schematically in Figure 10. By this testing method, transportation of hydrogen is considered one dimensional diffusion. Hydrogen transportation through the metal is determined by the competition between diffusion though interstitial lattice sites and trapping of hydrogen at microstructural features such as grain boundaries, dislocations, carbides, inclusions, and precipitates. This can be mathematically modeled as:

$$\frac{\delta C}{\delta t} = D\frac{\delta^2 C}{\delta x^2} - N_r\frac{\delta \theta_r}{\delta t} - N_i\frac{\delta \theta_i}{\delta t} \qquad \textbf{(39)}$$

where C is the concentration of hydrogen atoms in the interstitial sites, D is the lattice diffusion coefficient of atomic hydrogen, N_r and N_i are the density of reversible and irreversible trap sites, and θ_r and θ_i are the fractional occupancy of the reversible and irreversible trap sites. In general, the contribution of short circuit paths such as dislocations and grain boundaries are usually neglected due to their small volume fraction and their small flux contribution relative to the matrix [99].

When the permeation behavior conforms to Fick's law, then effective diffusion can be calculated by:

$$D_{eff} = \frac{L^2}{6t_{lag}} \quad \textbf{(40)}$$

where L is the steel sample thickness and t_{lag} is 0.63 the total diffusion time it takes to achieve the steady-state current [99, 100]. Permeation data can further be analyzed by calculating the steady state flux:

$$J_{ss} = \frac{i_p^{ss}}{F} \quad \textbf{(41)}$$

where i_p^{ss} is the steady-state permeation current density and F is Faraday's constant. With knowledge of J_{ss} and D_{eff}, the concentration of subsurface hydrogen concentration in interstitial lattice sites and hydrogen in traps can be calculated by:

$$C_H = \frac{J_{ss}L}{D_{eff}} \quad \textbf{(42)}$$

This value is also commonly termed solubility as it the amount of surface hydrogen that will be in thermodynamic equilibrium with subsurface hydrogen. The permeation detected by this method indicates the concentration of hydrogen in irreversible and reversible traps [99]. As irreversible trap are occupied with increasing time, the

transportation of hydrogen through the sample will become faster. At steady-state, the irreversible traps are fully occupied [99].

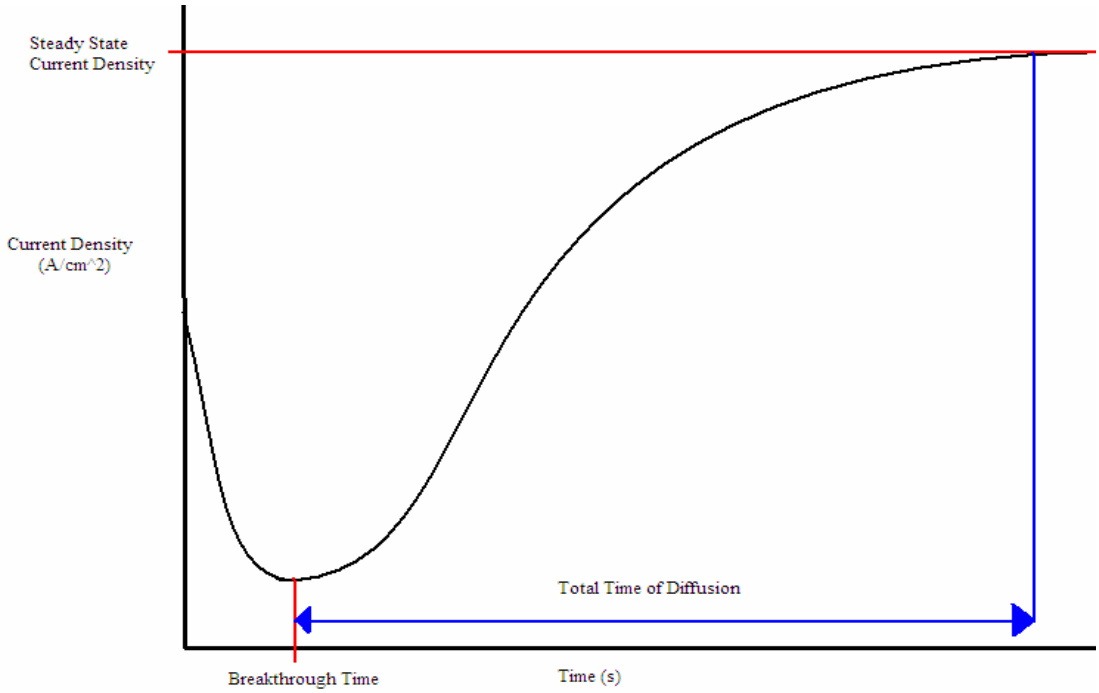

Figure 10 - Schematic of hydrogen permeation curve and parameters extracted from the curve

4.7 Hydrogen Microprinting

Hydrogen microprinting was used to detect and observe the location of hydrogen accumulation in pipeline steel by modifying the procedure developed by Ovejero-Garcia [76, 101-104]. Initially, the sample was polished to 0.05 micron finish and etched with 2% nital enchant in order to reveal the microstructure. The etched surface was then coated with Corona Dope Red X insulating varnish to eliminate the possibility of corrosion on the surface that would be examined. The other side of the steel sample was

then used to charge hydrogen in 1 N NaOH solution with -1.5 V_{SCE} for three hours. This time was considered sufficient in order to allow hydrogen to diffuse completely through the sample to be detected at the coated surface. After three hours, the sample was removed from solution, and the coating was removed from the sample with acetone. The sample was then lightly polished at 0.05 micron to remove hydrogen adsorbed on the surface and ensure that all coating was removed. The sample was then rinsed with acetone again to make sure the surface was free from oil, grease or debris. Once the sample was clean, the microprinting process began where care was taken to reduce the amount of time in-between charging and microprinting.

In a dark room under red light, the microprinting was accomplished by initially coating the sample with 1 g Ilford L-4 nuclear emulsion, with a grain size of 140 nm, diluted into 2 mL of 5% wt solution of $NaNO_2$. The addition of $NaNO_2$ reduces spurious corrosion and false accumulation of silver grains. After dilution the solution was heated to 45^{o}C and held for 20 minutes to achieve homogenization. The solution was cooled to room temperature prior to application. Care was taken not to heat the solution to 50^{o}C as it would breakdown the emulsion. The dark room environment was necessary as the L4 emulsion is sensitive to natural light. Exposure to blue range wavelengths would produce a latent image that would obscure any detection of hydrogen atoms.

To achieve a monogranualr layer of AgBr crystals, the emulsion was applied using the wire loop method [102]. The wire loop method is accomplished by means of 0.2 mm diameter wire that forms a loop of 3cm diameter. Once the emulsion is applied to the surface, the loop is kept on the sample until the emulsion hardens into a gel consistency. Time taken for the hydrogen to diffuse through the metal and affect surface

detection previously determined to be roughly one hour. The expected reaction at the steel surface between silver bromide and hydrogen is:

$$AgBr + H \rightarrow Ag(s) + HBr \quad \textbf{(43)}$$

Subsequently, the emulsion was removed from the sample after one hour of exposure.

The "fixing" stage in this experiment involves the removal of excess HBr in order to observe deposited silver grains. In this process, the sample was soaked in a solution with 250g sodium hyposulphite + 10g sodium sulphite + 50 mL sodium bisulphate + 30g $NaNO_2$ + distilled water to make the total solution volume to one liter [102]. The sample was soaked in fixing solution for 3 minutes and then rinsed with distilled water for 30 seconds three times. The sample was then hot air dried and observed under SEM. Silver grains, approximately 10 nanometers in size, are observed at the locations of hydrogen traps near the surface. Samples not subjected to hydrogen charging were also microprinted to verify the technique and verify the accuracy of silver grain deposition.

CHAPTER 5

RESULTS AND DISCUSSION

5.1 Hydrogen Generation in Near-Neutral pH Environment

The first step in this research was to validate the NNPHG mechanism by determining if the proposed reactions could account for an increase in hydrogen production as compared to hydrogen generated by the cathodic reaction associated by simple anodic dissolution of the steel. This was accomplished by coupon exposure tests outlined in Procedures 4.2.

Table 9 shows the thermodynamic calculations for the reactions involved in the NNPHG mechanism. It is apparent from these calculations that the dissolution of CO_2 in water to form carbonic acid is thermodynamically favorable in a narrow temperature range between ~15^{o}C to 35^{o}C. Although presence of other ions may affect the temperature range, it is expected that the mechanism for TGSCC based on CO_2/H_2O chemistry will be bound by the upper and lower temperatures at the pipeline surface. Subsequently, exposure tests were performed within the temperature range of 15^{o}C to 35^{o}C.

Table 9 - Thermodynamic calculations for the reactions involved in the Colwell-Leis mechanism

Reaction:	$H_2CO_3 + Fe = FeCO_3 + H_2$			$Fe^{2+} + CO_3^{2-} = FeCO_3$			$H_2O + CO_2 = H_2CO_3$		
Temperature (^oC)	ΔH (kcal)	ΔS (cal/K)	ΔG (kcal)	ΔH (kcal)	ΔS (cal/K)	ΔG (kcal)	ΔH (kcal)	ΔS (cal/K)	ΔG (kcal)
5	-12.00	1.88	-12.52	4.60	63.31	-13.01	1.33	4.68	0.03
10	-11.92	2.16	-12.53	4.98	64.39	-13.33	0.97	3.43	0.01
15	-11.84	2.45	-12.54	5.37	66.02	-13.66	0.64	2.23	-0.01
20	-11.76	2.73	-12.56	5.76	67.37	-13.99	0.30	1.08	-0.02
25	-11.67	3.01	-12.57	6.16	68.72	-14.33	-0.03	-0.03	-0.02
30	-11.59	3.29	-12.59	6.56	70.07	-14.68	-0.35	-1.01	-0.02
35	-11.51	3.57	-12.60	6.98	71.41	-15.03	-0.66	-2.14	-0.01
40	-11.42	3.84	-12.62	7.39	72.75	-15.39	-0.98	-3.16	0.01
45	-11.34	4.11	-12.64	7.81	74.08	-15.76	-1.29	-4.15	0.03

Coupon exposure tests were carried out to study the effect of bicarbonate concentration in the solution, temperature and carbon dioxide flow on the overall NNPHG reaction mechanisms. Figures 11, 12 and 13 show the effect of bicarbonate concentration on the solution pH at 15^{o}C, 25^{o}C and 35^{o}C. pH of each solution under tested condition was measured at regular intervals; however, solution pH in each case became stable typically within two to four hours. The pH values plotted in Figures 11 to 13 are the values for each solution after 72 hours of exposure and are referred to as equilibrium pH. As predicted by the calculations given in equations 29 and 30 in Chapter 3, the pH of the solution increases with an increase in the bicarbonate concentration for a given concentration of CO_2 flowing through the solution. Comparing the results in Figures 11, 12 and 13 indicates that the availability of CO_2 in the solution has a significant effect on the equilibrium pH of a solution with given initial composition. Shaded area in these figures indicates the range of pH that has typically been associated with TGSCC of pipeline steels. As expected, when 100% CO_2 was bubbled through the

solution, higher concentrations of bicarbonate ions were required to achieve a near-neutral equilibrium pH as compared to equivalent tests with 5%CO_2 + N_2 gas mixture bubbled at the same flow rate. For the tests in open air, with no CO_2 bubbling, the pH of the solution came to an equilibrium value of approximately 8.6. This corresponds to the thermodynamically predicted value as shown by the minima of Figure 2.

The first TGSCC failures were identified in Canada and the initial indications were that the TGSCC may be favored in cold climates. However, TGSCC has been reported to occur in areas with warm climates, indicating that the environments responsible for the TGSCC of pipeline steels may also form at higher temperatures. As shown in Figures 11-13, there is relatively small difference in the pH value for a given solution composition within the tested temperature range. The largest difference in the pH with temperature occurs in the very dilute solutions (0.1 g/L $NaHCO_3$) where an increase in the temperature from 15 to 35^oC resulted in an increase in the pH by approximately one unit. The lower pH values at lower temperatures are attributed to the higher solubility of carbon dioxide at lower temperatures and subsequently the higher rate of carbonic acid production. This allows the buffered low temperature (15^oC) solutions to equilibrate at pH values lower than the solutions at 35^oC. The decrease in carbon dioxide solubility for 35^oC tests results in lower concentrations of carbonic acid formed and subsequently an average pH increase of 0.608 compared to the equivalent solution at 15^oC with 5% CO_2 test environments.

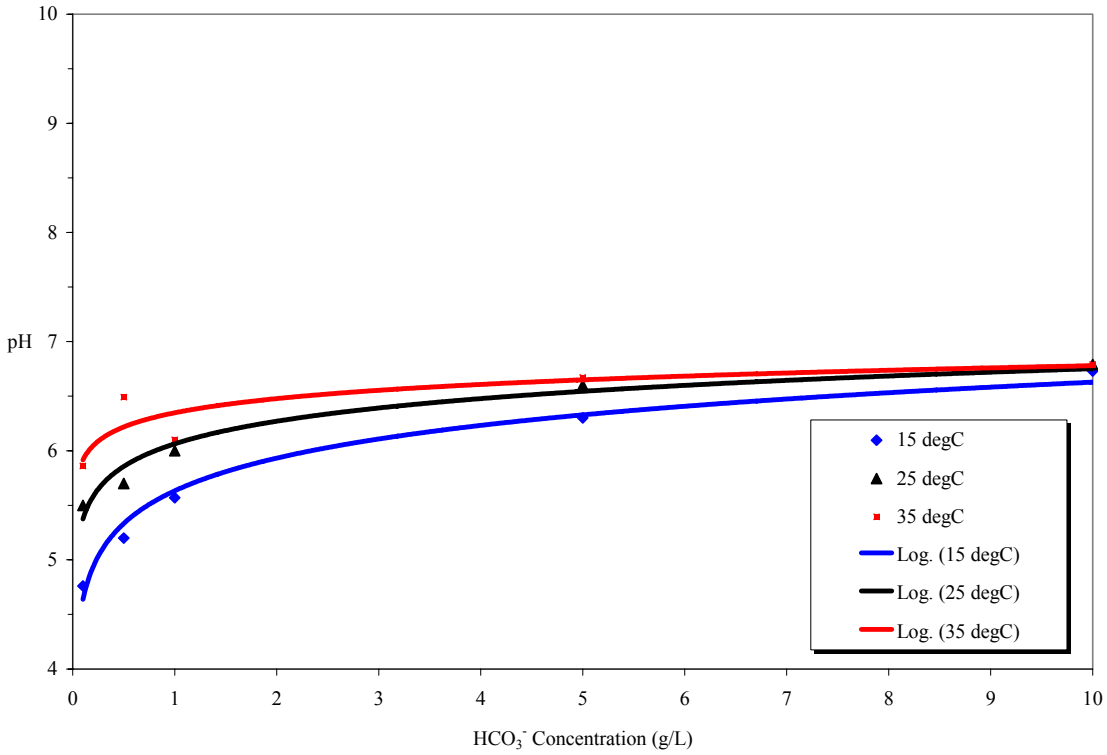

Figure 11 - pH values after 72 hours as a function of bicarbonate concentration at 15°C, 25°C and 35°C with 100% CO_2 bubbled through the solution.

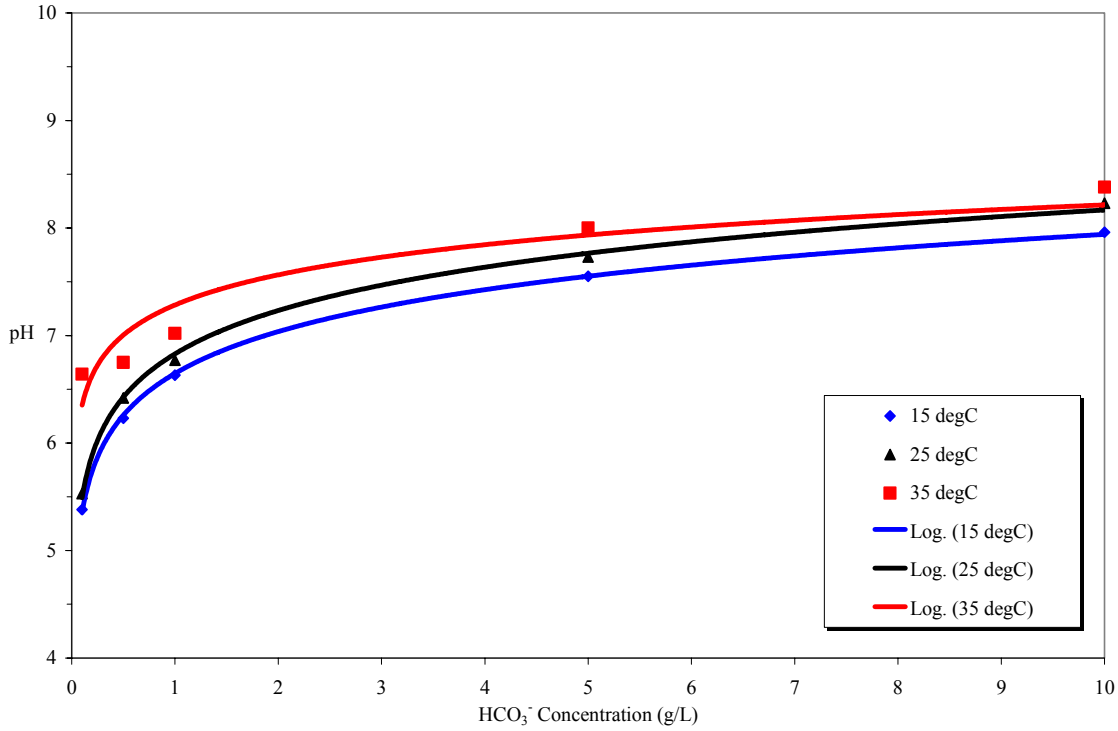

Figure 12 - pH values after 72 hours as a function of bicarbonate concentration at 15°C, 25°C and 35°C with 5% CO_2 bubbled through the solution.

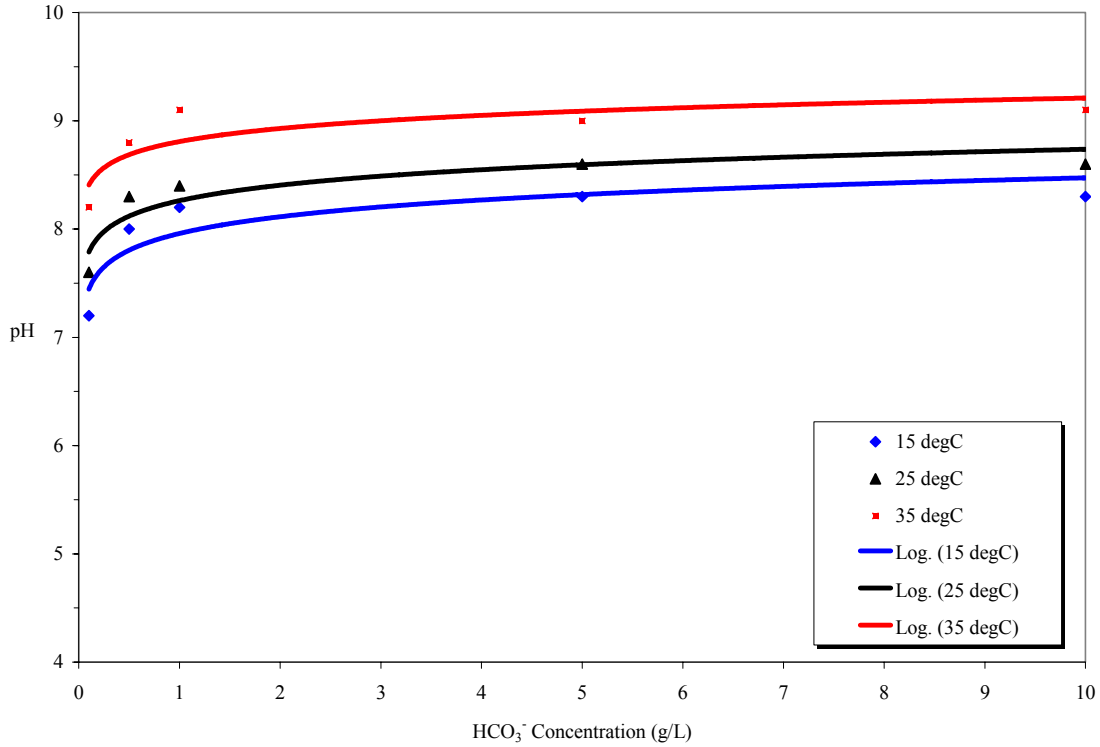

Figure 13 - pH values after 72 hours as a function of bicarbonate concentration at 15°C, 25°C and 35°C with solution exposed to air with no CO_2 bubbling.

5.1.1 Verification of Carbonate Formation by NNPHG Mechanism

In solutions where carbonic acid and bicarbonate ion are at equilibrium, the NNPHG mechanism suggests that the hydrogen may be released by dissociation of carbonic acid and by the reaction of bicarbonate ions with the metal ions, forming metal carbonates such as iron carbonate. To verify this reaction, the solution and precipitates were analyzed for the amount of carbonate formed under each condition. The amount of carbonate was then corelated to the hydrogen generation by the reactions proposed in the NNPHG mechanism. Hydrogen was calculated based on carbonate formation because the carbonates could be directly measured in the solution, the precipiates, and the film of reaction products formed on the steel sample. Total or parts of the hydrogen produced by

any mechanism could be abosrbed into the steel, or may recombine to form molecular hydrogen to become incorporated into the enviorment. Direct measurement of the hydrogen produced by any given mechanism is very difficult and prone to high amounts of error.

Solution after each test was filtered and the carbonates present in the test solution were quantified by the titration method, as described in section 4.6. Results from titrations are given in Table 10 and 11. The carbon steel sample surface exposed in each test solution was characterized by the XRD method to verify the formation of any carbonates on the steel surface. XRD results are summarized in Table 12. In cases where the carbonate concentration in the solution was less than the solubility limit, carbonates did not precipitate on the surface and were not detected by the XRD analysis. Carbonates at the steel surface were only detected at high temperatures and high initial solution concentrations as described in Table 12. Subsequently, prepipates formed in the test solution, which were collected after filteration, were subjected to ICP analysis to quantify cations in the precipitates and the the amount of carbonate in precipitates was determined by electrophoresis method. Results for the composition of precipitates formed in bicarboante solutions at 15^{o}C and 5% CO_2 bubbling are given in Table 10. Precipitates were predominately iron based. Electrophoresis results indicate that there was relatively very small amount of carbonate and bicarbonates in the precipitates, indicateing that most of precipitates in the solution were oxides and hydroxides of iron. Total carbonate ions detected in the solution, in precipitates, and on the steel suface were then used to calculate the maximum amount of hydrogen that could be produced under a given condition.

Table 10 - Concentration of iron, carbonate, and bicarbonate ions after 72 hour in tested solutions at 15°C and 35°C with 5% CO_2 bubbling

HCO_3^- Conc. (g/L)	Test Temp (°C)	Iron Conc. (mg/L)	Carbonate Conc. (mg/L)	Bicarbonate Conc. (mg/L)
0.1	15	0	0	71
5	15	0	0	5390
10	15	0.024	463	9800
0.1	35	0	0	156
5	35	0.034	0	7420
10	35	0.318	810	16600

Table 11 - Concentration of iron, carbonate, and bicarbonate ions after 72 hour test in the precipitates at 15°C and 35°C with 5% CO_2 bubbling

Solution Composition HCO_3^- Conc. (g/L)	Test Temp (°C)	Iron Conc. in precipitates (mg/kg)	Carbonate Conc. in precipitates (mg/kg)	Bicarbonate Conc. In precipitates (mg/kg)
0.1	15	0	0	0
5	15	526000	1180	5900
10	15	536000	1250	6240
0.1	35	425000	434	2170
5	35	537000	0	0
10	35	520000	0	0

Table 12 - Summary of XRD peaks on pipeline steel coupon in bicarbonate solutions with 5% CO_2

HCO_3^- Conc. (g/L)	Temp (°C)	Phases
0.1	15	Fe_3O_4, Fe
0.5	15	Fe_3O_4, Fe
1.0	15	Fe_3O_4, Fe
5.0	15	Fe_3O_4, Fe
0.1	35	Fe_3O_4, Fe
0.5	35	Fe_3O_4, Fe, Na_2O, **$FeCO_3$**
1	35	Fe_3O_4, Fe
5	35	Fe_3O_4, Fe, FeO, Fe_2O_3, **$FeCO_3$**, Na_2CO_3, Fe_3C
10	35	Fe_3O_4, Fe, FeO, **$FeCO_3$**, Na_2CO_3

The weight of each pipeline coupon was recorded after 72 hour exposure. Corrosion scale was removed from the surface without affecting the metal and the final weight of the metal coupon was recorded again. If we assume that the hydrogen was released due to the cathodic reaction only then the weight loss of metal could be used to calculate the theoretical hydrogen produced by the hydrogen reduction reaction due to anodic dissolution of pipeline steel. Similarly if we assume that the hydrogen was produced from NNPHG mechanism reactions then the total carbonates in the system, which includes carbonates in the solution, in precipitates, and on the metal surface, can be used to calculate the total hydrogen produced in each system. This can be calculated by the following equation:

$$H_{total} = \frac{M_{H_2}}{M_{CO_3^-} * \frac{m_{ppt-ICP}}{1000 * m_{ppt-sol}}} + \frac{M_{H_2}}{M_{FeCO_3} * 1000(wt_{loss} + wt_{scale})} \quad \textbf{(44)}$$

where:

H_{total} = is the total mass of hydrogen produced through the NNPHG mechanism reactions given in mg

M_{H2} = molar mass of molecular hydrogen given in g/mol

M_{CO3}- = molar mass of the CO_3^- ion given in g/mol

M_{FeCO3} = molar mass of $FeCO_3$ given in g/mol

$m_{ppt\text{-}ICP}$ = mass of CO_3^- ion in precipitates given in mg/kg

$m_{ppt\text{-}sol}$ = total mass of precipitates in solution given in g

wt_{loss} = overall weight loss of sample given in mg

wt_{scale} = weight loss of scale given in mg.

Comparison of the calculated amount of hydrogen from the two sources, as shown in Table 13, indicates that the total hydrogen produced via the NNPHG mechanism was almost four times more than that from the hydrogen produced from the reduction reaction alone. While the amount of hydrogen generated will depend upon the temperature and other environmental factors, these calculations indicate that the postulated hydrogen generation mechanism can significantly increase the available hydrogen for diffusion into the pipeline steel that may participate in the TGSCC mechanism for pipeline steels under near-neutral pH conditions.

Table 13 - Calculated hydrogen produced through Colwell-Leis mechanism or through cathodic reaction in bicarbonate solutions with 5% CO_2 at 15°C.

Solution Conc. HCO_3^- (g/L)	CO_3^{-2} in precipitate (ppm)	Weight Loss (g)	Weight of Scale (g)	Weight of precipitate (g)	Hydrogen calculated based on NNPHG mechanism (mg)	Hydrogen calculated based on cathodic reaction alone (mg)
0.1	600	0.0262	0.0319	0.0257	1.0114	0.2281
1	500	0.0306	0.0219	0.0435	0.9141	0.2664
5	2500	0.0333	0.0352	0.0382	1.1950	0.2899

To produce significant amount of hydrogen atoms, anodic dissolution of the steel must occur to produce electrons that may cathodically react with available hydrogen ions. This anodic dissolution is evident on field failures and is observed both on the base metal and crack walls. The novelty in this NNPHG mechanism is that the cathodic reaction to generate hydrogen atoms does not result in an increase in pH. Hydrogen generated by the cathodic reaction of water will result in the accumulation of hydroxide ions and result in an increase in pH.

5.1.2 Summary

The present series of experiments indicate that TGSCC of pipeline steels is possible in simple groundwater solutions containing bicarbonate ions and carbon dioxide. Near-neutral pH conditions can occur in a wide range of concentrations and temperatures as long as sufficient carbon dioxide is present in order to maintain reactant species. pH of the solution is predominantly determined by the relative ratios of the carbonic acid, and bicarbonate ions. Hydrogen can be generated by the NNPHG mechanism which proposes that the generation of hydrogen and formation of $FeCO_3$ on the surface of pipeline steel can occur from bicarbonate solutions without changing the bulk pH of the solution, thereby maintaining the pH of the solution in the near-neutral pH region. Hydrogen generated by the NNPHG was detected by carbonate formation which allowed for calculation of hydrogen. It was determined that NNPHG mechanism can significantly increase the available hydrogen for diffusion into the pipeline steel that may participate in the TGSCC mechanism for pipeline steels under near-neutral pH conditions.

5.2 Understanding Hydrogen Interactions with Pipeline Steel

Since it was determined from experimental results discussed in Section 1 that the NNPHG mechanism could account for an increase in hydrogen production, by the interaction of metal cations with bicarbonate solutions. If all produced hydrogen goes into the pipeline steel, then the next inquiry of this research was to determine how steel microstructure will effect hydrogen permeation and trapping. It was desirable to understand how the produced hydrogen could interact with the steel in order to induce TGSCC damage.

Once hydrogen enters the steel it will diffuse though the steel by means of lattice diffusion at room temperature [76, 105-108]. Hydrogen atoms can jump from one interstitial site to a neighboring vacant site allowing for diffusion over large distances and high diffusivity as there is a high probability of finding a vacant neighboring site for diffusive jumps [105]. As the pipeline microstructure is an imperfect crystal, the structure will contain a distribution of traps such as dislocations, grain boundaries, vacancies or inclusions that will capture and delay the diffusion of hydrogen atoms [70]. Traps are classified according to the strength in which they will hold the captured hydrogen atoms. Reversible traps are considered weak and will release hydrogen at the same rate as hinder diffusion. Irreversible traps have high binding energies and require external energy in order for hydrogen to be released from the trap. Hydrogen captured in irreversible traps are permanently removed from the diffusion process [105].

Main focus was to determine how different microstructural features of pipeline steel may participate in hydrogen permeation. To accomplish this task, X-65 pipeline steel samples were modified by heat treatment to produce varying microstructures as described by Procedures 4.6. Permeation quantified hydrogen diffusivity by electrochemical method whereas hydrogen microprinting technique, as outlined in procedures 4.7, was used to verify the role of different microstructural features on hydrogen trapping and permeation.

5.2.1 Microstructure Characterization

Heat treatments were chosen to produce distinctly different microstructures of the pipeline steel with varying interfaces. The microstructure of pearlite/ferrite samples was quantified and results are given in Table 14. The as-received microstructure, as seen in

Figure 14 is the typical ferrite-pearlite microstructure found in X-65 pipeline steels with a average grain size of ~12 microns. There is a slight degree of banding due to the manufacturing rolling process where the pearlite colonies align themselves in the rolling direction. The annealed air quenched, or normalized, microstructure, shown in Figure 15 is due to a heat treatment where the sample was annealed at a temperature over 150^{o}C above austenitizing temperature. This resulted in ferrite forming at prior austenite grain boundaries and within the grain of a matrix of pearlite upon cooling, producing an average pearlite grain size of ~8 microns [109]. This heat treatment was performed deliberately to create an increase in the pearlite surface area in the normalized pipeline steel as seen in Table 14.

Table 14 - Microstructure Characterization of Pearlite Structure Pipeline Steel

	As Received	**Normalized**
Pearlite Volume Fraction	0.645	0.635
Sampling Error (95% Confidence)	0.0108	0.0126
Pearlite Surface Area (mm^2/mm^3)	160.9	242.9
Sampling Error (95% Confidence)	0.0321	0.0483
Pearlite Mean Intercept Grain Size (mm)	0.0124	0.0082
Pearlite ASTM Grain Size Number	9.37	10.55
Pearlite Mean Chord Length (mm)	0.0160	0.0105

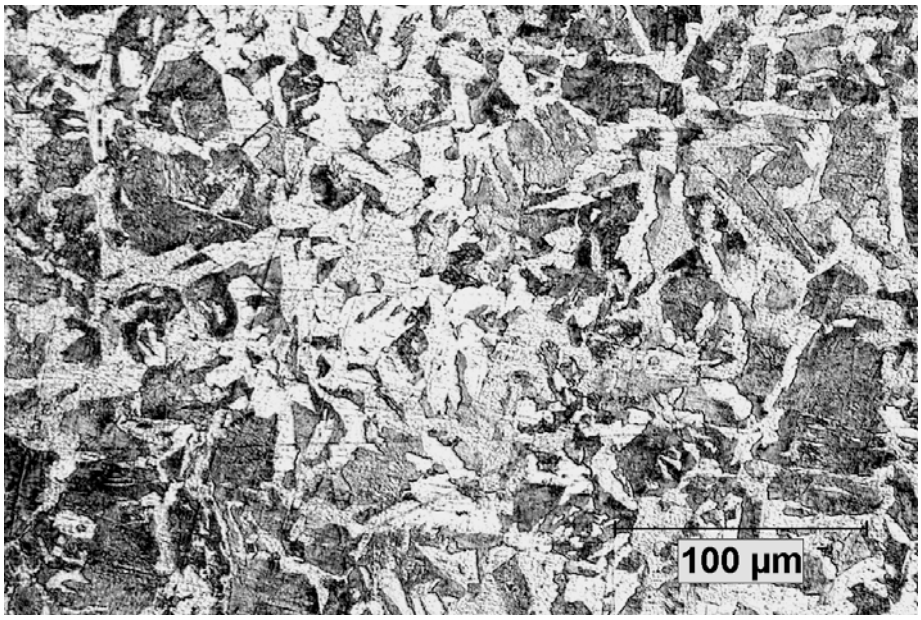

Figure 14 - Ferrite-Pearlite microstructure of as-received X-65 pipeline. The light regions are ferrite and the dark regions are pearlite.

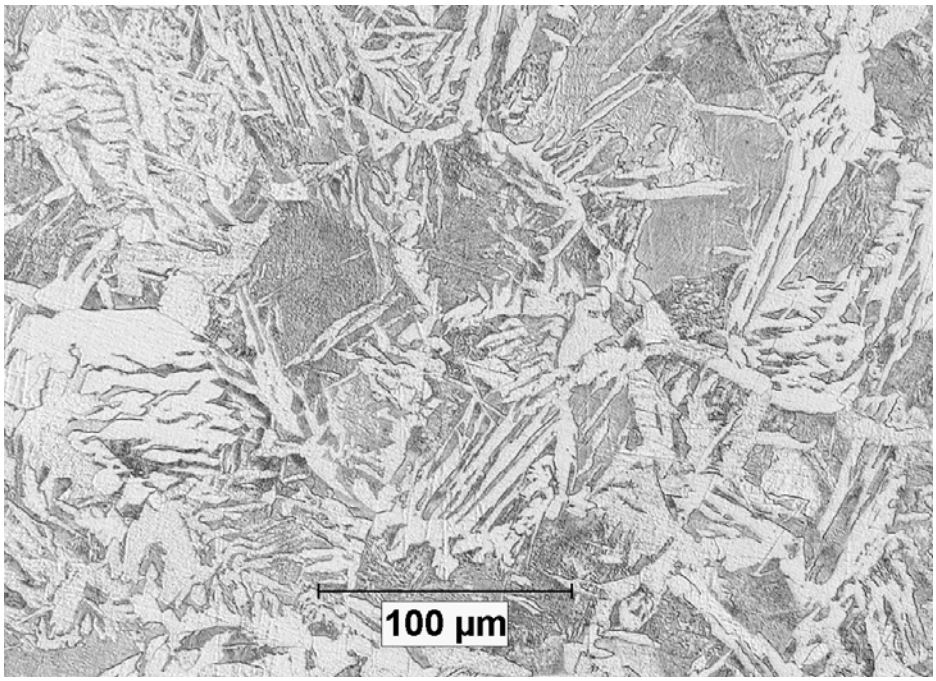

Figure 15 - Ferrite-Pearlite microstructure of annealed air cooled X-65 pipeline. The pearlite forms within ferrite grains due to overheating.

Microstructures of the water quenched and tempered samples were obtained by SEM. The water quenched sample produced a microstructure of white needle-like features that was identified as lath martensite based on carbon content of the steel and observed structure morphology, as seen in Figure 16. The sample was not quenched rapidly enough to produce a full martensitic structure so there is also ferrite grains in the microstructure. The ferrite grains, confirmed by EDS, have a fine distribution of carbides that appear white against the grey ferrite. Characterization for percentage ferrite is given in Table 15. It can be considered that the structure of the quenched sample is composed of only ferrite and lath martensite. Subsequently, the quantity of martensite was determined based on knowledge of ferrite amount. It was determined that only 27% of the sample was ferrite, meaning that 73% of the sample is martensite. As the majority of the sample was martensite, the hydrogen permeation and interaction behavior of the sample should be affected by the martensite microstructure more than by the small percentage of ferrite present in this microstructure.

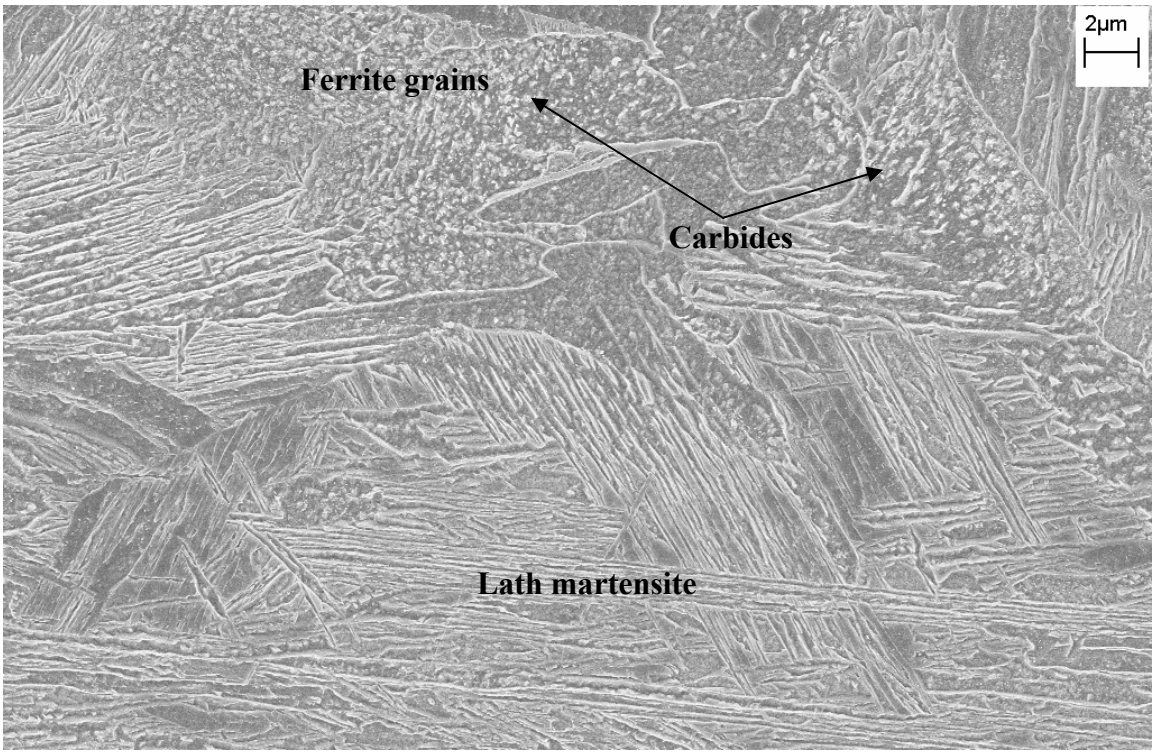

Figure 16 - Microstructure of Annealed and Water Quenched (AWQ) pipeline steel showing lath martensite with ferrite grains.

Table 15 - Microstructural quantification for the annealed and water quenched (AWQ) sample

	AWQ
Ferrite Volume Fraction	0.2754
Sampling Error (95% Confidence)	0.0228
Ferrite Surface Area (per mm)	0.398
Sampling Error (95% Confidence)	0.0291
Ferrite Mean Intercept Grain Size (micron)	5.0233
Ferrite Mean Chord Length (micron)	2.7670

Tempering treatment was performed on the AWQ samples to vary the carbide size and induce lattice relaxation. Initial tempered samples were produced to determine the effect of lattice relaxation on the hydrogen behavior. It has been established that tempering times of 15 minutes have as much affect on lattice relaxation as tempering for

100 hours [110]. This means that relaxation of the structure is a rapid process. By limiting the time to only one hour, relaxation should be achieved without drastically changing the carbide size. Tempering temperatures were selected in order to minimize the carbide growth. EDS was performed on all tempered samples to confirm the presence of carbide phase, and a representative carbide spectra is given in Figure 17 along with the image of spot analysis for the Tempered 400°C sample. Confirmation of the ferrite phase was also made and EDS is shown in Figure 18. No speculation on carbide composition was made based on EDS as carbide composition can change with increased tempering time and temperature.

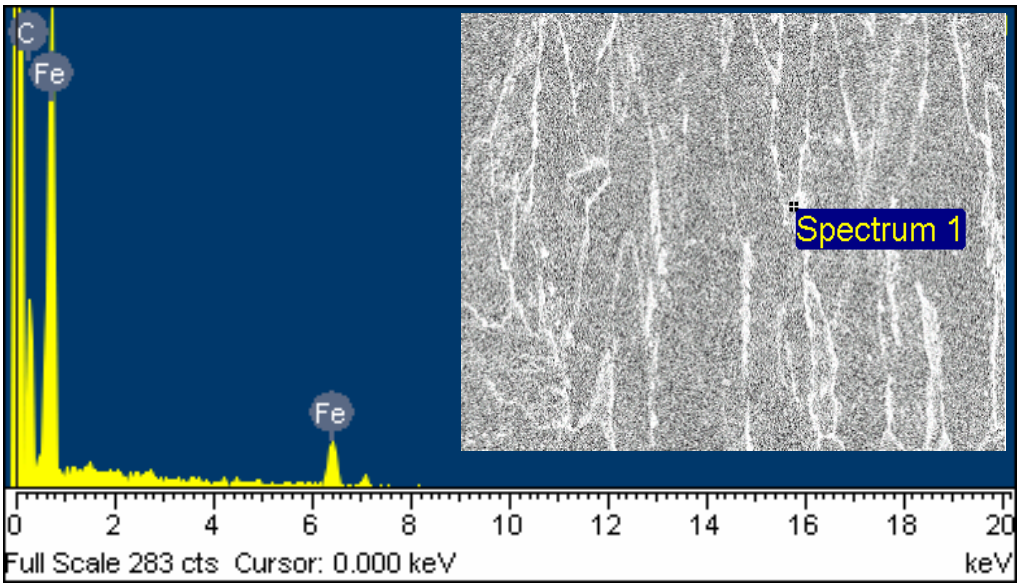

Figure 17 - EDS spectra of carbide in tempered martensitic structure

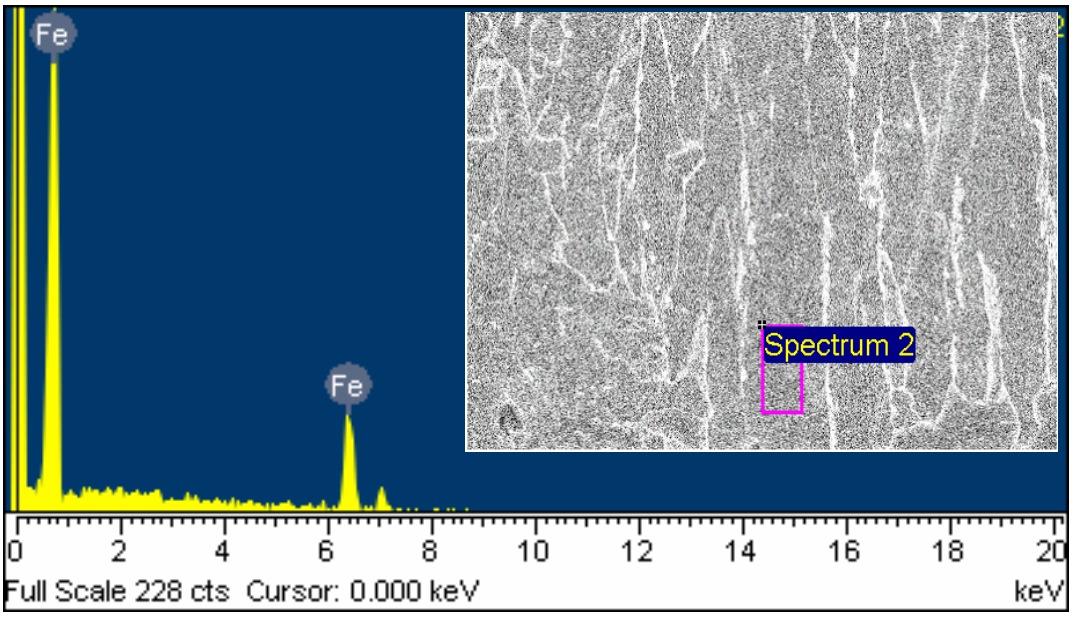

Figure 18 - EDS confirming the ferrite phase in tempered martensitic structure

The martensitic transformation temperature for X-65 pipeline steel is around 350°C as seen in Figure 8, so Table 16 shows that there was very little carbide growth for the sample tempered at 350°C [95, 98]. Characterization of volume fraction of carbides in the tempered 350°C sample indicates an unrealistic amount of carbides based on the lever rule and known amount of carbon for this steel. This is due to etching effects that make carbides more apparent on the imaged surface. This effect is stronger when precipitates are very small. However, as tempering temperature is just above martensite start temperature, there is little precipitate coarsening or growth, resulting in small carbides that can be observed in Figure 19. The tempered 350°C samples exhibited ferrite grains morphology that was similar to the ferrite grains found in the water quenched sample. Carbides were evenly distributed throughout the grain and displayed no preference to grain boundaries.

Table 16 - Carbide size with varying tempering temperatures

	Temper 350°C	Temper 400°C	Temper 475°C
Carbide Volume Fraction	0.425	0.159	0.179
Sampling Error (95% Confidence)	0.018	0.017	0.017
Carbide Surface Area (per micron)	11.042	3.965	2.902
Sampling Error (95% Confidence)	0.052	0.049	0.032
Carbide Mean Intercept Grain Size (micron)	0.181	0.504	0.689
Pearlite Mean Chord Length (micron)	0.154	0.160	0.247

Carbide size for samples tempered at higher temperature show substantial growth. Carbide increased from 0.181 microns to 0.504 microns with only a 50°C increase in tempering temperature for one hour. The tempered 400°C sample had grains with even carbide distribution and grains where the carbides had coarsen to form larger particles, as shown in Figure 20. This sample also exhibited a tendency for carbides to cluster at the grain boundaries of ferrite. Carbide's size was similar for both samples tempered at 400°C and 475°C. This indicates that tempering spurred initial carbide growth which rapidly stabilized. The tempered 475°C sample, shown in Figure 21, was similar to tempered 400°C sample with carbide clustering at grain boundaries. Carbides were no longer evenly distributed carbides within the grain; rather, carbides had coalesced to form well defined particles within the grain.

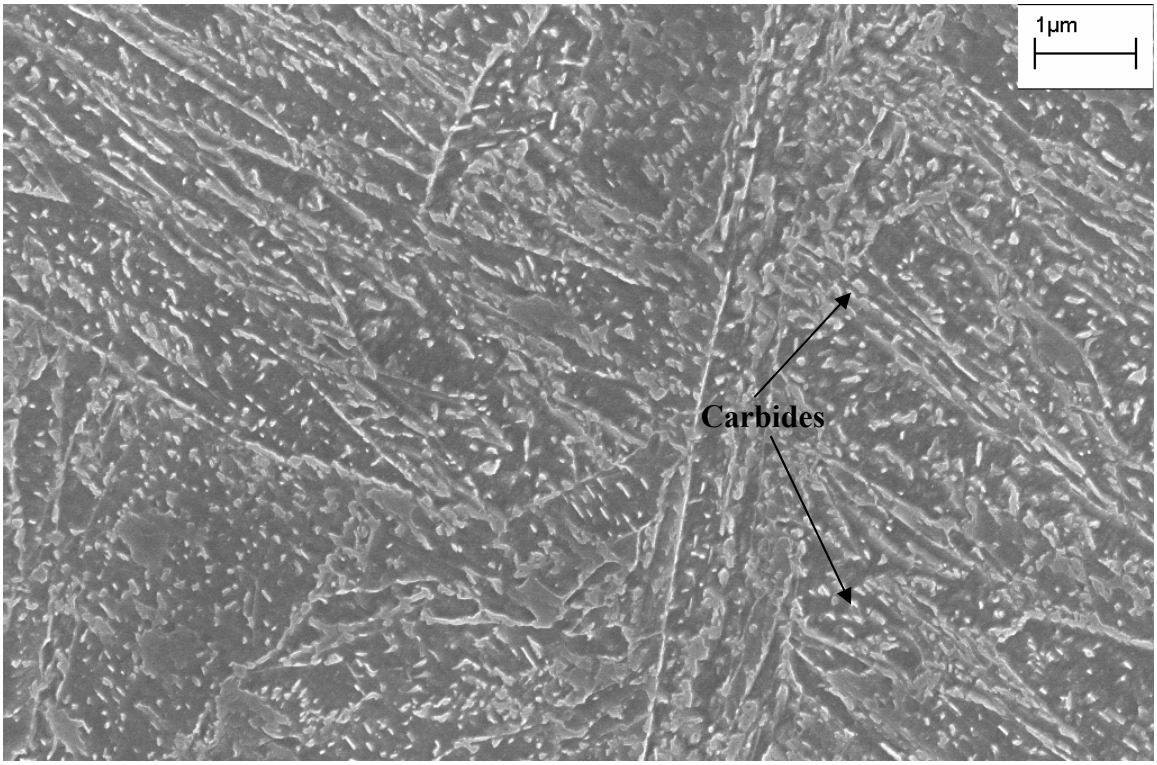

Figure 19 - SEM of microstructure of Tempered 350^{o}C pipeline sample. Carbides appear as lighter phase stand in relief from the grey ferrite

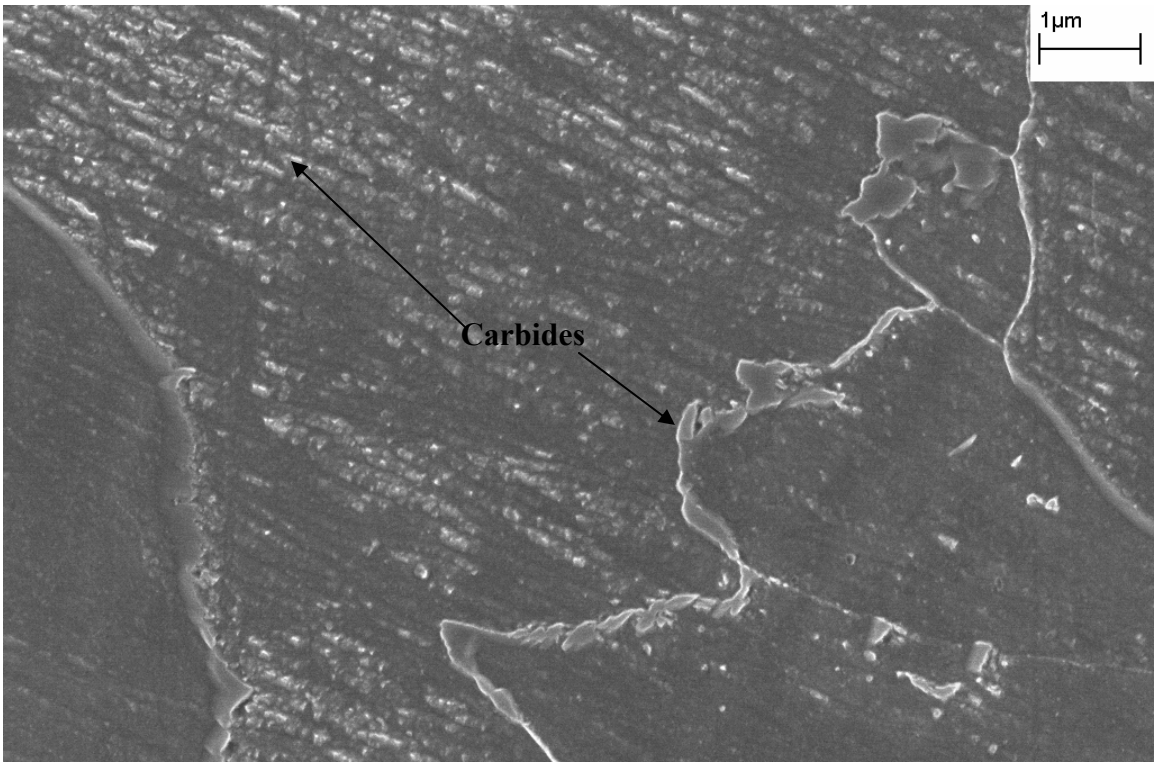

Figure 20 - SEM of microstructure of Tempered 400°C pipeline sample. Carbides appear as lighter phase and stand in relief from the dark grey ferrite

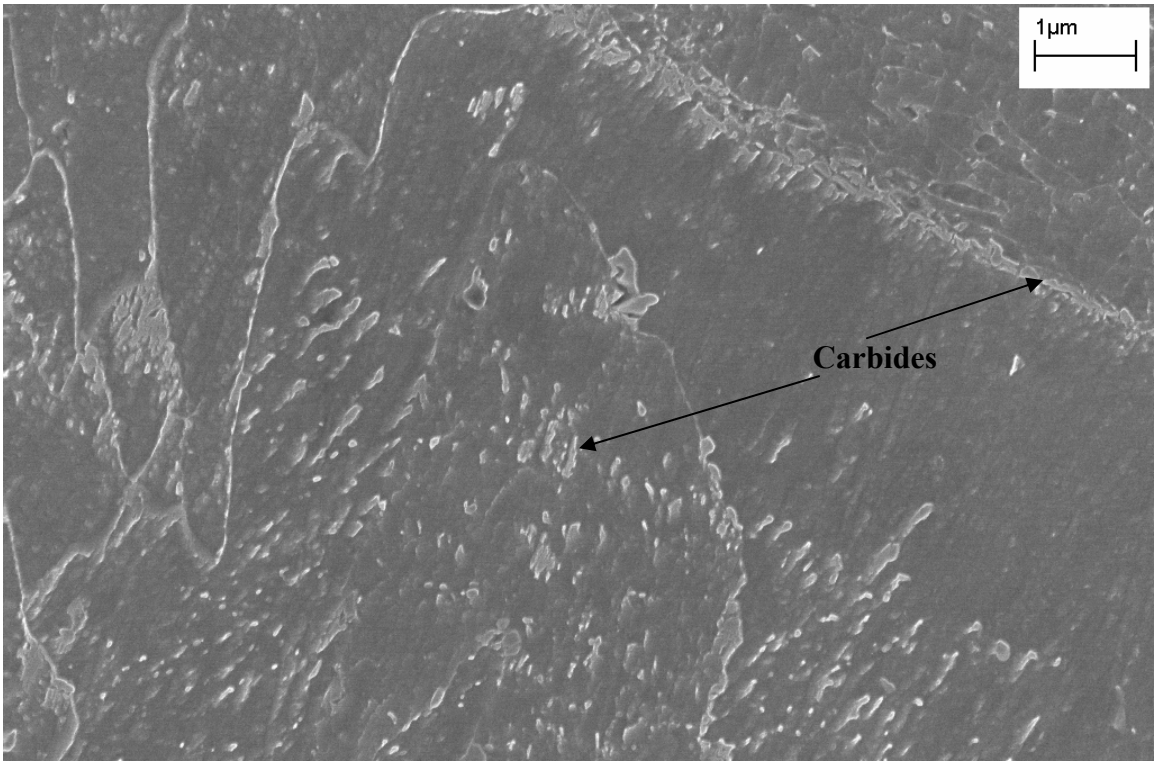

Figure 21 - SEM of microstructure of Tempered 475°C pipeline sample. Carbides appear as lighter phase and stand in relief from the darker ferrite

To characterize the lattice relaxation of the tempering process, heat treated pipeline steel samples were characterized by XRD. Representative spectra for the normalized sample and the annealed water quenched sample along with associated BCC peak family identification are given in Figure 22. Other spectra obtained in this research are given in Appendix A. Although the martensitic structure is known to deviate from BCC to form a more BCT structure, the XRD peaks generated were symmetrical and the line pattern could be interpreted on the basis of the BCC iron crystal structure [111]. In this figure it can seen that the martensitic steel has broad XRD profiles along with a decrease in intensity. It is also interesting to note that carbide peaks were not observed by XRD. This is attributed to the small size of the carbides. Any structure in the nanometer size range will have a low intensity peak with extreme peak broadening.

Although several XRD peaks were examined, the (200) peak ($2\theta = 64^{o}$) was the most responsive to lattice changes. Results, given in Table 17, show that there was very little change in lattice parameters between the original water quenched sample and the sample tempered at 350^{o}C. Results also show that the lattice relaxation resulted in a smaller d-spacing indicating that the strain induced by the quenching process caused lattice dilation. With increasing tempering temperature, the lattice parameters decreased as dislocations were annealed out of the system and carbon diffused out of the lattice to form carbides. Lattice relaxation also was observed by the decrease in the peaks full-width-half-max (FWHM) as sharper peaks were observed with increase in tempering.

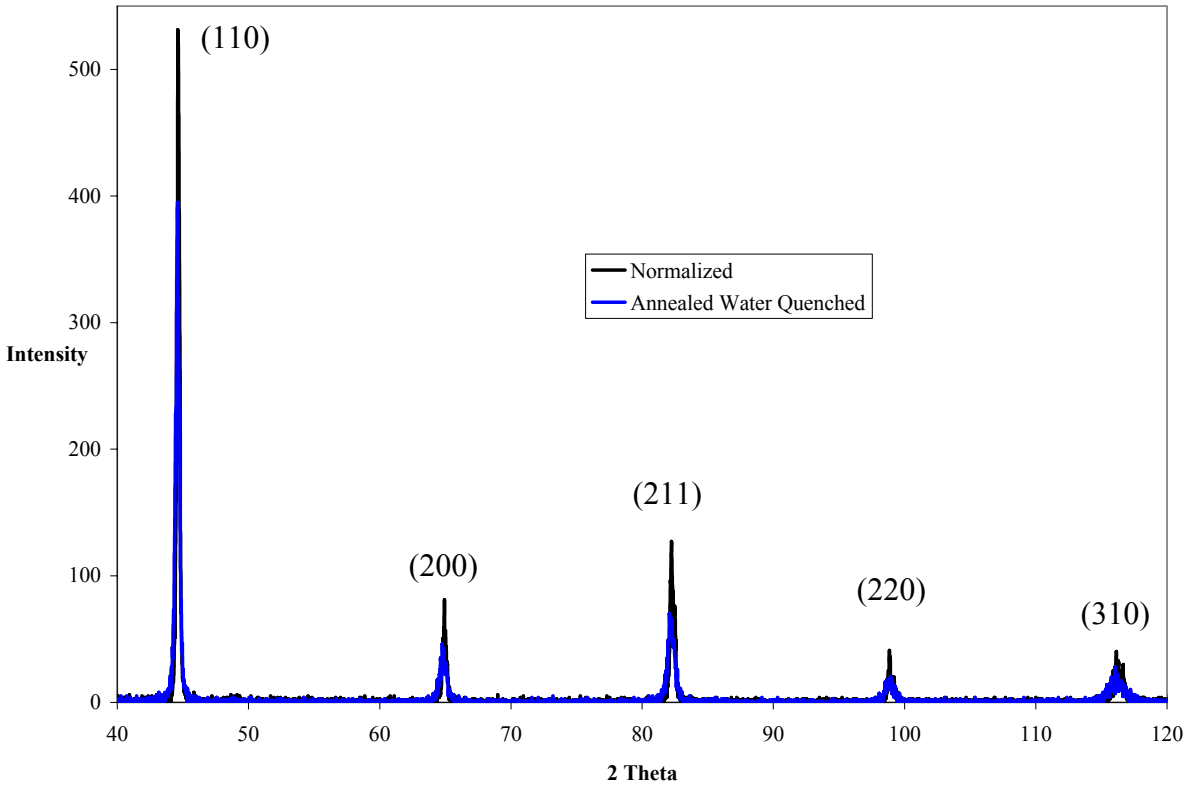

Figure 22 - Representative XRD peaks for Normalized and Annealed Water Quenched samples with peak families identified

Table 17 - XRD results for the 64^{o} 2θ Peak for samples with differing tempering temperatures

Sample	2 Theta	d-spacing (Å)	Intensity	FWHM
AWQ	64.857	1.4364	70.8	0.567
T350	64.865	1.4363	83.2	0.567
T400	64.909	1.4354	85.2	0.479
T475	64.968	1.4343	62.1	0.327

In order to determine the effect of carbide size on permeation, pipeline steel X-65 water quenched samples were tempered at 650^{o}C for one hour, one day, and seven days. This allowed for carbide coarsening while maintaining equivalent lattice relaxation. This permitted the effect of coarsening verses lattice dilation to be distinguished in terms of hydrogen diffusion. Characterization of the carbides after these heat treatments is given in Table 18.

The microstructure of the one hour tempered sample shows that carbides formed in clusters, in well defined spheres and ellipsoids, similar to pearlite structure, as seen in Figure 23. Carbide formation occurred preferentially around grain boundaries. Otherwise the carbides formed randomly throughout the grain. In the one day sample, carbides were mostly spherical, as seen in Figure 24. Carbide coarsening occurred preferentially at the grain boundaries, although there were still a significant amount of carbides left within the grain. In the seven day sample, carbides were located mostly at the grain boundary, leaving the ferrite grain relatively free of internal carbides. This can be seen in Figure 25.

Carbide size was characterized by micrographic methods, and it was determined that there was a direct relationship between the tempering time and the carbide mean intercept size. Carbide size for the one hour tempered sample at 650^{o}C was equivalent to

the low temperature tempering samples shown in Figures 21. Higher temperatures resulted in a greater degree of coarsening. This reaffirms the assertion that time is the key variable in order to observe changes in carbide size [112].

Table 18 - Carbide size properties for samples tempered at 650°C at varied times

	T650°C 1 hour	T650°C 1 day	T650°C 1 week
Carbide Volume Fraction	0.157	0.115	0.114
Sampling Error (95% Confidence)	0.016	0.011	0.008
Carbide Surface Area (per micron)	4.344	1.693	1.080
Sampling Error (95% Confidence)	0.056	0.045	0.041
Carbide Mean Intercept Grain Size (micron)	0.460	1.182	1.852
Pearlite Mean Chord Length (micron)	0.145	0.271	0.421

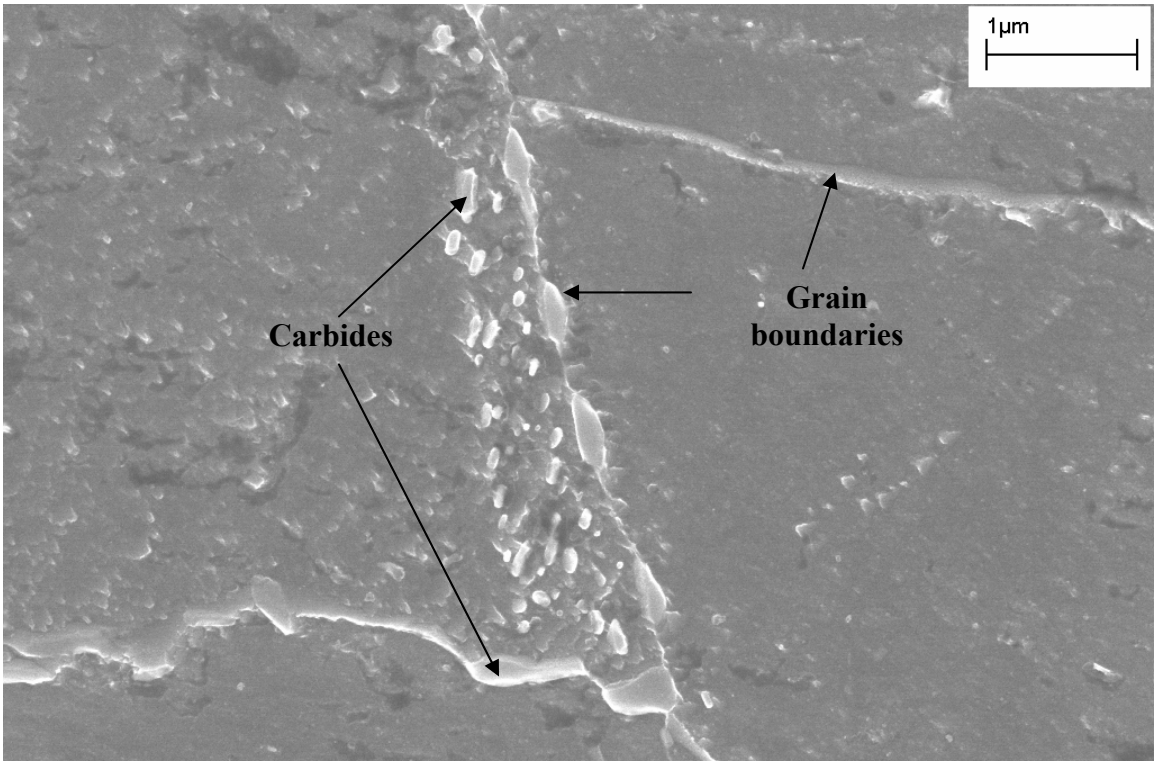

Figure 23 - SEM image of the microstructure of Temper 650°C for 1 hour.

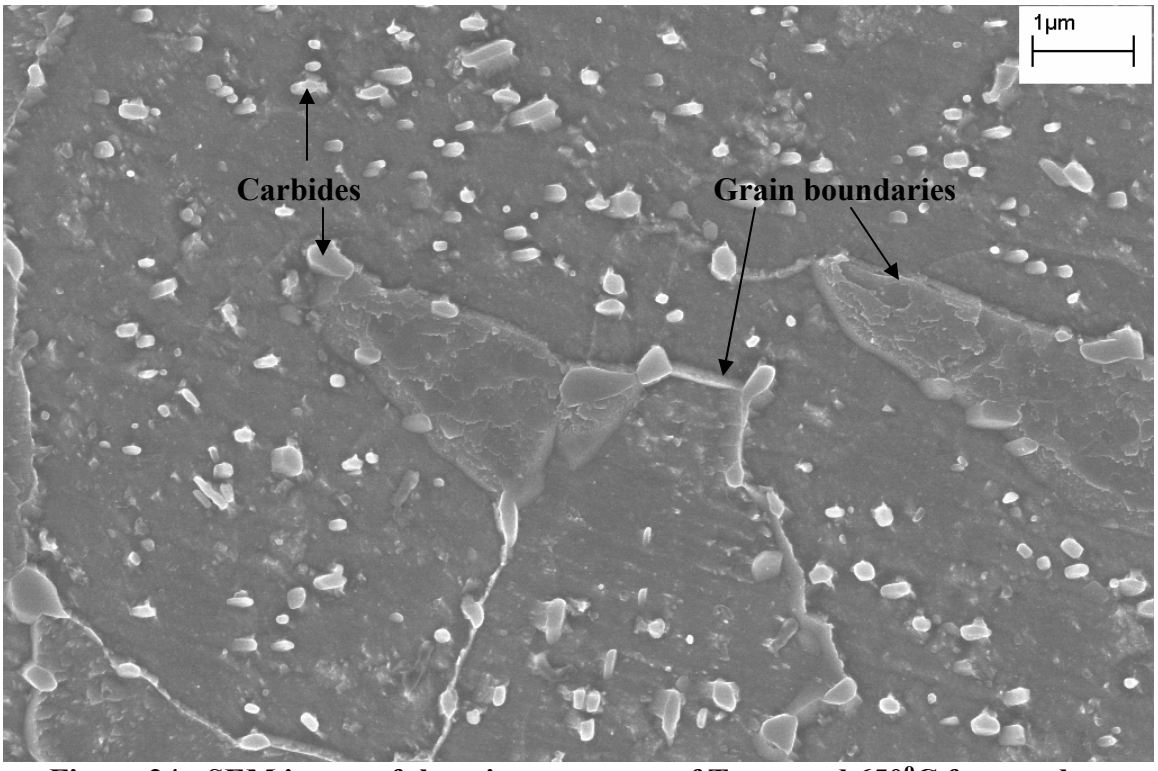

Figure 24 - SEM image of the microstructure of Tempered 650^{o}C for one day.

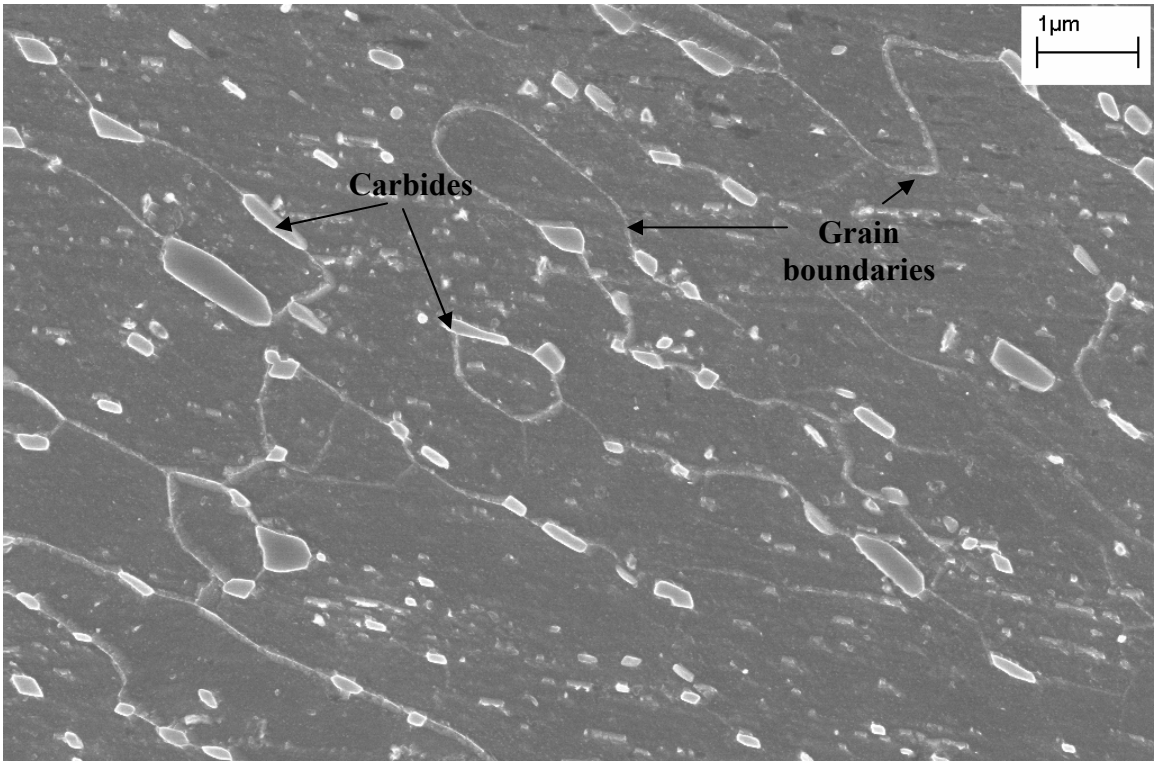

Figure 25 - Figure 8 - SEM image of the microstructure of Tempered 650^{o}C for one week (7 days).

5.2.2 Hydrogen Permeation

Hydrogen permeation study was performed in order to understand the diffusion behavior of hydrogen in pipeline steel with different microstructure. A detailed description of the testing technique and the theory behind this method is given in 4.6. In these tests, hydrogen is formed on one side of the sample in a cathodic chamber. The hydrogen diffuses through the sample and is oxidized on the exiting side of the sample. The change in current density on the exiting side of the sample is representative of the diffusion behavior of the sample.

It has been well established that the method of hydrogen diffusion in low alloy carbon steel is via lattice diffusion. Diffusivity has been reported to be highest in BCC metals, smaller in FCC and lowest in BCT. This is due to the difference in near-neighbor

interstitial distance, *d*. As the values of *d* increases there will be a larger energy barrier between the interstitial sites and subsequently higher activation energies for hydrogen diffusion. In BCC metals, the *d* distances are so small that tunneling becomes a dominant mechanism in the hydrogen jump process at low temperatures, resulting in high diffusivity [105].

A representative permeation curve for as-received samples exposed to the TGSCC groundwater environment of 0.5g/L $NaHCO_3$ with 5%CO_2 and deionized water are given in Figure 26. All permeation graphs are provided in the Appendix B. As shown in this figure, the cathodic reaction associated with the anodic formation of iron oxide in deionized water did not produce sufficient hydrogen in order to observe hydrogen peak. This test was reproduced twice with the same results. However, the TGSCC environment (0.5g/L $NaHCO_3$ with 5%CO_2) produced enough hydrogen to not only be detected but also produce Fick's Law diffusion behavior. Similar diffusion behavior was observed on all steel microstructures tested in the TGSCC groundwater environment.

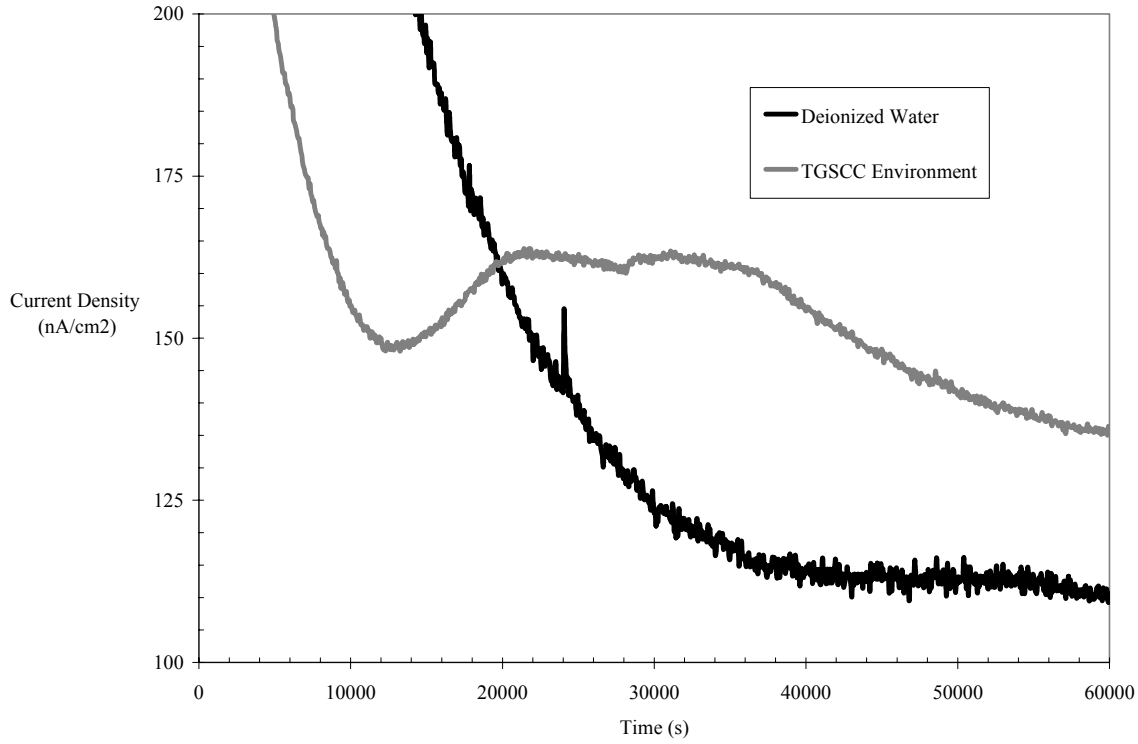

Figure 26 - Permeation curve of As-received sample exposed to cathodic environments of deionized water and 0.5g/L $NaHCO_3$ with 5%CO_2 both at OCP.

Results from the hydrogen permeation tests are shown in Table 19. Permeation results for all tested heat treatments and environment are given in Appendix B. Results summarized in Table 19 clearly indicate that the hydrogen is produced and diffuses through the pipeline steel in simple bicarbonate solutions with CO_2. As the cathodic chamber was kept at open circuit potential (OCP), the hydrogen is produced without the assistance of applied cathodic current. Diffusion rates obtained were similar to those produced on as-received X-65 pipeline steel subjected to a cathodic current density of -20A/m^2 in 0.1 N NaOH solution [71]. This reinforces the hypothesis that additional hydrogen can be generated through the proposed NNPHG mechanism and that the hydrogen produced by this mechanism is available to diffuse into the pipeline steel.

Table 19 – Summary of Hydrogen Permeation Results for Heat Treated X-65 Pipeline Steel Samples. Data is average of at least 2 tests under OCP conditions

Heat Treatment	Diffusion Rate (e^{-10} m^2/s)	Permeation Current Density (e^{-7} A/cm^2)	Steady State Flux (e^{-12} mol/cm^2s)	Solubility (e^{-9} mol/m^3)
None (As Received)	2.76 ± 0.41	2.01 ± 0.59	2.09 ± 0.62	1.98 ± 0.83
Normalized	4.74 ± 0.40	3.79 ± 0.85	3.93 ± 0.88	2.12 ± 0.78
Annealed Water Quenched (AWQ)	1.33 ± 0.098	2.29 ± 0.25	2.37 ± 0.26	4.87 ± 0.74
Temper 350°C	1.89 ± 0.067	2.27 ± 1.1	2.35 ± 1.1	3.25 ± 1.4
Temper 400°C	2.15 ± 0.037	1.73 ± 0.32	1.79 ± 0.34	2.33 ± 0.32
Temper 475°C	2.52 ± 0.066	1.81 ± 0.29	1.88 ± 0.31	2.03 ± 0.30
Temper 650°C - 1 hour	5.66 ± 0.28	3.17 ± 0.38	3.29 ± 0.40	1.63 ± 0.24
Temper 650°C - 1 day	5.08 ± 0.073	2.78 ± 0.87	2.88 ± 0.90	1.55 ± 0.47
Temper 650°C - 1 week	5.48 ± 0.091	2.40 ± 0.14	2.49 ± 0.15	1.27 ± 0.083

Table 19 provides the permeation results for the steel microstructures tested. The diffusion rate was calculated based on the time lag method developed by Devanathan [100]. In this method the time lag is directly proportional to the square of the thickness, meaning that the hydrogen measured is the diffusion constant of hydrogen in bulk of the metal. Further, the linear variation of the reciprocal of the sample thickness shows that the transportation process across the surface is not rate-controlling [100]. Permeation current density is directly measured from the test setup and is used to calculate steady state flux. In understanding the difference of microstructural features, the difference in solubility of hydrogen in the steel matrix provides a direct measurement of hydrogen

trapping [108]. It is the measure of concentration of subsurface hydrogen concentration in interstitial lattice sites and hydrogen in traps. Trap sites that are included in this measurement are considered to be reversible as it is assumed that irreversible sites are considered to be filled with hydrogen before steady state hydrogen permeation is achieved [99].

Since only one permeation transient was performed to obtain diffusion behavior, the permeation data reflects both irreversible and reversible trap sites. It is assumed that irreversible traps are saturated and do not have significant influence on the diffusion process [106]. Further, permeation data is considered to reflect interstitial diffusion only, as discontinuous interfaces such as dislocations and grain boundaries are assumed to contribute only a small fraction of flux compared to the matrix of the sample. Subsequently, the variation in permeation behavior can be attributed to the direct difference in trapping behavior of the different microstructures.

Permeation results shown in Table 19 indicate that the normalized pipeline steel samples had one of the higher diffusion rates and had the largest steady state flux. This can be correlated to a decrease in trap sites within the relaxed steel microstructure [75]. The microstructure of this normalized structure indicated a higher surface area of the grains. This suggests that continuous interfaces such as grain boundaries may also contributed to hydrogen diffusion. Continuous high energy interfaces may shield the hydrogen from other low energy traps, facilitating hydrogen transportation through the structure. It is interesting to note that the concentration of trap sites for the normalized sample was higher than the as-received sample, yet there was a 40% increase in diffusion. The increase in trap sites may be attributed to the higher surface area of pearlite. The as-

received sample still maintains some straining due to pipeline fabrication and sample machining conditions, producing dislocations that can trap the hydrogen. However, the normalized sample represents the most relaxed and stress free structure.

The water quenched steel sample had the slowest diffusion rate. Similar results have been reported by several other researchers [76, 107]. This is counter to the idea that high interfacial area could increase diffusion by hydrogen trap shielding. However, it has been well documented that the martensitic structures have significantly low hydrogen diffusion than ferritic structures [77, 107]. However, the method of hydrogen transportation is still interstitial diffusion. The decrease in hydrogen diffusivity is accounted for by the lattice strain caused by the formation of BCT structure. Further, the increase in interstitial distance can also attribute to the decrease in diffusivity [106]. This is also attributed to the number of trap sites that slow down the hydrogen diffusion through the material. Traps in water quenched carbon steels are most likely the dislocations formed during the martensitic transformation to create the lath structure. This assertion is supported by the work of Luppo et al. who reported that the high density of dislocations decreased the diffusivity and steady state flux of hydrogen through quenched X-60 steel [76].

As shown in Table 19, the low temperature temper steel demonstrated an increase in diffusion and a decrease in the trap concentration as reflected by the measure of solubility with an increase in the tempering temperature. Diffusion systematically increased with an increase in tempering temperature. This indicates that lattice relaxation facilitated the diffusion of hydrogen through the structure. As the sample is tempered, dislocations relax out of the structure as carbide particles precipitate in the ferrite grain.

This results in a progressively relaxed structure with decreasing dislocation density. This results in a decrease in reversible and irreversible hydrogen traps which prohibits the accumulation of hydrogen in the steel and affects embrittlement [76]. Ultimately, tempering on 475^{o}C resulted into the diffusion rate and the trap concentrations equivalent to the as-received sample.

Increasing tempering time allowed for carbide coarsening as demonstrated in Table 18. Carbides could act as traps. Results from permeation tests and microstructure characterization showed a decrease in the trap site concentration with an increase in carbide size. However, there was no trend in the diffusion rate with carbide coarsening. This indicates that the effect of lattice relaxation to facilitate lattice diffusion has a more significant effect than the carbide interface trapping. It is also interesting to note that the highest diffusion rates occurred on these high temperature tempered samples. This is attributed to the decrease in hydrogen traps with maximum relaxation occurring at high tempering temperatures. Further, Figure 25 demonstrates the small ferrite grain size of the samples tempered at 650^{o}C. Although the grain size was not characterized, this reaffirms the theory that hydrogen diffusion may be facilitated by high energy continuous interfaces such as grain boundaries.

5.2.3 Hydrogen Microprinting

To validate the sites of trapping in the studied microstructures, hydrogen microprinting was performed. In the hydrogen microprinting process, silver bromide is deposited on the surface of a sample to undergo a chemical reaction with trapped hydrogen near the surface of the sample. Hydrogen will react with the bromide leaving

deposits of nano-silver grains wherever hydrogen was once trapped. Details of this procedure are given in 4.7

It was determined through experimentation that the microprinting technique could only be accomplished on ferrite-pearlite structures. This is because it was impractical to distinguish silver grains from carbides in tempered and water quenched samples as the silver grains had the same brightness and morphology when viewed by SEM. Further, observation of small scale silver grains was obstructed by carbides charging.

Microprinted as-received sample is shown in Figures 27 and 28. Silver particles are approximately 10 nm and appear bright and imposed on the microstructure. Samples that were microprinted but not exposed to hydrogen did not show any of these silver grains. EDS was performed on these grains to confirm the presence of silver and results are given in Figure 29. Figure 27 demonstrates that the hydrogen accumulated evenly throughout the ferrite and pearlite grains, providing further evidence of lattice diffusion. Figure 28 shows that within the pearlite, hydrogen accumulates in the ferrite structure as compared to the cementite. Within the ferrite grain, the hydrogen is most likely trapped by the dislocations and interfaces. Within the pearlite grain, the hydrogen is most likely trapped by the cementite-ferrite high energy interfaces.

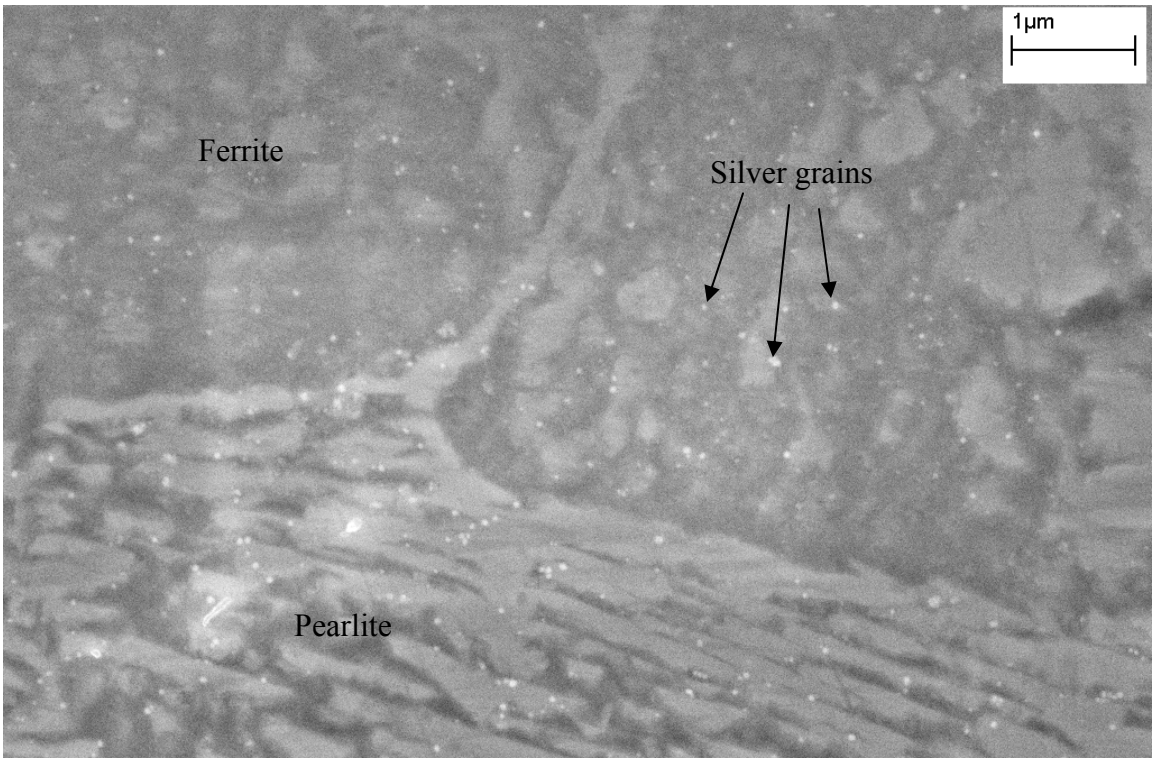

Figure 27 - SEM of hydrogen microprinted as-received sample.

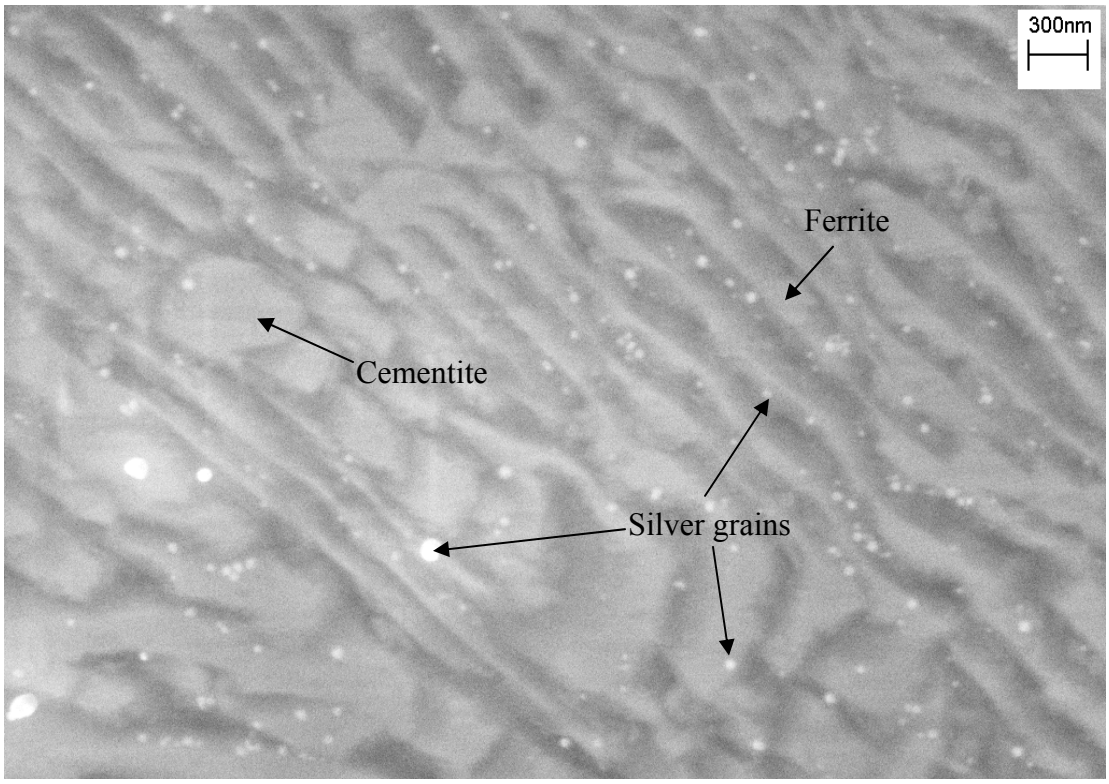

Figure 28 - SEM of hydrogen microprinted as-received sample. This image shows that hydrogen preferentially accumulates in the ferrite as oposed to cementite in pearlite grains.

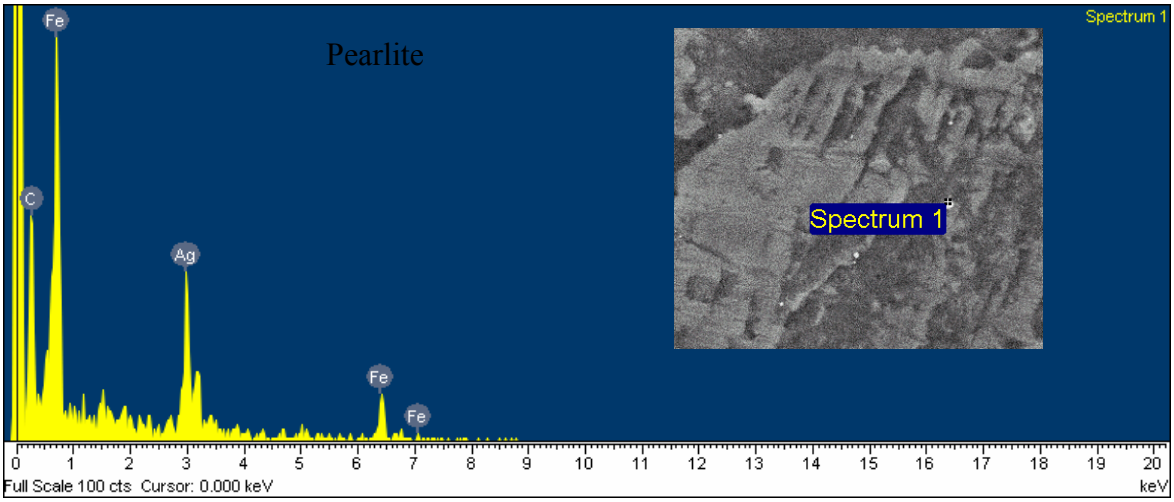

Figure 29 - EDS results for silver particles to confirm the hydrogen microprinting

Microprinting was also performed on normalized pipeline steel samples and the results are given in Figure 30. In this sample, very little hydrogen was observed in the pearlite grains. Rather, most silver grains, and associated hydrogen, was located in the ferrite grain. The concentration of these sliver grains was significantly less than in the as-received sample. Contrary to permeation results, this indicates that the trapping concentration in the normalized sample is less than the as-received. This indicates that hydrogen is most likely trapped by dislocations within the ferrite grain. The decrease of silver grains in normalized sample exhibit the decrease in dislocation density and trap sites, causing in increase in diffusivity.

The normalized sample also exhibited the effect of hydrogen distribution around inclusions, as shown in Figure 31. Around the inclusion, hydrogen occurred in high concentrations in comparison to the bulk sample. The inclusions were determined to be MnS by EDS. This accumulation of hydrogen is attributed to the interface and high dislocation density that develops around an incoherent inclusion/precipitate. This confirms the previous assertion that interfaces and dislocations act as hydrogen traps. Subsequently, pipeline steels that have lower concentrations of inclusions should have high hydrogen diffusivity.

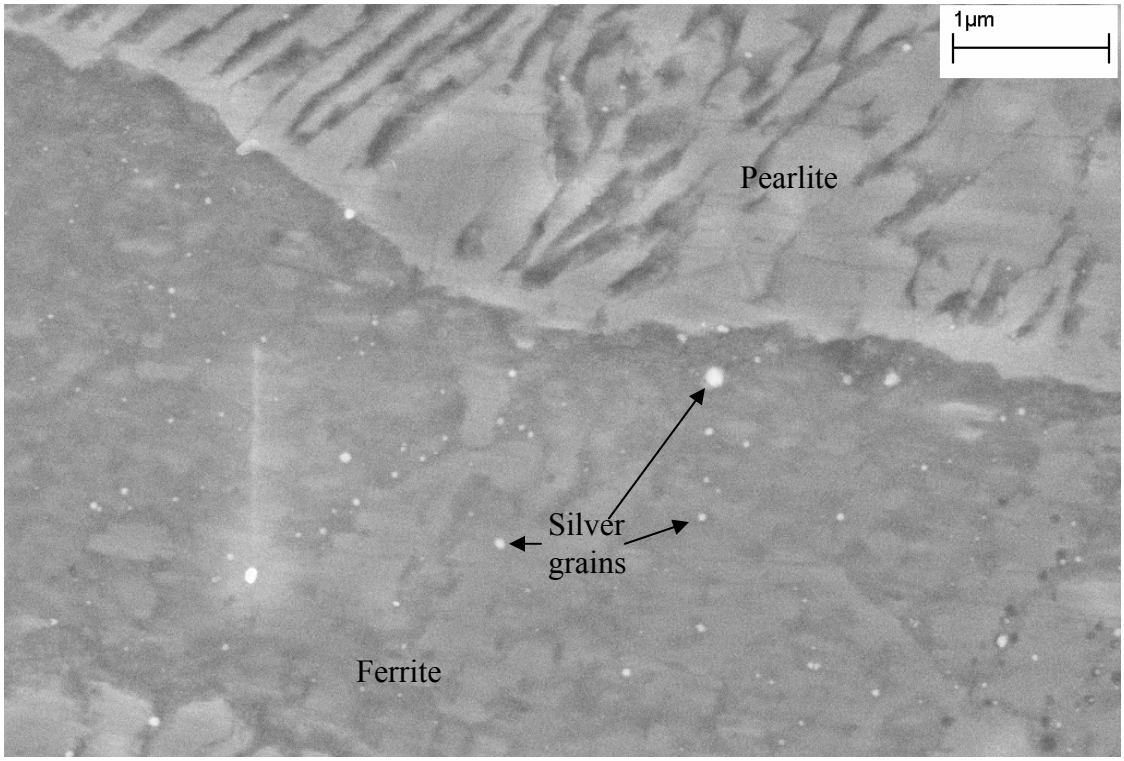

Figure 30 - SEM of hydrogen microprinted annealed sample. As compared to the as machined sample, the annealed sample has a significantly less hydrogen. However, the preference of hydrogen to accumulate within ferrite is still apparent.

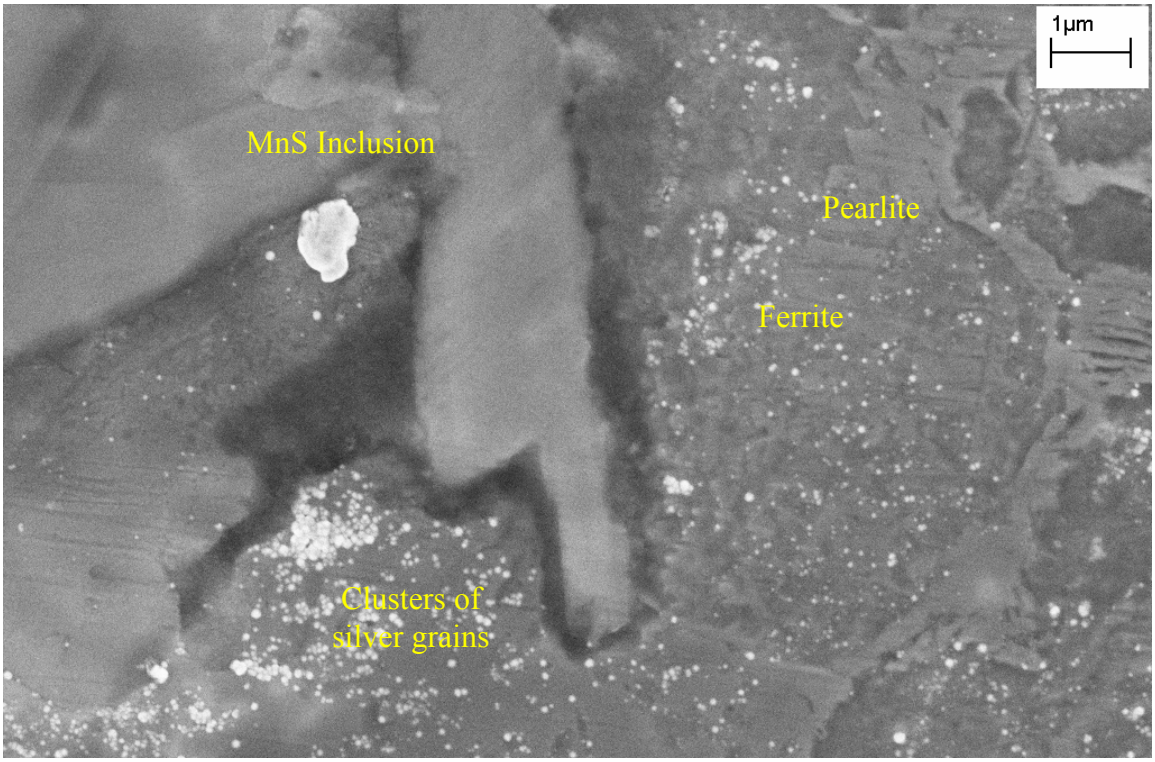

Figure 31 - Hydrogen concentration around a MnS inclusion was much higher than what was observed in the bulk of the sample. Hydrogen concentration around a MnS inclusion was still concentrated in ferrite grains rather than pearlite

5.2.4 Summary

These results confirm that the NNPHG mechanism can produce significant amounts hydrogen under open circuit potentials, which was almost 4 times the amount possible by the cathodic reactions to counter anodic activity on pipeline surface. Further, sufficient hydrogen is generated in simple bicarbonate environments exposed to 5% CO_2 to be detected by hydrogen permeation. The hydrogen produced in near-neutral environments at open circuit potential permeates through the pipeline steel with diffusion behavior consistent with Fick's Law. Microstructural characterization coupled with hydrogen permeation indicated that carbide size does not strongly influence the hydrogen permeation. Rather, the level of strain in the lattice has the most influence on hydrogen

diffusivity with water quenched and as received structures producing the lowest diffusivity. Highest diffusivity occurred on normalized samples and sample subjected to high temperature tempering. Hydrogen microprinting detected hydrogen accumulation in ferrite grains and at high energy discontinuous interfaces around inclusions.

5.3 Hydrogen Effects on Cracking of Pipeline Steel

Since it was determined in the previous section that hydrogen solubility in the pipeline steel is dependent on the microstructure and lattice strain, the next stage of research was to determine the conditions that hydrogen will ingress into the pipeline to effect mechanical properties of the steel and induce TGSCC cracking. Main aim for these experiments was to determine environmental conditions under which TGSCC cracks could be produced in a laboratory environment on X-65 pipeline steel that were similar in morphology to those found in field failures.

5.3.1 - Cracking Behavior for Cathodically Induced Hydrogen:

To examine the effect of hydrogen on the mechanical properties of pipeline steels, initial tests were performed in the standard TGSCC environment with applied cathodic protection to ensure that the hydrogen was being produced on the steel surface to diffuse into the pipeline sample. The results from these slow strain rate tests are given in Figure 32 as the plot of stress verses percent strain. As expected, an increase in hydrogen production at the steel surface by increasing the applied cathodic density (decreasing applied potential value) resulted in a direct decrease in the % strain to failure thereby indicating embrittlement of pipeline steel samples, as shown in Table 20. The ductility is reduced by half when only -850 mV (vs. SCE) was applied as compared to the steel samples tested at open circuit potential, which was measured to be around -780 mV.

It is interesting to note that there was only a small difference in the stress-strain behavior between -1.25 V and -1.75 V tests. This is attributed to the saturation of hydrogen into the pipeline steel. This is also noteworthy as -1.25 V is often the potential that pipelines are held at to cathodically protect the pipeline in field service.

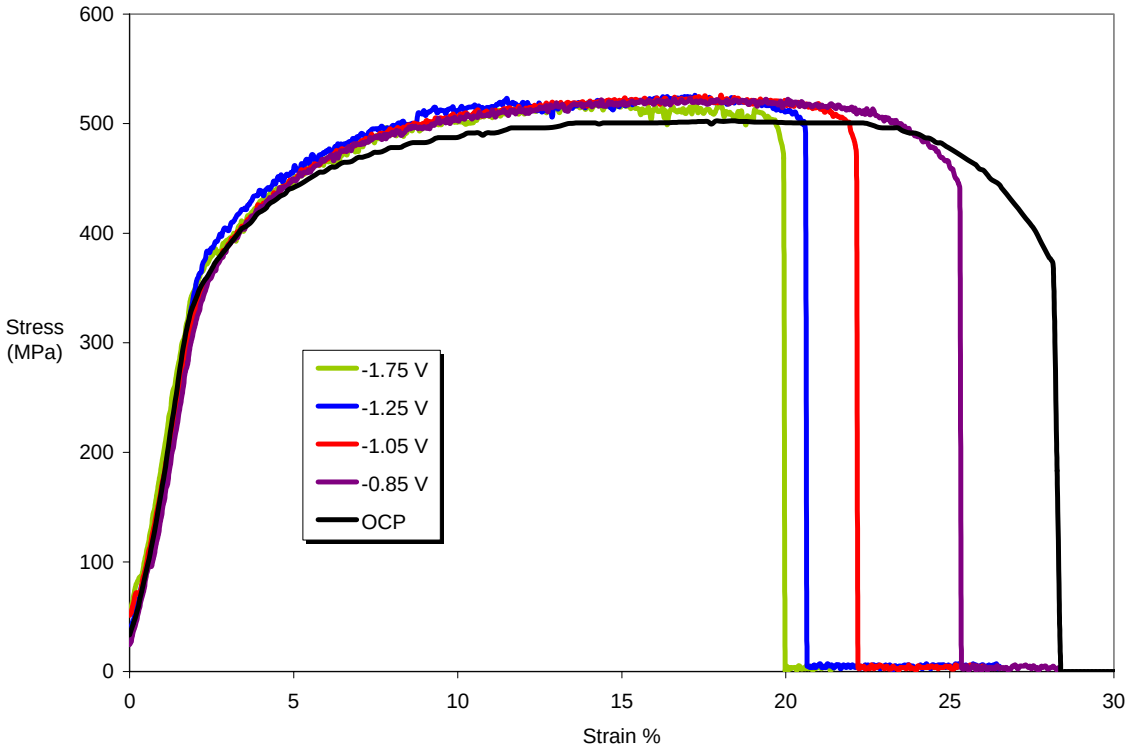

Figure 32 - Effect of Hydrogen Charging on the Mechanical Behavior of X-65 Pipeline Steel during Slow Strain Rate Testing

% elongation and % reduction in area results were recorded by measuring the test samples after each test and comparing these dimensions with the initial dimensions. These mechanical properties show a higher sensitivity to hydrogen charging than the crack velocity or crack length. Crack length measured in these tests was for the second longest crack in the polished sample. This may not indicate a true effect of crack growth rates due to possible problems in measurements. Crack density appears to be proportional

to the applied potential until it peaks at -1.25 V_{SCE}. This appears to be potential at which the sample experiences maximum hydrogen saturation and subsequently maximum crack initiation. However, the cracks that formed were short with the longest crack length being only 35 microns. The decrease in crack density at higher potentials is attributed to brittle failure occurring at one dominate crack before multiple cracks can initiation.

Table 20 - Mechanical properties of pipeline steel subjected to different applied voltages in 0.5g/L $NaHCO_3$ solution with 5% CO_2 bubbling at room temperature

Applied Voltage (V_{SCE})	% Elongation	% Reduction in Area	% Strain at Fracture	Linear Crack Length	Crack Velocity (mm/s)	Crack Density (cracks/mm)
OCP	19.5	43.9	27.8	56.7	4.99E-07	1.60
-0.85	16.3	22.4	25.4	163.4	2.35E-06	1.80
-1.05	14.7	12.4	22.2	60.88	1.02E-06	2.50
-1.25	14.8	12.1	20.6	36.29	6.50E-07	3.60
-1.75	13.8	9.2	20.0	68.01	1.26E-06	2.40

Crack morphology of these cathodically polarized samples consisted of wide cracks with little to no dissolution of the crack walls, as shown in Figures 33-36. The crack yawning is attributed to the large amount of plastic deformation that occurs towards the end of the testing process. Crack morphology generally has sharp tips but cracks often were blunted when they encountered inclusions, as shown in Figure 36 for the -1.75V sample.

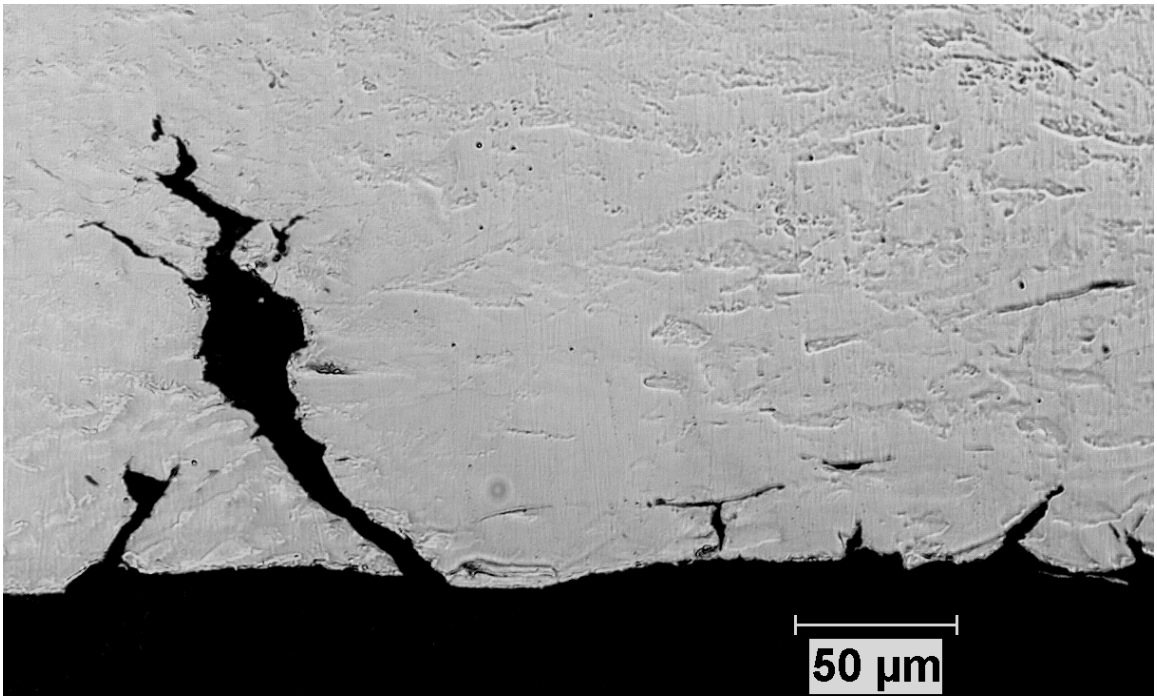

Figure 33 - Crack formed on X-65 pipeline sample exposed to 0.5 g/L $NaHCO_3$ with 5% CO_2 with -0.850V applied potential at room temperature

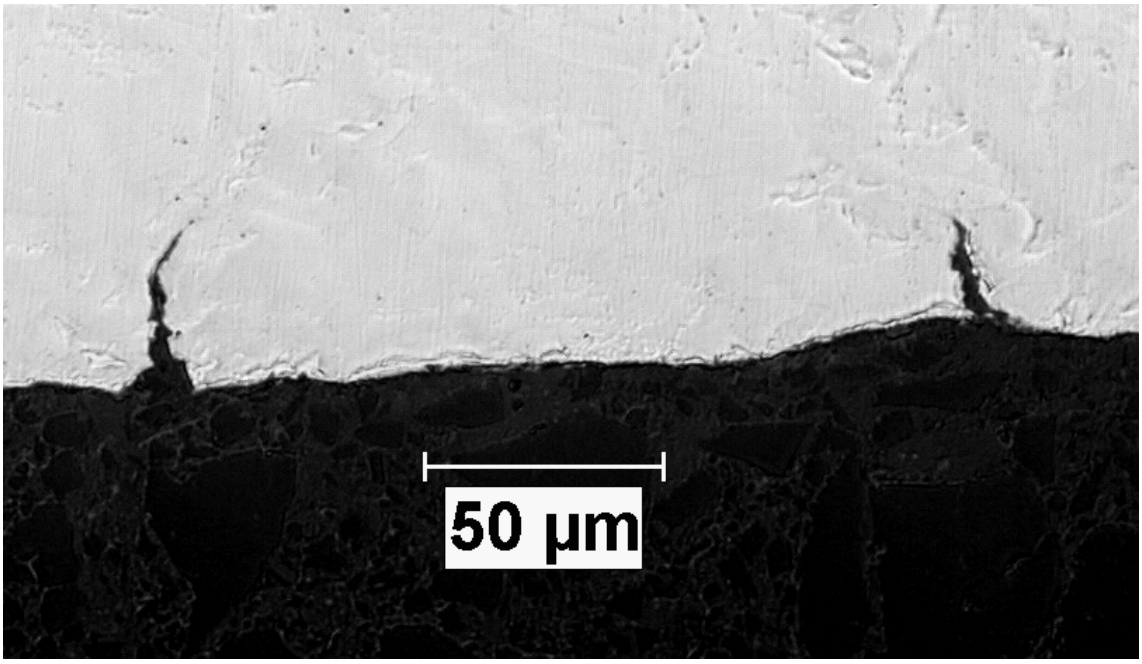

Figure 34 - Crack formed on X-65 pipeline sample exposed to 0.5 g/L $NaHCO_3$ with 5% CO_2 with -1.05V applied potential at room temperature

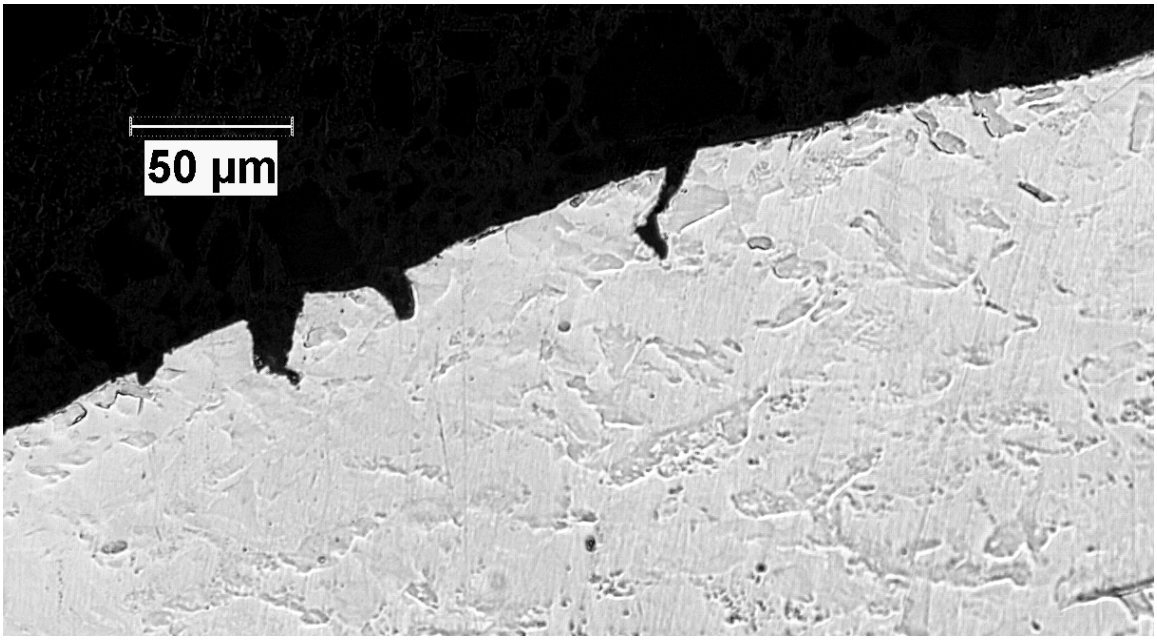

Figure 35 - Crack formed on X-65 pipeline sample exposed to 0.5 g/L $NaHCO_3$ with 5% CO_2 with -1.25V applied potential at room temperature.

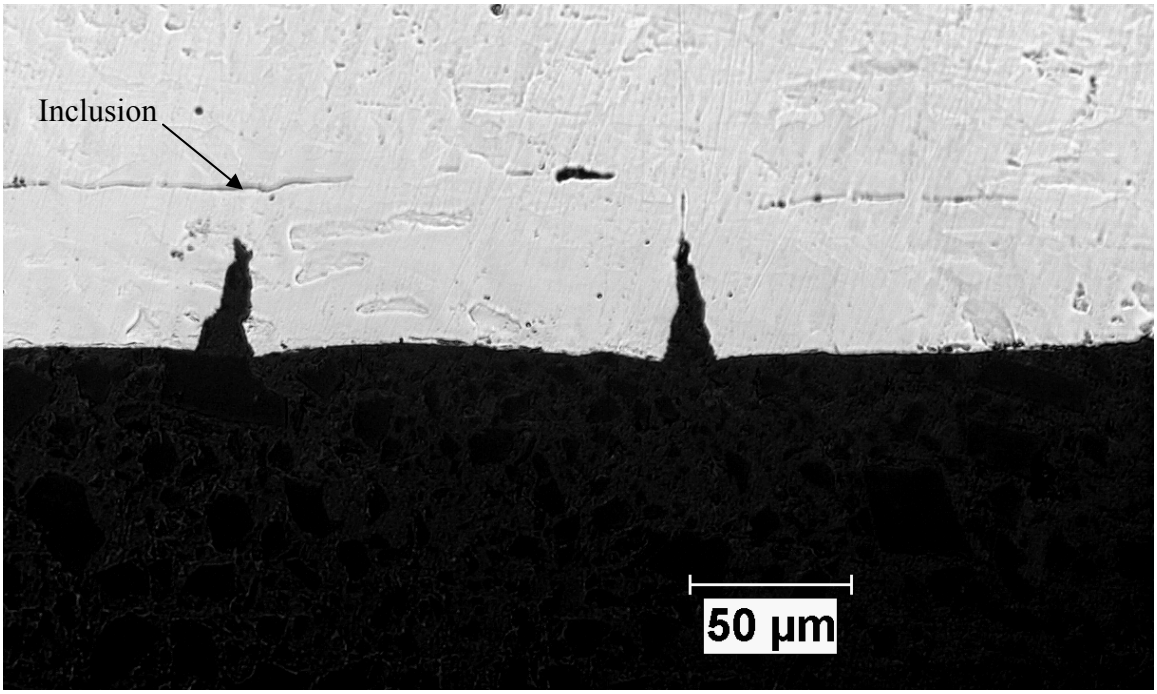

Figure 36 - Crack formed on X-65 pipeline sample exposed to 0.5 g/L $NaHCO_3$ with 5% CO_2 with -1.75 V applied potential at room temperature cathodic polarization. Note that crack walls are sharp and cracks extend linearly into the sample without significant dissolution of the crack walls.

5.3.2 - Cracking of Pipeline Steels by NNPHG Mechanism Induced Hydrogen

To observe TGSCC cracking behavior and the effect of hydrogen produced though the NNPHG mechanism reactions, smooth slow strain rate samples were exposed to various environments determined in Section 5.1 to produce TGSCC conditions. Table 21 shows that the crack velocities did not significantly differ as long as TGSCC conditions were maintained. This is consistent with the field TGSCC pipeline failures that are found in a wide range of solution concentrations and temperatures. Tests were also carried out in deionized water to see if the general corrosion in water and associated hydrogen production by possible cathodic reaction was be enough to cause cracking or induce embrittlement in slow strain rate tests. Samples tested in deionized water did not exhibit any signs of stress corrosion cracking or embrittlement.

Table 21 - Crack velocity (mm/sec.) for pipeline steel samples tested by slow strain rate tests in different bicarbonate solutions with 5% CO_2

Bicarbonate Conc. (g/L)	Linear Crack Velocity (mm/sec)			
	With 5% CO_2 + N_2			With 100% CO_2
	15 ºC	25 ºC	35 ºC	15ºC
0.1	$1.2e^{-6}$	$7.8e^{-7}$	$3.3e^{-7}$	-
0.5	$9.3e^{-7}$	$2.9e^{-7}$	$3.2e^{-7}$	-
1	$7.3e^{-7}$	$1.2e^{-6}$	$6.3e^{-7}$	-
5	$9.3e^{-7}$	-	-	$1.0e^{-6}$
10	$7.6e^{-7}$	-	-	$9.8e^{-7}$

Crack morphology of these slow strain rate samples is shown in Figures 37-39. It can be seen that the crack walls experienced significant dissolution that masked previous crack path. However, these TGSCC cracks produced sharp crack tips that are the unlike field crack morphology. This may be due to the continuous straining conditions of the

testing method that allows for continued crack growth at stresses not experienced by pipelines. However, the sharpness of the crack was restricted to the very tip of the crack, usually less than 15 microns. Crack path was torturous and did not extend linearly into the sample. This means that cracks had formed prior to the severe plastic deformation. The high levels of stress and strain applied during the testing process did not impact crack initiation and early growth. Consequently, this testing method is suitable to study the TGSCC process.

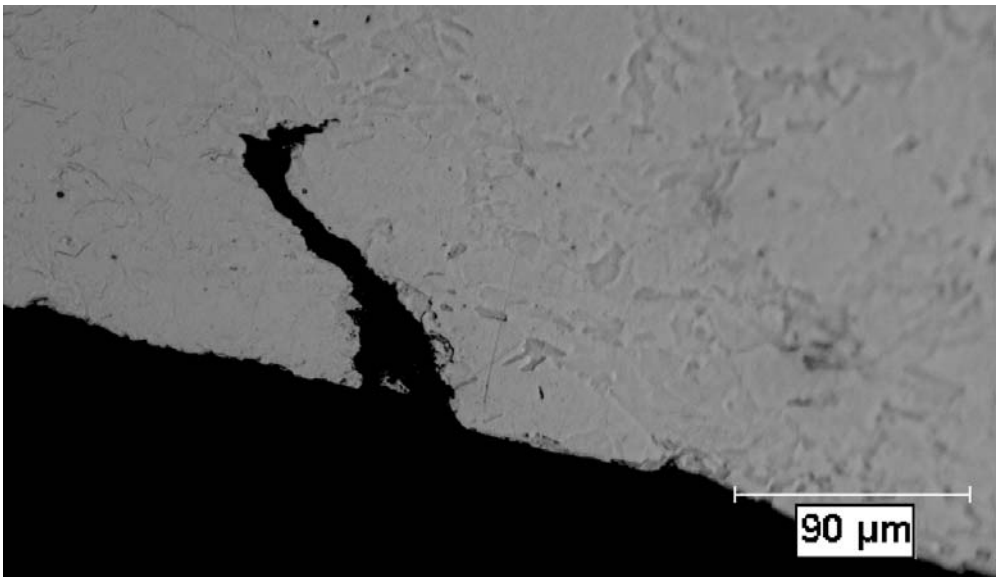

Figure 37 – TGSCC crack that occurred near the fracture surface on an X-65 pipeline sample exposed to 0.1 g/L $NaHCO_3$ solution with 5% CO_2 at room temperature and OCP

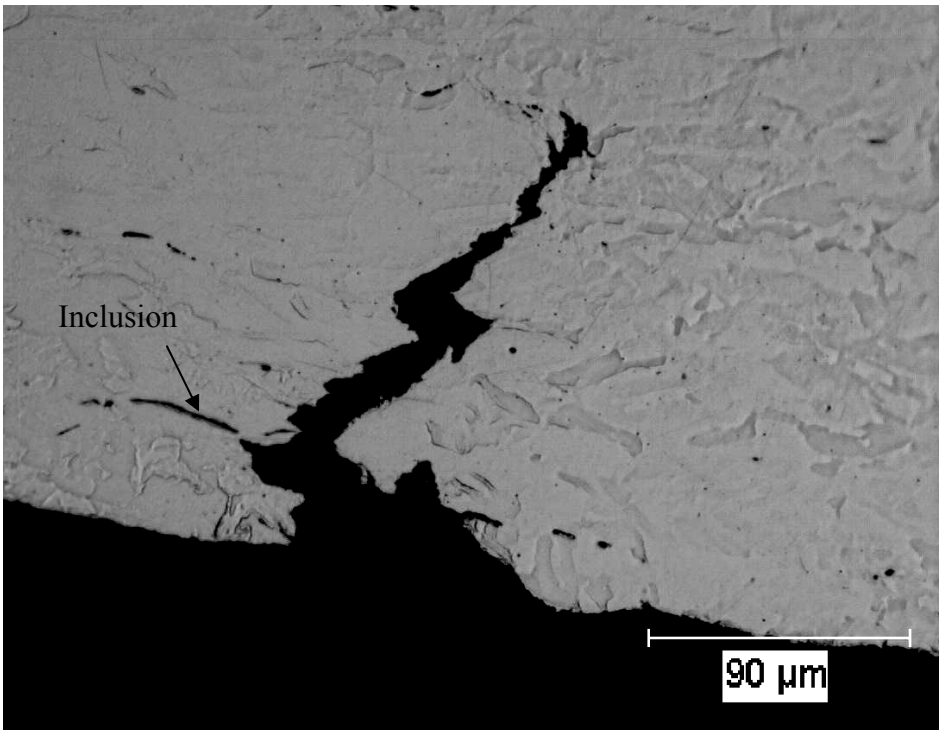

Figure 38 - TGSCC crack that occurred near the fracture surface on an X-65 pipeline sample exposed to 0.5 g/L $NaHCO_3$ solution with 5% CO_2 at room temperature and OCP

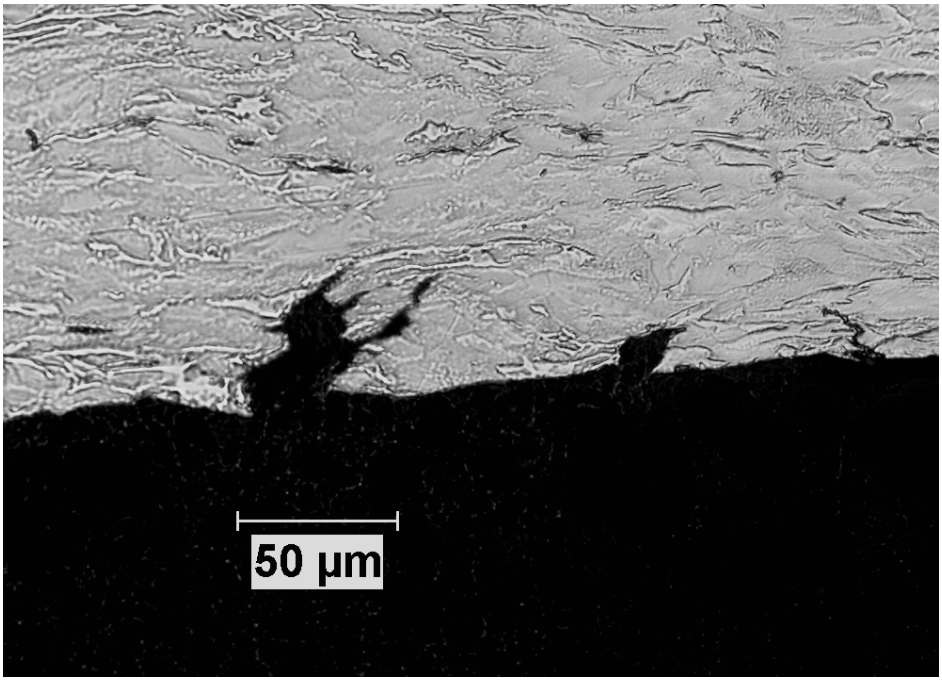

Figure 39 - TGSCC crack formed at the region of necking on an X-65 pipeline sample exposed to 1g/L $NaHCO_3$ with 5% CO_2 at room temperature and OCP

Most of stress corrosion cracks were found in two locations on tested tensile samples: at the transition point for necking or directly next to the fracture surface. This indicated that some degree of stress concentration was required to initiate TGSCC cracking in tested environments. There were also a few examples of crack tip splitting as seen in Figure 39. This generally is an indication that the crack had reached and exceeded the maximum stress intensity and had experienced unstable crack growth. Most cracks had wide mouths that indicate that the crack initiation occurred before the onset of severe plastic deformation. The isolation of cracking into only regions of high plasticity and triaxial stress indicate that the stress concentration may facilitate hydrogen diffusion and assist in the TGSCC cracking process.

To further observe the effect of hydrogen on the cracking process, evidence of hydrogen induced cracking was sought by examining the area ahead of the crack tip by SEM. Microcracking ahead of a crack tip is a characteristic of hydrogen embrittlement. The formation of these small scale cracks is generally used as an evidence for the decohesion mechanism of embrittlement. It has been well established that hydrogen will accumulate in regions with large dilatative stresses. This leads to hydrogen accumulation ahead of the crack tip and the formation of microcracks [105].

For samples exposed to simple bicarbonate environments, microcracks ahead of the crack tip were observed for almost every crack formed on slow strain rate samples. However, microcracks were also observed in samples subjected to cathodic protection, as shown in Figure 40. These microcracks formed close to the main crack tip and were generally 0.5 to 1 micron in length. This confirms the assertion that microcracks are an indication of hydrogen embrittlement.

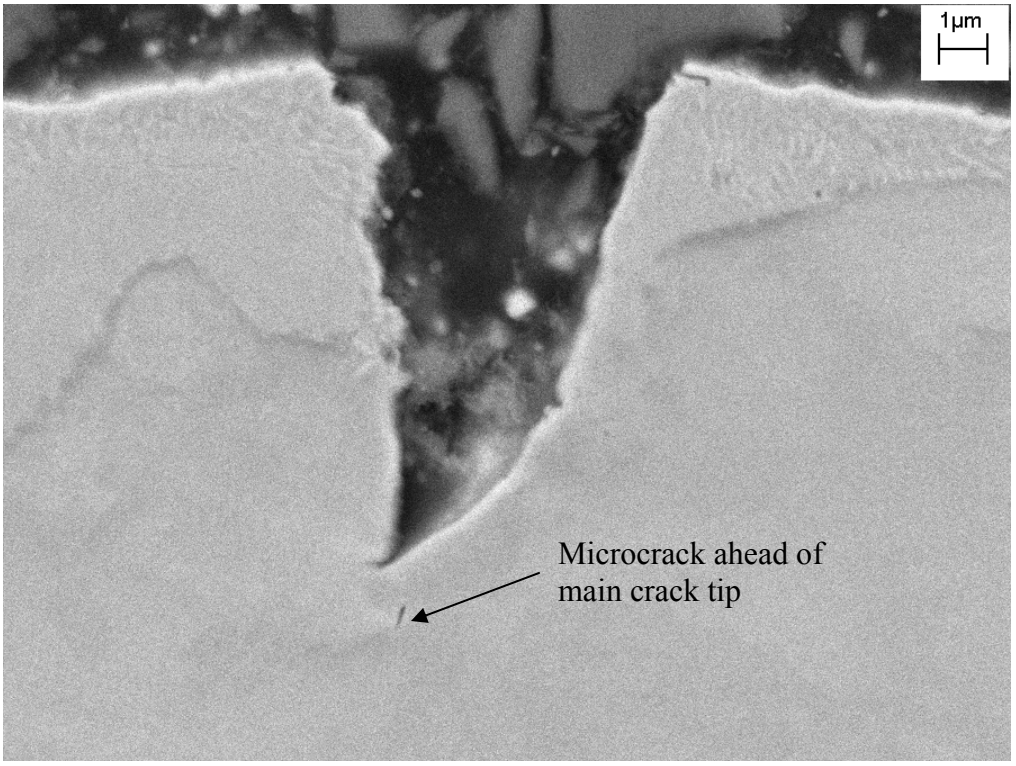

Figure 40 - Microcrack ahead of main crack tip for sample subjected to -1V cathodic potential in 0.5 g/L $NaHCO_3$ with 5%CO_2 exposure

As an example of the observed microcracking, the entire crack for a sample exposed to 0.1 g/L $NaHCO_3$ is given in Figure 37 whereas the image of microcracking is given in Figure 41. In general, microcracking occurred predominately in the ferrite grain, as seen in Figure 42. However, delaminating of pearlite as seen in Figure 43 was also observed at least in one occasion. This microcrack appeared to originate at the ferrite-pearlite grain boundary and propagate into the pearlite grain by decohesion of the pearlite lamella. Microcracks appeared to form at a distance of around 8 to 10 microns ahead of the main crack tip.

These microcracks appeared to propagate towards the main crack, providing the method of crack propagation for the main crack. This indicates that the crack propagation occurs by the formation of microcracks ahead of a stress raiser such as a pit,

scratch, or microstructural small crack. The microcracks then grow towards the main crack. When the microcrack joins with the main crack, anodic dissolution occurs on the fresh crack surface. Hydrogen produced by NNPHG and other sources would then diffuse into the steel and the process of microcrack initiation and coalescence would repeat.

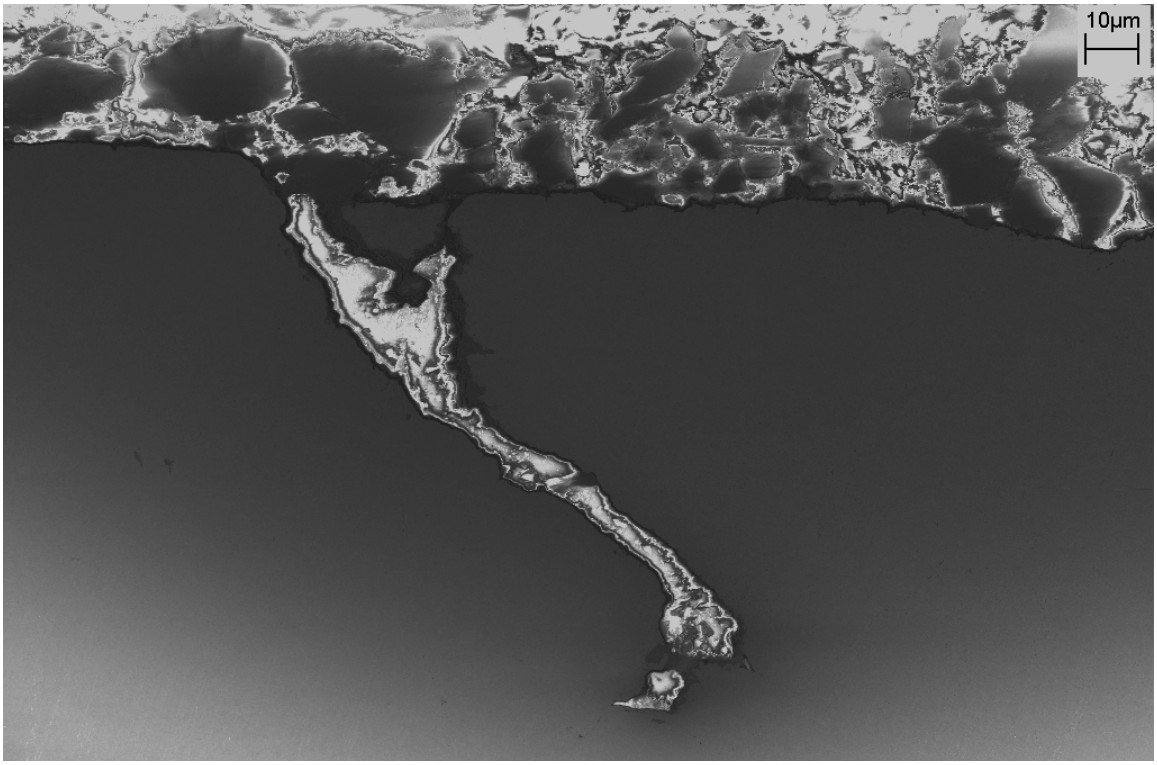

Figure 41 – SEM image of entire crack on slow strain rate sample exposed in 0.1 g/L $NaHCO_3$ with 5% CO_2 at room temperature. This is the same crack as seen in Figure 37.

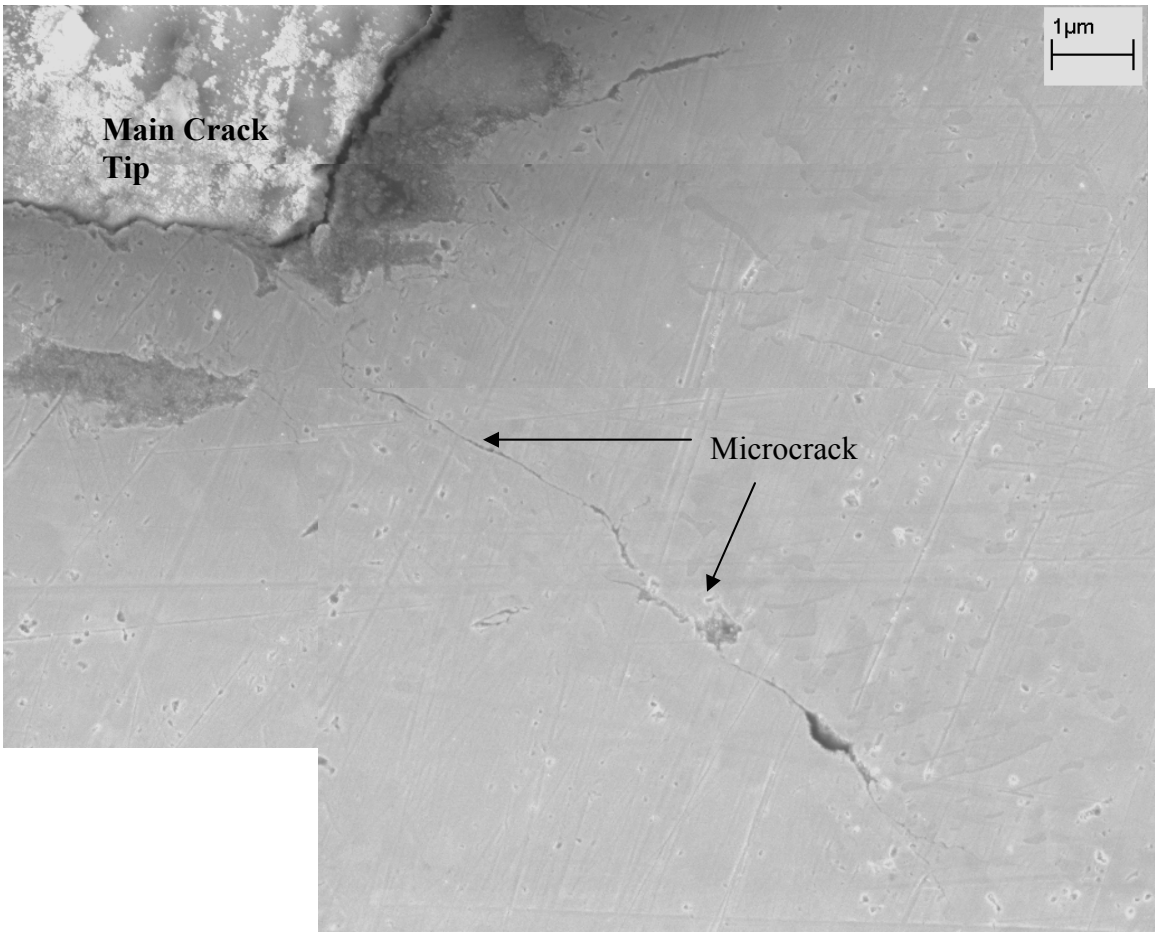

Figure 42 - Microcrack ahead of main crack tip formed on sample exposed to 0.1 g/L $NaHCO_3$ with 5%CO_2 at room temperature. The microcrack has formed ~10 microns ahead of the main crack tip.

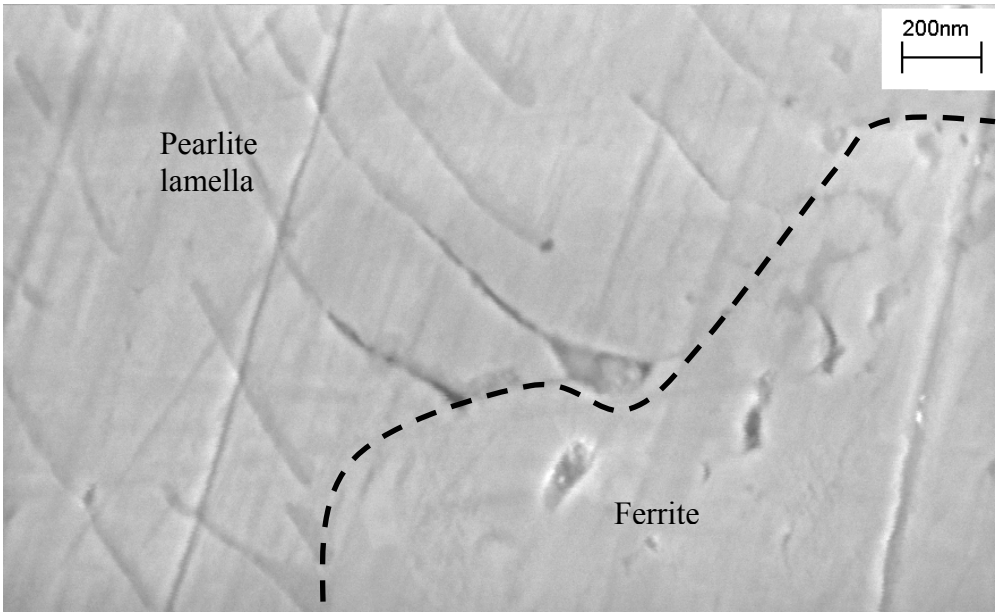

Figure 43 - Microcracking at the lamella of pearlite phase on sample strained in 0.1 g/L $NaHCO_3$ with 5% CO_2 at room temperature. This microcracking occurred approximately 13 microns from the main crack tip.

5.3.4 - Microstructural Effect on TGSCC Susceptibility

To determine the effect of microstructure on the susceptibility of TGSCC, a finite number of samples were heat treated to produce a normalized microstructure in the same manner as for the permeation samples. Out of the four normalized pipeline steel tensile samples tested by SSRT, only one produced stress corrosion cracks. The crack was located near to the main fracture surface and it could not be confirmed if the crack was a separate TGSCC crack or a remnant of final fracture. The normalized pipeline steel sample had typical stretched surface appearance of a ductile steel failure as seen in Figure 44. The as-received sample exposed in the same environment, shown in Figure 45, showed clear signs of stress corrosion cracks on the gauge surface and some areas with brittle mode of cracking on the fracture surface. Clearly this indicates that the

normalized, is less susceptible to TGSCC in bicarbonate solution with carbon dioxide bubbled through it.

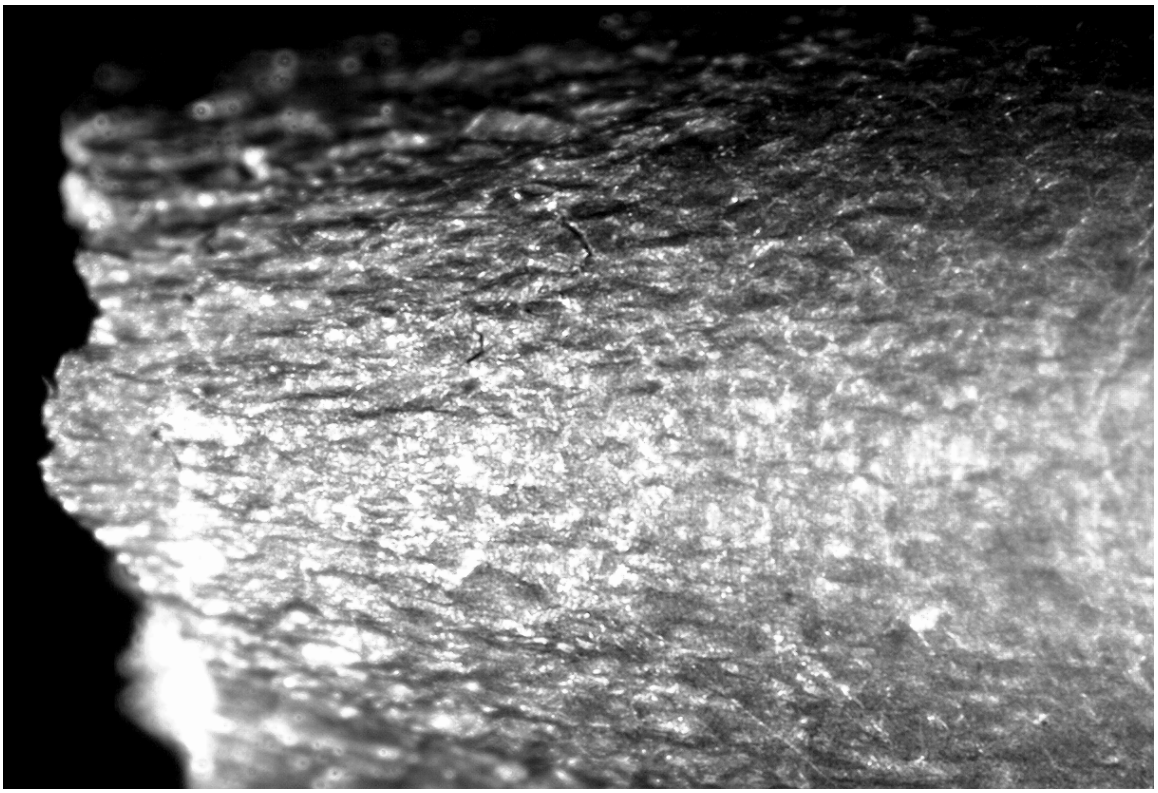

Figure 44 - Gauge surface of normalized sample after failure when exposed to 0.5 g/L $NaHCO_3$ with 5% CO_2 at room temperature and OCP

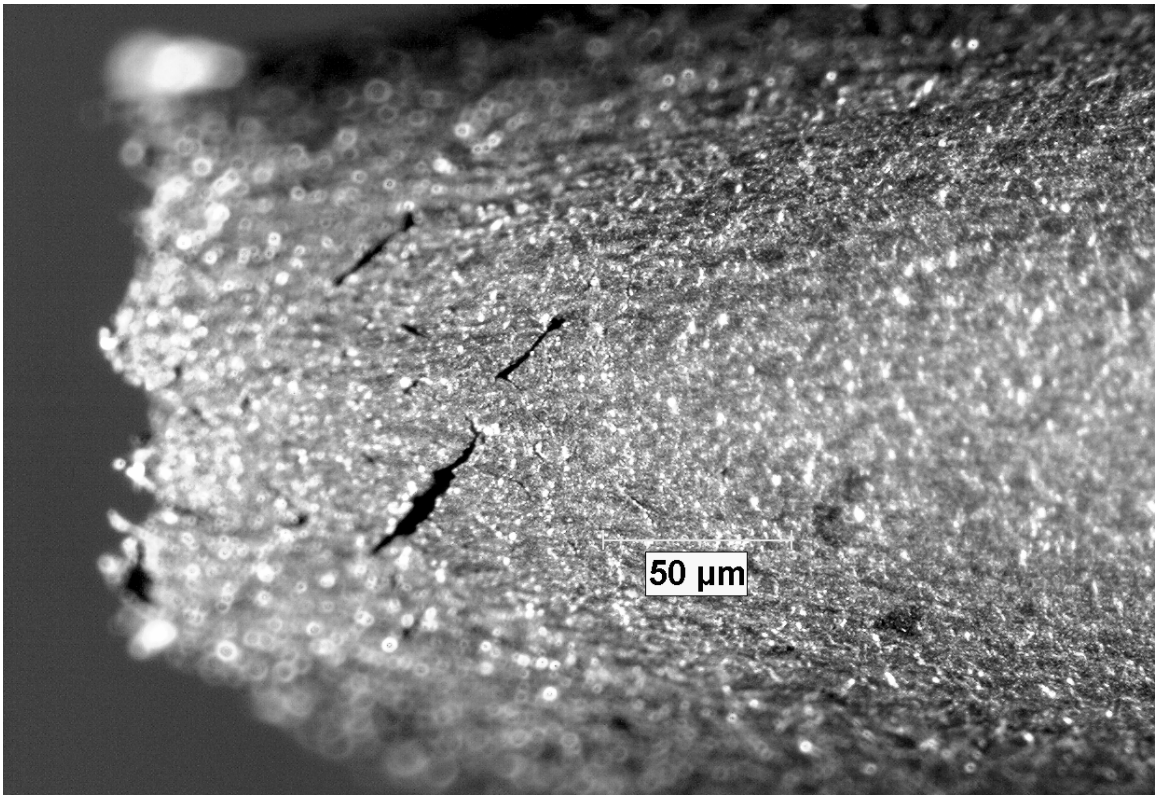

Figure 45 - Gauge surface of as-received sample after failure when exposed to 0.5 g/L $NaHCO_3$ with 5% CO_2 at room temperature and OCP

5.3.5 – Effect of Applied Anodic Potential on Cracking Behavior

Results from this study have shown that hydrogen can be produced at open circuit potentials to create TGSCC cracking through the NNPHG mechanism. To further study the role of hydrogen in the cracking process, a finite number of samples were tested under different applied anodic potentials by slow strain rate testing to observe the method of cracking.

To determine the potential range in which NNPHG mechanism may be possible, Pourbaix diagrams were generated for the carbon dioxide-iron system at 25°C. These diagrams, shown in Figure 46, indicate that for the pH of interest (6.0-7.5) there is a very small potential range where $FeCO_3$ is the stable corrosion product. The region of near-

neutral condition was specifically examined and is shown in Figure 47. The blue lines in these figures indicate the water stability regime. Two regions are possible for the NNPHG. Below the lower blue line cathodic hydrogen is evolved. This contributes an additional source of possible hydrogen, and is designated by the red region in Figure 47. This blue water stability line is governed by the equation:

$$E_H = -0.059\,pH \quad \textbf{(44)}$$

and the lower $FeCO_3$ line is modeled as:

$$E_H = -0.0436\,pH - 0.2043 \quad \textbf{(45)}$$

At a pH of 7, there is a potential regime of 96 mV in which the both the NNPHG mechanism and cathodic hydrogen is viable.

At higher anodic potentials above the water stability line, cathodic hydrogen will not be feasible, reducing the amount of possible generated hydrogen. However, anodic dissolution at these potentials may facilitate the production of Fe^{+2} ions for NNPHG mechanism to operate and therefore produce hydrogen and $FeCO_3$. This range of potentials is designated by the pink region in Figure 47.

At higher anodic potentials, $FeCO_3$ will not be thermodynamically stable and the favored corrosion product will be Fe_3O_4. This will eliminate the possibility of NNPHG induced TGSCC.

Open circuit potential for the X-65 pipeline steels in simple bicarbonate solutions with 5% CO_2 was measured to be -760 mV vs. SCE which is -519 mV vs. SHE. This potential falls within the region highlighted in red. In the near-neutral pH region, cathodic hydrogen can be generated at potentials below the hydrogen stability line. Subsequently, it was expected that the NNPHG mechanism will be still be active at

slightly anodic potentials within the region where hydrogen can be cathodically generated and $FeCO_3$ produced (within 50 mV from OCP at any given near-neutral pH).

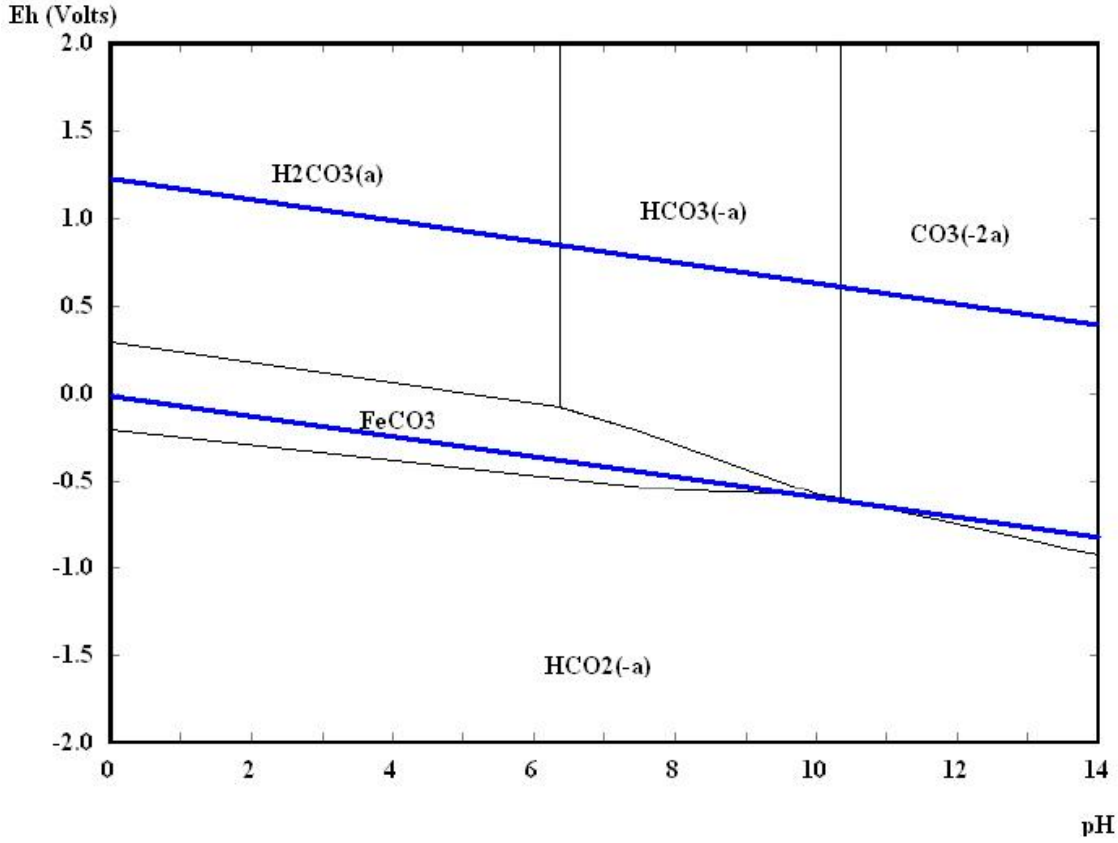

Figure 46 - Pourbaix diagram of Fe-C- H_2O showing the bicarbonate environment at pipeline steel at 25°C.

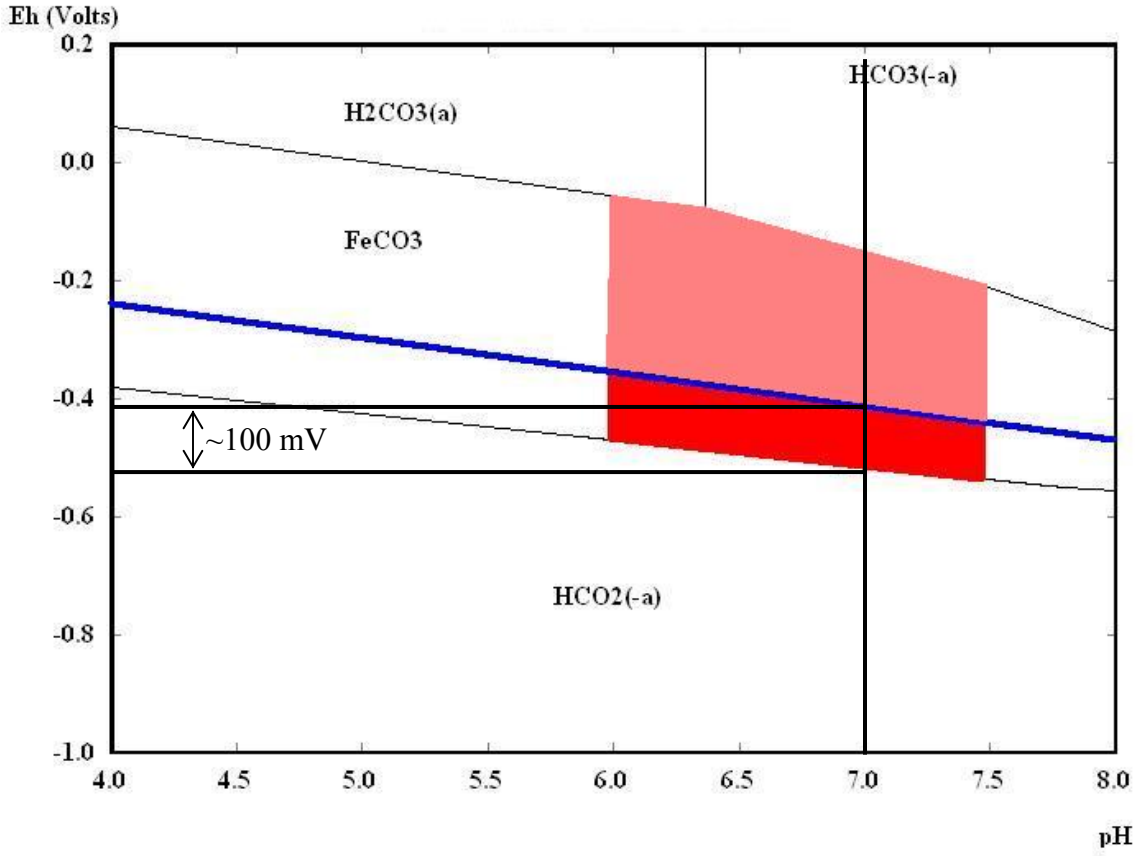

Figure 47 -Pourbaix diagram of Fe-C- H_2O showing the region of NNPHG feasibility for pipeline steel at 25°C. The red area is where both NNPHG hydrogen and cathodic hydrogen can be feasible. The pink region is where only NNPHG hydrogen is possible.

Results from these tests are given Table 22, and the stress-strain diagrams from these tests are shown in Figure 48. Open circuit potential for pipeline steel, X-65, in these test environments varied from -729 mV to -770 mV depending on how long the sample was allowed to equilibrate. It was determined that one hour was sufficient to record a stable OCP value. However, regardless of the initial OCP, the behavior of the material was consistent with applied potential. Samples held at -693 mV, -700 mV, and -709 mV exhibited similar reduction in area and strain at fracture.

The sample subjected to -650 mV_{SCE} was at a potential slightly above the water stability potential but within the potential range where $FeCO_3$ is the dominate corrosion product. Therefore, the NNPHG mechanism was still considered to be valid. The slow strain rate behavior did exhibit more embrittlement compared to samples strained at OCP, as seen in Figure 48. On this sample, the entire length of the gauge experienced general dissolution. Further, sample surface had irregularities and was extremely rough due to general corrosion.

Table 22 - Mechanical properties and cracking data of X-65 pipeline samples subjected to slow strain rate tests in 0.5 g/L $NaHCO_3$ with 5% CO_2 at room temperature and given anodic potentials

Applied Voltage (mV)	% RA	Strain at Fracture	Linear Crack Length (microns)	Crack Profile Length (micron)	Linear Crack Velocity (mm/s)	Profile Crack Velocity (mm/s)	Crack Density (mm^{-1})
-650	35.38	16.99	45.16	65.74	$3.21\ e^{-7}$	$4.67\ e^{-7}$	0.6
-693	34.35	13.50	96.41	135.9	$8.60e^{-7}$	$1.21e^{-6}$	3.5
-700	34.61	14.37	62.33	82.18	$5.23e^{-7}$	$6.90e^{-7}$	3.6
-709	25.23	14.00	212.4	276	$1.84e^{-6}$	$2.39e^{-6}$	1.0
-751	20.63	10.74	118.4	128.9	$1.34e^{-6}$	$1.46e^{-6}$	2.0

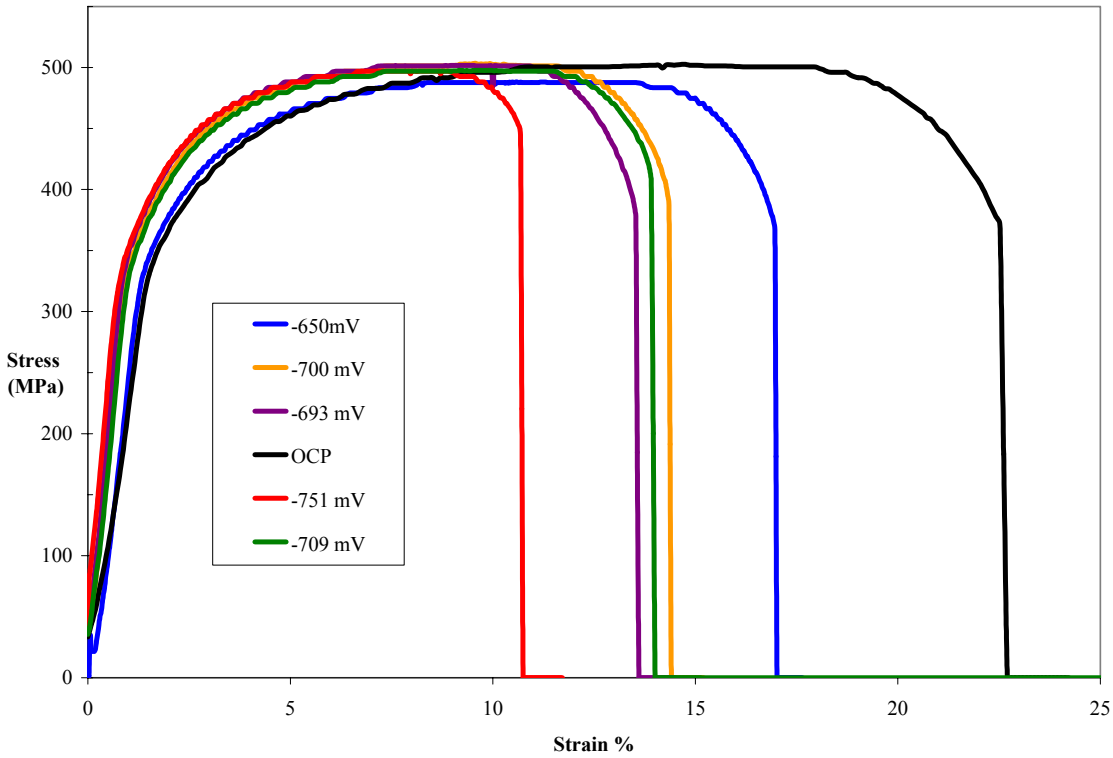

Figure 48 - Stress-Strain behavior of pipeline steel samples subjected to slow strain rate testing in 0.5 g/L $NaHCO_3$ with 5% CO_2 at room temperature and given applied anodic potentials. Note drastic decrease in mechanical properties with a small anodic potential

It was observed that samples held at slightly anodic potentials, i.e. 20 mV from OCP, produced TGSCC cracking that was similar to field morphology, as seen in Figure 49. However, these anodic samples had higher crack velocity and higher crack density. This is attributed to the increased production of hydrogen by NNPHG mechanism near OCP. In fact, the crack velocities and crack lengths of anodic samples are consistent with samples tested in cathodic environments that produced additional hydrogen. However, as the applied anodic potential was increased, % reduction in area and % strain to failure increased indicating less effect of hydrogen and more general corrosion on the surface leading to other corrosion reactions.

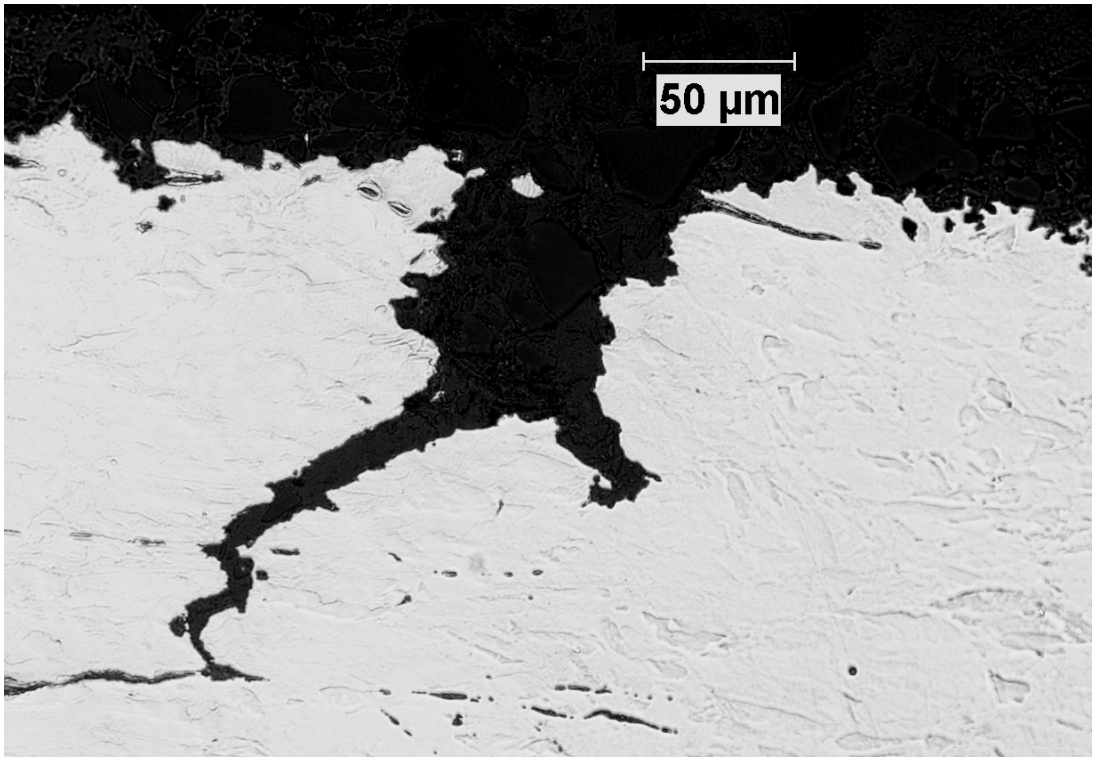

Figure 49 - TGSCC crack formed on smooth slow strain rate sample exposed to 0.5 g/L $NaHCO_3$ with 5% CO_2 at room temperature and 20mV anodic potential from OCP

To further validate the applicability of the NNPHG mechanism at slightly anodic potentials, surface pH measurements were made on a pipeline sample subjected to 20 mV anodic from OCP. As shown in Figure 50, near-neutral pH was maintained at the surface of the sample as well as the bulk of the sample. This means that the rate of hydroxide production by cathodic reactions and iron ions is not sufficient to alter the NNPHG mechanism reactions under these applied anodic potentials.

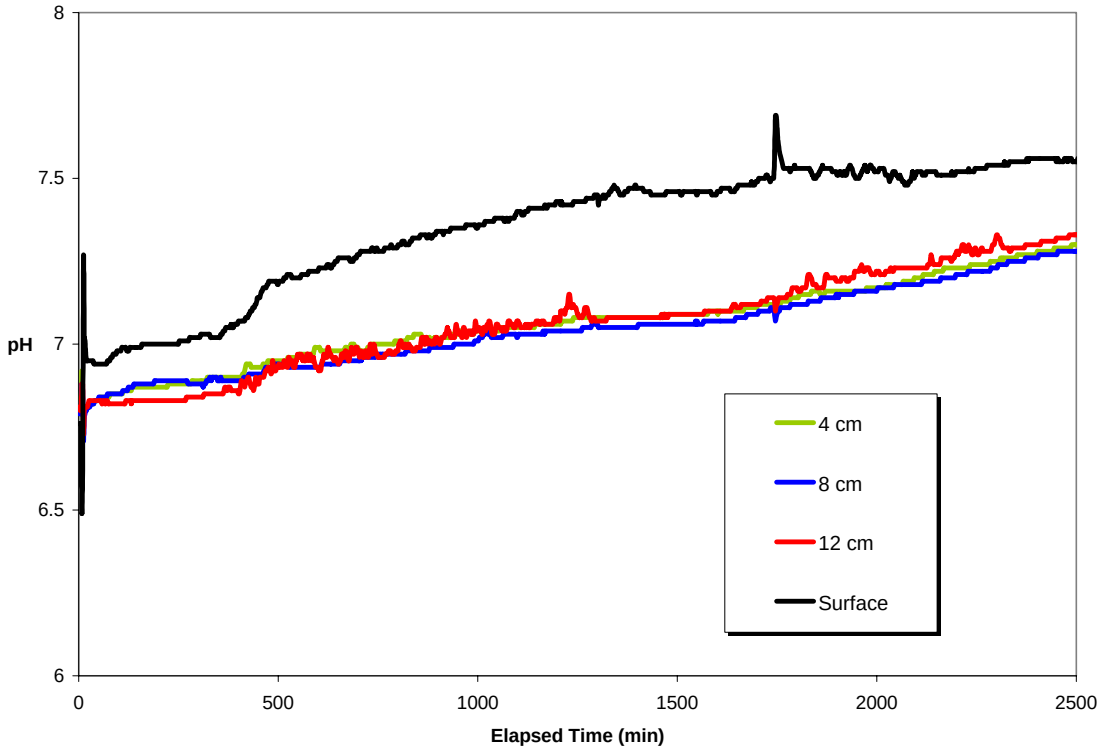

Figure 50 - pH vs. Time profile for 0.5 g/L $NaHCO_3$ solution saturated with CO_2 at -750mV. Note that surface pH is greater than the bulk solution. However, the surface pH does maintain near-neutral conditions for the majority of the test, especially during the initial time when CO_2 is most available.

5.3.6 – Summary

Samples subjected to cathodic charging demonstrate the embrittlement effect of hydrogen on the mechanical properties of pipeline steel. Samples subjected to near-neutral pH environments produced cracks that were similar in morphology to the cracks found on failed fuel transmission pipelines. TGSCC occurred in a wide range of compositions and temperatures as long as near-neutral conditions were maintained at the pipeline surface. TGSCC cracks were found primarily at sites of stress concentration either at transition of necking or near the fracture surface. Evidence of hydrogen in these cracking processes was confirmed by the presence of microcracks ahead of the main

crack tip. Normalized samples proved to be less susceptible to TGSCC. This is attributed to the lower amount of hydrogen trap sites and less hydrogen accumulation in the relaxed steel structure. It was also determined that TGSCC could occur at slightly anodic potentials from OCP. These potentials allow for the production of metal ions that can contribute to the NNPHG mechanism.

5.4 - Effect of Stress Concentration on Hydrogen Induced TGSCC

5.4.1 - Smooth Samples under NNPHG Conditions

Results from slow strain rate tests on pipeline steel samples in bicarbonate solutions have shown transgranular stress corrosion cracking near the necked region and areas of stress concentration. Further work was carried out to determine how stress concentrations affected hydrogen ingress and crack propagation.

To further study the interaction of hydrogen with pipeline steel, slow strain rate tests were performed by soaking the smooth samples in 1 g/L $NaHCO_3$ with 5% CO_2 for 16 days with no applied stress. This time was used to allow the hydrogen produced at the steel surface by the NNPHG mechanism to ingress into the steel and affect its mechanical properties. Results from these tests are given in Table 23. No cracking was found in any tested steel sample after simple soaking and the reduction of area and percent elongation did not drastically differ from the samples strained in dry air. This indicates that hydrogen did not diffuse into the sample. This behavior has been observed by Parkins et al. and Fang et al. who determined that the presence of environment during straining was critical in observing the hydrogen effect on TGSCC [56, 82].

Table 23 - Slow Strain Rate Results for Pre-Soaked Samples

Test #	% Reduction of Area	% Elongation
1	44.98	17.63
2	44.57	18.23
3	41.28	17.32
In Air	43.18	19.03

It is known that the hydrogen may diffuse and accumulate in the steel at sites of high stress concentration and or produce a significant loss of ductility or embrittlement [55]. However, previous research on TGSCC has produced cracks similar to field failures by using SSRT testing in TGSCC environments [19]. This means that the environment must be present at the time of straining in order for the cracking process.

To examine this relationship between straining and hydrogen absorption, smooth slow strain rate samples were held at 85% yield strength for 2 days and 15 days to observe the effect of hydrogen on mechanical behavior and cracking. After this hold period, sample was strained under normal SSRT condition to failure. It was expected that the samples subjected to longer exposure times, under strain, would have a more brittle fracture and have a higher crack density. Contrary to what was expected, samples held for longer times did not experience any difference from the samples continuously strained, as shown by results in Table 24. Rather, samples held at yield strength had fewer tendencies to crack. This is attributed to the larger amount of general dissolution rather than localized dissolution. This indicates that a stress concentration is required in order for the hydrogen to accumulate in the material and create cracking.

Table 24 - Mechanical response to smooth slow strain rate sample subjected to holding time at yield strength

Load Hold Time	% Elongation	% Reduction of Area	Strain at Fracture
2 days	16.24	33.23	24.45
15 days	19.67	31.87	28.28
None	19.54	43.89	27.8

5.4.2 - Effect of Stress Concentration on Hydrogen Intake

To determine the role of stress concentration on the cracking process a number of smooth samples were notched and tested with varying hold times as outlined in the Section 4.1. The stress concentration of these notched samples was determined using Roark's equation for a u-notch in a circular shaft in axial tension under elastic stress [113]. It was determined that the stress concentration for these samples was determined to be approximately 2.5.

Mechanical behaviors of these tested samples are summarized in Table 25. After the sample had failed, one half of the sample was mounted and the profile roughness parameter was calculated to determine fracture profile to quantify the degree of ductility. Fracture roughness parameter indicates the ratio of real fracture area with apparent area for a given fracture surface. Fracture surface with profile roughness parameter value of 1.0 will be for a perfectly brittle fracture. Samples with low profile roughness parameter values would be more brittle as their fracture surfaces would be smoother.

SEM observation, shown in Figure 51, indicated that the sample tested in air produced a ductile fracture surface with microvoid coalescence shown by dimpled fracture surface. Sample fracture surface was uniform regardless of distance from the notch edge. Larger voids on the surface, as seen in Figure 51, are due to inclusions. This sample also had the highest profile roughness parameter of 2.35.

Table 25 - Slow Strain Rate Data for Notched Samples

Test Condition	% Elongation	% Reduction in Area	% Strain at Fracture	Profile Roughness Parameter
In Air	9.55	14.31	12.98	2.35
Continuous	8.76	10.35	10.90	2.02
15 day hold	8.02	6.14	10.20	1.92
30 day hold	7.26	6.88	11.45	1.74
With -1.0 V_{SCE} during test	1.81	3.95	6.74	2.35
With -1.0 V_{SCE} pre-charged and tested without applied potential	7.03	10.18	9.89	1.88

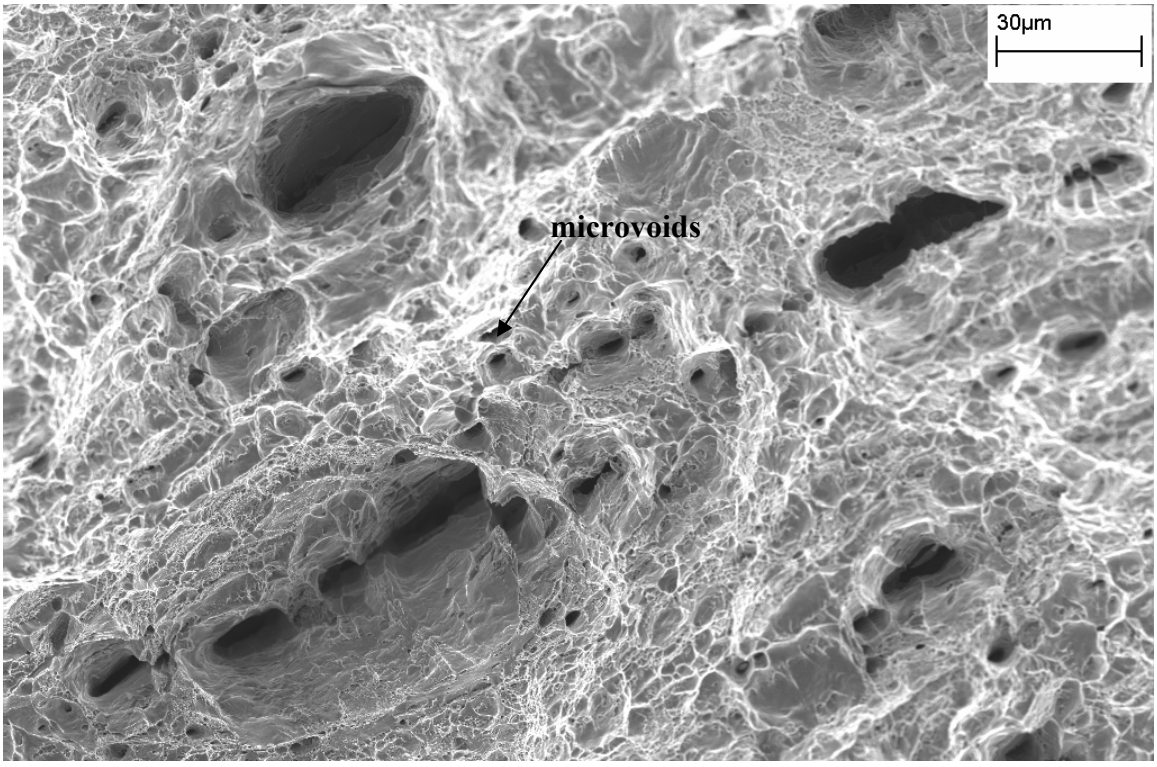

Figure 51 - Fracture surfaces of notched slow strain rate samples imaged at 500X for notched sample strained in air. Note the dimpled surface and formation of microvoids.

Exposure of notched tensile sample of pipeline steels to the bicarbonate solutions, with carbon dioxide bubbling through it, degraded the mechanical properties of the steel as indicated in Table 25. However, continuous elongation without any hold time also produced a ductile fracture surface, as seen in Figure 52. The ductile nature of the fracture is also reflected in the profile roughness parameter which was measured to be 2.02. Fracture surface profile was again rough, dimpled and had uniform topography regardless of distance from notch edge. However the roughness for this notched tensile sample was lower than the similar sample tested in air, indicating the effect of environment.

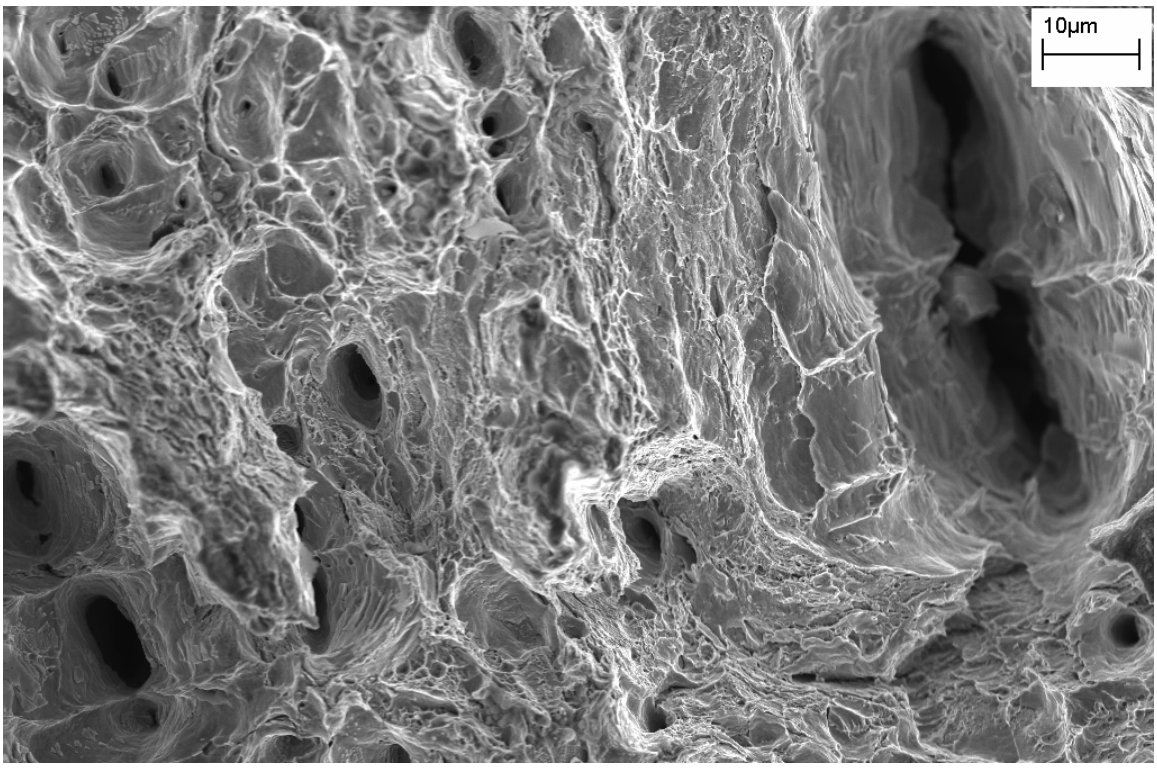

Figure 52 - SEM image of fracture surface of notched sample continuously strained in 0.5g/L $NaHCO_3$ with 5%CO_2 at room temperature and at OCP. Sample exhibits the same dimpled surface as the sample exposed to air.

However, the notched tensile sample that was held in bicarbonate solution, with 5% CO_2 bubbling through it, below its yield strength for a period of 15 days exhibited a quasicleavage fracture surface under open circuit conditions, as shown in Figure 53. Holding the material in solution where hydrogen could be produced by NNPHG mechanism allowed for the hydrogen accumulation and embrittlement at microstructural defects ahead of the notch. Cleavage occurred primarily near the notch edge and extended approximately 500 microns into the fracture surface. The reduction in area for the 15 day hold sample was 40.67 percent less than that for the sample tested continuous SSRT conditions. Fracture roughness parameter for the sample held for 15 days was 1.92 compared to 2.02 for the SSRT sample without prior exposure. This means that more hydrogen accumulation is required in order to observe hydrogen effects on steel properties.

Subsequently, a 30 day loading test was performed to understand the time effects of this problem. Fracture surface of this sample is shown in Figure 54. This fracture surface was also quasicleavage with areas of smooth brittle fracture and ductile dimpling. The cleavage area of fracture was also predominating at the notch edge and it extended approximately 1000 microns into the sample. This is twice the cleavage area that was experienced by the 15 day hold sample. Fracture roughness parameter after 30 day hold was 1.74 compared to 1.92 after 15 day hold, indicating a more brittle nature of fracture. This indicates that even under notched conditions, where hydrogen intake is favored ahead of the crack tip in a region of stress concentration and triaxial stresses, an extended

period of time is required for hydrogen diffusion into the steel. Increase in stress may increase hydrogen intake further.

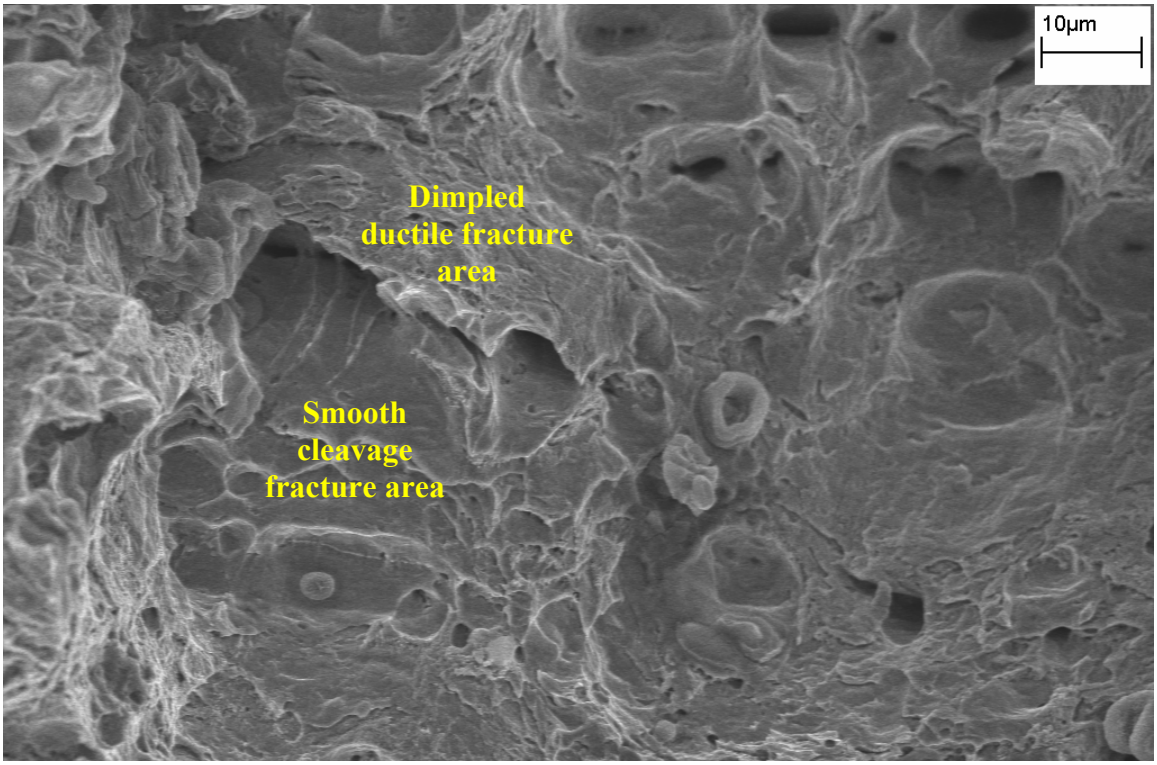

Figure 53 - SEM image of fracture surface of notched sample exposed to 0.5g/L NaHCO3 with 5% CO_2 at room temperature and OCP and held at 85% yield strength for 15 days. This surface has a large area of smooth cleavage surfaces along with areas of dimpling.

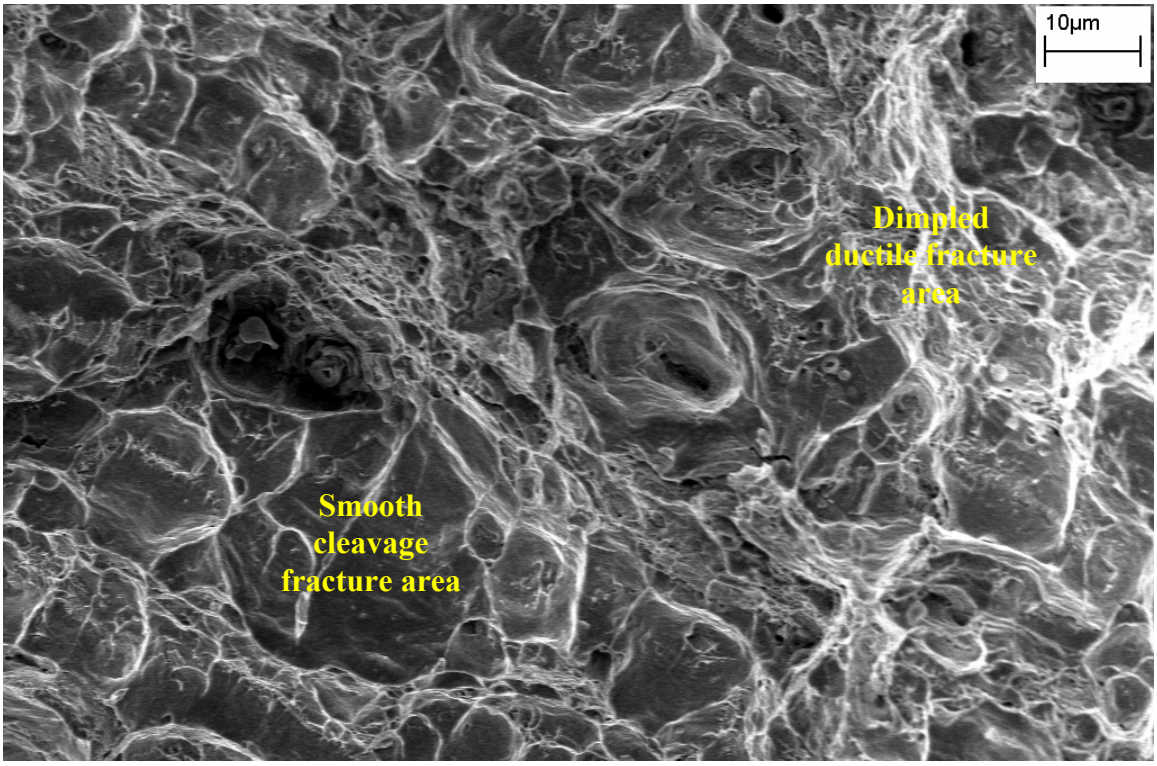

Figure 54 - SEM image of fracture surface of notched sample exposed to 0.5g/L $NaHCO_3$ with 5% CO_2 at room temperature and OCP and held at 85% yield strength for 30 days. Sample surface is primarily smooth indicating a cleavage fracture, with small areas of dimpling indicating ductile tearing between brittle regions.

Hydrogen ingress under open circuit conditions did not reach saturation in the TGSCC environments where the NNPHG mechanism could operate, as the cathodically polarized sample showed significantly more loss in ductility with predominately a brittle fracture surface as shown in Figure 55. The profile roughness parameter for this sample is deceiving as more a ductile value. This was due to a high degree of internal cracking that increased the surface area of fracture.

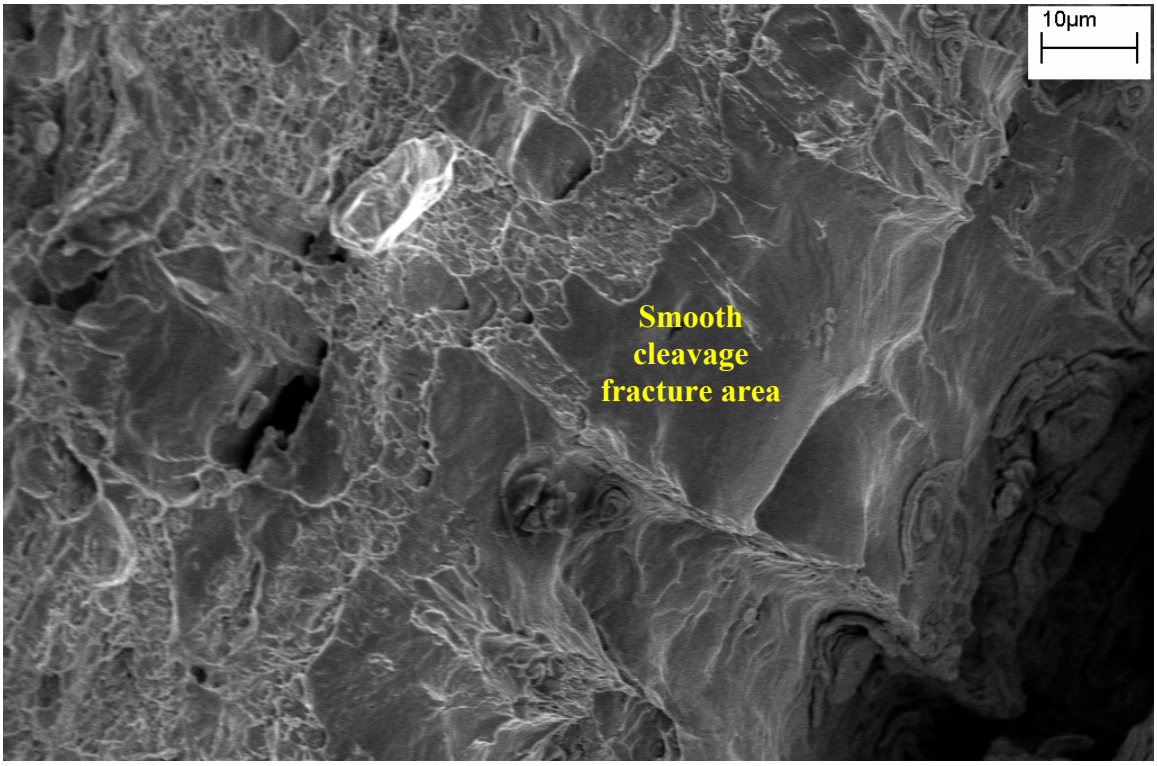

Figure 55 - Fracture surface of notched sample exposed to 0.5g/L $NaHCO_3$ with 5% CO_2 at room temperature and -1V_{SCE} during continuous straining. Note the large areas of cleavage that is similar to 30 day load hold sample.

Pre-charging also produced a small amount of quasicleavage fracture surface toward the notched surface, but there was no significant loss in ductility as seen in Figure 56. These results indicate that the pipeline steel needs to be under plastic strain in order for the hydrogen generated under OCP to accumulate in the metal matrix and have an effect on the mechanical properties.

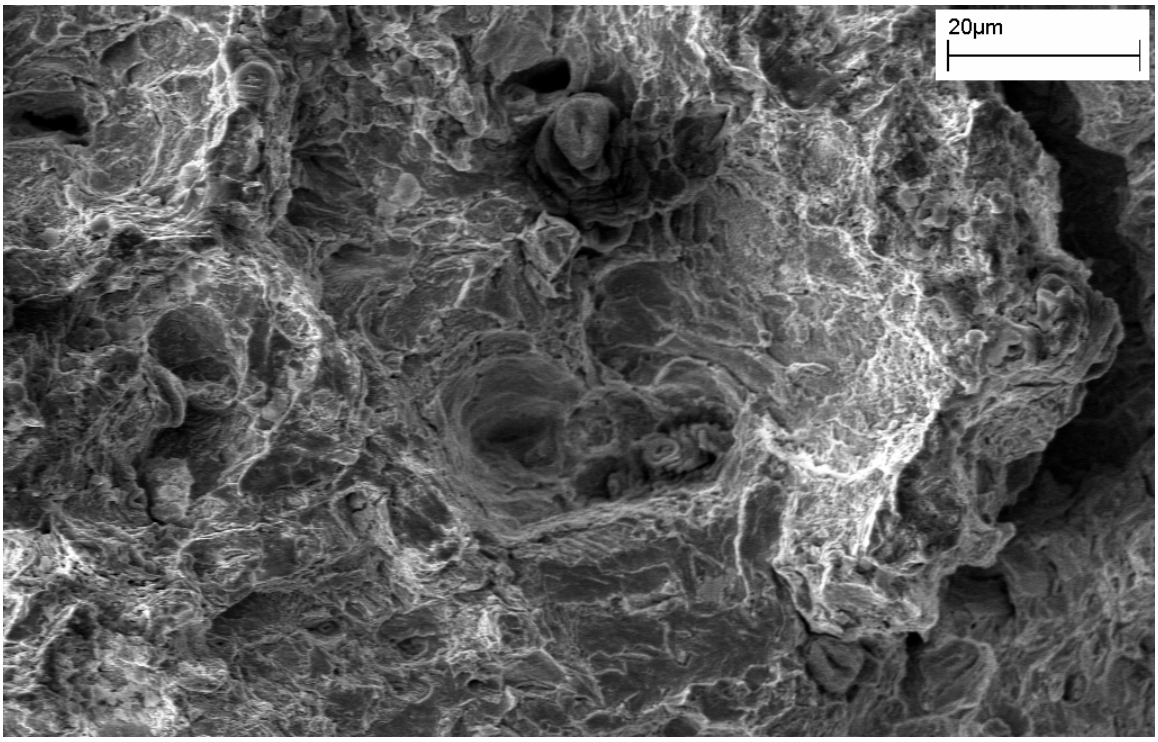

Figure 56 - SEM image of fracture surface of -1V_{SCE} pre-charged notched sample. This image is taken near the notch edge. The fracture surface has significant dimpling and very little cleavage area, indicating a ductile fracture.

Dislocations have been shown to act as hydrogen traps to embrittle the pipeline steel [69]. In stress free conditions, hydrogen will not accumulate in the material in quantities large enough to cause a loss in the mechanical behavior. To examine this effect of plastic deformation and resulting dislocations in the steel on hydrogen embrittlement in the TGSCC environment, samples were pre-strained to five percent strain in dry air. Samples were then unloaded and tested under SSRT conditions in the test environment. Samples were either exposed to 0.5 g/L $NaHCO_3$ with 5% CO_2 at room temperature and OCP or dry air. Results are given in Table 26. The sample tested in air produced no cracks and had a ductile fracture surface as shown in Figure 57. There was not a significant difference in the mechanical response of the two pre-strained samples. Strain at fracture and reductions of area were very similar. Further, the samples

exposed to the environment but not pre-strained produce similar results to the samples which were pre-strained. Crack length and crack velocity was similar for these samples. However, pre-strained samples had a more brittle fracture, as shown in Figure 58. Cracks also formed uniformly around the sample rather than in a patch on one side of the sample as with continuously strained samples. It can be concluded that hydrogen did cause embrittlement of the material since TGSCC cracks did form and the sample did fail with a brittle nature. However, the impact of global deformation of the pipeline steel does not appear as important as localized stress concentration that may occur at the site of a pit or scratch.

Table 26 - Mechanical properties of samples subjected to 5% pre-straining and then strained to failure.

Test Condition	% RA	Strain at Fracture	Linear Crack Length (microns)	Linear Crack Velocity (mm/s)	Profile Crack Length (micron)	Profile Crack Velocity (mm/s)	Crack Density (cracks /mm)
Pre-strain Air	42.3	21.16	0	0	0	0	0
Pre-strain Env.	43.5	20.6	45.44	5.49E-07	51.04	6.17E-07	0.5
No pre-strain in Env.	43.9	27.8	56.7	4.99E-07	69.17	6.09E-07	1.6

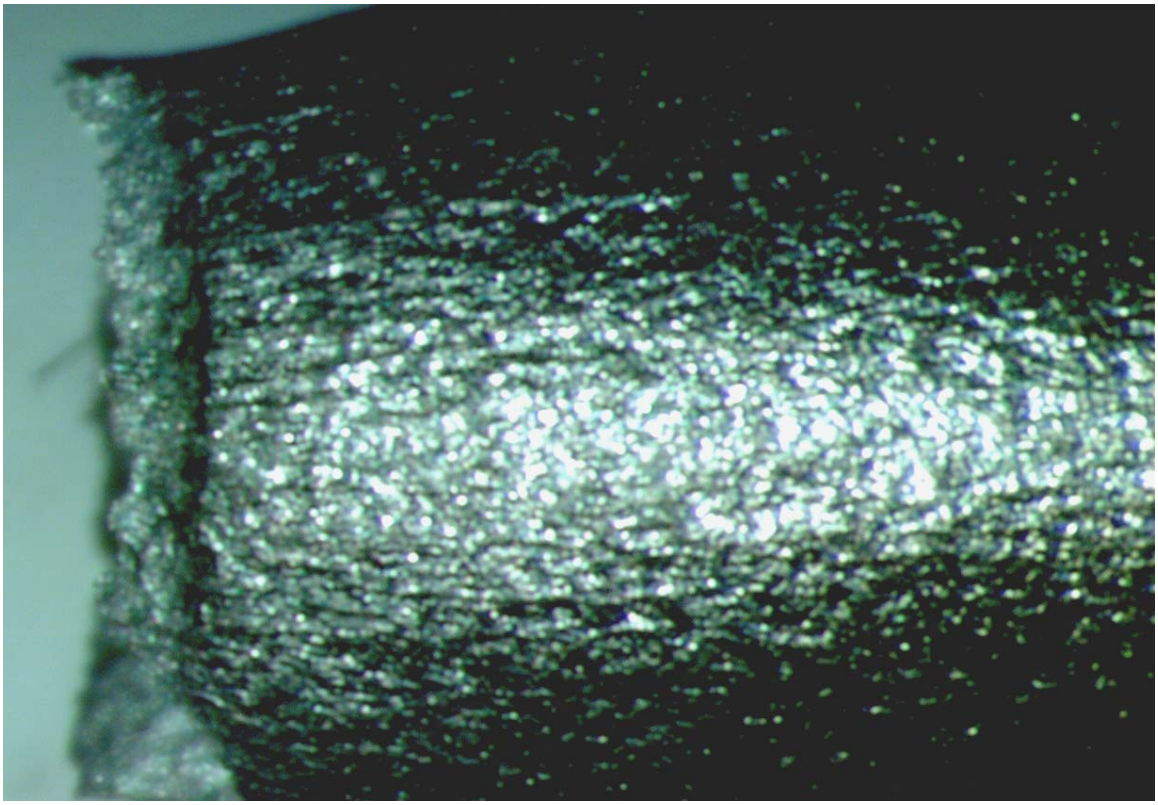

Figure 57 - Slow strain rate sample gauge of sample 5% pre-strained and then strained to failure in dry air

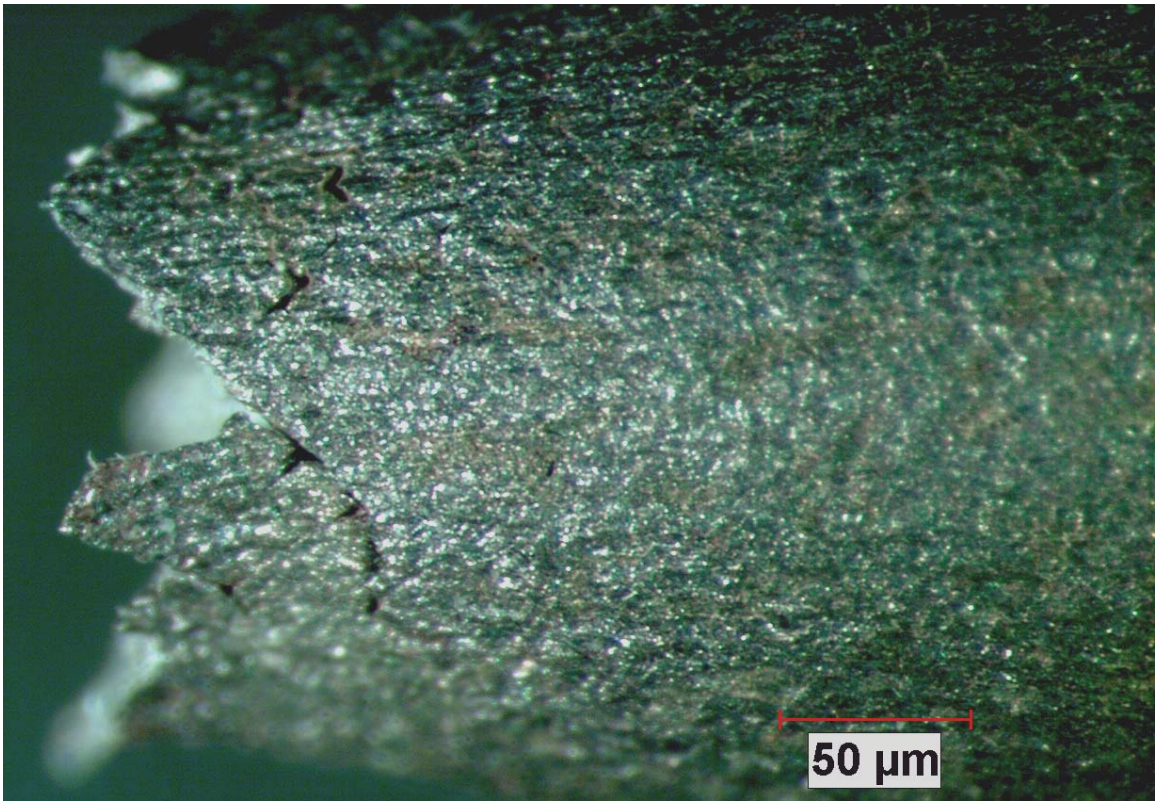

Figure 58 - Slow strain rate sample gauge of sample 5% pre-strained and then strained to failure in TGSCC environment

5.4.3 – Summary

It was determined that samples exposed to TGSCC environments under stress free conditions did not experience any deterioration of mechanical properties nor did the samples display any higher tendency to crack. Samples held at 85% yield stress in TGSCC environment did not experience any significant deterioration of mechanical properties or any higher susceptibility to cracking. However, samples with a notch machined in them for stress concentration exhibited quasicleavage fracture surface when samples were held at 85% yield strength. An increase in exposure time for these notched samples resulted in an increase in brittle nature of the fracture surface. Further, samples pre-strained to 5% strain did not result in an increase in susceptibility indicating that

global straining is not as detrimental to the pipeline steel as localized straining that may occur in front of a defect or crack feature, which helps hydrogen ingress and accumulation.

5.5 - Source of Crack Initiation

Results in Section 5.4 clearly indicate that TGSCC on pipeline steel, in bicarbonate solutions with CO_2, initiated at the areas of high stress concentration. Stress concentration facilitates hydrogen ingress and accumulation for embrittlement of steel. However, design of pipeline is such that notches are not expected at the surface. Field failures have shown that generally there were no design, machining or welding related external stress raisers near TGSCC failures. Stress raisers may develop on smooth surface due to environmental effect or corrosion. Further tests were carried out to determine if stress concentrator develop on existing pipeline under ground water environmental conditions. For this, interrupted slow strain rate tests were performed, where smooth tensile samples were exposed under different environmental and loading conditions while examining the surface for localized attack at microstructural features. Test details are described in Procedures 4.1.

In the first stage, samples were loaded to ~35% yield strength and the test sample was removed for observations in SEM. It was observed that preferential dissolution occurred at sites of inclusions and scratches from sample preparation as shown in Figure 59. At this stage, with only about 27 hours of exposure, inclusions had already fallen out to produce crack-like features as shown in Figure 60. EDS analysis on intact surface inclusions confirmed that the secondary intermetallic inclusions were predominately MnS, as shown in Figure 61. Dominate features were recorded as point of reference for

future inspections after further exposure of these samples to SSRT conditions in bicarbonate solutions with CO_2.

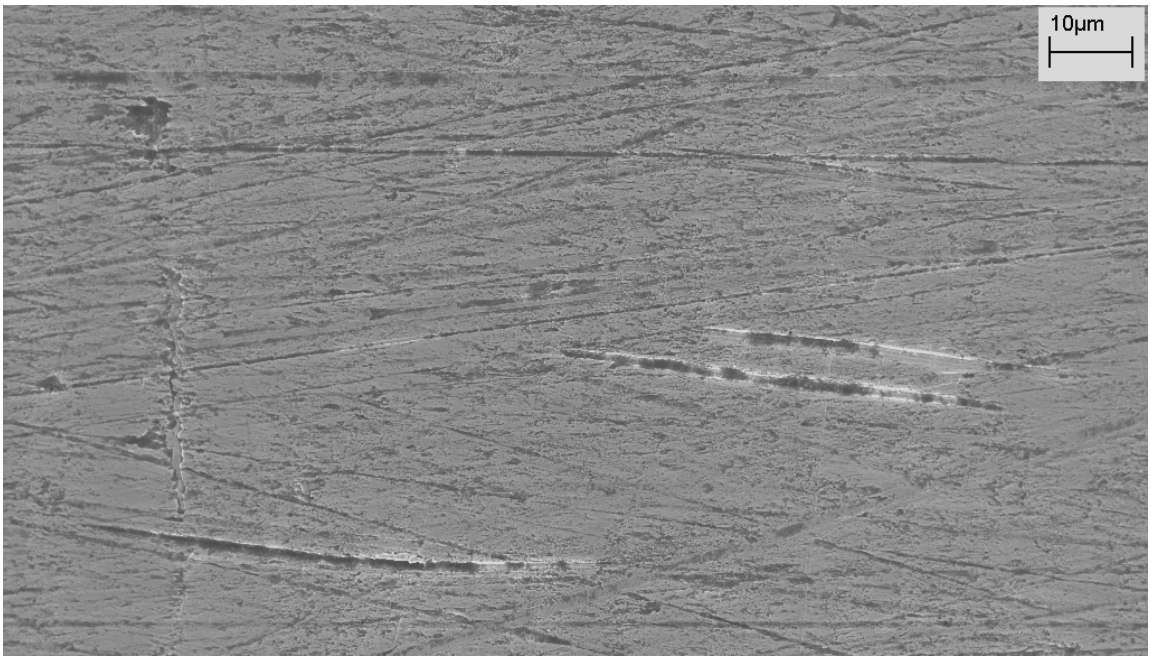

Figure 59 - Sample surface after loading to one-third the yield strength. This image shows the preferential dissolution at scratches that were created during sample preparation.

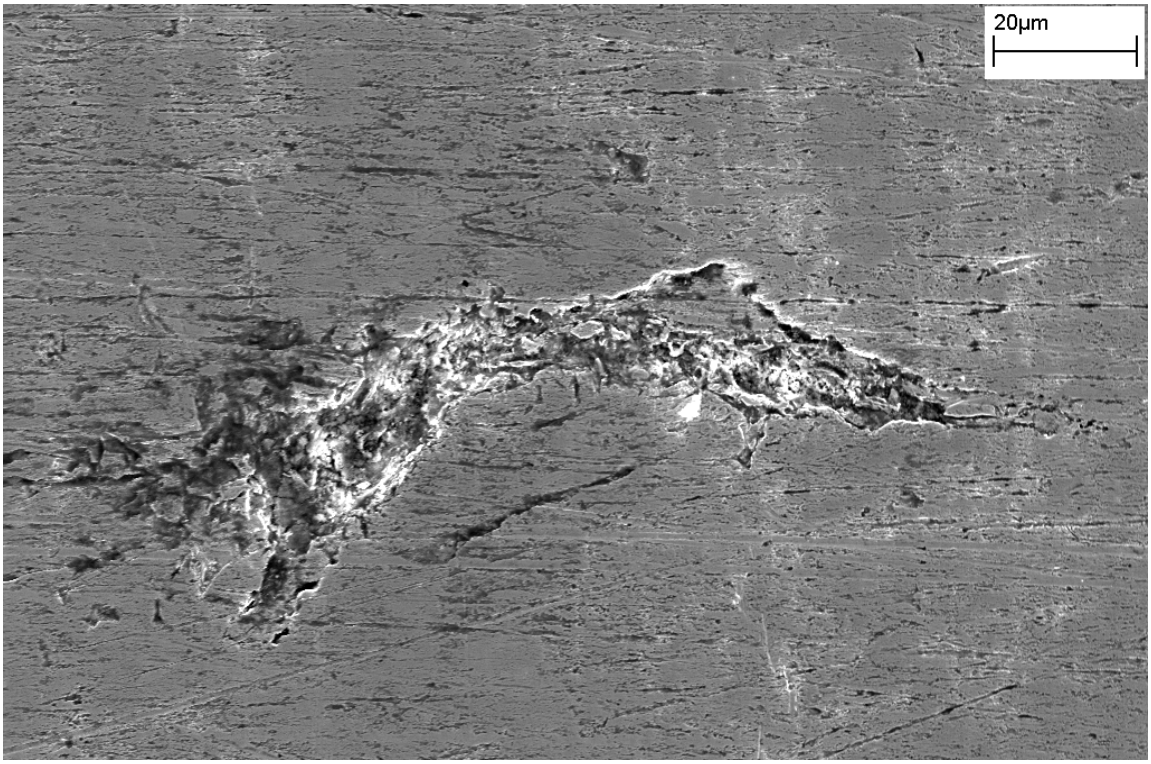

Figure 60 - Site of inclusion dissolution to produce crack like feature at loading to one-third yield strength

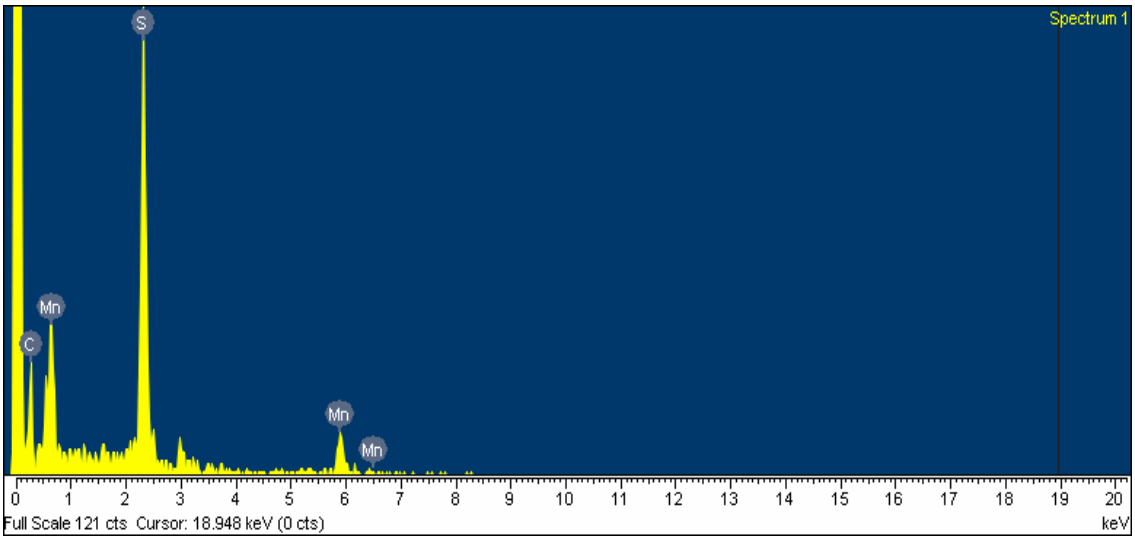

Figure 61 - EDS Spectrum of Inclusion found at the surface of the pipeline steel

In the second stage, samples were loaded to about 65% of yield strength of X-65 pipeline steel. It was observed that localized dissolution had become more predominant, creating pitting and promoting dissolution around smaller inclusions shown in Figure 62. Pits created at this stage were around 1 to 2 microns in size and clustered around previously identified defects, as seen in Figure 63. At this stage, fracture of the secondary intermetallic particles also occurred, creating "mud-like" cracking within the particles as seen in Figure 62. Growth of the previously identified inclusion/crack feature was also observed by crack growth near the edge of microstructural features.

Figure 62 - Dissolution around smaller inclusions at the pipeline surface. Note the mud-like cracking that occurs on the internal surface of the inclusion.

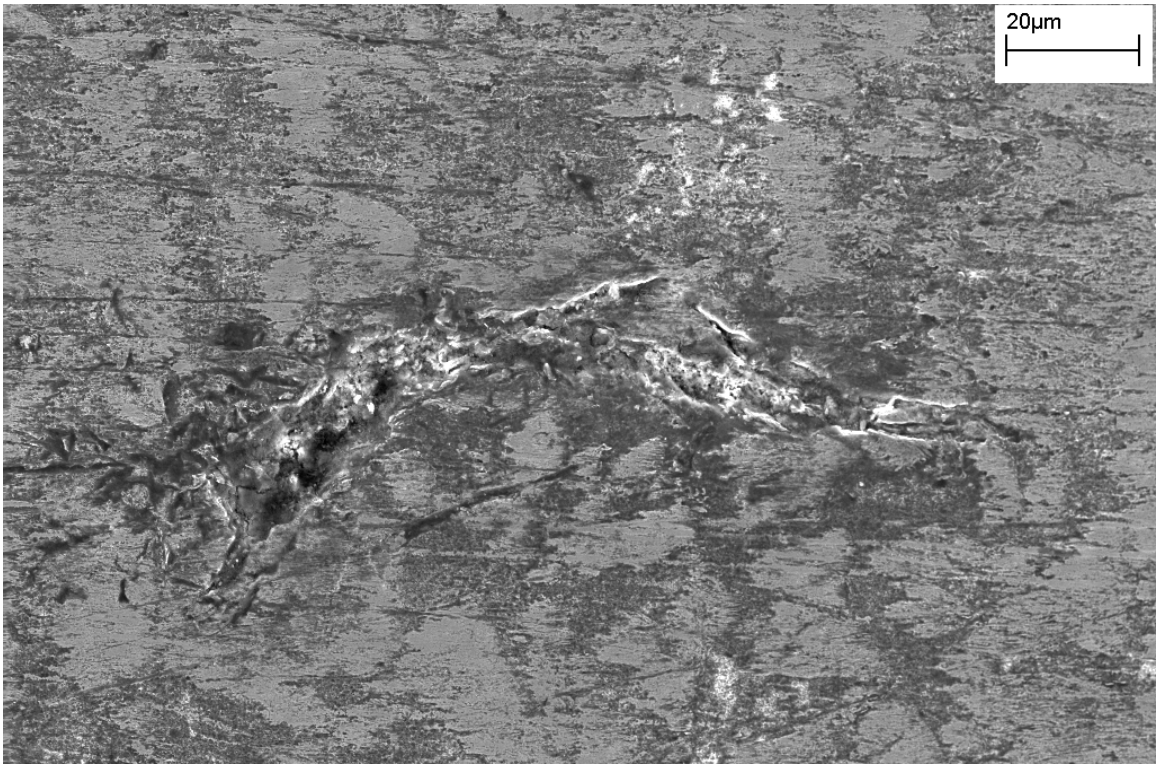

Figure 63 - Continued growth of the feature shown in Figure 60

In the third stage, the sample was strained to 300 MPa under SSRT conditions, just below the yield strength of X-65 steel. Imaging the sample surface showed clear and defined pits like those shown in Figure 64 that had developed due to inclusions falling out of the surface of the steel. At this point, all inclusions demonstrated fracture and internal cracking. Uniform dissolution of the sample became evident as all sample preparation scratches present at the beginning of the test were no longer observed. This indicates that general dissolution competes with localized dissolution due to galvanic effects near inclusions and other second phase particles.

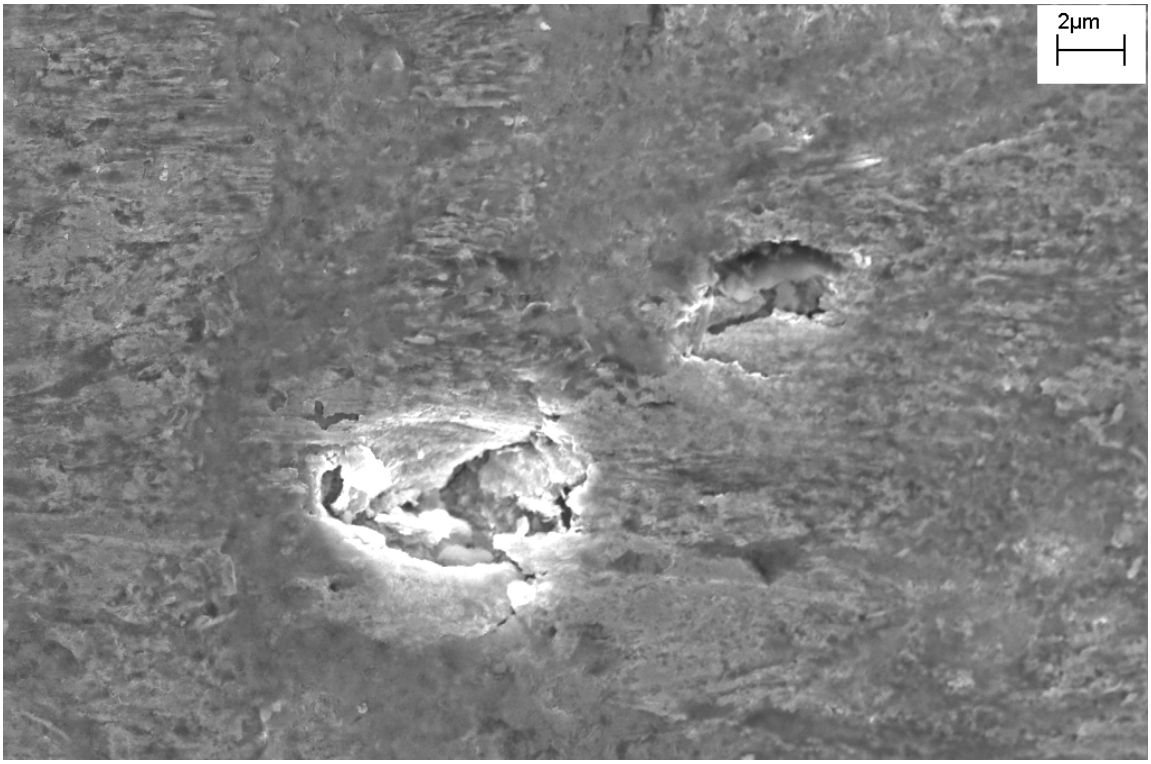

Figure 64 - Pits formed by small inclusions falling out of the sample surface

In the fourth stage of this test, the sample was interrupted after about 350 MPa applied stress, which is just above the yield strength. Sample exhibited crack initiation from pits as seen in Figure 65. Pits became larger, deeper, and increased in number. This furthers the assertion that stress corrosion cracks can initiate from the bottom of pits that act as a source of stress concentration. Pits in this system form due to galvanic corrosion of manganese sulfide inclusions. Stress can help with breaking these brittle phases and making pit formation easier. Cracks can initiate from these pits due to stress concentration at the bottom of these corrosion pits. In presence of environment where hydrogen may be produced on the steel surface, hydrogen may ingress and accumulate ahead of these pits by the mechanism described earlier. Cracks were seen at stresses as

low as ~65% yield strength of the pipeline steel in relatively short exposure time compared to the field exposures.

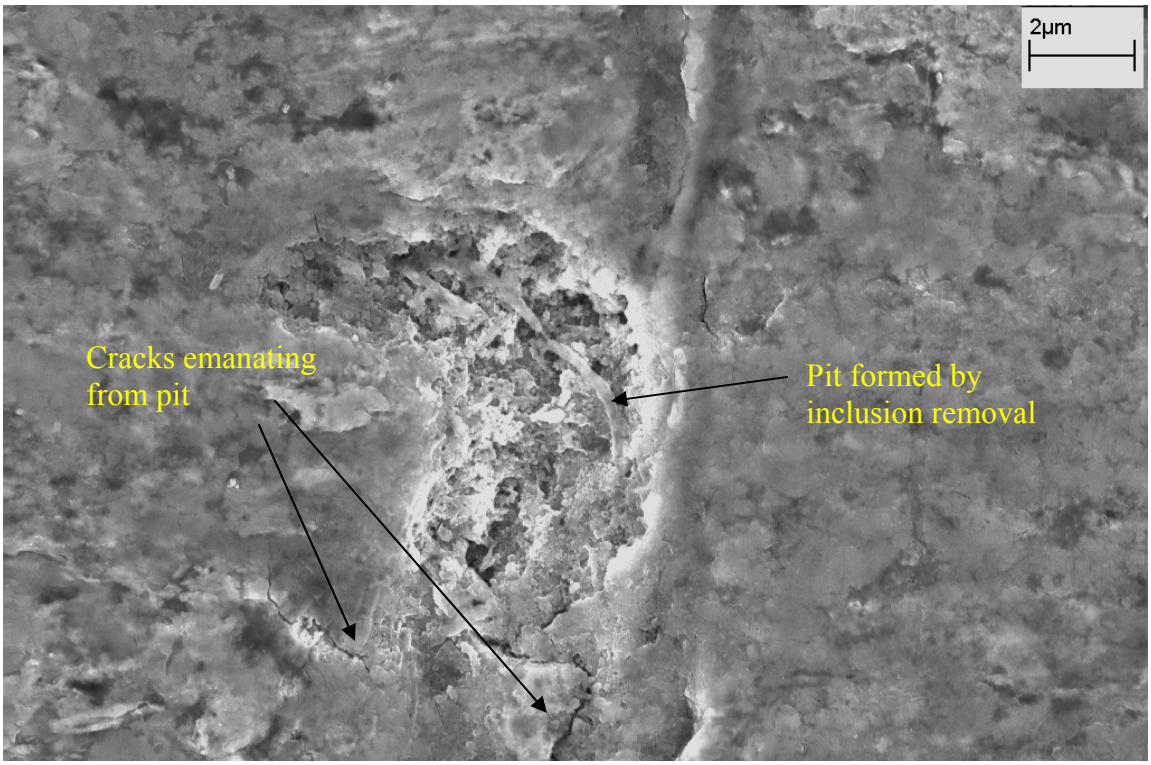

Figure 65 - Pit that has developed a crack that propagated into the pipeline steel. This occurred just after yield stress.

At the fifth stage the sample was strained to 410 MPa, which is approximately 100 MPa above the yield strength. No significant changes were observed from stage 4. Pits grew in size and cracking from those pits became more prevalent, as shown in Figure 66. Sample was allowed to crack under SSRT conditions to see the final fracture but the sample was examined immediately prior to failure. It was determined that the feature identified in Figure 60 had contributed in the failure of the sample.

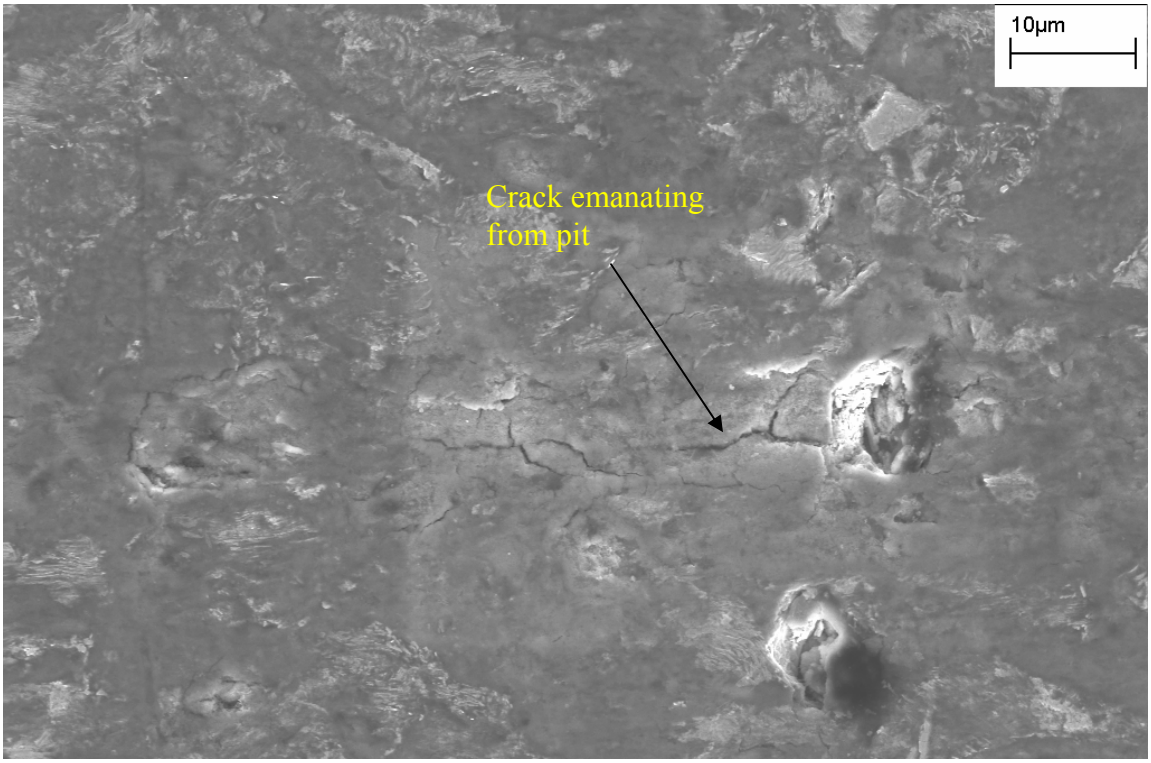

Figure 66 - Image of cracks originating from pits on the surface during interruption after 410 MPa of load.

It was observed in these interrupted SSRTs that preferential localized dissolution occurred at sites of inclusions. To further examine this preferential dissolution, a pipeline coupon was exposed to the bicarbonate solutions with CO_2 while frequently observing the machined surface by optical microscope. Inclusions were identified and their positions were recorded on the surface prior to exposing the sample to the test solution. One of the images showing the inclusions is given in Figure 67. The sample was exposed for 7 days without any applied stress and then observed under optical microscope. The post exposure image with and overlay of the initial inclusions is given in Figure 68. Although there was a considerable general dissolution at the surface, preferential

dissolution was observed at the sites of inclusions. After seven days of exposure inclusions were found to have completely dissolved leaving pits behind.

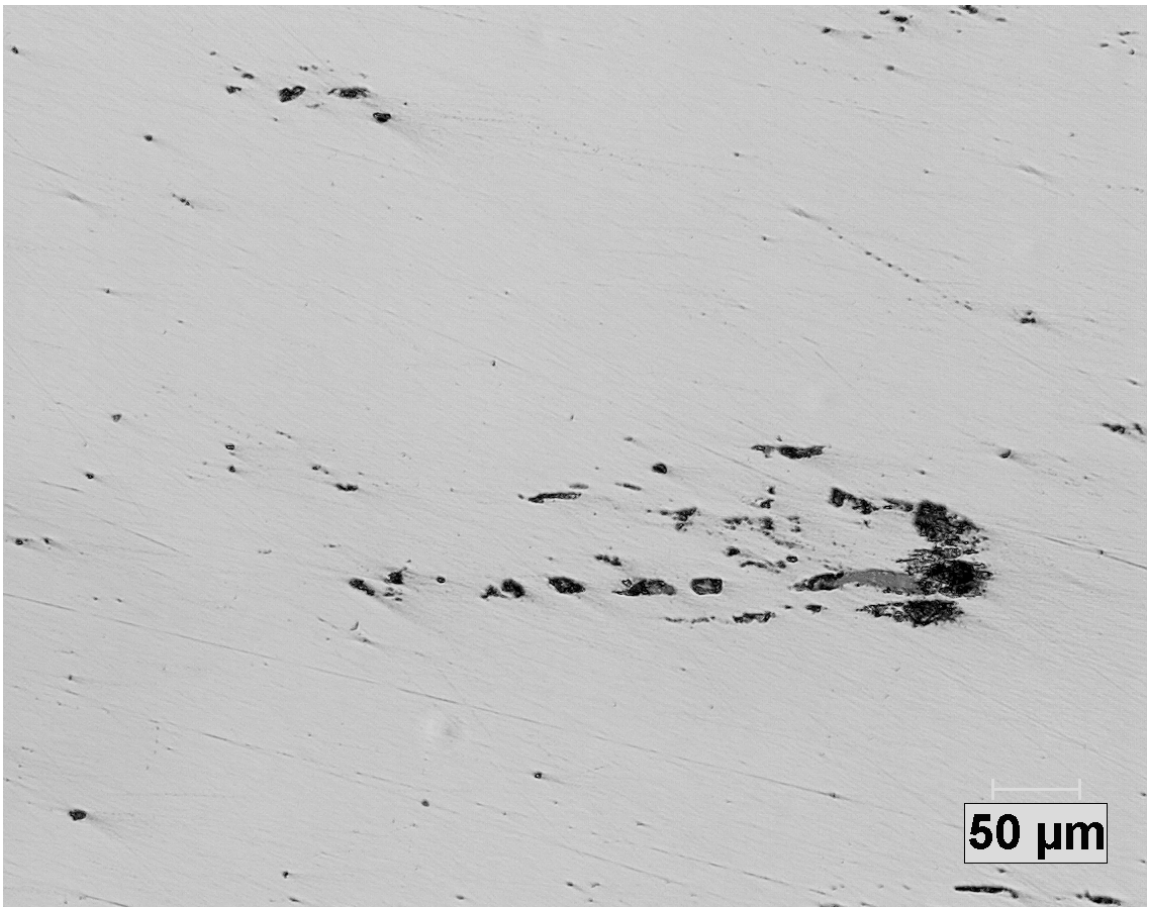

Figure 67 - Pipeline steel imaged prior to exposure to TGSCC environment. The surface was polished to 0.05 micron to reveal inclusions, which are the dark regions on the surface.

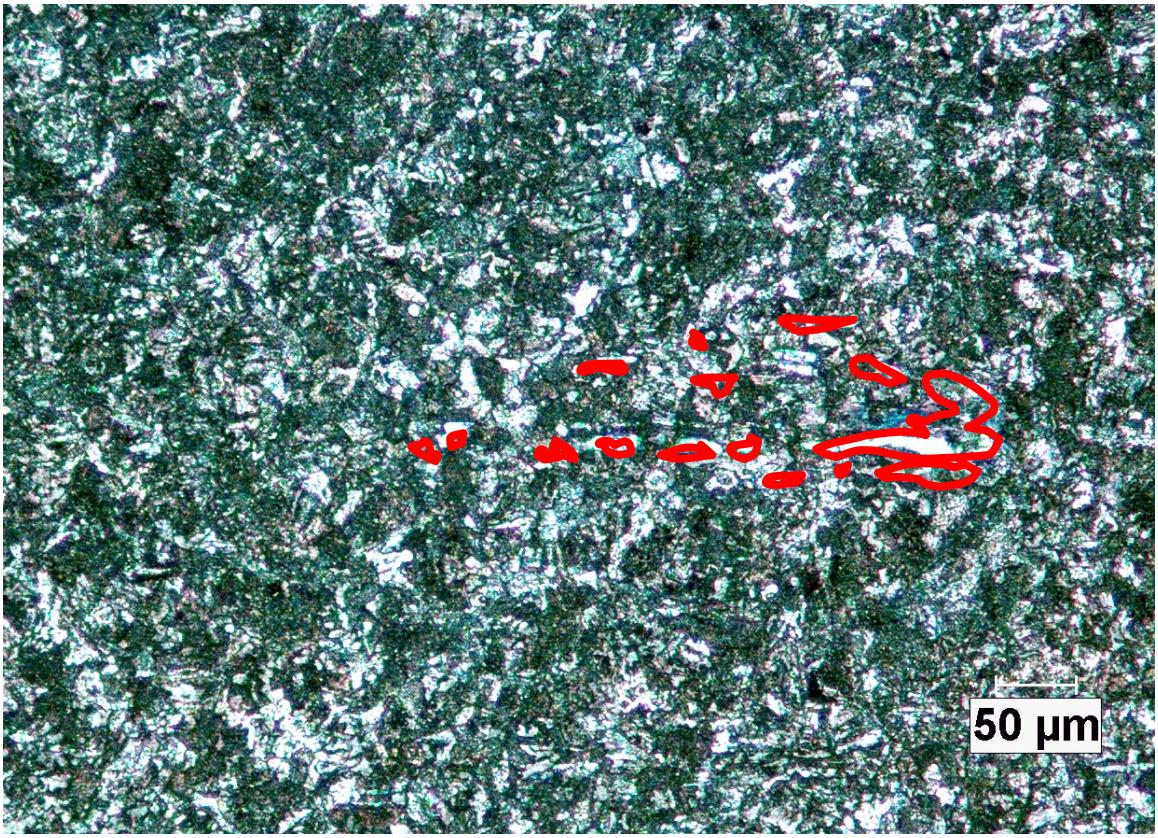

Figure 68 - Pipeline sample after 7 days of exposure with overlay of inclusions shown in Figure 67. Note that several previous inclusions are no longer visible.

5.5.1 – Summary

Tests were done to determine different effects of stress concentration on hydrogen induced TGSCC in bicarbonate solutions with CO_2. It was found that stresses have a critical role in hydrogen ingress in steels. Interrupted tests were designed to understand the formation of stress raisers at the pipeline surface due to galvanic corrosion or other mechanisms. Results indicate that stressed samples show localized corrosion attack at or near inclusions on the pipeline surface, typically related to MnS inclusions. This lead to the development of pits at the pipeline surface at approximately 30% yield strength. It was also determined that inclusions can form pits even in non-stress conditions. Some inclusions at the steel surface may also experience brittle fracture around 65% yield

strength. At stresses just below the yield strength, cracks emanated form pits previously formed at lower stress, providing a site of crack initiation.

5.6 - Effect of Environmental Variables on TGSCC of Pipeline Steel

The previously discussed results from this study have shown that hydrogen can be produced through the reaction of dissociation of carbonic acid and reaction of bicarbonate ions and metal ions as described by the NNPHG mechanism. Previous sections were mainly focused on studying the effect of simple bicarbonate environments on TGSCC. However, field research on the environment next to failed pipelines shows that there are several other ions present in the ground water and the environment may shift between the high pH and neutral pH solution based on the applied potential, moisture level, and temperature [23]. Therefore, the changes in the pH and composition of environment, and associated hydrogen production, are critical in understanding the overall mechanism of TGSCC. Understanding of hydrogen generation mechanism in near-neutral pH solution is key to understanding the mechanism of TGSCC of pipeline steel.

Near-neutral pH cracking by hydrogen generation, as has been described by the NNPHG mechanism in Chapter 3, is consistent with a failed or erratic cathodic protection on the pipeline. Applied cathodic current will limit TGSCC by the NNPHG mechanism in two ways; one by limiting the hydrogen generation from the bicarbonate due to lack of metal ions, second by changing the solution pH due to hydroxyl ion production at cathode surface. Proper cathodic protection of pipeline steel will lead to alkalization of trapped solution and favor IGSCC by promoting a shift in pH toward the other buffered region (pH 10.34), where carbonate and bicarbonate ions are at equilibrium, as shown in Figure 2. In this context it is not hard to conclude that the trapped solution pH might

cycle from one buffered region to the other, i.e., 6.4 to 10.3, depending upon the stability of cathodic protection, the amount of CO_2 and other ions, or the solution concentration. Higher concentrations would be expected to take longer for any shifts to occur.

Further, this possibility of environmental shifts between the near-neutral pH solutions to high pH solution at the pipeline steel surface may explain how both IGSCC and TGSCC could be found near each other on the same pipeline. It is known that each mode of stress corrosion cracking in pipeline steel is associated with a very specific solution pH which also affects the stability of ions present in the accumulated solution at the pipeline surface [43, 44].

5.6.1 - Effect of CO_2 and Applied Potential

Alterations in the CO_2 levels in the ground water have been reported to occur due to seasonal changes and biological activities related to the season [14]. At the same time the extent of cathodic protection is also known to vary due to equipment failure or soil resistance. Therefore, it was of interest to develop an understanding of how the pH of trapped solution at the pipeline surface can change with the change in CO_2 and applied potential.

Results from the coupon exposure tests with applied potential demonstrated the influence of CO_2 on solution pH in the bulk solution, as shown in Figures 69-71. When applied potential was initially applied with CO_2 bubbling through the solution, no significant change to pH was recorded. However, once CO_2 bubbling was stopped, pH continuously increased until the environment reached a new equilibrium state, depending upon the potential and initial solution compositions. When CO_2 was reintroduced in the test solution, the pH decreased to near-neutral range within 10 minutes. These results

clearly indicate that both the availability of CO_2 supply in the ground water and applied cathodic potential values determine the solution pH or the equilibrium between carbonic acid, bicarbonate ions and carbonate ions in this system, in accordance with the equilibrium calculation results plotted in Figure 2. If the cathodic protection is properly working on pipelines, then a large amount of CO_2 will be required for the bulk-solution pH to be maintained in the near-neutral range. If carbon dioxide supply is not sufficient, production of hydroxyl ions due to applied cathodic potential will drive the pH to higher values and eventually to the IGCSS regime.

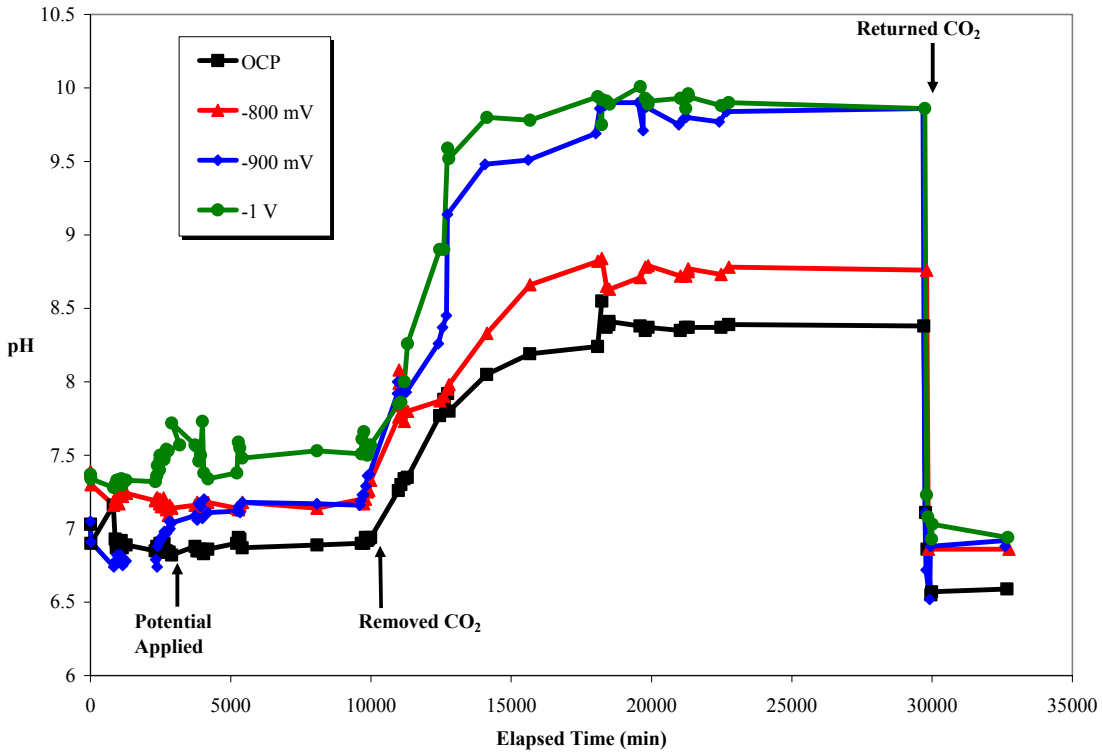

Figure 69 - pH vs. Time for 0.5 g/L $NaHCO_3$ solution at 23°C and 5% CO_2 for varying levels of cathodic protection. Initial OCP was measured to be -670mV$_{SCE}$.

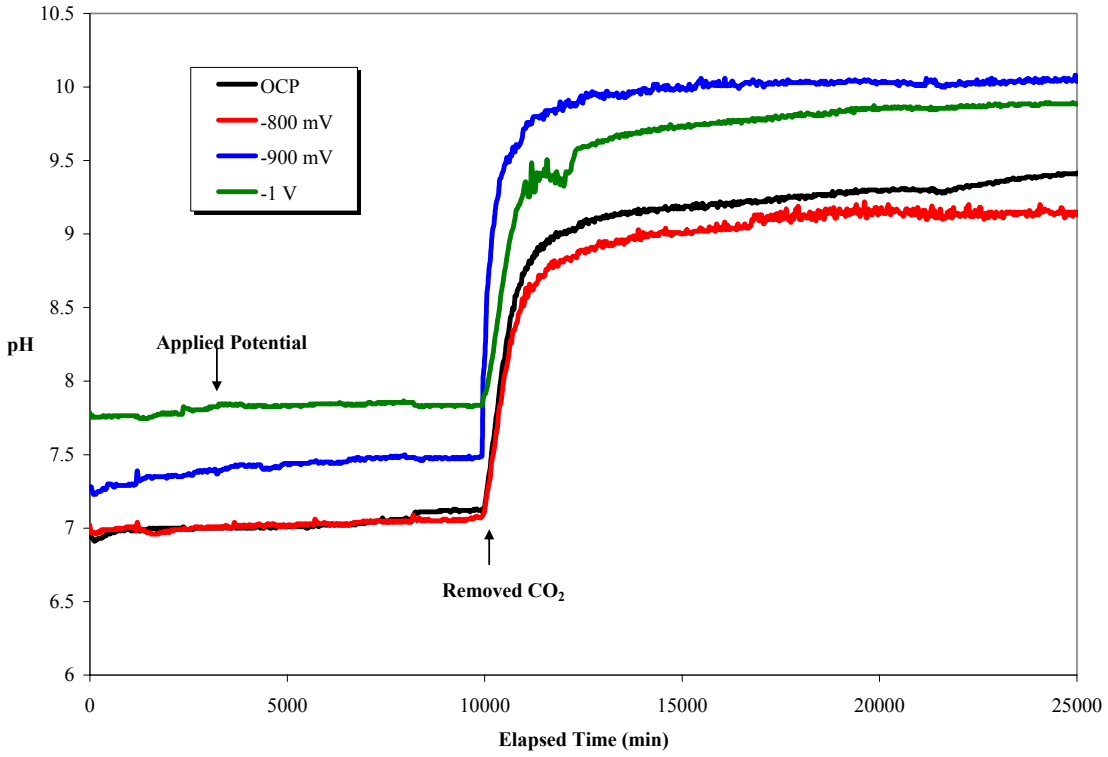

Figure 70 - pH vs. Time for 0.5g/L $NaHCO_3$ solution at 35°C and 5% CO_2 for varying levels of cathodic protection.

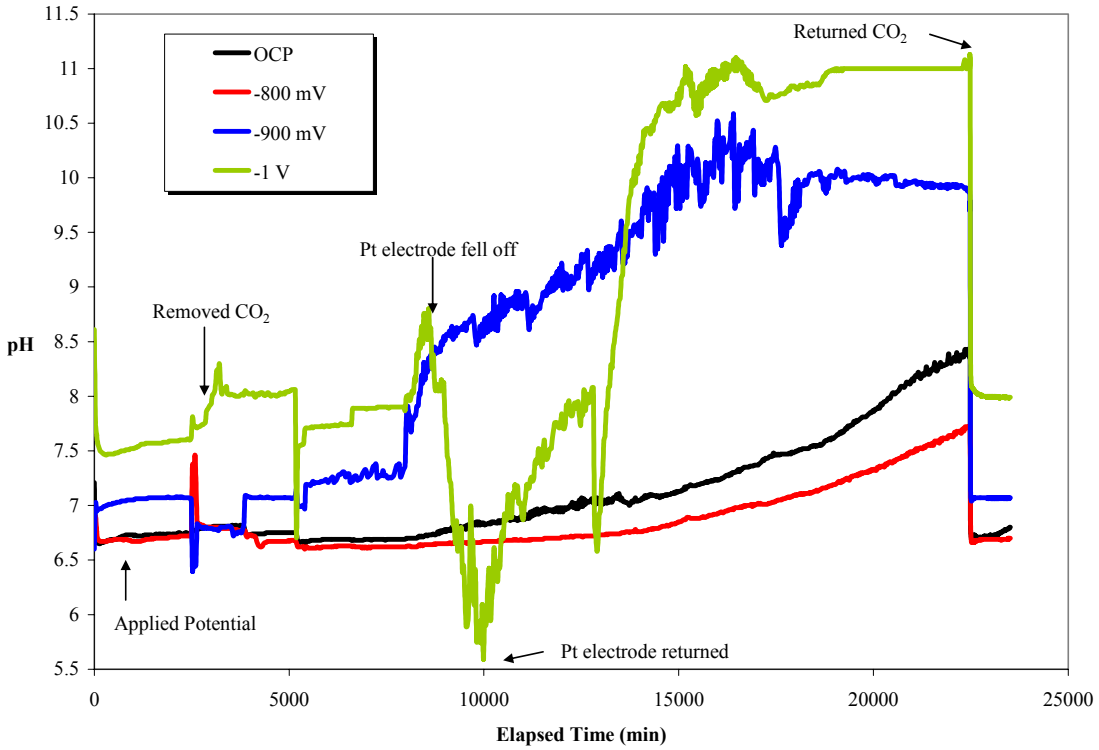

Figure 71 - pH vs. Time for 0.5g/L $NaHCO_3$ Solution at 15°C and 5% CO_2 for varying levels of cathodic protection.

Removal of cathodic protection can also rapidly shift the environment as well especially when the carbon dioxide is available. This can be seen in Figure 71 when the platinum electrode fell off accidentally in this experiment, removing applied potential from the sample, the solution pH rapidly decreasing to about near-neutral conditions. However, when the platinum electrode was restored, the bulk solution returned to a high pH value. This means that pipelines that experience transient cathodic protection may experience rapidly shifting environments between low and high pH. Whereas, if the cathodic protection is not applied to the pipeline or is not functioning adequately, then the trapped solution pH will be in the near-neutral range.

Coupon test results indicated that even with application of high cathodic voltage, near-neutral bulk solution pH can be maintained as long as the environment was continuously saturated with CO_2. However, these experiments were performed with a large volume of test solution as compared to the ground water volumes trapped under coatings on the pipeline surface. To understand the effect of applied potential at or near surface of pipeline steel, a series of tests were performed where the surface pH at the steel surface was measured. Results from these tests, shown in Figures 72-76, are closer to the environmental conditions at the pipeline steel surface.

For the test at open circuit potential (OCP), surface pH throughout the test duration is shown in Figure 72. Once the steel sample was inserted a large spike in surface pH was observed, which is attributed to the initial corrosion on the steel sample. The surface pH continuously dropped to reach a steady value of around 7.1. The bulk pH initially rose steadily as the reaction products at the steel surface diffused into the bulk solution. Bulk pH also achieved a steady state pH of around 7.1 slightly after the surface pH had equilibrated. Steady state was maintained for a short time, and then the pH increased again. This is due to the depletion of CO_2 in the solution as the carbon dioxide was not bubbled through the solution to avoid solution agitation and mixing and simulate the relatively calm conditions for the trapped solution on the pipeline surface.

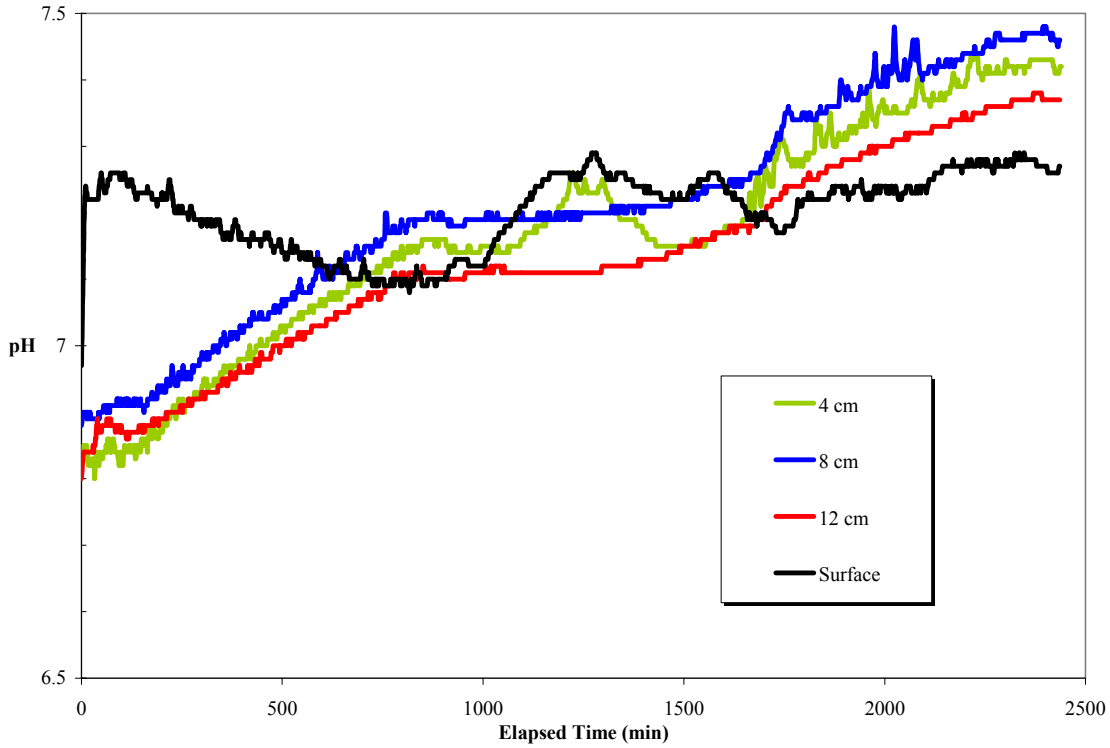

Figure 72 - pH at the X-65 pipeline steel surface as well as at different distances away from the surface as a function of time for 0.5 g/L $NaHCO_3$ solution saturated with CO_2 under open circuit potential (-780mV_{SCE}).

Results for the tests performed with the application of applied potential are shown in Figure 73-76. Previous coupon tests had indicated that near-neutral conditions could still be achieved with applied cathodic potential as long as the environment was saturated with 5% CO_2. However, in these tests, surface of the pipeline steel invariability became high pH environments. Open circuit potential for these samples was measured to be between -760 to -780 mV. Samples subjected to -800 mV which is only about 20 to 40 mV cathodic to the OCP, showed a rapid increase in the surface pH beyond near-neutral conditions within 100 minutes. Application of more cathodic applied potential resulted in higher surface pH. Pipeline steels are cathodically protected from -900 mV to -1.25 V, depending on the industry standards. It can be seen in Figures 75 and 76 that at these

potentials, even with saturation of CO_2, the surface pH of the steel will generate a high pH environment that favors the formation of IGSCC rather than TGSCC. It is also interesting to note that the pH gradient with distance was maintained throughout the test for the bulk pH values, as shown in Figure 72. However, as the surface conditions are important for the corrosion reactions, surface pH effects and resulting local environments are important in determine the mechanism of cracking.

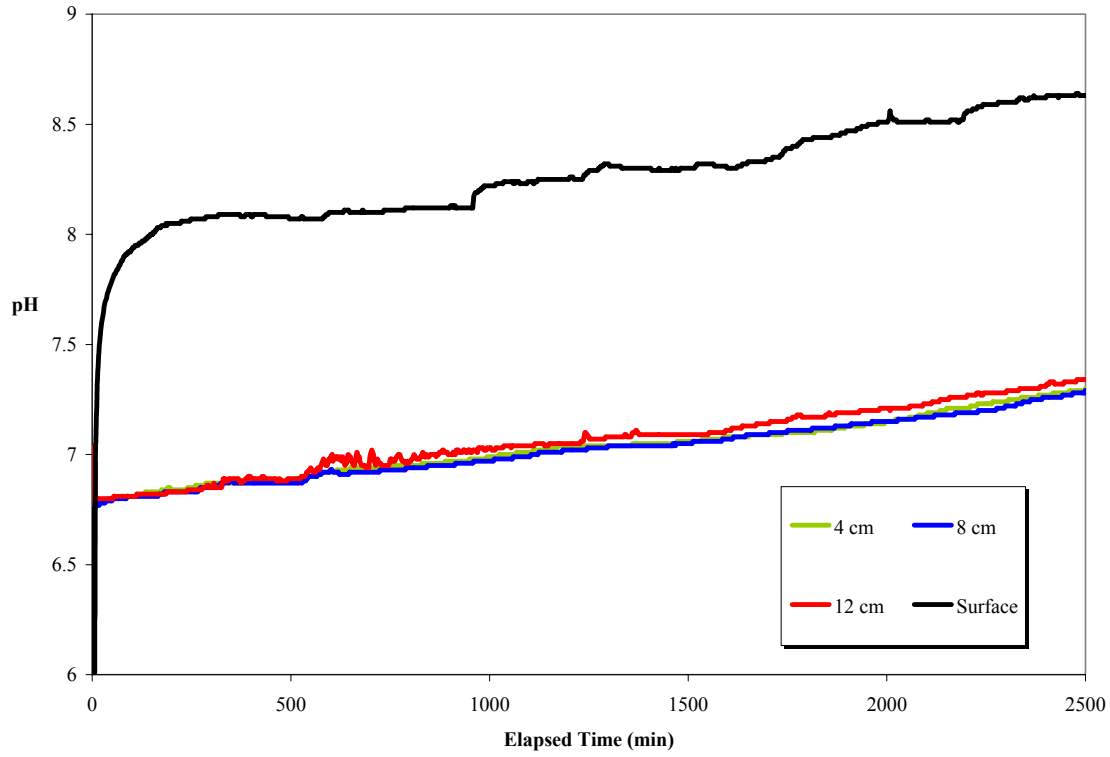

Figure 73 - pH at the X-65 pipeline steel surface as well as at different distances away from the surface as a function of time for 0.5 g/L $NaHCO_3$ solution saturated with CO_2 with applied potential of -800mV_{SCE}. Note that surface pH rapidly increases and is not near-neutral almost immediately.

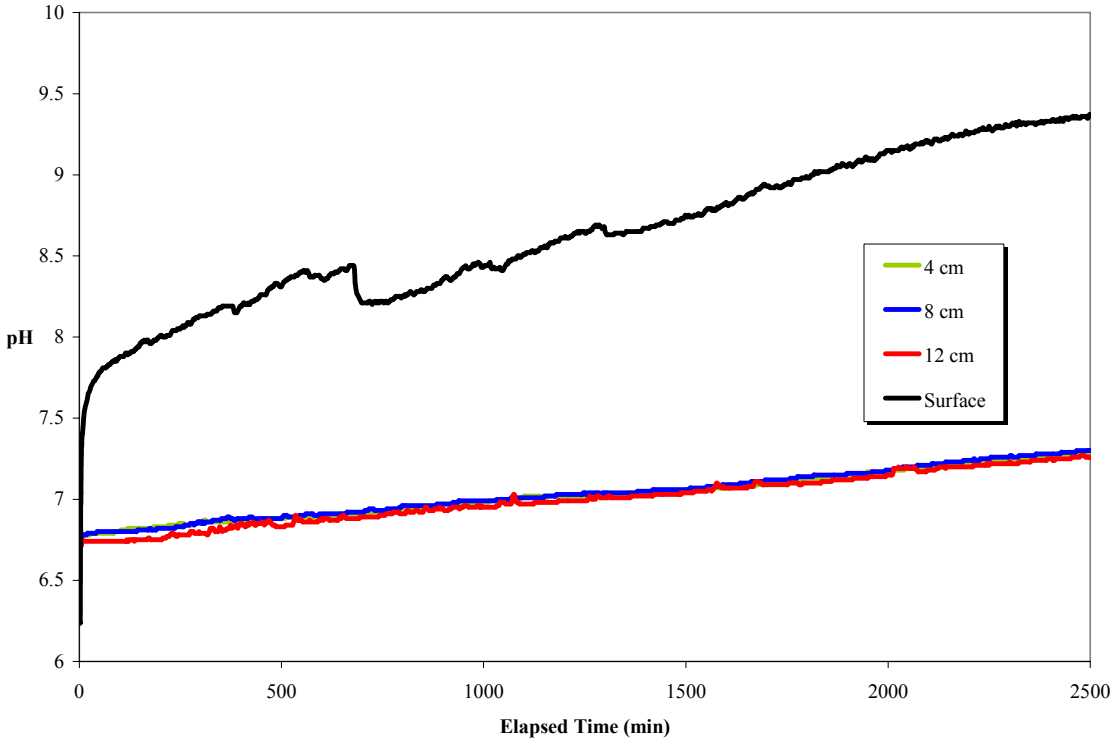

Figure 74 - pH at the X-65 pipeline steel surface as well as at different distances away from the surface as a function of time for 0.5 g/L $NaHCO_3$ solution saturated with CO_2 with applied potential of -850mV_{SCE}.

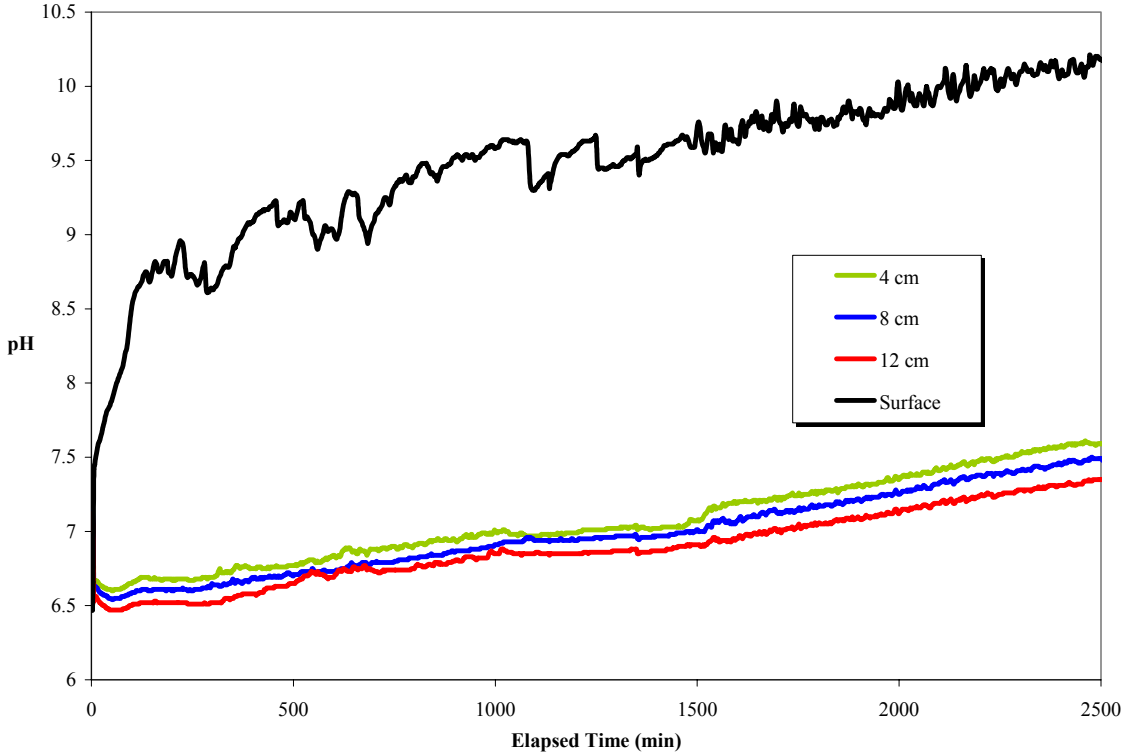

Figure 75 - pH at the X-65 pipeline steel surface as well as at different distances away from the surface as a function of time for 0.5 g/L $NaHCO_3$ solution saturated with CO_2 with applied potential of -900mV_{SCE}.

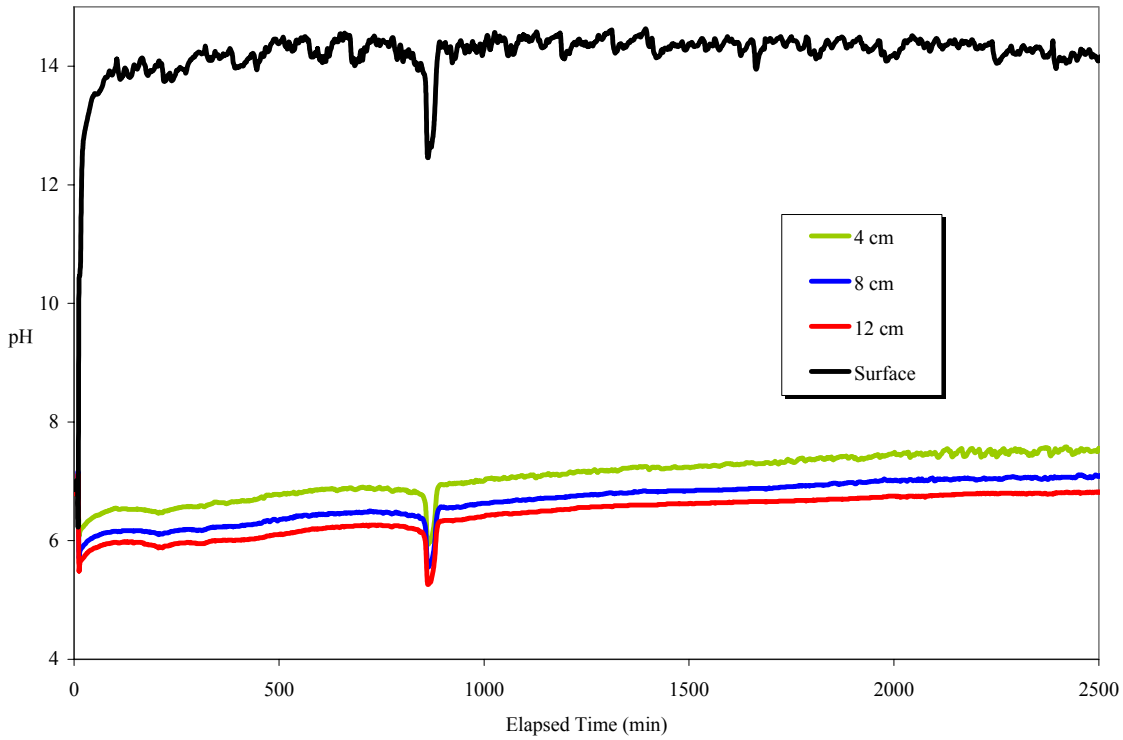

Figure 76 - pH at the X-65 pipeline steel surface as well as at different distances away from the surface as a function of time for 0.5 g/L $NaHCO_3$ solution saturated with CO_2 with applied potential of -1.250V_{SCE}.

5.6.2 - Effect of Other Groundwater Ions on TGSCC of Pipeline Steels

Analyses of trapped solutions near field failures have shown the presence of other common ground water constituents. Although our results have indicated that the TGSCC could be explained through NNPHG mechanism in simple bicarbonate solutions with carbon dioxide, but the role of other ions in pH buffering, hydrogen production and/or poisoning are not clear. To study the effect of addition of other ions on TGSCC and the NNPHG mechanism, coupon exposure tests were performed in the same manner as for the tests described earlier, 5.1, with solution and precipitates being analyzed for the amount of carbonate formed under each condition. Amount of carbonate dectected after each test was related to the hydrogen generation by NNPHG mechanism.

Thermodyamics predict that bicarbonate ions can react with caclium ions in the solution to form calcium carbonate. This and other similar reactions with cations would further the hydrogen generation by NNPHG mechanism. Results from coupon exposure tests indicate that the addition of $CaCl_2$ significantly increased the amount of carbonate and bicarbonate in the precipitates, as shown in Table 28. The amount of carbonate and bicarbonate in the solution was also increased slightly with the addition of calcium salts in the test solution. At low concentrations (0.1 g/L) of $NaHCO_3$, additions of $CaCl_2$ increased the amount of iron in the precipitate, indicating an increase in the corrosion rate. XRD peaks for surface scale indicated the presence of $CaCO_3$ on the surface of the pipeline steel sample, validating the proposed reaction mechanism.

Magnesium can also potentially form carbonates in bicarbonate solutions with CO_2 bubbling, assisting in hydrogen generation. Coupon exposure results, shown in Table 27 and 28, show that addition of magnesium salts did not have any significant effect on the amount of solution carbonate compared to the simple bicarbonate solutions. The only noticeable deviation was that the solutions of 0.1g/L $NaHCO_3$ exhibited an increased amount of iron precipitate. This was similar to the results with $CaCl_2$ additions to the solution, and supports the assertion that a higher corrosion rate occurs with more dilute solutions. However, $FeCO_3$ was detected on the surface of the sample for all tested concentrations. This means that the presence of magnesium ions in the solution could decrease the solubility of $FeCO_3$, allowing it to precipitate on the surface at lower solution concentrations.

Table 27 - Concentration of iron, carbonate, and bicarbonate ions in the solution after 72 hour test at 15°C and 35°C with 5% CO_2 bubbling

HCO_3^- (g/L)	Temp. (°C)	Additional Chemical	Fe Conc. (mg/L)	Carbonate Conc. (mg/L)	Bicarbonate Conc. (mg/L)
0.1	15	KCl	0	0/0	111
5	15	KCl	0	537	5640
10	15	KCl	0.019	1020	11400
0.1	15	$MgSO_4$	0	0	111
5	15	$MgSO_4$	0	507	5880
10	15	$MgSO_4$	0.067	630	12900
0.1	15	$CaCl_2$	0	0	135
5	15	$CaCl_2$	0	462	5980
10	15	$CaCl_2$	0.108	512	12700
0.1	15	KCl, $MgSO_4$, $CaCl_2$	0.616	0	114
5	15	KCl, $MgSO_4$, $CaCl_2$	0	0	5480
10	15	KCl, $MgSO_4$, $CaCl_2$	0.035	792	13100
0.1	35	KCl	0	0	146
5	35	KCl	0.042	352	6760
10	35	KCl	0.035	803	11600
0.1	35	$MgSO_4$	0	0	152
5	35	$MgSO_4$	0.034	0	5730
10	35	$MgSO_4$	0.123	766	12800
0.1	35	$CaCl_2$	0.004	0	118
10	35	$CaCl_2$	0.76	690	13300
0.1	35	KCl, $MgSO_4$, $CaCl_2$	0	0	115
5	35	KCl, $MgSO_4$, $CaCl_2$	0.034	0	5860
10	35	KCl, $MgSO_4$, $CaCl_2$	0.04	665	11800

Results from coupon exposure tests indicate that the presence of KCl in test solutions appeared to increase the amount of iron in precipitates at very low and very high concentrations of bicarbonate ions. KCl also promoted high amounts of

bicarbonates in the precipitates. Further, XRD analysis of steel surface indicated the presence of $FeCO_3$ and Na_2CO_3 for these tests.

Table 28 - Concentration of iron, carbonate, and bicarbonate ions in the precipitate after 72 hour test at 15°C and 35°C with 5% CO_2 bubbling

HCO_3^- (g/L)	Temp (°C)	Additional Chemical	Fe Conc. (mg/kg)	Carbonate Conc. (mg/kg)	Bicarbonate Conc. (mg/kg)
0.1	15	KCl	573000	0	0
5	15	KCl	531000	1300	6500
10	15	KCl	517000	1980	9910
0.1	15	$MgSO_4$	548000	178	890
5	15	$MgSO_4$	532000	2260	11300
10	15	$MgSO_4$	506000	2130	10600
0.1	15	$CaCl_2$	548000	717	3590
5	15	$CaCl_2$	196000	72500	363000
10	15	$CaCl_2$	129000	74000	370000
0.1	15	KCl, $MgSO_4$, $CaCl_2$	558000	0	0
5	15	KCl, $MgSO_4$, $CaCl_2$	228000	63000	315000
10	15	KCl, $MgSO_4$, $CaCl_2$	159000	77900	389000
0.1	35	KCl	544000	0	0
5	35	KCl	424000	0	0
10	35	KCl	515000	5160	25800
0.1	35	$MgSO_4$	520000	0	0
5	35	$MgSO_4$	51000	1860	9290
10	35	$MgSO_4$	524000	278	1390
0.1	35	$CaCl_2$	547000	0	0
10	35	$CaCl_2$	96000	93500	468000
0.1	35	KCl, $MgSO_4$, $CaCl_2$	562000	0	0
5	35	KCl, $MgSO_4$, $CaCl_2$	189000	75800	379000
10	35	KCl, $MgSO_4$, $CaCl_2$	48200	102000	510000

Coupon exposure tests in NS4 solution, with composition of 0.5 g/L $NaHCO_3$ + 0.122 g/L KCl + 0.137 g/L $CaCl_2$ + 0.131 g/L $MgSO_4$, indicated lower amounts of iron in the precipitate and significantly more carbonate and bicarbonate in the precipitate. XRD of the steel sample surface after the test indicated the presence of a variety of corrosion products but no metal carbonates were detected in NS4 solution.

5.6.3 - Electrochemical Behavior of X-65 Steel in Bicarbonate Containing Solutions

Potentiodynamic polarization tests were performed on X-65 pipeline steel samples to verify the amount of cathodic current density at each applied cathodic potential and also to see if during anodic polarization the carbon steel had any tendency to passivate in the tested groundwater solutions. Potentiodynamic polarization behavior of pipeline steel in different solutions is shown in Figure 77. Results indicate that irrespective of other NS4 constituents addition solutions with similar bicarbonate composition showed a similar anodic and cathodic polarization behavior for the pipeline steel tested. Corrosion potential for pipeline steel in all tested solutions at the room temperature was within ±20 mV of -766 mV. Simple bicarbonate test solution gave the lowest corrosion potential of -780 mV and did not show any signs of surface film after the polarization tests. Corrosion potential for pipeline steel in NS4 was found to be -766 mV, and the test samples had a light, grey film after polarization tests. The cathodic polarization curve for the carbon steel in NS4 solution corresponds to the one tested in $NaHCO_3$ + $CaCl_2$ solution (NC), with OCP of -758 mV. This similarity in the polarization behavior continues into the anodic region, up to approximately -550 mV, where both samples had a similar light-grey film after the test. In contrast, $NaHCO_3$ +

$MgSO_4$ samples had a grey-green film and an OCP of -783 mV. Whereas, the samples tested in $NaHCO_3$ + KCl solutions had an OCP of -774 mV and had a light-grey film.

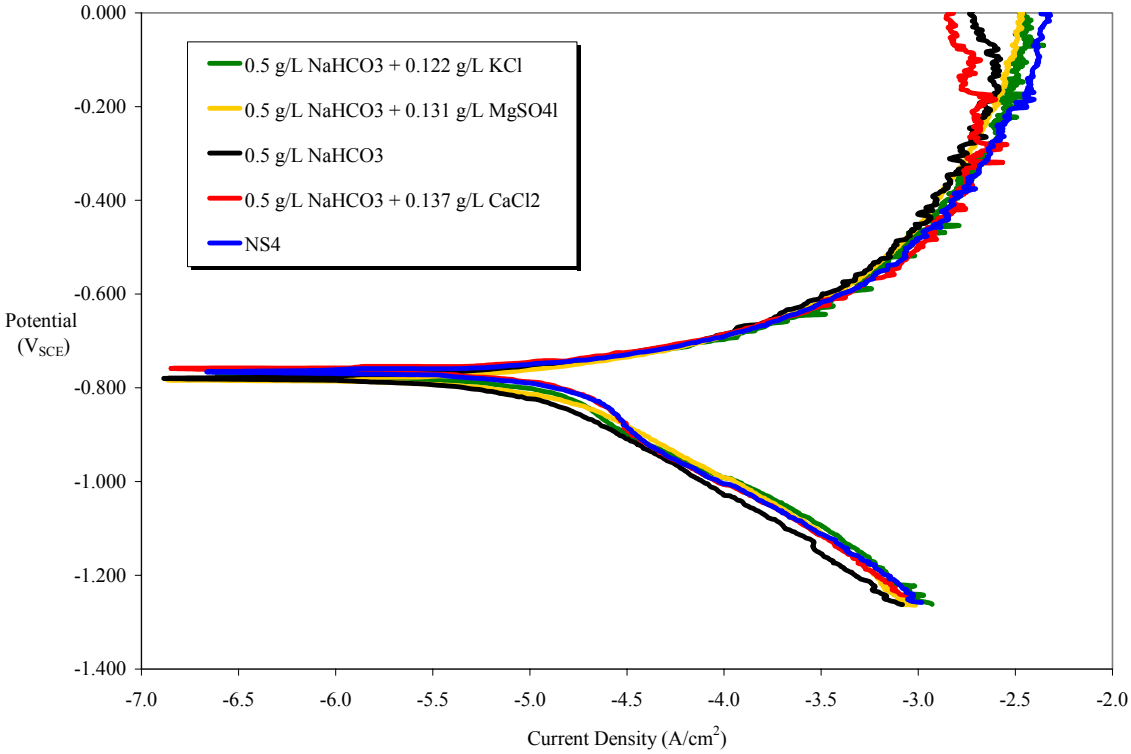

Figure 77 - Potentiodynamic results for solutions at room temperature with 5% CO_2

These electrochemical results indicate that in test solutions with bicarbonate and carbon dioxide pipeline steels showed no indication of passivation, regardless of additional NS4 components. However, evidence of discoloration due to product film was detected on certain samples. This means that any film formed is not protective. Cathodic polarization behavior of pipeline steel samples in tested solutions show that the cathodic reactions were not affected by the addition of NS4 constituents. Although constituents did not have any effect on electrochemical generation of hydrogen, they could affect hydrogen ingress through recombination reactions.

5.6.4 - Effect of Solution Constituents on TGSCC Susceptibility of X-65 Steel

The effect of additional ions was examined to determine their effect on TGSCC susceptibility. The addition of cations was the primary focus as they may contribute to the NNPHG mechanism by the addition of metal cations that may react with bicarbonate. However, anions could also participate by affecting hydrogen ingress or by action as poisons for the recombination reaction for hydrogen. The effect of additives was observed by indirect evidence of cracking morphology and crack density.

Slow strain rate tests were performed to determine the effect of chemical additions to the 0.5 g/L $NaHCO_3$ solutions on TGSCC cracking of pipeline steel. Results are given in Table 29. It was determined that samples that exhibited cracking had no significant variation in the crack velocity. Maximum crack length was also similar for all tested conditions in this series of tests and was typically 3-4 grains in length. Highest crack density in 0.5 g/L $NaHCO_3$ solutions with added chemicals occurred on NS4 solutions. However, even for NS4 the crack velocity and crack density was less that that for the pure 0.5 g/L $NaHCO_3$ with 5% CO_2 bubbled through it.

Crack morphology for the addition of magnesium sulfate in 0.5 g/L $NaHCO_3$ solution is given in Figure 78. Cracking in these solutions appeared to form from the base of a pit with a crack extending form the base of the pit. Cracks were generally short and appeared mostly in the neck transition region rather than near the fracture surface. Cracks were generally short and appeared mostly in the neck transition region rather than near the fracture surface.

Table 29 - Mechanical Properties of X-65 pipeline steel tested in a variety of solution compositions to determine the effect of addition of other ions to the mechanism of TGSCC

Solution	% RA	Strain at Fracture	Linear Crack Velocity (mm/s)	Profile Crack Velocity (mm/s)	Crack Density (cracks/mm)
0.5 g/L $NaHCO_3$.	43.9	27.8	4.99 e^{-7}	6.09e^{-7}	1.60
0.5 g/L $NaHCO_3$ + 0.131 g/L $MgSO_4$	37.8	24.0	3.49 e^{-7}	3.74 e^{-7}	0.20
0.5 g/L $NaHCO_3$ + 0.137 g/L $CaCl_2$	43.9	22.0	1.80 e^{-7}	2.82 e^{-7}	0.30
0.5 g/L $NaHCO_3$+ 0.122 g/L KCl	41.0	22.0	2.27e^{-7}	2.38 e^{-7}	0.20
NS4	39.5	15.7	4.2e^{-7}	4.23 e^{-7}	0.60

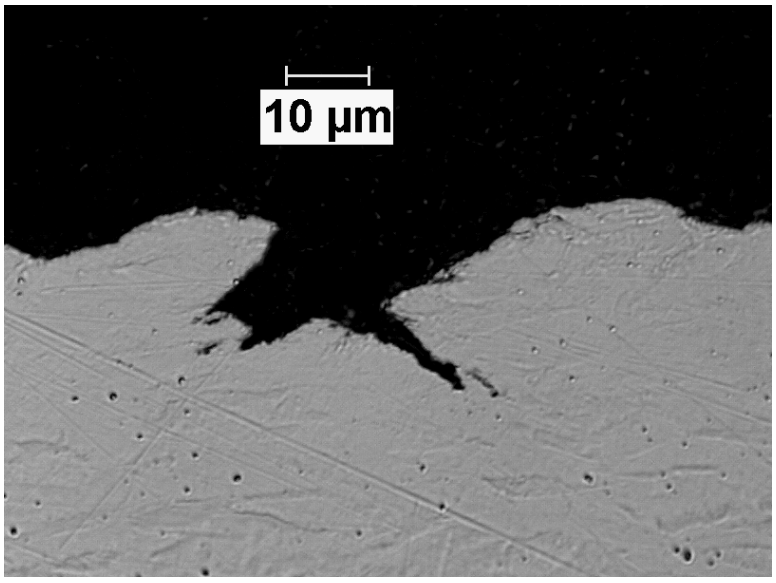

Figure 78 - Crack morphology of pipeline steel strained while exposed to 0.5 g/L $NaHCO_3$ with 0.131 g/L $MgSO_4$ and 5%CO_2 at room temperature and OCP

SSRT samples tested in potassium chloride containing 0.5 g/L $NaHCO_3$ solution showed general corrosion and some shallow pits on the steel surface. Crack morphology

for the addition of potassium is given in Figure 79. This crack appears to have formed from the base of a pit as the mouth of the crack is wide and round. Crack density for samples tested in this environment was very low. Chloride ions are known to increase the probability of localized attack like pitting. It has also been shown in this study that crack initiation is encouraged by the presence of pits. However, samples tested in solutions with Cl^- addition did not show any further susceptibility to pitting or cracking. This behavior coupled with carbonate results given in 5.6.2 indicates that potassium and chlorides have little effect on the cracking process in these solutions.

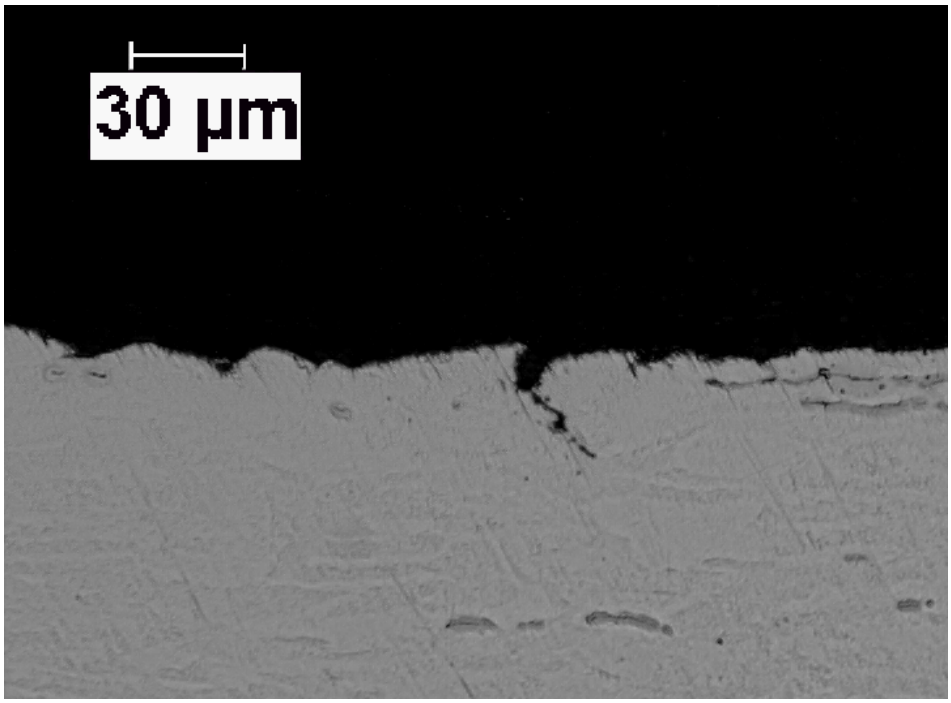

Figure 79 - Crack morphology for samples exposed to 0.5 g/L $NaHCO_3$ with 0.122g/L KCl with 5% CO_2 at room temperature and OCP.

Pipeline steels samples tested by SSRT method in solution with addition of $CaCl_2$ in 0.5 g/L $NaHCO_3$ with 5% CO_2 solution produced cracks similar to that seen in Figure

80. The cracks were sharp and were clearly transgranular. Crack walls appear to have a small degree of dissolution as they were not jagged with matching opposite surfaces.

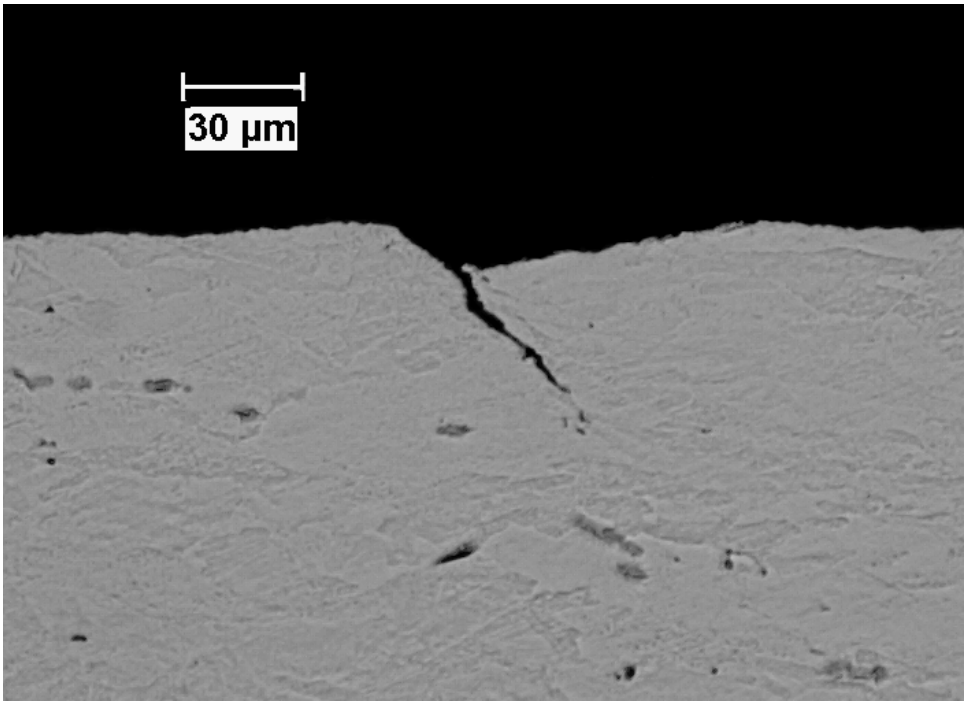

Figure 80 - Crack morphology of sample exposed to 0.5 g/L $NaHCO_3$ with 0.137 g/L $CaCl_2$ with 5% CO_2 at room temperature and OCP

Test in NS4 solution produced cracks with morphology similar to one shown in Figure 81. Cracks were typically wide and exhibited significant dissolution of walls. The crack shown in Figure 81 grew toward and eventually past the inclusion shown as a dark gray streak. Cracks growing towards inclusions were observed often. However, cracks were sometimes bunted or appeared to progress horizontally in the direction of the inclusion due to opening of inclusion interface. Rarely did cracks grow past inclusions, which were always perpendicular to the crack growth direction due to sample design.

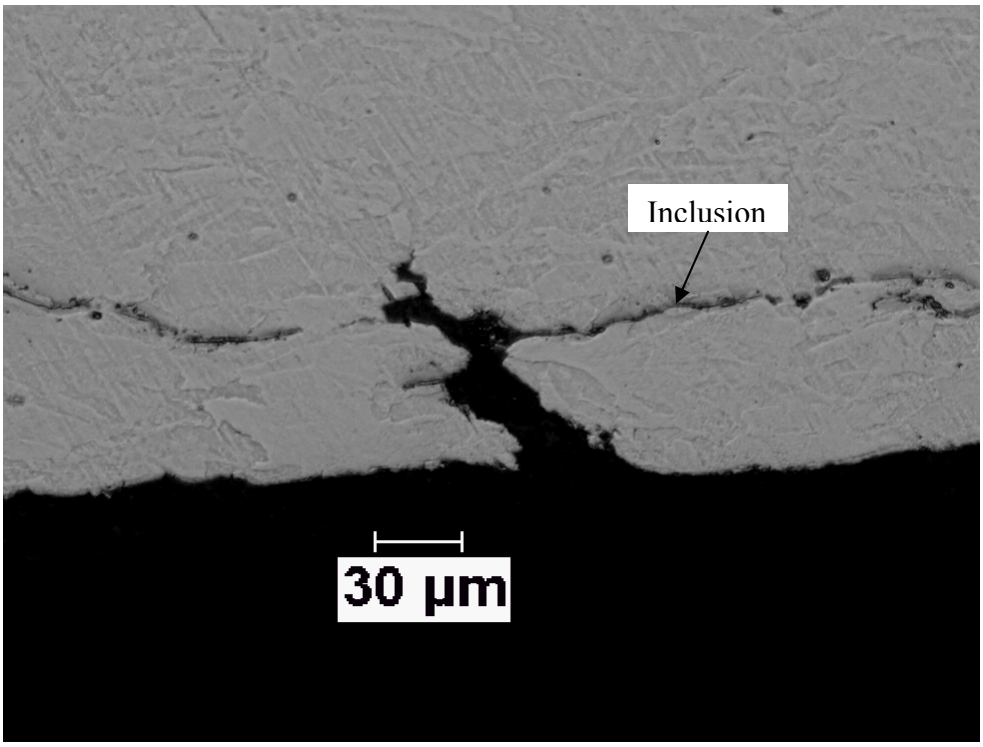

Figure 81 - Crack morphology of pipeline steel strained in NS4 solution with 5% CO_2 at room temperature and OCP

5.6.5 - Role of Groundwater Constituents on TGSCC Environment Stability

Role of groundwater constituents on TGSCC was not clear. One postulation was that the some constituents may help with stability of buffer solution and help maintain pH in the cracking range where NNPHG mechanism may operate. To study this, surface pH experiments were performed in bicarbonate solutions with individual components of NS4 added to the solution. Results are given in Figure 82. It can be seen that the simple bicarbonate solutions had the lowest surface pH. The calcium chloride addition is not significantly change the behavior of simple bicarbonate solutions. However, addition of calcium may help with NNPHG mechanism by providing metal cations to react with the carbonic acid and bicarbonates to produce extra hydrogen. Additions of magnesium

sulfate and potassium chloride increase the pH slightly but still within near-neutral conditions. Results indicate that magnesium and potassium ions do not contribute to the NNPHG mechanism. NS4 solution has the highest pH of the tested solutions which may be due to the presence of the magnesium and potassium ions.

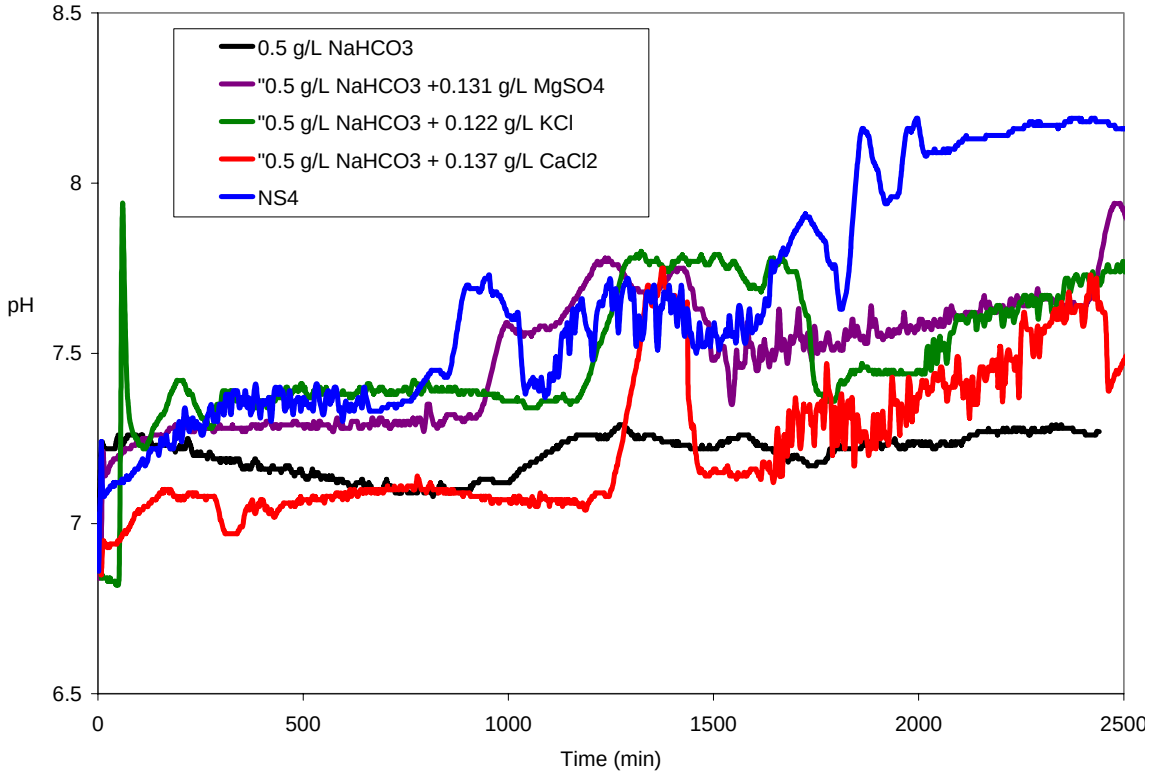

Figure 82 - Surface pH measurement with time for solution components of TGSCC environments

5.6.6 - Effect of Temperature on TGSCC of Pipeline Steel

Initial TGSCC failures were reported from Canadian pipelines and were associated with the cold climate. However, TGSCC failures have now been reported on the pipelines in warm climates as well. Thermodynamic calculations indicate that the

reaction of carbon dioxide dissolving in the pure water to form carbonic acid is possible in temperatures between ~15 to 35^{o}C. To check the effect of temperature on the solution stability and reaction kinetics, tests were done at different test temperatures. The effect of temperature can be clearly seen in the time required for the pH to increase when cathodic protection is applied in the coupon exposure tests as shown by the results in Figures 69-71. When the test environment was at 35^{o}C, there was a rapid increase in the pH once the CO_2 bubbling was stopped. For the tests run under open circuit conditions, it took approximately 2460 minutes (41 hours) to reach the equilibrium pH value at 35^{o}C. However, at 15^{o}C under OCP conditions equilibrium could not be achieved till the end of the test which was 19800 minutes (330 hours) in duration. This indicates that, as expected, the reactions involved are slow at lower temperatures within the range where carbonic acid formation is thermodynamically stable.

Corrosion potentials for pipeline steels at different temperatures, shown in Figures 83 and 84, have very similar values. Anodic polarization behavior, as shown in Figures 83 and 84, were generally very similar at different temperatures for the tested solutions in this study. However, the current densities for the cathodic region were higher at the higher temperature for a given applied potential compared to the lower test temperatures. This indicates that the difference in cathodic behavior is an increase in kinetics rather than a different mechanism.

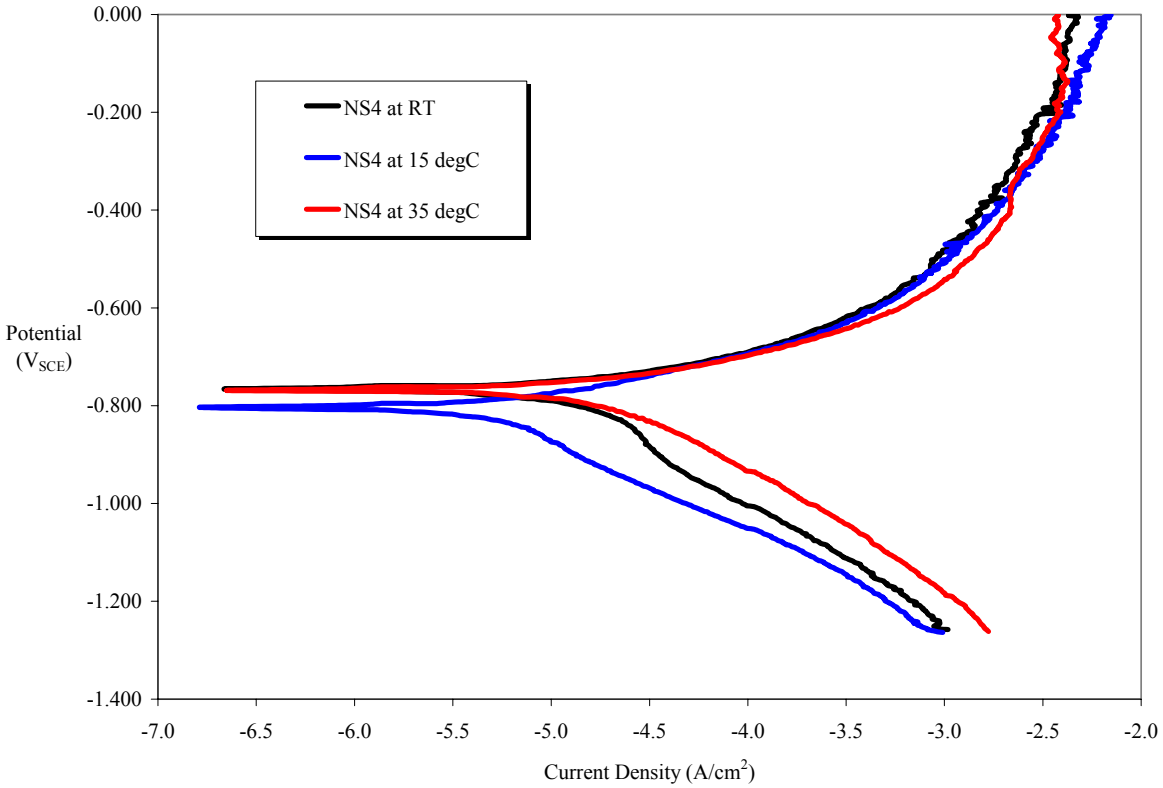

Figure 83 - Potentiodynamic results for NS4 solutions with 5% CO_2 at different temperatures

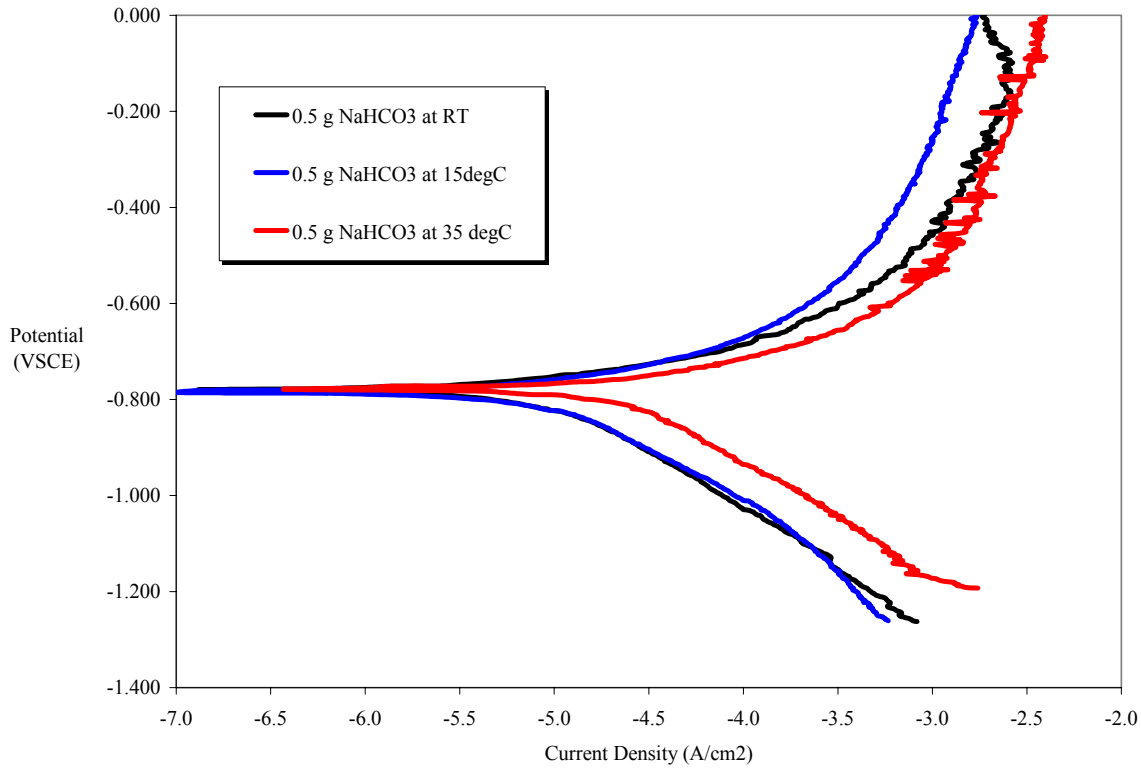

Figure 84 -Potentiodynamic results for simple bicarbonate solutions with 5% CO_2 at different

Slow strain rate tests were performed to examine the effect of temperature. It was determined that the crack morphology in groundwater solutions were similar at all tested temperatures. However, crack wall sides appeared to have more dissolution at 25°C compared to 15°C. Crack density also was higher at higher temperatures.

5.6.7 – Mix Mode Cracking on Pipeline Steel in SCC Cracking Environments

Slow strain rate tests were performed to determine if the IGSCC and TGSCC could form on the same test samples or if the transition between IGSCC to TGSCC could be observed. Samples were initially exposed to IGSCC environments and strained to 85% yield strength and held for 5 days. The environment was then shifted to TGSCC conditions.

It was determined that crack density significantly increased with environmental shift. Crack density ranged from 1.3 to 3.8 cracks/mm for samples with shifting environments. This is compared to a crack density of around 1 for TGSCC environments and a crack density of 17 for IGSCC environments. Crack density values do not reflect the large amount of pits formed on the sample. Pits are thought to form due to the breakdown of the magnetite film when exposed to the TGSCC environment. Example of pits formed is given in Figure 85. Pits and cracks formed along the whole gauge of the sample. This is different from the simple TGSCC environments where the cracks only formed at the neck transition region or at near the fracture surface. This supports the theory that pits can act as a stress concentrators to assist in TGSCC initiation. This is supported by the formation of a sharp tip, possibly the beginning of a crack, at the bottom of the pit shown in Figure 85.

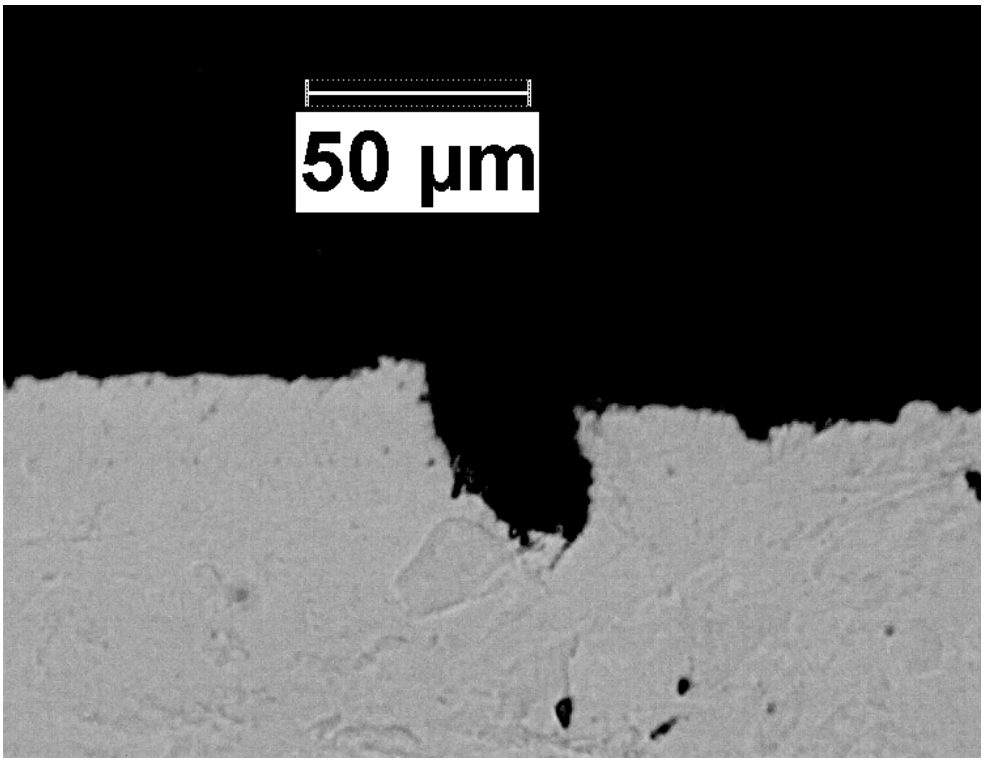

Figure 85 - Pit formed on X-65 pipeline steel exposed to shift between IGSCC and TGSCC environments. Note the formation of what appears to be a crack tip at the bottom of the pit.

To further study the initiation method for these interrupted tests, the sample surface was examined after the sample was subjected to IGSCC environment exposure and held at 85% yield strength for 5 days. After the 5 day exposure, the sample had a uniform blue-black magnetite film. Examination by SEM showed the film had ruptured in 4 locations under applied load, and representative rupture morphology is given in Figure 86. The sample was then placed in TGSCC environment and held at 85% yield strength. After 3 days of exposure the sample surface had significant amount of pits and localized deformation as shown in Figures 87. Figure 88 demonstrates that the previous location of film rupture continued to act as a defect that may contribute to TGSCC.

.

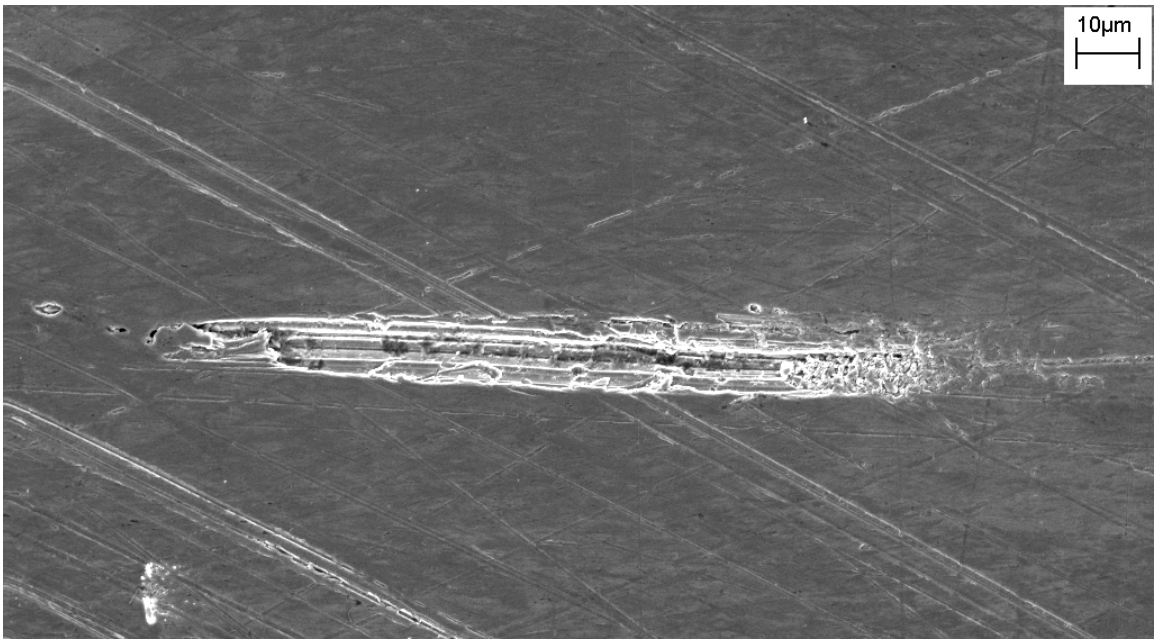

Figure 86 - Rupture of magnetite film formed when X-65 pipeline sample is exposed to 1N $NaHCO_3$ with 1N Na_2CO_3 at 70°C and -650 mV and held at 85% yield strength for 5 days

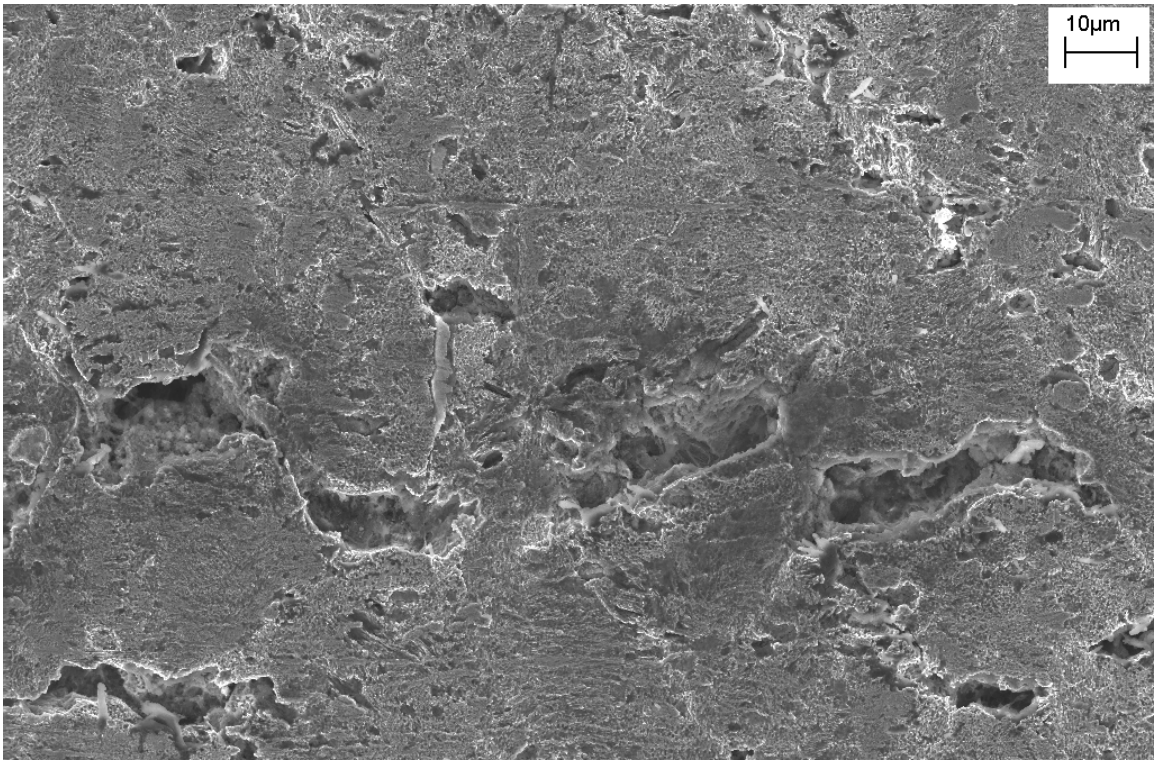

Figure 87 - General sample surface morphology of sample once environment has been shifted from IGSCC conditions to TGSCC conditions

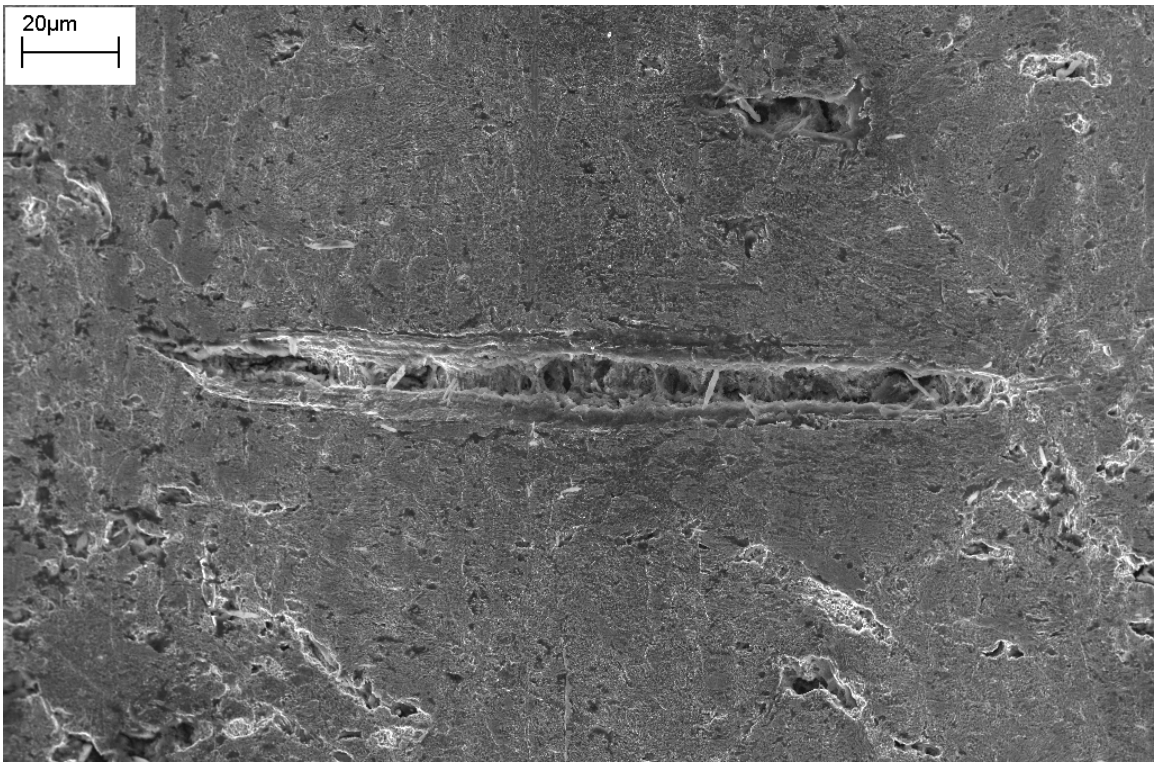

Figure 88 - Development of previous film rupture in TGSCC environment

Cracks that formed on these transition tests were primarily transgranular although there were a few cracks that also appeared to be intergranular. It was difficult to determine the nature of the crack path after exposure to the near-neutral solution as dissolution occurred on the crack walls. An example of an IGSCC crack is given in Figure 89. Although the crack sides show evidence of dissolution and are smooth, the crack is bordered by white ferrite grain and a dark pearlite grain. TGSCC crack morphology shown in Figure 90 was consistent with that found in field failures and a majority of the cracks did display a sharp tip.

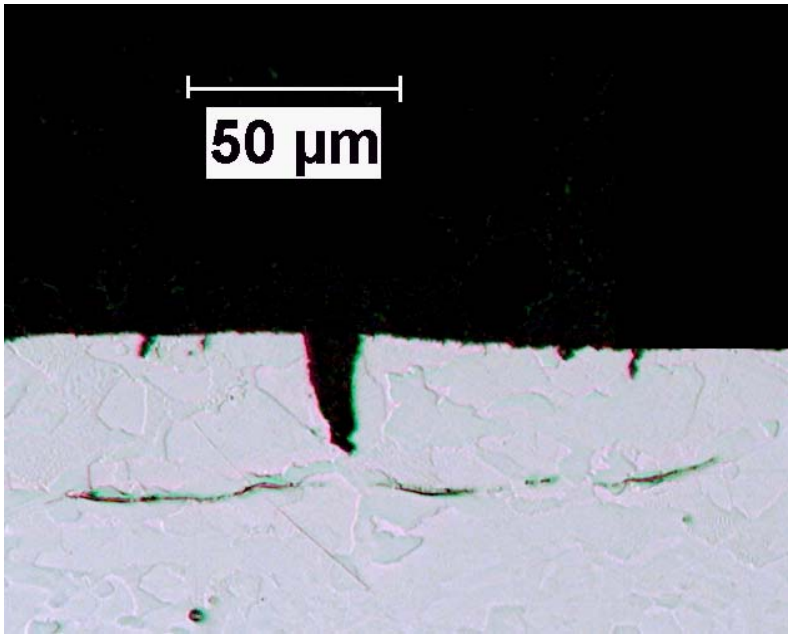

Figure 89 - Crack formed on pipeline sample exposed to shift between IGSCC and TGSCC environments. The crack appears to be IGSCC and is bordered by two distinct grains.

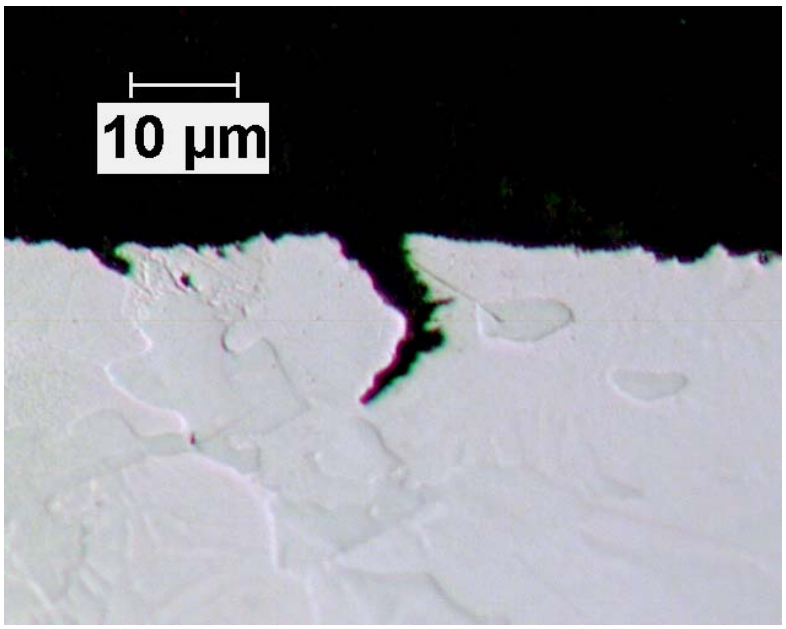

Figure 90 - TGSCC crack formed on pipeline steel exposed to shifts between IGSCC and TGSCC environments. Note the crack propagates through the light ferrite grain.

Subsequently, SEM was used to examine the sample and identify crack morphology. The transition from IGSCC to TGSCC was observed and shown in Figure 91. As seen in this image, the initial short crack progressed between the ferrite and the pearlite grain. The crack path then splits. The dominant crack path progresses into the ferrite grain, where hydrogen most likely accumulates during near-neutral pH solution exposure. The minor crack path continues to outline the pearlite grain. This splitting point seems to be the point when the environment shifts. This behavior could only be observed on microstructurally short cracks because larger cracks experienced significant dissolution that masked initial crack path.

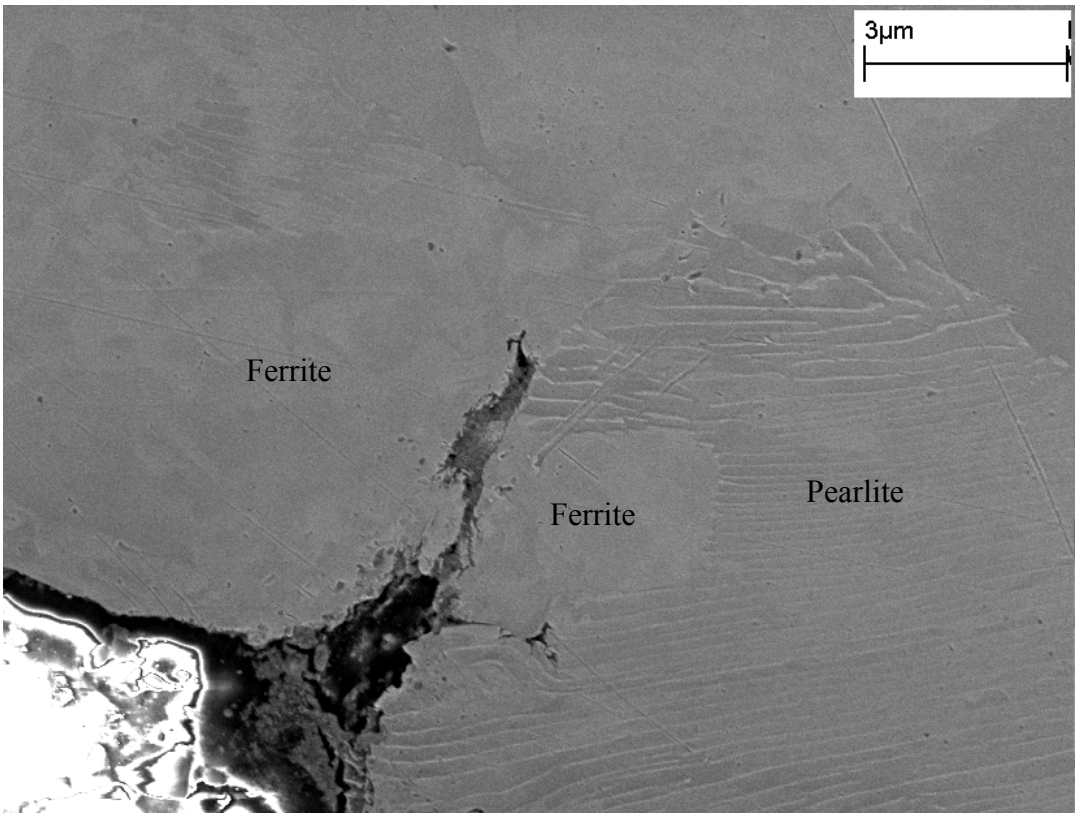

Figure 91 - Crack formed on pipeline sample exposed to shift between IGSCC and TGSCC environments. The crack initially is intergranular, progressing between pearlite and ferrite grains. Crack path then becomes to be transgranular as it cuts though ferrite grain.

On this sample presence of both IGSCC and TGSCC cracks were detected. This is significant as mix mode cracking has yet to be reproduced in laboratory environment using shifting environmental conditions. An example of formed IGSCC crack is given in Figure 92. The crack path clearly follows the boundary of the pearlite-ferrite grain. On this same sample, the TGSCC crack shown in Figure 92 was also observed only 20 microns from the crack shown in Figure 91.

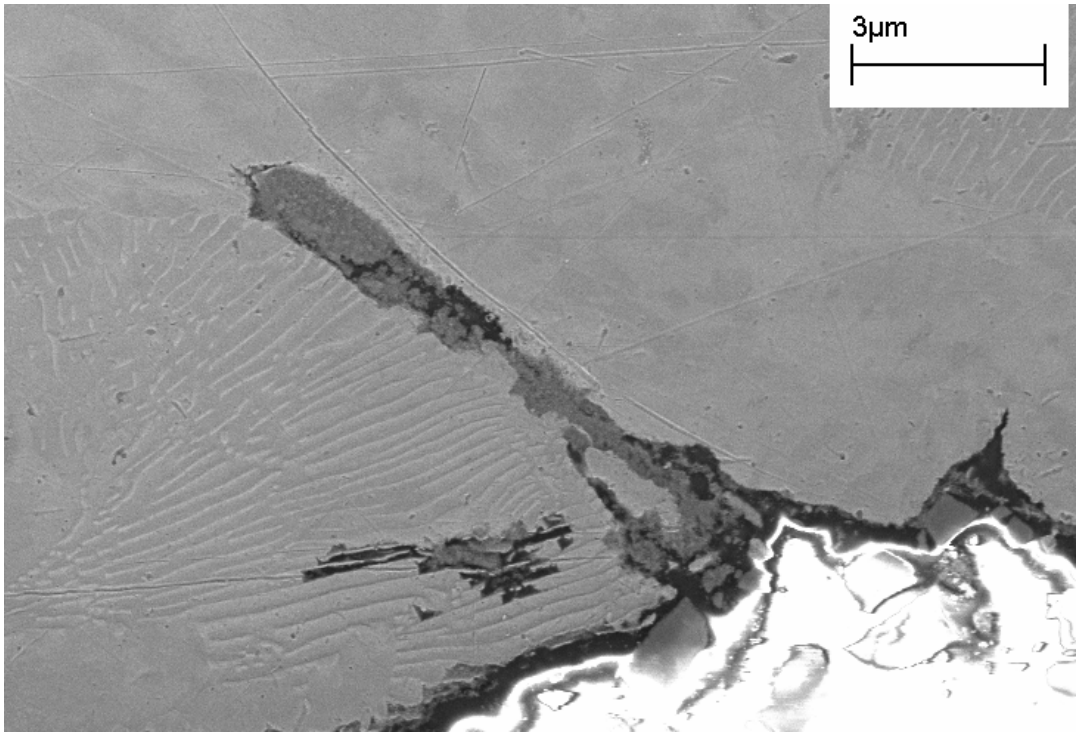

Figure 92 - Intergranular Stress Corrosion Crack formed on slow strain rate sample subjected to shifting environmental conditions

These results explain why IGSCC and TGSCC may be seen on the same piece of pipeline in field. Solution shift may occur due to various reasons but most important are the shifts in season and availability of cathodic current at the pipeline surface, which may also change with the season due to changes in the soil resistance. Solution concentration

may increase in the trapped solutions due to evaporation of water while the dilution may occur during rainy seasons.

5.6.8 - Summary:

Present series of tests were done to understand the conditions at the pipeline surface to maintain the environmental conditions conducive to cause TGSCC. It was clear that the carbon dioxide supply is an important requirement to maintain solution pH in the desired near-neutral pH range. Amount of the carbon dioxide required will also depend upon the applied cathodic current on the pipeline surface, which induces catholic reactions that increase the solution pH by production of hydroxyl ions in the presence of oxygen or may consume H^+ ions in the solution. Under open circuit potential, when cathodic protection is not available to the pipeline, NNPHG mechanism reactions may contribute to produce hydrogen by the reaction of bicarbonate ions and carbonic acid with the metal cations like Fe^{+2} or Ca^{+2} in the solution. In presence of significant applied potential, the pH of the solution will move to higher pH region and the conditions for IGSCC mechanisms may be induced on the pipeline surface rather than the TGSCC. This may also explain how the two conditions are related and may cause both IGSCC and TGSCC on the same section of pipelines under different environments, depending upon the season, reliability of cathodic protection, and the trapped water compositions.

CHAPTER 6

CONCLUSIONS

In near-neutral pH environments, hydrogen may be generated along with the formation of $FeCO_3$ by the reaction of metal ions with bicarbonate ions and carbonic acid in solutions. These reactions occur without changing the bulk pH of the solution, thereby maintaining the pH of the solution in the near-neutral pH region. This NNPHG mechanism can increase the available hydrogen for diffusion into the pipeline steel that may participate in the TGSCC mechanism for pipeline steels under near-neutral pH conditions.

TGSCC of pipeline steels can occur in a wider range of environments. It was determined that near-neutral conditions are possible in simple groundwater solutions containing bicarbonate ions and carbon dioxide. pH of these solution is predominantly determined by the relative ratios of the carbonic acid and bicarbonate ions. Other groundwater constituents did not have a significant role in the mechanism of TGSCC or enhance the susceptibility of the pipeline to TGSCC. Subsequently, higher solution concentrations of bicarbonate require higher concentrations of CO_2 exposure. It was also determined that TGSCC can occur in a range of temperatures from ~15^{o}C to ~35^{o}C. The potential regime of TGSCC and the NNPHG mechanism is limited to the potentials where $FeCO_3$ is the thermodynamically favored corrosion product. However, application of cathodic potential will increase the surface pH at the pipeline steel and prohibit the NNPHG mechanism.

In examining the pipeline steel susceptibility to hydrogen produced TGSCC, the role of microstructure on hydrogen ingress and accumulation was examined. Microstructural characterizations of pipeline steel coupled with hydrogen permeation tests indicate that the level of lattice strain in the microstructure has the most influence on hydrogen diffusivity. Hydrogen diffuses though the steel by lattice diffusion and disperses evenly amongst pearlite and ferrite grains. Hydrogen accumulation occurs at high energy discontinuous interfaces such as inclusion or precipitate interfaces. Normalized samples proved to be less susceptible to TGSCC. This is attributed to the lower amount of hydrogen trap sites and less hydrogen accumulation in the relaxed steel structure.

In studying the mechanism of TGSCC crack initiation it was determined that TGSCC cracks produced by SSRT were found primarily at sites of stress concentration either at transition of necking or near the fracture surface. Stress concentration is required to facilitate sufficient hydrogen accumulation in the pipeline steel in order to produce TGSCC and quasicleavage fracture surface. It was determined that stress concentrations on X-65 pipeline steels develop from localized corrosion attack at inclusions exposed to the pipeline surface. At stresses below yield strength, crack initiation was observed to emanate from these formed pits.

Crack propagation was determined to occur by the formation of microcracks ahead of the main crack tip. These microcracks provide further evidence of the hydrogen embrittlement mechanism, as hydrogen diffuses into the steel and accumulates to form a microcrack 10-12 microns below the exposed surface. Morphology of these microcracks indicates that cracks propagate by the coalescence of microcracks with the main crack tip.

Due to applied stress, the microcrack will propagate towards the surface of the pipeline. This propagation can be ductile tearing or cleavage depending on the amount of hydrogen embrittlement between the two features. This crack propagation creates fresh surface that experience anodic dissolution and further hydrogen generation. This process repeats forming several TGSCC cracks in a dense patch on the exposed pipeline surface. Ultimate failure occurs due to coalescence of smaller cracks to form one dominate crack.

CHAPTER 7

IMPACT OF RESERACH

This work has significant impact in understanding TGSCC mechanism in near-neutral pH environments on pipeline steel. No prior work has been able to predict the environment regime of this cracking process and account for production of hydrogen in a buffered neutral pH solution. By understanding the environment that generates this mode of failure, prohibitive steps can be implements to reduce to the number of TGSCC occurrences.

This work also provides an explanation on the method of TGSCC crack initiation. It was determined that inclusions are the primary site for pit production. Subsequently, future pipeline steel design and manufacturing should consider the amount and morphology of inclusions at the surface of the steel. Special attentions should be paid to inclusion content that is exposed to the external surface of the pipeline.

This work has also contributed to understanding the effect of heat treatment and resulting microstructure on hydrogen ingress and resulting hydrogen embrittlement. It was determined that lattice strain directly influences the hydrogen trapping, with higher strained structures having a higher concentration of trapped or retained hydrogen. Therefore, microstructures on pipeline structures should be at a maximum relaxed microstructure while still maintaining desired mechanical properties. Steel microstructures that have a low diffusivity and solubility would be the least susceptible to TGSCC and should be considered for further application in pipeline construction. For example, work in this study has shown that normalized steel has significantly less

susceptibility to TGSCC. Low temperature, short tempering time martensitic steel has shown to very low hydrogen solubility and should be considered for use in high risk areas where cathodic protection is known to be intermediately applied.

This research also indicates that hydrogen will accumulate in high stress regions and around microstructural features that contain high energy interfaces such as inclusions. Subsequently, welding procedures on pipelines should be modified to ensure that such microstructural features are avoided and residual tensile stresses are minimized.

By understanding the environment that creates TGSCC on pipeline steel, new inspection techniques can be developed to facilitate pipeline companies in ensuring pipeline integrity. There is extreme difficulty in detecting flaw on the outer surface of the pipeline as the pipeline is typically buried 5-20 feet below the surface. Further, inspection equipment is designed to travel though the inside of the pipeline. As hydrogen is the main cause of TGSCC, *in situ* measurements of toughness and other mechanical properties can be performed on the inside of the pipeline to determined if there is a degradation of mechanical properties associated with hydrogen embrittlement. Further, knowledge of the cracking process can facilitate lifetime predictions of pipeline known to have cathodic protection failure.

Additionally, as hydrogen is known to be the source of damage, coating could be applied that are imbedded with hydrogen inhibitors that decrease the probability of forming molecular hydrogen. Specific polar organic compounds such as sulphoxides or hydroxyl amino acids that have proven to have an inhibitive effect on hydrogen ingress in steels [70].

Finally, this work has contributed to the general understanding of how hydrogen interacts with pipeline steel. This knowledge is vitally important as the existing pipeline infrastructure is being considered for the transportation of hydrogen in a potential hydrogen fuel economy.

CHAPTER 7

FUTURE WORK

This work has made significant strides in furthering the understanding of TGSCC on pipeline steels and asserting a new mechanism of hydrogen generation in carbon dioxide environment. However, further work could still be performed to extend the understanding of pipeline TGSCC.

Measurement of hydrogen generation in near-neutral solutions has been made in this work by the indirect measurement of carbonates. It would be useful to support this study by directly measuring hydrogen by other means. This could be accomplished by secondary ion mass spectroscopy (SIMS) of the sample post exposure to determine the amount of hydrogen absorbed into the pipeline steel. This could also assist in learning where the hydrogen accumulates ahead of stress concentrations in a manner similar to work done by Gu et al. [89]. SIMS may also be implemented to understand where hydrogen accumulates in reference to microstructural features if prior knowledge of microstructure is obtained prior to exposure and analysis.

To understand the mechanism of hydrogen embrittlement of pipeline steels in near-neutral pH environment, work could be furthered by refining the understanding of crack propagation. Cyclic tests with compact tensile samples in simple bicarbonate solutions could be performed. Microscopic examination coupled with cyclic loading, and imaging the sample throughout the test could confirm the proposed method of microcrack formation ahead of the crack tip. This testing procedure could also confirm the proposed method of propagation of microcrack coalescence with the major crack tip.

Microprinting could also be implemented on the fractured compact tensile sample to observe and quantify the amount of hydrogen that diffuses ahead of the crack tip. This could provide direct insight to the mechanism of hydrogen accumulation ahead of the crack tip.

Microprinting could also be performed on simple bicarbonate solutions rather than forcing hydrogen into the sample with charging conditions. It has been determined that stress conditions are required in order to observe hydrogen effects on pipeline steels. Samples should be loaded to different strain percentages to determine the effect of strain on hydrogen diffusivity. These loaded samples could be microprinted to confirm the increase in hydrogen concentration with increase in straining.

This work was accomplished using only X-65 pipeline steel. Future work on TGSCC in near-neutral conditions should explore other pipeline grades. Specifically, the effect of alloying elements on hydrogen diffusion and accumulation should be studied with hydrogen permeation and microprinting.

The effect of microstructure could also be further explored by performing SSRT with different heat treatments such as those used in this work. This would confirm the assertion that hydrogen accumulation in the pipeline is directly related to the susceptibility to TGSCC.

The effect of inclusion addition should also be explored. As it has been determined that inclusions are sites of hydrogen accumulation and crack initiation, a reduction in the inclusion content should decrease the susceptibility of TGSCC. Samples with varying inclusion content could be tested with SSRT and hydrogen permeation to confirm the effect of inclusion content on TGSCC.

APPENDIX A

XRD SPECTRA

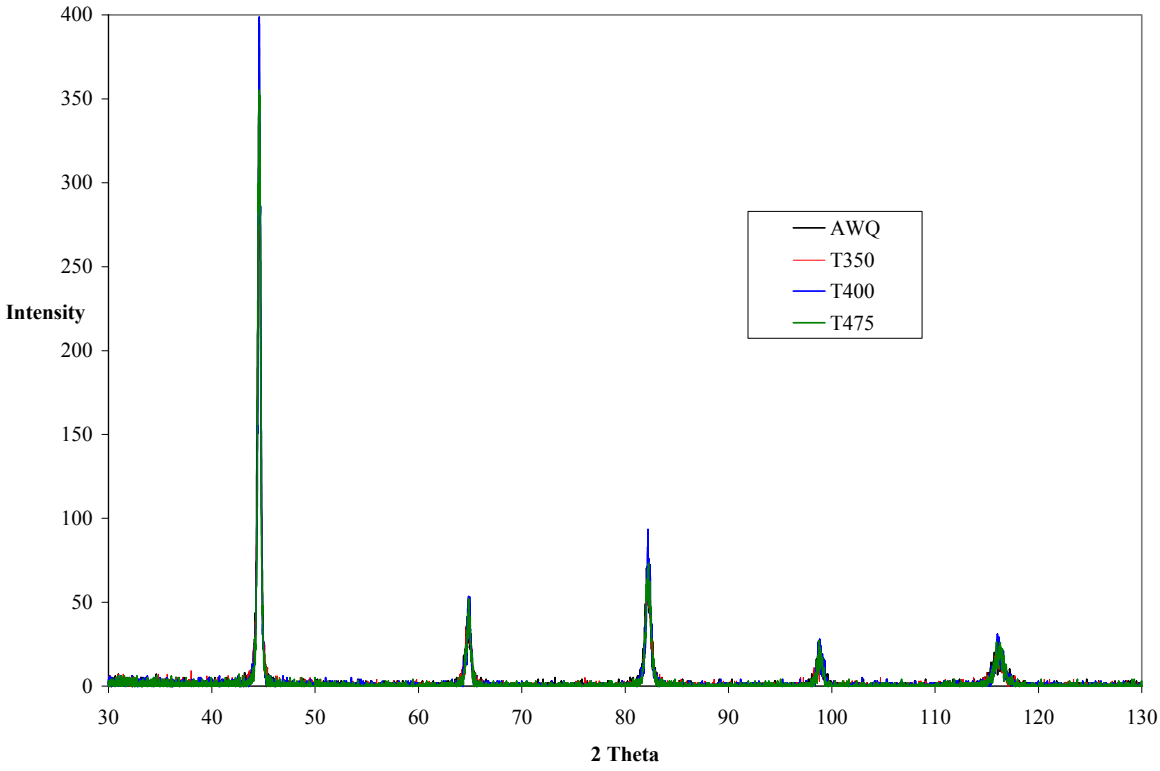

Figure 93 - Comparison of spectra for all quenched pipeline microstructures

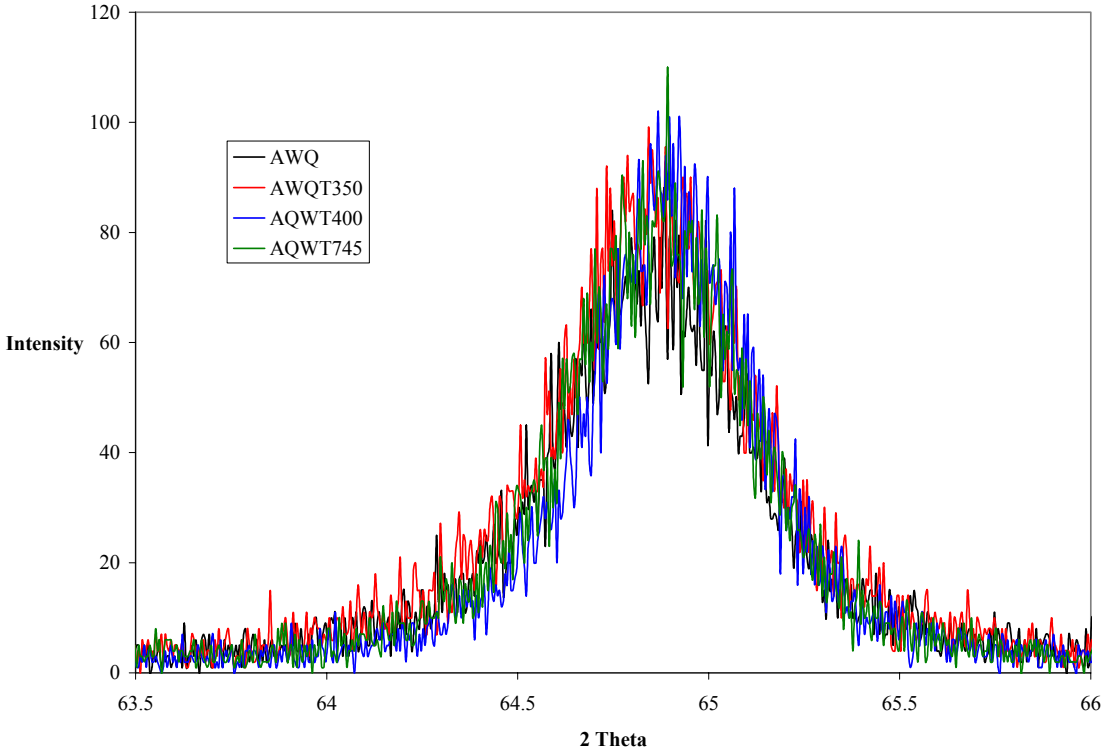

Figure 94 - Spectra from 64 2Theta peak for water quenched pipeline microstructure

Table 30 - XRD results for the 98 2Theta peaks for samples with differing tempering temperatures

Sample	Peak	2 Theta	d spacing (Å)	Intensity	FWHM	% Area
AWQ	1	98.932	1.0135	39.7	0.657	100.0
T350	1	98.734	1.015	24.4	0.441	100.0
	2	98.941	1.0134	17.2	0.481	66.3
T400	1	98.849	1.0141	41.5	0.372	100.0
	2	99.097	1.0123	24.3	0.321	49.6
T475	1	98.802	1.0145	30.3	0.494	100.0
	2	99.081	1.0124	11.1	0.338	19.2

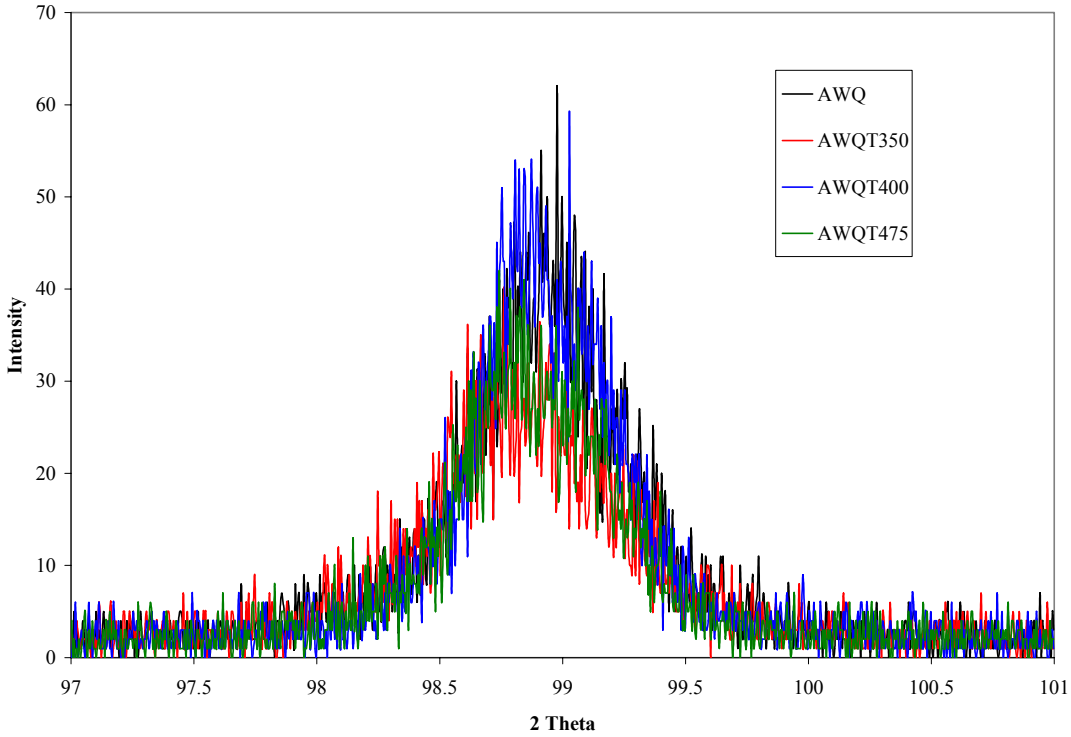

Figure 95 -Spectra from 98 2Theta peak for water quenched pipeline microstructure

APPENDIX B

HYDROGEN PREMEATION DATA

Table 31 - All Permeation Data from Hydrogen Permeation Testing

Heat Treatment	Diffusion Rate (m^2/s)	Permeation Current Density (A/cm^2)	Steady State Flux (mol/cm^2s)	Solubility (mol/m^3)
As Received	3.040E-10	1.63E-07	1.69E-12	1.61E-09
	2.960E-10	2.90E-07	3.00E-12	2.89E-09
	2.281E-10	1.81E-07	1.88E-12	2.38E-09
AVERAGE	2.761E-10	2.01E-07	2.09E-12	1.98E-09
Standard Deviation	4.168E-11	5.94E-08	6.15E-13	8.27E-10
Normalized	5.056E-10	3.85E-07	3.99E-12	2.15E-09
	4.286E-10	4.00E-07	4.15E-12	2.61E-09
	4.870E-10	4.68E-07	4.85E-12	2.71E-09
AVERAGE	4.737E-10	3.79E-07	3.93E-12	2.12E-09
Standard Deviation	4.016E-11	8.49E-08	8.80E-13	7.83E-10
Annealed Water Quenched	1.259E-10	2.52E-07	2.61E-12	5.68E-09
	1.478E-10	2.17E-07	2.25E-12	4.18E-09
	1.296E-10	2.00E-07	2.07E-12	4.32E-09
	1.302E-10	2.47E-07	2.56E-12	5.31E-09
AVERAGE	1.334E-10	2.29E-07	2.37E-12	4.87E-09
Standard Deviation	9.809E-12	2.48E-08	2.57E-13	7.38E-10
AWQ Temper 350	1.867E-10	7.25E-08	7.51E-13	1.14E-09
	1.818E-10	2.20E-07	2.28E-12	3.30E-09
	1.979E-10	3.24E-07	3.36E-12	4.41E-09
	1.895E-10	2.90E-07	3.01E-12	4.14E-09
AVERAGE	1.890E-10	2.27E-07	2.35E-12	3.25E-09
Standard Deviation	6.733E-12	1.11E-07	1.16E-12	1.48E-09
AWQ Temper 400	2.127E-10	1.50E-07	1.55E-12	2.11E-09
	2.180E-10	1.96E-07	2.03E-12	2.55E-09
AVERAGE	2.153E-10	1.73E-07	1.79E-12	2.33E-09
Standard Deviation	3.757E-12	3.25E-08	3.37E-13	3.17E-10

Table 32 - Continuation of All Permeation Data

Heat Treatment	Diffusion Rate (m^2/s)	Permeation Current Density (A/cm^2)	Steady State Flux (mol/cm^2s)	Solubility (mol/m^3)
AWQ Temper 475	2.565E-10 2.472E-10	2.02E-07 1.60E-07	2.09E-12 1.66E-12	2.24E-09 1.82E-09
AVERAGE	2.519E-10	1.81E-07	1.88E-12	2.03E-09
Standard Deviation	6.583E-12	2.97E-08	3.08E-13	3.02E-10
AWQ T650 1 hour	5.558E-10 5.441E-10	3.53E-07 3.21E-07	3.66E-12 3.33E-12	1.81E-09 1.72E-09
AVERAGE	5.500E-10	3.37E-07	3.49E-12	1.76E-09
Standard Deviation	8.310E-12	2.26E-08	2.35E-13	6.49E-11
AWQ T650 1 day	5.131E-10 5.012E-10	4.07E-07 2.20E-07	4.22E-12 2.28E-12	2.26E-09 1.26E-09
AVERAGE	5.071E-10	3.14E-07	3.25E-12	1.76E-09
Standard Deviation	8.398E-12	1.32E-07	1.37E-12	7.04E-10
AWQ T650 1 week	5.497E-10 5.379E-10 5.558E-10	2.26E-07 2.55E-07 2.40E-07	2.34E-12 2.64E-12 2.49E-12	1.18E-09 1.35E-09 1.27E-09
AVERAGE	5.478E-10	2.40E-07	2.49E-12	1.27E-09
Standard Deviation	9.081E-12	1.45E-08	1.50E-13	8.33E-11

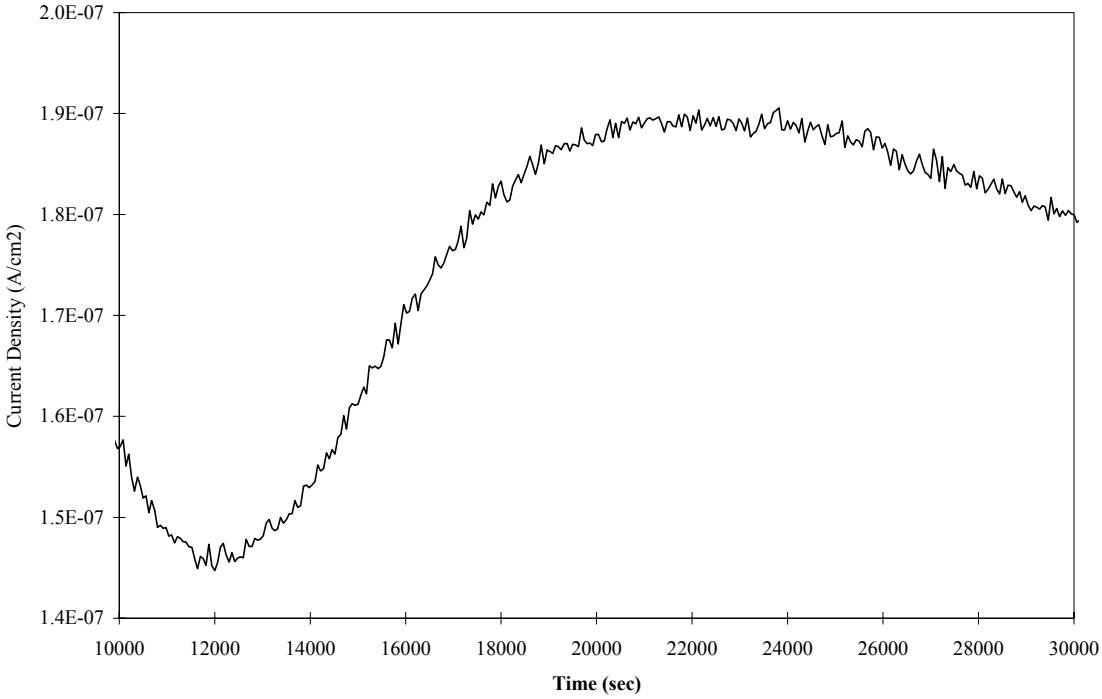

Figure 96 - Representative permeation curve for as-received pipeline steel

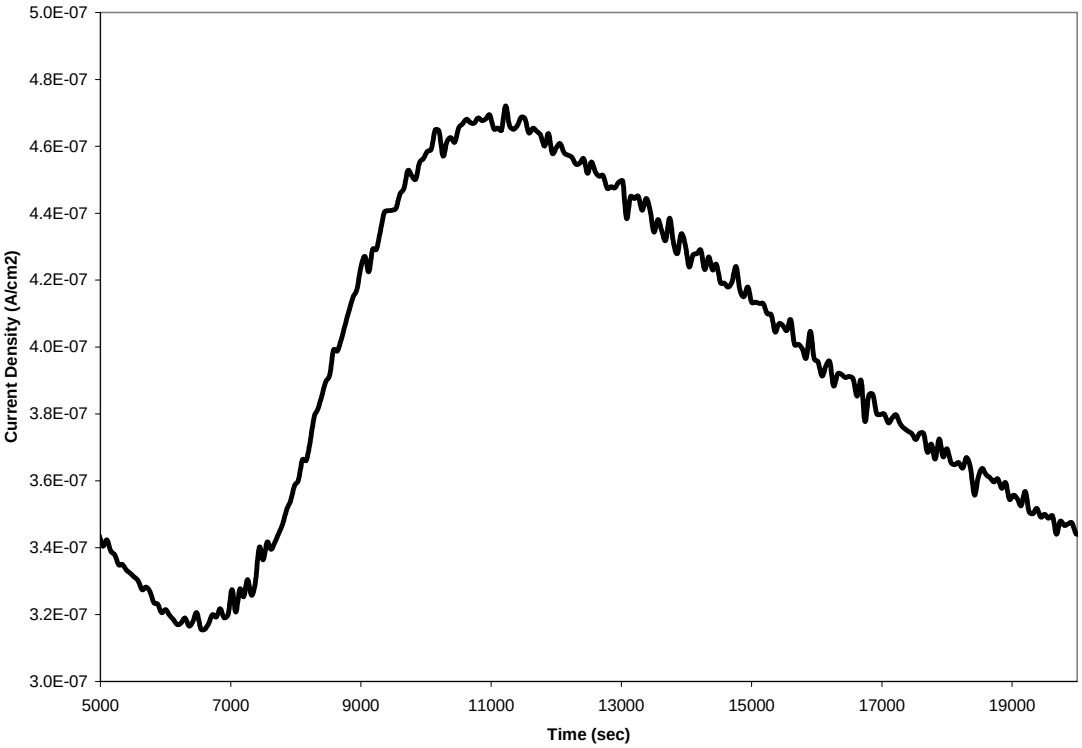

Figure 97 - Representative permeation curve for normalized pipeline steel

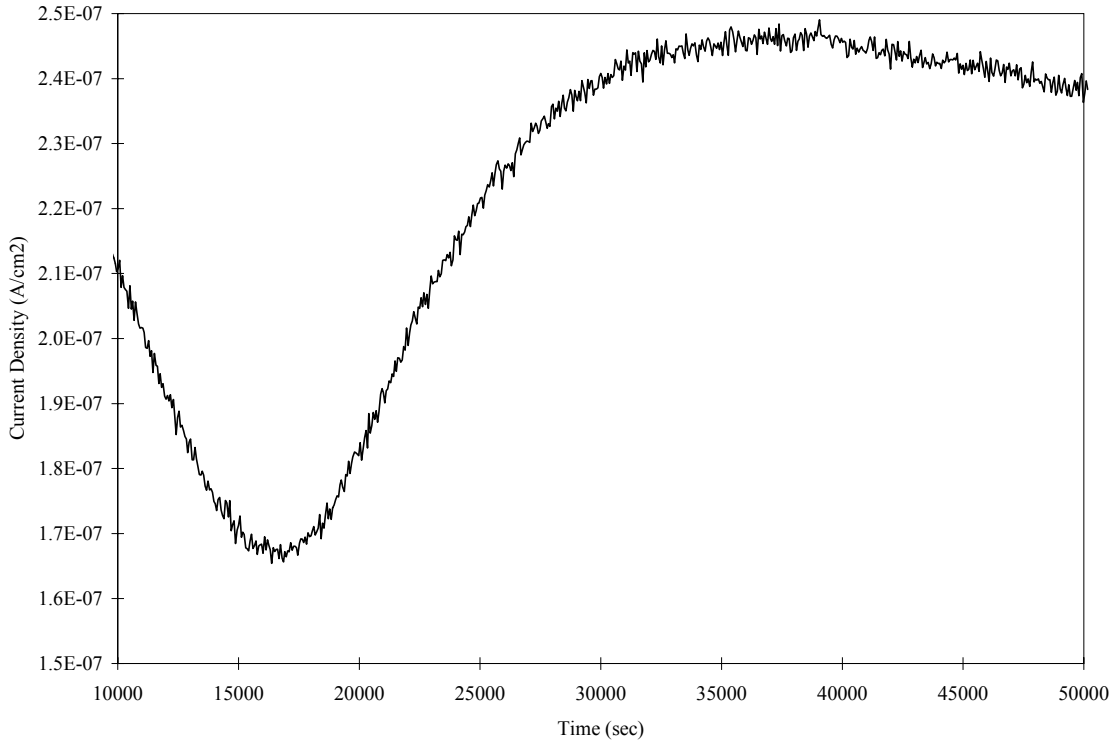

Figure 98 - Representative permeation curve for Annealed Water Quenched pipeline steel

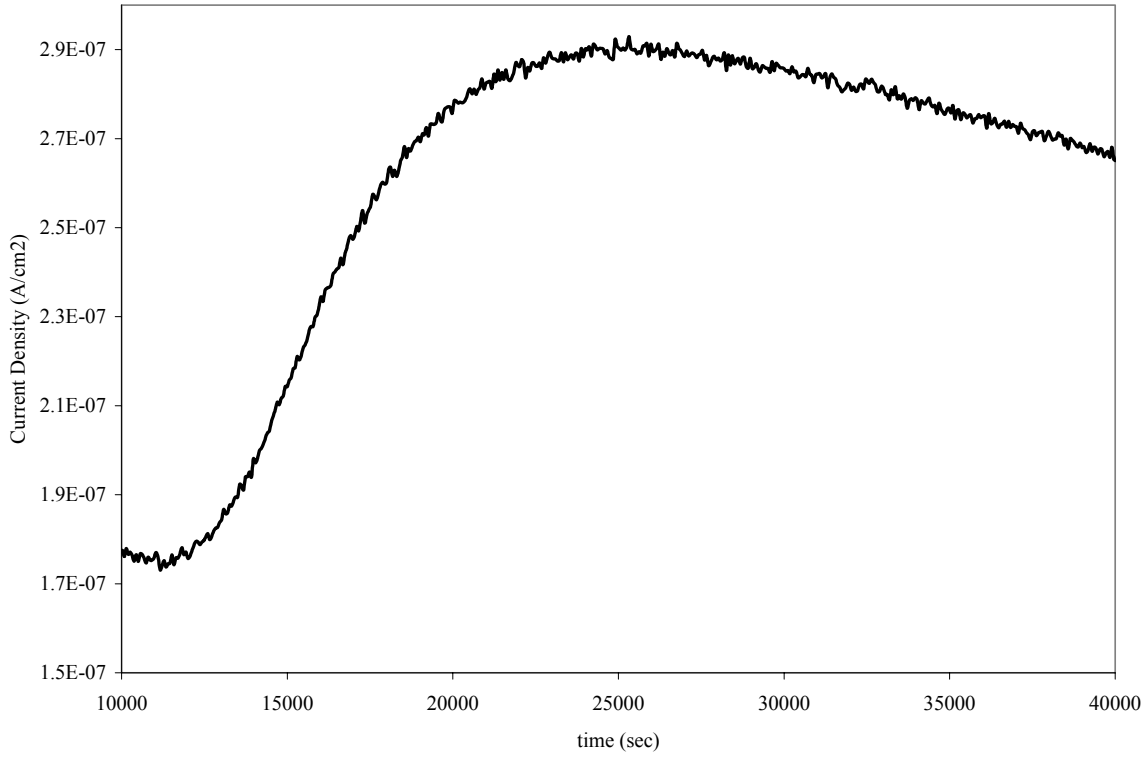

Figure 99 – Representative hydrogen permeation curve for Tempered 350^{o}C pipeline steel microstructure

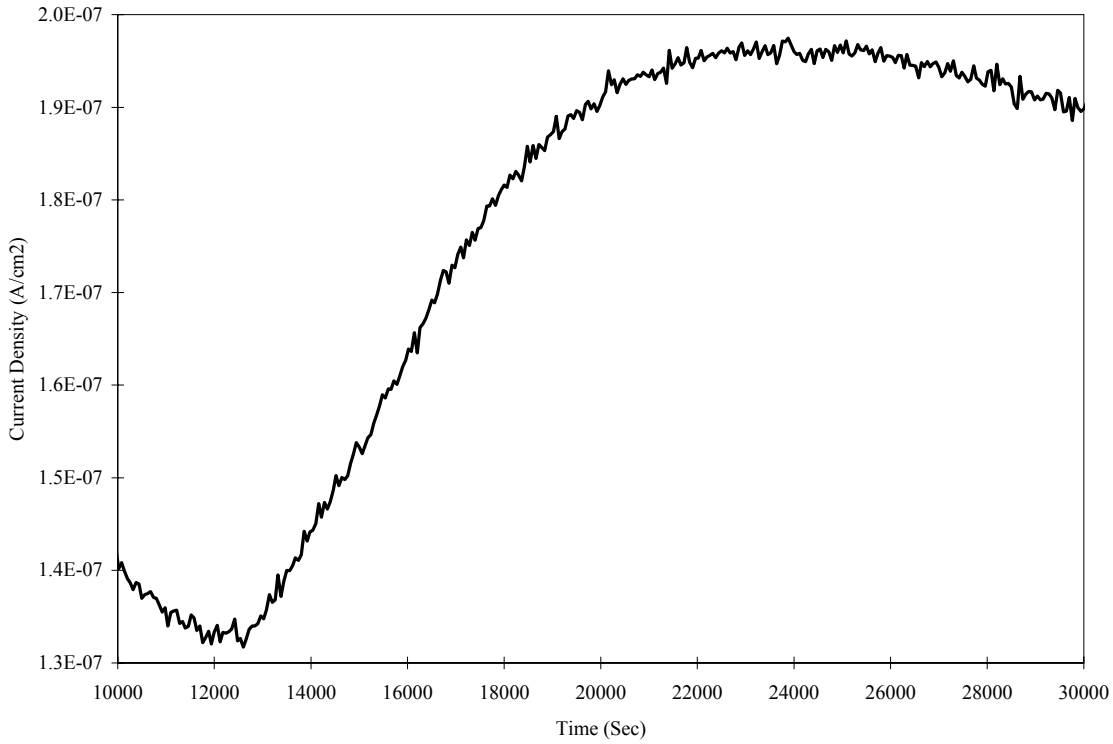

Figure 100 - Representative hydrogen permeation curve for Tempered 400^{o}C pipeline steel microstructure

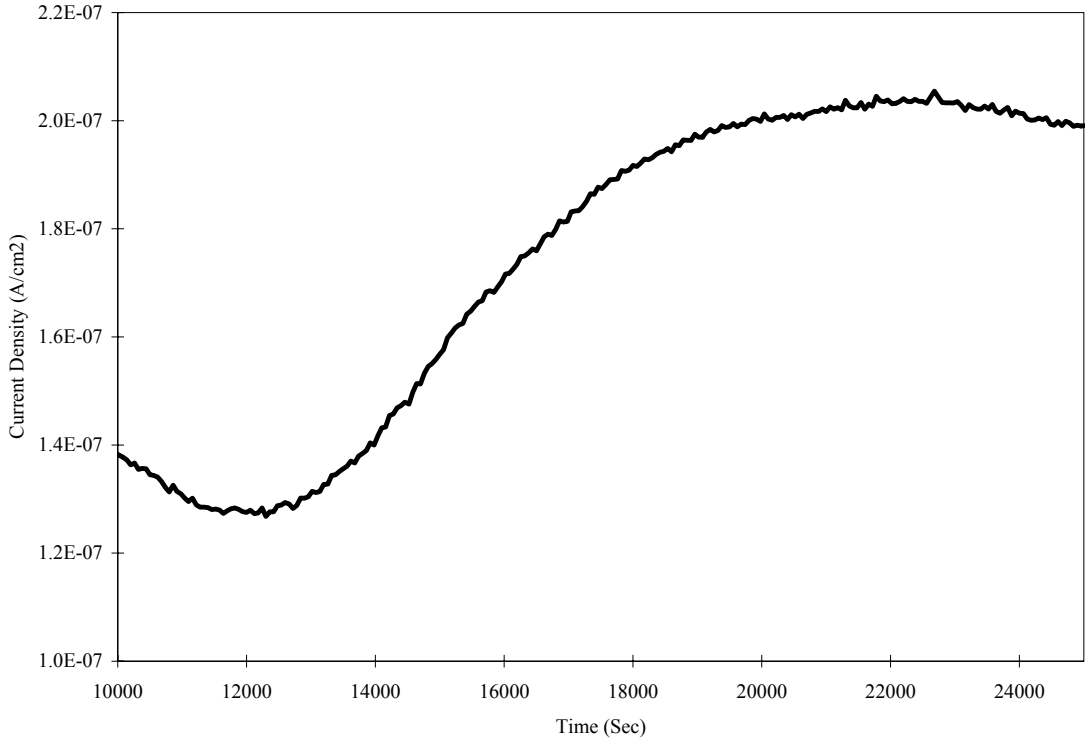

Figure 101 - Representative permeation curve for Temper 475^{o}C pipeline steel microstructure

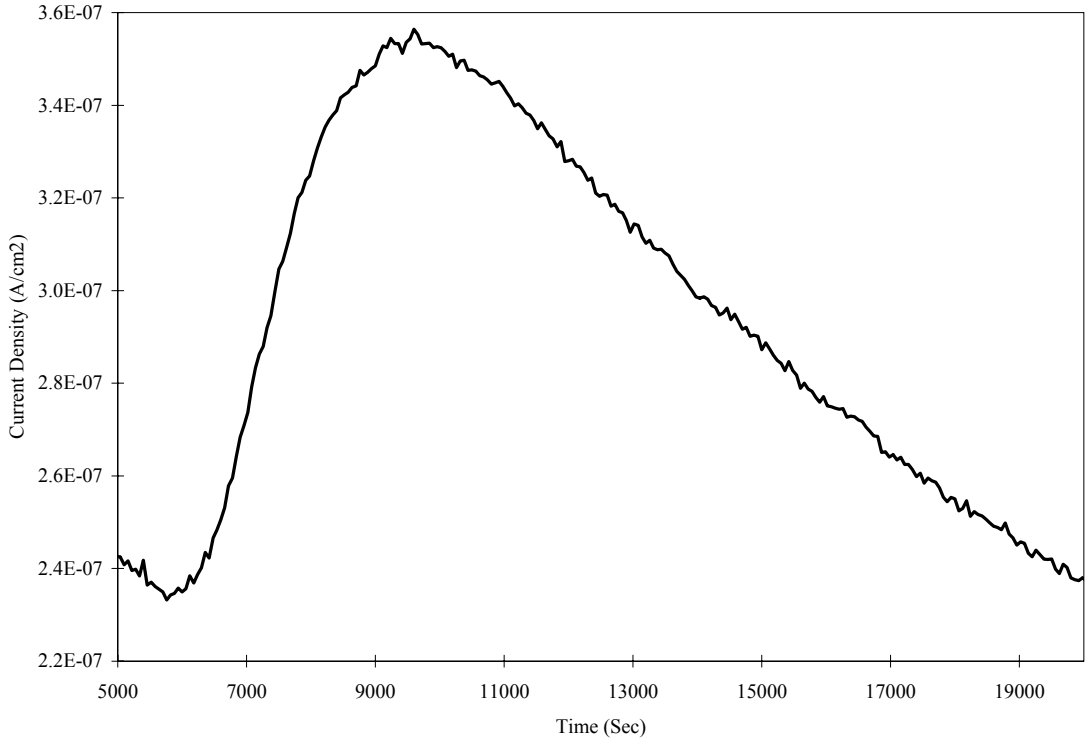

Figure 102 - Representative permeation curve for Temper 650^{o}C for one hour pipeline steel microstructure

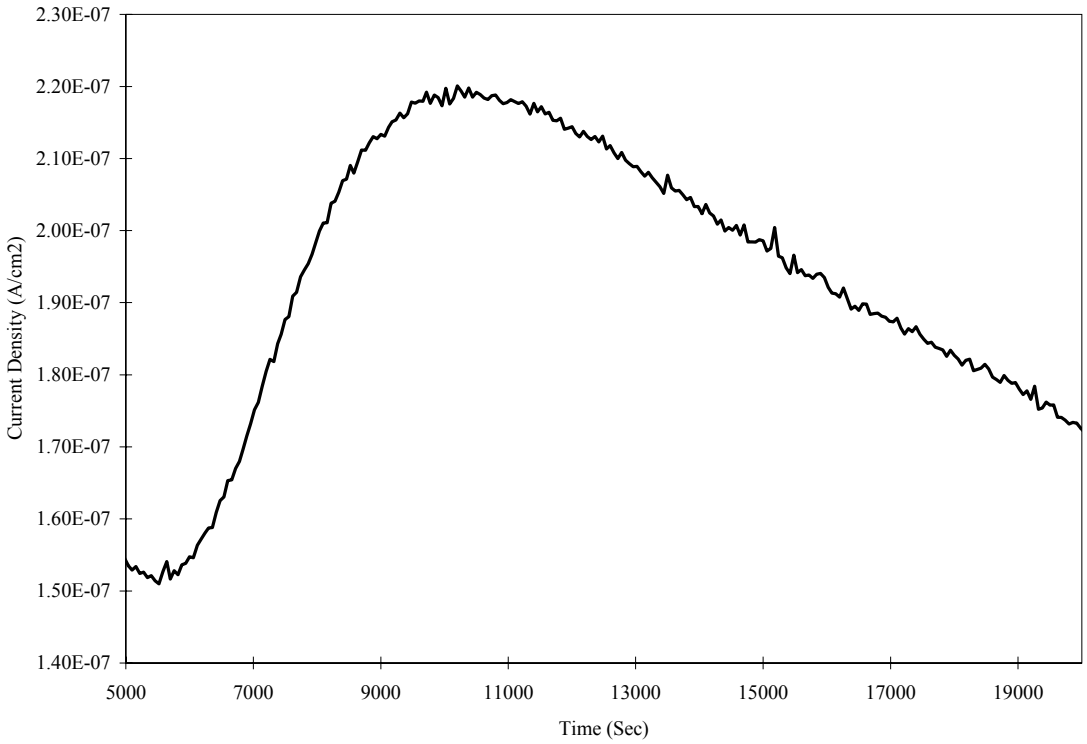

Figure 103 - Representative permeation curve for Temper 650^{o}C for one day pipeline steel microstructure

Figure 104 - Representative permeation curve for Temper 650oC for one week pipeline steel microstructure

REFERENCES

1. Jones, D.A., *Principles and Prevention of Corrosion*. Second ed. 1996, Upper Saddle River, NJ: Prentice Hal.

2. Jones, D.A., *Localized Surface Plasticity During Stress Corrosion Cracking.* Corrosion, 1996. **52**(2): p. 356-362.

3. Ford, F.P., *Stress Corrosion Cracking*, in *Corrosion Processes*, R.N. Parkins, Editor. 1982, Applied Science Publishers: London. p. 271-303.

4. Parkins, R.N., *Mechanistic Aspects of Intergranular Stress Corrosion Cracking of Ferritic Steels.* Corrosion, 1996. **52**(5): p. 363-374.

5. Galvele, J.R., *Surface mobility mechanism of stress-corrosion cracking.* Corrosion Science, 1993. **35**(1-4 Advances in Corrosion and Protection, Pt. 1): p. 419-434.

6. Gabetta, G., G.S.D. Liberto, and A. Bennardo, *Laboratory Tests Reproduce Transgranular Stress Corrosion Cracking Observed in Field*, in *Corrosion NACExpo 2000*. 2000, NACE International: Orlando, FL.

7. Sofronis, P. and I.M. Robertson. *Viable Mechanism of Hydrogen Embrittlement-A Review*. in *Hydrogen in Matter: Second International Symposium on Hydrogen in Matter*. 2006: American Institute of Physics.

8. Lufrano, J., P. Sofronis, and H.K. Birnbaum, *Modeling of Hydrogen Transport and Elastically Accommodated Hydride Formation Near a Crack Tip.* Journal of Mechanical Physics and Solids, 1996. **44**(2): p. 179-205.

9. Beachem, *A New Model for Hydrogen-Assisted Cracking.* Metallurgical Transactions, 1972. **3**(2): p. 437.

10. Birnbaum, H.K. and P. Sofronis, *Hydrogen-enhanced localized plasticity-a mechanism for hydrogen-related fracture.* Materials Science and Engineering, 1994. **A176**: p. 191-202.

11. Birnbaum, H.K. and P. Sofronis, *Hydrogen-enhanced localized plasticity-a mechanism for hydrogen-related fracture.* Materials Science & Engineering, 1994. **A176**: p. 191-202.

12. Sofronis, P., Y. Liang, and N. Arava, *Hydrogen induced shear localization of the plastic flow in metals and alloys.* European Journal of Mechanics: A - Solid Mechanics, 2001(20): p. 857-872.

13. Mishin, Y., P. Sofronis, and J.L. Bassani, *Thermodynamic and kinetic aspects of interfacial decohesion.* Acta Materialia, 2002. **50**: p. 3609-3622.

14. Board, N.E., *Public Inquiry Concerning Stress Corrosion Cracking on Canadian Oil and Gas Pipelines*, N.E. Board, Editor. 1996, National Energy Board: Canada.

15. Leis, B.N. and R.J. Eiber. *Stress-Corrosion Cracking on Gas-Transmission Pipelines: History, Causes, and Mitigation*. in *First International Business Conference on Onshore Pipelines*. 1997. Berlin.

16. U. S. Department of Transportation, Pipeline and Hazardous Materials Safety Administration - Office of Pipeline Safety (OPS). *Significant Pipeline Safety Incidents*. [website] 2007 07/20/07 [cited 2007 August 29, 2007].

17. Delanty, B. and J. O'Beirne, *Major field study compares pipeline SCC with Coatings.* Oil & Gas Journal, 1992: p. 39-44.

18. Parkins, R.N., *A Review of Stress Corrosion Cracking of High Pressure Gas Pipelines*, in *Corrosion NACExpo 2000*. 2000, NACE International: Orlando, FL.

19. Parkins, R.N., W.K.B. Jr., and B.S. Delanty, *Transgranular Stress Corrosion Cracking of High-Pressure Pipelines in Contact with Solutions of Near Neutral pH.* Corrosion 1994. **50**(5): p. 394-408.

20. Pilkey, A.K., S.B. Lambert, and A. Plumtree, *Stress Corrosion Cracking of X-60 Line Pipe Steel in a Carbonate-Bicarbonate Solution.* Corrosion, 1995. **51**(2): p. 91-96.

21. Parkins, R.N., *Factor Influencing Stress Corrosion Crack Growth Kinetics.* Corrosion, 1987. **43**(3): p. 130-139.

22. Fang, B.Y., et al., *Review of stress corrosion cracking of pipeline steels in "low" and "high" pH solutions.* Journal of Materials Science, 2003. **38**: p. 127.

23. Parkins, R.N., E. Belhimer, and W.K.B. Jr., *Stress Corrosion Cracking Characteristics of a Range of Pipeline Steels in Carbonate-Bicarbonate Solution.* Corrosion, 1993. **49**(12): p. 951-966.

24. Beavers, J.A. and K.C. Garrity, *100 mV Polarization Criterion and External SCC of Underground Pipelines*, in *Corrosion 2001*. 2001, NACE International.

25. Fessler, R., *Stress-Corrosion-Cracking Gap Analysis*, I. BIZTEK Consulting, Editor. 2002, Corrosion and Inspection Technical Committee of Pipeline Research Council International, Inc.

26. Parkins, R.N. and P.M. Singh, *Stress Corrosion Crack Coalescence.* Corrosion, 1990. **46**(6): p. 485-499.

27. Manfredi, C. and J.L. Otegui, *Failures by SCC in buried pipelines.* Engineering Failure Analysis, 2002. **9**: p. 495-509.

28. Jack, T.R., et al., *Generation of Near Neutral pH and High pH SCC Environments on Buried Pipelines*, in *Corrosion NACExpo 2000*. 2000, NACE International: Orlando, FL.

29. Dolgov, I.A., et al., *Distribution of Corrosive Flaws Along a Trunk Gas Pipeline Section.* Russian Journal of Nondestructive Testing, 2003. **39**(11): p. 843-851.

30. Chen, W., F. King, and E. Vokes, *Characteristics of Near-Neutral-pH Stress Corrosion Cracks in an X-65 Pipeline.* Corrosion, 2002. **58**(3): p. 267-275.

31. Clover, D., et al., *The influence of microstructure on the corrosion rate of various carbon steels.* Journal of Applied Electrochemistry, 2005. **35**(139-149).

32. American Pipeline Institute, ed. *API Specification for line pipe: Specification 5L, 5LS, and 5LX*. 33rd ed. API Specifications, ed. American Pipeline Institute Production Department. 1983, American Petroleum Institute, Production Department: Dallas, Texas.

33. Asahi, H., et al., *Role of Microstructures on Stress Corrosion Cracking of Pipeline Steels in Carbonate-Bicarbonate Solution.* Corrosion, 1999. **55**(7): p. 664-652.

34. Hillenbrand, H.-G., M. Graf, and C. Kalwa, *Development and Production of High Strength Pipeline Steels*, in *International Symposium Niobium 2001*. 2001, Niobium 2001 Ltd. & TMMS: Orlando, FL

35. Grabke, H.J. and E. Riecke, *Absorption and Diffusion of Hydrogen in Steel.* Materiali in Tehnologije, 2000. **34**(6): p. 331-342.

36. Michael Baker Jr. Inc.., *Stress Corrosion Cracking Study: Final Report*. 2005, Department of Transportation, Research and Special Programs Administration, Office of Pipeline Safety. p. 201.

37. Kushida, T., et al., *Effects of metallurgical factors and test conditions on near neutral pH SCC of Pipeline Steels*, in *Corrosion2001*. 2001, NACE International.

38. Kimura, M., et al., *Effects of Metallurgical Factors and Test Conditions on Low-pH Type Stress Corrosion Cracking of Pipelines.* Fitness-for-Service Evaluations in Petroleum and Fossil Power Plants, 1998. **PVP-Vol 380**: p. 265-272.

39. Chu, R., et al., *Microstructure Dependence of Stress Corrosion Cracking Initiation in X-65 Pipeline Steel Exposed to a Near-Neutral pH Soil Environment.* Corrosion, 2004. **60**(3): p. 275-283.

40. Chen, W., et al., *Effect of Precyclic Loading on Stress-Corrosion-Cracking Initiation in an X-65 Pipeline Steel Exposed to Near-Neutral pH Soil Environment.* Metallurgical and Materials Transactions, 2003. **34A**(11): p. 2601.

41. Wang, Y.-Z., R.W. Revie, and R.N. Parkins, *Mechanistic Aspects of Stress Corrosion Crack Initiation and Early Propagation*, in *Corrosion NACExpo 99*. 1999, NACE International: San Antonio, Texas.

42. Chen, W., et al., *Environmental Aspects of Near-Neutral pH Stress Corrosion Cracking of Pipeline Steels.* Metallurgical and Materials Transactions, 2002. **33A**(5): p. 14291436.

43. Parkins, R.N. and S. Zhou, *The Stress Corrosion Cracking of C-Mn Steel in CO_2-HCO_3^--CO_3^{2-}- Solutions. II. Electrochemical and Other Data.* Corrosion Science, 1997. **39**(1): p. 175-191.

44. Parkins, R.N. and S. Zhou, *The Stress Corrosion Cracking of C-Mn Steel in CO_2-HCO_3^--CO_3^{2-} Solutions. I. Stress Corrosion Data.* Corrosion Science, 1997. **39**(1): p. 159-173.

45. Parkins, R.N., *Investigations Relating to Environment Sensitive Fracture in the TransCanada Pipeline System*. 1988, University of Newcastle upon Tyne - Department of Metallurgy and Engineering Materials.

46. Harle, B.A. and J.A. Beavers, *Technical Note: Low-pH Stress Corrosion Crack Propagation in API X-65 Line Pipe Steel.* Corrosion, 1993. **49**(10): p. 861-863.

47. Gabetta, G., *Transgranular Stress Corrosion Cracking of Low Alloy Steels in Diluted Solutions.* Corrosion, 1997. **53**(7): p. 516-524.

48. Johnson, J.T., et al., *Effects of O_2 and CO_2 on Near-Neutral-pH Stress Corrosion Crack Propagation*, in *Corrosion NACExpo 2001*. 2000, NACE International: Houston, TX.

49. Gu, B., et al., *Transgranular Stress Corrosion Cracking of X-80 and X-52 Pipeline Steels in Dilute Aqueous Solution with Near-Neutral pH.* Corrosion, 1999. **55**(3): p. 312-318.

50. Ahmed, T.M., et al., *Cyclic Crack Growth Rates of X-60 Pipeline Steel in a Neutral Dilute Solution.* Corrosion, 1997. **53**(7): p. 581-590.

51. King, F., et al., *Cathodic Protection of Pipelines in High Resistivity Soils and the Effect of Seasonal Changes*, in *CORROSION2006*. 2006, NACE International: San Diego, CA.

52. Rebak, R.B., et al., *Effect of Solution Composition and Electrochemical Potential on Stress Corrosion Cracking of X-52 Pipeline Steel.* Corrosion, 1996. **52**(5): p. 396.

53. Liu, X. and X. Mao, *Electrochemical Polarization and Stress Corrosion Cracking Behaviors of a Pipeline Steel in Dilute Bicarbonate Solution with Chloride Ion.* Scripta Metallurgica et Materialia, 1995. **33**(1): p. 145-150.

54. Leis, B.N. and R.N. Parkins, *Mechanics and Material Aspects in Predicting Serviceability Limited by Stress-Corrosion Cracking.* Fatigue & Fracture of Engineering Materials & Structures, 1998. **21**: p. 583-601.

55. Fessler, R.R. and K. Krist, *Research Challenges Regarding Stress-Corrosion Cracking of Pipelines*, in *Corrosion NACExpo 2000*. 2000, NACE International: Orlando, FL.

56. Parkins, R.N. and J.A. Beavers, *Some Effects of Strain Rate on the Transgranular Stress Corrosion Cracking of Ferritic Steels in Dilute Near-Neutral-pH Solutions.* Corrosion, 2003. **59**(3): p. 258-273.

57. Qin, Z., et al., *Localized Dissolution of Millscale-Covered Pipeline Steel Surfaces.* Corrosion, 2004. **60**(10): p. 906-914.

58. Eadie, R., et al. *Near-Neutral pH Stress Corrosion Cracking in Steel Pipelines*. in *16th International Corrosion Congress*. 2005. Beijing, China.

59. Yunovich, M., Z. Xia, and Z. Szklarska-Smialowska, *Factors Influencing Stress Corrosion Cracking of Caron Steel in Diluted Bicarbonate Environments.* Corrosion, 1998. **54**(2): p. 155-161.

60. Evans, J.T. and R.N. Parkins, *Creep Induced by Load Cycling in a C-Mn Steel.* Acta Metallurgical, 1976. **24**: p. 511.

61. Hagiwara, N. and N. Oguchi, *Fracture Toughness of Line Pipe Steels Under Cathodic Protection Using Crack Tip Opening Displacement Tests.* Corrosion, 1999. **55**(5): p. 503-511.

62. Guo, H., et al., *SCC Propagation Behavior of X-70 Pipeline Steel Undercyclic Loading in Near-Neutral pH Solutions*, in *16th International Corrosion Congress*. 2005, 16th ICC: Beijing, China.

63. Kermani, M.B. and A. Morshed, *Carbon Dioxide Corrosion in Oil and Gas Production - A Compendium.* Corrosion, 2003. **59**(8): p. 683.

64. Schwenk, W., *Corrosion of unalloyed steel in oxygen-free carbonic acid solution.* Werkstoffe und Korrosion, 1974. **25**(9): p. 643-646.

65. Waard, C.D., U. Lotz, and D.E. Milliams, *Predictive model for carbon dioxide corrosion engineering in wet natural gas pipelines.* Corrosion, 1991. **47**(12): p. 976-985.

66. Ogundele, G.I. and W.E. White, *Observations on the influence of dissolved hydrocarbon gases and variable water chemistries on corrosion of an API-L80 steel.* Corrosion, 1987. **43**(11): p. 665-673.

67. Crolet, J.L. and M.R. Bonis, *pH Measurements in aqueous carbon dioxide solutions under high pressure and temperature.* Corrosion, 1983. **39**(2): p. 39-46.

68. Kinsella, B., Y.J. Tan, and S. Bailey, *Electrochemical Impedance Spectroscopy and Surface Characterization Techniques to Study Carbon Dioxide Corrosion Product Scales.* Corrosion, 1998. **54**(10): p. 835.

69. Sofronis, P. and R.M. McMeeking, *Numerical Analysis of Hydrogen Transport near a blunting crack tip.* Journal of Mechanical Physics and Solids, 1989. **37**(3): p. 317-359.

70. Flis, J., ed. *Corrosion of Metals and Hydrogen-Related Phenomena: Selected Topics*. Materials Science Monographs, ed. J. Flis. Vol. 59. 1991, Elsevier: Amsterdam, Oxford, New York, Tokyo. 240-371.

71. Scoppio, L. and M. Barteri. *Methods of Hydrogen Uptake Measurements by Electrochemical Permeation Test on Low Alloy Steel*. in *Hydrogen Transport and Cracking in Metals*. 1994. Teddington, UK: The Institute of Materials.

72. Beavers, J.A., et al., *Near-Neutral pH SCC: Crack Propagation in Susceptible Soil Environments*, in *NACExpo 2001*. 2001, NACE International.

73. Hardie, D., E.A. Charles, and A.H. Lopez, *Hydrogen embrittlement of high strength pipeline steels.* Corrosion Science, 2006. **48**: p. 4378-4385.

74. He, D.X., W. Chen, and J.L. Luo, *Effect of Cathodic Potential on Hydrogen Content in a Pipeline Steel Exposed to NS4 Near-Neutral pH Soil Solution.* Corrosion, 2004. **60**(8): p. 778-786.

75. Yan, M. and Y. Weng, *Study on hydrogen absorption of pipeline steel under cathodic charging.* Corrosion Science, 2006. **48**: p. 432-444.

76. Luppo, M.I. and J. Ovejero-Garcia, *The Influence of Microstructure on the Trapping and Diffusion of Hydrogen in a Low Carbon Steel.* Corrosion Science, 1991. **32**(10): p. 1125.

77. Albert, S.K., et al., *Influence of alloying on hydrogen-assisted cracking and diffusible hydrogen content in Cr-Mo steel welds.* Sadhana, 2003. **28**(3&4): p. 383-393.

78. Ohmisawa, T., S. Uchiyama, and M. Nagumo, *Detection of hydrogen trap distribution in steel using a microprint technique.* Journal of Alloys and Compounds, 2003. **356-357**: p. 290-297.

79. Qiao, L.J., J.L. Luo, and X. Mao, *The role of hydrogen in the process of stress corrosion cracking of pipeline steels in dilute carbonate-bicarbonate solution.* Journal of Materials Science Letters, 1997. **16**: p. 516-520.

80. Qiao, L.J., J.L. Luo, and X. Mao, *Hydrogen Evolution and Enrichment Around Stress Corrosion Crack Tips of Pipeline Steels in Dilute Bicarbonate Solution.* Corrosion, 1998. **54**(2): p. 115-120.

81. Ananta, G., A. Nagu, and T. Namboodhiri, *Effect of heat treatments on the hydrogen embrittlement susceptibility of API-65 grade line-pipe steel.* Bull. Mater. Sci., 2003. **26**(4): p. 435-439.

82. Fang, B.Y., et al., *Hydrogen in stress corrosion cracking of X-70 pipeline steels in near-neutral pH solution.* Journal of Materials Science, 2006. **41**: p. 1797-1803.

83. Puiggali, M., S. Rousserie, and M. Touzet, *Fatigue Crack Initiation on Low-Carbon Steel Pipes in a Near-Neutral-pH Environment Under Potential Control Conditions.* Corrosion, 2002. **58**(11): p. 961-970.

84. Vasil'ev, V.Y., et al., *Internal Stresses, Corrosion and Electrochemical Behavior in Soils, and Stress Corrosion of Pipe Steels.* Protection of Metals, 2002. **38**(2): p. 166-171.

85. King, F., et al., *Mechanistic Studies of Initiation and Early Stage Crack Growth for Near-Neutral pH SCC on Pipelines*, in *Corrosion NACExpo 2000*. 2000, NACE International: Orlando, FL.

86. Eadie, R.L., K.E. Szklarz, and R.L. Sutherby, *Corrosion Fatigue and Near-Neutral pH Stress Corrosion Cracking of Pipeline Steel and the Effect of Hydrogen Sulfide.* Corrosion, 2005. **61**(2): p. 167-174.

87. Zhang, Z.-Y., et al., *Transgranular Stress Corrosion Cracking of X-60 Pipeline Steel in Simulated Ground Water.* Corrosion, 1999. **55**(3): p. 297-305.

88. Mao, S.X., et al., *The mechanism of hydrogen-facilitated anodic-dissolution-type stress corrosion cracking: theories and experiments.* Philosophical Magazine A, 2001. **81**(7): p. 1813-1831.

89. Gu, B., J. Luo, and X. Mao, *Hydrogen-Facilitated Anodic Dissolution-Type Stress Corrosion Cracking of Pipeline Steels in Near-Neutral pH Solution.* Corrosion, 1999. **55**(1): p. 96-106.

90. Mao, S.X. and M. Li, *Mechanics and Thermodynamics on the Stress and Hydrogen Interaction in Crack Tip Stress Corrosion: Experiment and Theory.* Journal of the Mechanical Physics of Solids, 1998. **46**(6): p. 1125-1137.

91. Pourbaix, M., *Lectures on Electrochemical Corrosion*. Third ed. 1995, Houston, TX: NACE International. 342.

92. Asher, S., et al., *Stress Corrosion Cracking of Pipeline Steel in Near-Neutral pH Environments*, in *Corrosion 2006*. 2006, NACE International: San Diego, CA.

93. Asher, S., et al. *Crack Initiation of Line Pipe Steels in Near-Neutral pH Environments*. in *16th International Corrosion Congress*. 2005. Beijing, China.

94. Colwell, J.A., B.N. Leis, and P.M. Singh, *Recent developments in Characterizing the Mechanism of Near Neutral pH SCC*, in *Corrosion 2005*. 2005, NACE International.

95. *Atlas of Isothermal Transformation Diagrams of B.S. En Steels*. 2nd ed. Special Report No. 56. 1956, London: The Iron and Steel Institute.

96. Gonzalez-Rodriguez, J.G., et al., *Effect of Microstructure on the Stress Corrosion Cracking of X-80 Pipeline Steel in Diluted Sodium Bicarbonate Solutions.* Corrosion, 2002. **58**(7): p. 584-590.

97. Al-Hassan, S., et al., *Effect of Microstructure on Corrosion of Steels in Aqueous Solutions Containing Carbon Dioxide.* Corrosion, 1998. **54**(6): p. 480.

98. Voort, G.F.V., ed. *Atlas of Time-Temperature Diagrams for Irons and Steels*. Materials Data Series. 1991, ASM International: USA.

99. Turnbull, A. *Standardization of Hydrogen Permeation Measurement by the Electrochemical Technique*. in *Proceedings of a Conference held at The National Physical Laboratory*. 1994. Teddington, UK: The Institute of Materials.

100. Devanathan, M.A.V. and Z. Stachurski, *The adsorption and diffusion of electrolytic hydrogen in palladium.* Proceedings of the Royal Society, 1962. **270**: p. 90-102.

101. Yalci, H.K. and D.V. Edmonds, *Application of the Hydrogen Microprint and the Microautoradiography Techniques to a Duplex Stainless Steel.* Materials Characterization, 1995. **34**: p. 97-104.

102. Ovejero-Garcia, J., *Hydrogen microprinting technique in the study of hydrogen in steels.* Journal of Materials Science, 1985. **20**(7): p. 2623-2629.

103. Luppo, M.I. and J. Ovejero-Garcia, *A new application of the hydrogen microprint technique for the study of hydrogen behavior in steels.* Journal of Materials Science Letters, 1995. **14**: p. 682-684.

104. Ohmisawa, T., S. Uchiyama, and M. Nagumo, *Detection of hydrogen trap distribution in steel using a microprinting technique.* Journal of Alloys and Compounds, 2003. **356-357**: p. 290-294.

105. Wipf, H., *Solubility and Diffusion of Hydrogen in Pure Metals and Alloys.* Physica Scripta, 2001. **T94**: p. 43-51.

106. Ramunni, V.P., T.D.P. Coelho, and P.E.V.de Miranda, *Interaction of hydrogen with the microstructure of low-carbon steel.* Materials Science and Engineering 2006. **A 435-436**: p. 504-514.

107. Luppo, M.I. and J. Ovejero-Garcia, *Application of the hydrogen-permeation method to the study of carbide precipitation kinetics in a low-carbon martensite.* Materials Characterization, 1998. **40**(3): p. 189-196.

108. Luu, W.C. and J.K. Wu, *The Influence of Microstructure on Hydrogen Transport in Carbon Steels.* Corrosion Science, 1996. **38**(2): p. 239-245.

109. *Atlas of Microstructures of Industrial Alloys*. 8th ed. Metals Handbook, ed. A.H. Committee. Vol. 7. 1972, Metals Park, Ohio: American Society for Metals.

110. Jesicka, J., et al., *The evolution of dislocation density during heat treatment and creep of tempered martensite ferritic steels.* Acta Materialia, 2003. **51**: p. 4847-4862.

111. Pesicka, J., et al., *The evolution of dislocation density during heat treatment and creep of tempered martensite ferritic steels.* Acta Materialia, 2003. **51**: p. 4847-4862.

112. Brooks, C.R., *Principles of the Heat Treatment of Plain Carbon and Low Alloy Steels*. 1996, Materials Park, Ohio: ASM International.

113. Roark, R.J., ed. *Formulas for Stress and Strain*. 4th ed. 1965, McGraw-Hill Book Company: NY.